Computational screening of new inorganic materials for highly efficient solar energy conversion

Kuhar, Korina; Jacobsen, Karsten Wedel; Thygesen, Kristian Sommer

Publication date:
2017

Document Version
Publisher's PDF, also known as Version of record

Ph.D. Thesis
Doctor of Philosophy

DTU Physics
Department of Physics

Computational screening of new inorganic materials for highly efficient solar energy conversion

Korina Kuhar

Kongens Lyngby 2017

DTU Physics
Department of Physics
Technical University of Denmark

Fysikvej
Building 307
2800 Kongens Lyngby, Denmark
Phone +45 4525 3344
info@fysik.dtu.dk
www.fysik.dtu.dk

Summary

The world's energy consumption is rising, and the demand for energy is projected to increase even more in the future. At the moment, we rely on energy from fossil fuels, which are harmful to the environment, and the future increases in consumption will be strongly harmful to both the environment and human well being. Additionally, fossil fuels are non-renewable, and there are only limited reserves on the planet. An alternative to using fossil fuels is to harvest energy from renewable and environmentally benign sources, such as the sun, which theoretically provides the largest source of energy that we have access to. Despite the vast amounts of energy at our disposal, we are not able to harvest this solar energy efficiently. Currently, there are a few ways of converting solar power into usable energy, such as photovoltaics (PV) or photoelectrochemical generation of fuels (PC). PV processes in solar cells convert solar energy into electricity, and PC uses harvested energy to conduct chemical reactions, such as splitting water into oxygen and, more importantly, hydrogen, also known as the fuel of the future.

Further progress in both PV and PC fields is mostly limited by the flaws in materials used as photoabsorbers. Silicon as an absorber dominantes the PV community and all other semiconductors face significant challenges, for various different reasons, when suggested for large scale deployment. Advances in PC, on the other hand, are mostly held back due to the fact that no single material, which can both absorb light and catalyse the relevant chemical reactions, has been found. A proposed alternative, using two materials in tandem instead of one, has the potential to successfully perform the task. However, progress in this field is inhibited by the lack of high band gap photoabsorbing materials. In this work a high-throughput computational search for suitable absorbers for PV and PC applications is presented. A set of descriptors has been developed, such that each descriptor targets an important property or issue of a good solar energy conversion material. The screening study was performed step-wise, so that in each step a new descriptor and associated criterion were introduced and all the materials failing to satisfy the criterion are removed from the study. The corresponding descriptors were obtained within the scope of quantum mechanics using Density Functional Theory.

This method of materials design is first applied to materials found by substituting atomic cations in crystal structures of the ABS_3 stoichiometry, resulting in several candidates which we believe have the potential to work in a PV and PC device. One of these candidates has been successfully synthesized by our collaborators, and the mea-

sured band gap is in accordance with the theoretically calculated one. Furthermore, a study on previously synthesized semiconductors yielded a list of stable materials which have not yet been explored for PV or PC.

A similar study has been performed on II-IV-V_2 compounds, and has revealed some interesting trends within the class, resulting in several interesting candidate materials. A few of these have already been extensively investigated by others.

Resumé

Verdens energiforbrug er højt, og forventes at stige over de næste år. I øjeblikket stammer størstedelen af den energi vi bruger fra fossile brændstoffer, såsom kul og olie. Forbrændingsprocesserne, der er nødvendige for at bruge denne energi, er skadelige for klimaet, for miljøet og for det menneskelige helbred. Derudover er der kun begrænsede reserver af fossile brændstoffer på kloden, og vi risikerer på et tidspunkt at løbe tør.

En mulighed for at udfase brugen af fossile brændstoffer er i højere grad at benytte sig af alternative og vedvarende energiformer, såsom solenergi. Solen er den største energikilde vi har adgang til, og dens stråler leverer mere end nok energi til helt at kunne erstatte de fossile brændstoffer. Desværre er det endnu ikke muligt at udnytte denne energikilde effektivt.

Lige nu findes der to hovedmetoder til at udnytte energien fra solen: Den fotovoltaiske effekt, som vi kender i solceller, der omdanner lys direkte til elektricitet, og fotoelektrokemiske processer, hvor lyset for eksempel bruges til at spalte vand til ilt og brint, som så kan bruges som brændstoffer.

Den største hæmsko for udbredelsen af solenergi er de materialer der bruges til at absorbere lyset. I fotovoltaiske processer anvendes ofte silicium, og alle andre materialer, der har været foreslået, har ulemper der gør at de ikke kan anvendes i større skala. Hvad angår de fotoelektriske processer, har man endnu ikke fundet ét materiale der både kan absorbere lys effektivt og danne de rigtige kemiske produkter. En mulighed er i stedet at anvende to materialer, der arbejder i tandem, men her har det vist sig vanskeligt at finde materialer med relevante båndgab.

I denne afhandling foretages en systematisk undersøgelse af mange forskellige stoffer, for at se hvordan de egner sig til brug i fotovoltaiske eller -elektrokemiske processer. For at gøre dette findes en række nøgleparametre (såkaldte deskriptorer), således at hver deskriptor indfanger en vigtig egenskab, der afgører om et materiale kan anvendes eller ej. Undersøgelsen er lavet som trinvis screening: Ved hvert trin anvendes en ny deskriptor og en tilhørende grænseværdi, og alle materialer som hvor parameteren er på den forkerte side af grænseværdien, forksastes. Beregningerne af deskriptorerne foretages ved brug af kvantemekanikken og tæthedsfunktionalteori (DFT)

Først anvendes denne proces på materialer med den kemiske formel ABS_3, og resultatet er en håndfuld materialer, som potentielt kan anvendes til enten fotovoltaiske eller -elektrokemiske processer. En af disse er blevet syntetiseret, og det målte båndgap stemmer overens med det beregnede. Der er også foretaget en undersøgelse af kendte materialer, som viste at der er også her er nogle materialer som

potentielt kan anvendes.

Der er foretaget en lignende undersøgelse for materialer med formlen ABX_2, som viste nogle interessante tendenser blandt de forskellige materialer, og også gav en håndfuld potentielle materialer. Nogle af disse er er før blevet grundigt studeret til netop lysabsorption.

Preface

This thesis is submitted in candidacy for the Ph. D. degree in physics from the Technical University of Denmark. The work was carried out at the Center for Atomic-scale Materials design (CAMd) at the Department of Physics in the period November 2014 to October 2017, under supervision of professors Karsten W. Jacobsen and Kristian S. Thygesen. The Ph. D. project was funded by an internal scholarship from DTU and was affiliated with the VILLUM FONDEN (research grant 9455).

Kongens Lyngby, October 28, 2017

Korina Kuhar

Acknowledgements

I would like to express my gratitude to my supervisor, Karsten W. Jacobsen, for his guidance and support. I feel so privileged to have had the opportunity to work and learn from such an expert and enthusiast. Mostly, I am grateful for all his patiance and for keeping me motivated. Your door is always open and you mean it. Also, I would like to thank Kristian S. Thygesen for all the good scientific discussions and contributions to my projects. Thanks also to Thomas Bligaard for hosting me in his group at the Stanford University.

I was fortunate to collaborate with Andrea Crovetto, whom i shall thank for all the effort he put in the project and for all the good discussions.

I cannot thank enough Jens Jørgen Mortensen for always selflessly helping out with coding and software challenges. I could always count on you. Special thanks to Marianne for helping out with my relocation to Denmark and other administrative matters, but most of all, for her friendship which goes beyond the work place. Ole and Marcin, thank you for making sure we have a great computational support.

My friend and collegue Mohnish deserves a special thanks for helping me cope with all the challenges of my project. Your knowledge, intuition and enthusiasm was a true inspiration. I wish you all the best in the future. I am truly happy, I got to be part of your wedding in India, it was an unique and beautiful experience.

Thanks to my office mate Sten for all the essential distractions and good discussions. More importantly, thanks for your support during the tough times and giving me helpful advices. A further thanks to Per, for his kindness and for always being able to count on him. I would also like to acknowledge the people who took the time to read through my thesis and suggested improvements: Mohnish, Per, Sten, Peter, Hugh, Morten and Estafania, all the typos are on you.

My friends and colleagues at the CAMd really made this time count. I had so much fun to hanging out with you, whether it was at a conference or just during a coffee and cookies break. Kristian Ø, Niels, Kirsten, Chris, Nicki, Filip, Simone, Morten, Martin, Manuel, Chengjun, Mikkel, Jacob M., Jakob, Tuomas, Thorsten, Marianne S., Thomas, Peter, Anders, Estefania, Daniele, Thorbjørn, Diana, Mads, Mathias, Jacob L., and once again, Sten, Mohnish and Per, we had a good run and you will be missed.

Ivana deserves a special thank you since she has been a true friend in the past three years. Really meant a lot having you around, you are a family to me. Nicholas, thank you for your love and support but mostly for your understanding and patience,

as you suffered the most in the past few months.

The last one is for my family: I šećer na kraju, mama, tata, Andrej, Filip i nona, ne mogu opisati koliko sam sretna što vas imam i što ste uvijek uz mene. Ovaj uspjeh je vaš koliko i moj, jer ne znam kako bi uspjela bez vaše požrtvovnosti i potpore. Iako je bilo teško biti daleko od vas i vama daleko od mene, nije bitno koliko smo daleko na karti dok god ste najbliže u srcu.

Contents

Summary i

Resumé iii

Preface v

Acknowledgements vii

Contents ix

1 Introduction 1
- 1.1 Solar energy . . . 2
- 1.2 One- and two-photon devices . . . 3
- 1.3 Obtaining new solar energy conversion materials . . . 4
- 1.4 Outline . . . 6

2 Density Functional Theory 7
- 2.1 The electronic structure problem . . . 7
- 2.2 Density Functional Theory . . . 9
- 2.3 Practical implementation of DFT in the GPAW code . . . 11
- 2.4 Band gap calculations using DFT . . . 12
- 2.5 Calculating total energies and heats of formation of solid crystals . . . 16

3 Methods 23
- 3.1 Computational screening techniques . . . 23
- 3.2 Overview of screening descriptors and criteria . . . 27
- 3.3 Calculating descriptors in practice using DFT . . . 32

4 Summary of the results 39
- 4.1 Paper I: Defect-Tolerant Monolayer Transition Metal Dichalcogenides 39
- 4.2 Paper II: II−IV−V_2 and III−III−V_2 Polytypes as Light Absorbers for Single Junction and Tandem Photovoltaic Device . . . 42
- 4.3 Paper III: Sulfide Perovskites for Solar Energy Conversion Applications: Computational Screening and Synthesis of the Selected Compound $LaYS_3$ 44

4.4 Paper IV: High-Throughput Assessment of Experimentally Stable Materials for Single Junction and Tandem Photovoltaic Devices 48
4.5 Paper V: Trigonal Selenium as Large Band Gap Material in Tandem Photoelectrochemical Devices 51

5 Papers **53**
5.1 Paper I:Defect-Tolerant Monolayer Transition Metal Dichalcogenides . 53
5.2 Paper II: II−IV−V_2 and III−III−V_2 Polytypes as Light Absorbers for Single Junction and Tandem Photovoltaic Device 60
5.3 Paper III: Sulfide Perovskites for Solar Energy Conversion Applications: Computational Screening and Synthesis of the Selected Compound $LaYS_3$ 68
5.4 Paper IV: High-Throughput Computational Assessment of Previously Synthesized Semiconductors for Photovoltaic and Photoelectrochemical Devices. 86
5.5 Paper V: Trigonal Selenium as a Large Band Gap Material in Tandem Photoelectrochemical Devices 117

6 Additional information **129**
6.1 Paper I:Defect-Tolerant Monolayer Transition Metal Dichalcogenides . 129
6.2 Paper II: II−IV−V_2 and III−III−V_2 Polytypes as Light Absorbers for Single Junction and Tandem Photovoltaic Device 131
6.3 Paper III: Sulfide Perovskites for Solar Energy Conversion Applications: Computational Screening and Synthesis of the Selected Compound $LaYS_3$ 132

7 Additional results and implementation **135**
7.1 Unraveling low-dimensional structure of experimentally known compounds 135

8 Conclusion **145**

Bibliography **147**

CHAPTER 1

Introduction

Fossil fuels, which modern society relies on, draws finite resources that will dwindle, become too expensive or too environmentally damaging to retrieve in the foreseeable future. When these fuels are combusted for the production of energy, large amounts of greenhouse gases are emitted which not only pollute the environment but represent a serious threat to human health. In contrast, alternative, clean energy sources, such as wind and solar energy, are constantly replenished and will never be exhausted. In order to meet increased energy demand without harming the environment, it is necessary to increase the amount of energy produced from renewable sources. Most renewable energy comes from the sun, whose annual potential is several times larger than the total world energy consumption[1, 2]. However, due to the facts that i) the solar energy density is far lower than any of the fossil energy, and ii) that solar energy is difficult to be stored in the form of electricity or heat (as compared with fossil fuel), utilizing the solar energy in efficient and economic way remains a challenge for scientists and engineers. In 2015, solar power covered only slightly more than 1% of global electricity demand, as reported by Solar Power Europe[3]. Still, conversion of sunlight directly into electricity has the highest theoretical efficiency and flexibility compared to the conversion efficiencies of heat or biomass, so there is a large potential to be explored.

Inspired by nature's harnessing of solar energy through photosynthesis, the emerging technology of photocatalysis (PC) uses solar energy to drive chemical reactions. The potential applications of photocatalysis are found mainly in the following fields: (i) photolysis of water to yield hydrogen fuel; (ii) photodecomposition or photooxidization of hazardous substances; (iii) artificial photosynthesis and so forth[4].

Some of the current issues blocking a large scale deployment of current PV and PC materials are their toxicity, high production cost, long time stability, purity and efficiency. The idea behind the work reported in this thesis is to find new inorganic materials with features similar to those of known photovoltaic (PV) and PC materials. The focus is on describing macroscopic features using properties calculable at the atomic level using quantum mechanical methods. These properties are then used to perform a computational screening study involving a large number of known semiconductors, and also the design and investigation of new, yet-to-be synthesized materials. The obtained results are meant to guide experimental scientists by giving them insight in a material before it has been made. The scheme reported in this work can easily be adapted and applied to investigate other materials or classes of

materials.

1.1 Solar energy

The base for efficient solar energy conversion is the successful absorption of sunlight. The whole PV and PC industry relies on the absorption of light by a photoactive material, usually a solid semiconductor or a molecule. Generally, harvesting sunlight includes two successive procedures: the generation of excitons (photogenerated electron and hole pair) induced by photon absorption by semiconductor materials with the proper electronic band gap, and the separation of excitons by the built-in electric potential gradient. In 1961, William Shockley and Hans J. Queisser calculated the maximal theoretical efficiency of photovoltaic device (Shockley–Queisser limit or detailed balance limit[5]) of 33.7% for a material with a band gap of 1.34 eV. They assumed a single p-n junction and the only radiative recombination of hole-electron pairs. This means that a hypothetical "perfect" material could convert 33.7% of the input solar energy into electricity. Of course, reality is different so additional losses can massively decrease the efficiency. The up-to-date record of 28.8% is observed in gallium arsenide solar cells, one of the few cases where the reported efficiency is higher than 20 %. Up to now, a great effort has been made in finding ways to minimize those losses.

The current PV market is dominated by silicon modules with a total share of >90%[6]. With it's almost ideal band gap (1.12 eV) and the efficiency of it's cells reaching over 25%[7], silicon seems like an ideal PV material. However, major losses occur due to contact recombination so engineering solutions using minimal contact area are necessary. Furthermore, silicon is an indirect band gap material and as a consequence the absorption coefficient is low. Making thick wafers helps absorbing all photons with energies above the gap, but has the disadvantage of increasing Auger recombination and increasing the device cost. Additionally, obtaining 99.99999% silicon purity, which is a requirement for a working device is another down side. A trade-off between cost and efficiency limits the broader usage of silicon based cells.

The absolute record with 28.8%[7] efficiency is a GaAs solar cell. Solar cells made out of this direct band gap semiconductor (1.43 eV[8]) can achieve great efficiency on a small area, so they are mostly used in niche markets (ex. space technology). The main obstacle limiting the broader application is the usage of the toxic element arsenic. Similarly, CdTe (band gap 1.44 eV[8]) solar cells, where the record efficiency is reported to be 21.5% contains the toxic element cadmium.

Furthermore, InP (band gap 1.35 eV) and GaInP (band gap 1.81 eV), two other III-V compound semiconductors have reached high efficiencies, 22.1% and 20.8%, respectively[6]. One of the limitations is the cost and scarcity of indium, while the high band gap of GaInP has been turned into an advantage by building so called multijunction devices. The basic concept of a multijunction device is to use a high band gap material to absorb higher energy photons, allowing the lower energy photons to go through it and get absorbed by the lower band gap material. Multiple absorbers

in a device results in increased theoretical maximum efficiency with the number of junctions.

Multicomponent thin-film solar cells, known as CIGS ($Cu(In/Ga)(Se/S)_2$) and lately CZTS(Se) ($Cu_2ZnSn(S,Se)_4$) have also shown promising efficiencies, 21.7% and 12.6%, respectively[7]. Flexible (and complex) stoichiometry opens the possibility of band gap tuning but further progress in utilizing the synthesis conditions is necessary to prevent the formation of secondary phases or high defect concentration.

Flaws and limitations of PV devices currently in use confirm the fact that we are still in the incipient phase of harvesting solar energy efficiently. So far, a trade-off between cost, efficiency or potential hazardness had to be made. Addressing the issues and finding a material that is better in all segments is a key priority for bringing the PV technology to a new level. Designing of such material has been the aim of the many scientific studies in the past few decades. Even though great progress has already been made, we are still in search of suitable materials that can possibly be synthesized at the low cost and using small materials quantities.

1.2 One- and two-photon devices

Both PV and PC processes are based on similar principles, relying on materials with band gaps in the visible spectrum, making it possible to absorb visible light photons. Absorbed photon excites an electron an by doing so, generates electron-hole pair, called exciton. Separation of carriers into electrons and holes by the built-in electric potential gradient induces current in the material. If not separated, majority of electron-hole pairs recombine over time, dissipating the input energy. While inducing current is the final goal of the solar cells, a photoelectrochemical device, such as a water splitting device, uses energy of the carriers to overcome the reaction barrier and induce the splitting of water into hydrogen and oxygen.

The free energy cost for obtaining H_2 and O_2 from a water molecule is 1.23 eV, but due to additional energy losses, the total energy required is around 2.3 eV. As a result, the band gap of a PC material should be of the same order. Such a material could achieve only 7% efficiency, and because of large band gap, most visible photons would never be absorbed[9].

The efficiency can be increased by building a device of two absorbing semiconductors in a tandem architecture. A tandem, or two-photon device, consists of two semiconductors with different band gaps: the first one with a larger band gap absorbs high energy photons, while the second one absorbs remaining lower energy photons since it's band gap is much lower. This strategy allows much more of the solar spectrum to be absorbed. The estimated optimal band gap of a small band gap (SBG) material is 1 eV while the large band gap (LBG) materials is expected to have a band gap of 1.7 eV[9–12]. Figure 1.2a shows a device design in which oxygen evolution takes place on the LBG material (photoanode) and the hydrogen evolution takes place on SBG material (photocathode). Positions of band edges, in this case potentials of carriers, should align with the redox levers of water. An alternative design is required if

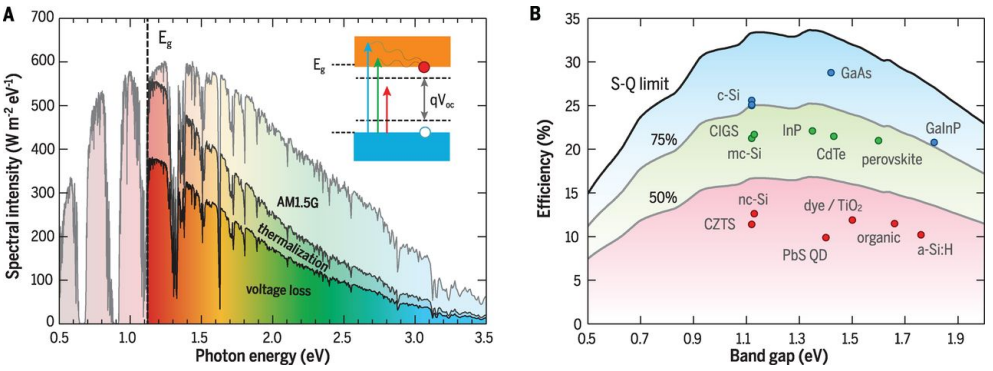

Figure 1.1: Fundamental solar cell efficiency limits and present-day records. (A) AM1.5 solar spectrum with distinct dips due to molecular absorption in the Earth's atmosphere. Photons with energies below the band gap (E_g, dashed black line corresponds to the band gap of Si) are not absorbed, whereas photons with energies above the band gap are not fully converted to electrical energy because of the thermalization of charge carriers. The maximum power generated by the cell is limited by voltage loss relative to the band gap voltage. Inset: Electronic band structure with the separation of the quasi-Fermi levels determining the open-circuit voltage V_{oc}. (B) Theoretical Shockley-Queisser detailed-balance efficiency limit as a function of band gap (black line) and 75% and 50% of the limit (gray lines). The record efficiencies for different materials are plotted for the corresponding band gaps. The figure is reprinted from reference [6].

silicon is used as the SBG material, as shown in figure 1.2b, since screening studies did not find a LBG materials satisfying the alignment criteria[13]. This way, hydrogen evolution moves to LBG materials and consequently oxygen evolution is expected on SBG material.

Additionally, a transparent protective layer can be added to the cathode and a metallic protective layer to the cathode to the device in Design 2 to shield it from corrosion.

1.3 Obtaining new solar energy conversion materials

Independent of the application, PV or PC, the core of a solar energy conversion device is a photoabsorbing material. Even though different applications and different device designs may require materials with different band gaps, a similar basic working

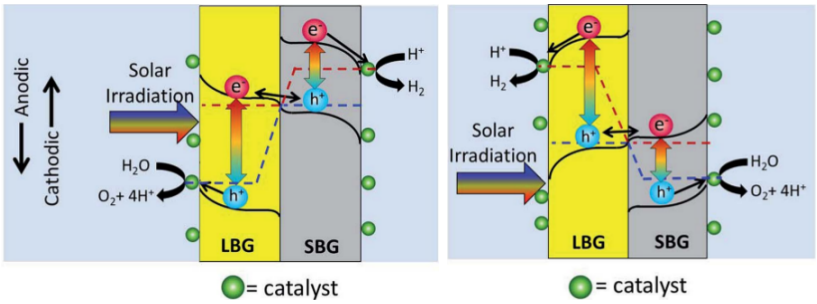

(a) Design 1 **(b)** Design 2

Figure 1.2: Proposed designs for a two-photon water splitting device. (a) The large band gap material (LBG) is the photoanode and the small band gap material (SBG) the photocathode. Vice versa in (b), LBG is the photocathode and SBG the photoanode. Figures from reference [13].

principle implies the materials used posses similar properties. However, this is only valid for properties related to photoabsorption, whereas stability, for example, should be addressed separately due to different environments in which the device should operate. Luckily, different engineering solutions, such as coating of the material, can solve these problems so we do not address it separately in this work. Overall, we can investigate material candidates for absorbers in single-photom and two photon devices simultaneously since majority of relevant properties are the same and it is only their value which distinguishes whether material is more suitable as PV or PC candidate.

Investigating those properties experimentally, for each material at the time, is extremely time consuming and there is no guarantee it will lead to the discovery of a promising material. On the other hand, modern computational techniques and a screening approach can identify relevant materials much faster, decreasing the number of candidates by orders of magnitude before manufacturing the material.

For screening to be successful, it is crucial to understand in depth the problem of investigation. For example, if the goal is to find good solar cell absorber, one needs a well defined set of quantities inherent to a good absorber. Once the properties have been defined, one needs to bring them down to a microscopic level. Combining quantities calculated on atomic scale with macroscopic quantities obtained in the experiments is achieved by so-called descriptors. Each descriptor is targeting an important property or issue of a good solar energy conversion material. A more detailed discussion of descriptors and their role can be found in the chapter 3. Calculated quantities are most often obtained from quantum mechanical calculations, and probably the most widely-used technique is the Density Functional Theory (DFT), which will be discussed in detail in chapter 2.

1.4 Outline

The first chapters (2 and 3) present the necessary background information needed to understand the papers of the thesis. Chapter 4 presents summaries of the papers highlighting the most significant results. Chapter 5 presents the papers and chapter 6 supplies additional information not contained in the papers. Finally, chapter 7 presents implementation and results which did not result in a scientific publication.

CHAPTER 2

Density Functional Theory

Density Functional Theory is a powerful tool used to investigate properties of materials. Based on only element types and atomic positions, total energy, and additionally, optical, electronic and chemical properties can be calculated. Also, a low temperature stable structure can be obtained by minimizing the energy of the system with respect to the atomic structure. This chapter explains the method in detail and its implementation in the electronic structure Grid-based Project Augmented Wave (GPAW) code[**GPAW**, 14]. Furthermore, the way DFT is is used to obtain co-called screening parameters important to the following part of this work is discussed in chapter 3.

2.1 The electronic structure problem

On the fundamental level matter can be understood as an ensemble of interacting atoms. Regardless of which type this ensemble of particles is (solid, liquid, molecules), to truly understand it's properties a relation between fundamental atomic properties and measurable macroscopic properties must be well established. This is essential in material design where different elements of the periodic table are combined to create materials with desirable macroscopic features. Such an approach requires a theory which can describe properties of atoms in different configurations.

Matter at the atomic scale obeys the laws of quantum mechanics. Within quantum mechanics, the material is described by its wavefunction, an abstract object which represents a statistical probability of the particles' (electrons and nuclei) quantum state as a function of position, momentum, time, and spin. In other words, the wavefunction contains all the information about the quantum system. It can be obtained by solving the time-dependent Schrödinger equation

$$i\hbar\partial_t\Psi(\mathbf{r},\mathbf{R},t) = \hat{H}\Psi(\mathbf{r},\mathbf{R},t) \tag{2.1}$$

where

$\Psi(\mathbf{r}_1, \mathbf{r}_2, ..., \mathbf{R}_1, \mathbf{R}_2, ..., t)$ is the wavefunction and $\mathbf{r}_*$ and $\mathbf{R}_*$ are electronic and nuclear coordinates, respectively. The total electronic wavefunction must be antisymmetric because electrons are fermions.

The total energy of the system is conserved for a time-independent potential so the stationary solution of the Schrödinger equation will be a product of a time-dependent and a time-independent part. Since the properties of interest in this work are time-independent, the relevant information is held in the stationary state of the Hamiltonian. The eigenvalues and eigenfunctions (wavefunctions) of the Hamiltonian can be obtained by solving the time-independent Schrödinger equation:

$$\hat{H}\Psi(\mathbf{r}, \mathbf{R}) = E\Psi(\mathbf{r}, \mathbf{R}), \tag{2.2}$$

where $E(\mathbf{R})$ is the eigenvalue.

The Hamiltonian $\hat{H}$ can be written as

$$\hat{H} = -\sum_{I=1}^{P} \frac{\hbar^2}{2M_I}\nabla_I^2 - \sum_{i=1}^{N} \frac{\hbar^2}{2m}\nabla_i^2 + \frac{e^2}{2}\sum_{i=1}^{N}\sum_{j\neq i}^{N} \frac{1}{|\mathbf{r}_i - \mathbf{r}_j|} + \frac{e^2}{2}\sum_{I=1}^{P}\sum_{J\neq I}^{P} \frac{Z_I Z_J}{|\mathbf{R}_I - \mathbf{R}_J|} - e^2\sum_{I=1}^{P}\sum_{i=1}^{N} \frac{Z_I}{|\mathbf{R}_I - \mathbf{r}_i|}. \tag{2.3}$$

Z_I and M_I are nuclear charge and masses, and m is the electron mass. The first two terms describe the kinetic energy of the nuclei and the electrons, respectively. The remaining terms represent electron-electron, nuclei-nuclei and electron-nuclei interactions, respectively.

Unfortunately, obtaining eigenvalues and eigenfunctions exactly is possible only in few cases: hydrogenoid atoms (analytically) and very small molecules (numerically). The main problem rises from the two-particle Coulomb interaction. The probability of finding one electron at the point $\mathbf{r}$ depends on the location of all the other electrons in the system. Such a phenomena, called *correlation*, is at odds with a one-electron wave function representation and makes the Schrödinger equation inseparable.

A few well-controlled approximations are introduced to decrease the number of coupled degrees of freedom and help make the theory applicable for many systems. The first approximation used to decouple nuclear and electronic motion is the Born-Oppenheimer approximation (also know as *adiabatic* approximation when a small correction of the order m/M is included)[15]. The mass ration between electrons and nuclei is very small ($m_e/m_p = 10^{-4}$) and allows the electrons to instantaneously follow the motion of the nucleai and adjust their wavefunction. Accordingly, the wavefunction can be be written in the following form[16]:

$$\Psi(\mathbf{R}, \mathbf{r}, t) = \Theta_n(\mathbf{R}, t)\Phi_n(\mathbf{r}; \mathbf{R}), \tag{2.4}$$

$\Theta_n(\mathbf{R}, t)$ being nuclear wavefunction and each adiabatic electronic eigenstate $\Phi_n(\mathbf{r}; \mathbf{R})$ satisfying the time-independent Schrödinger equation. The time-independent electronic Hamiltonian can therefore be reduced to:

$$\hat{H}_e = -\sum_{i=1}^{N} \frac{\hbar^2}{2m_i} \nabla_i^2 + \frac{e^2}{2} \sum_{i=1}^{N} \sum_{j \neq i}^{N} \frac{1}{|\mathbf{r}_i - \mathbf{r}_j|} - e^2 \sum_{I=1}^{P} \sum_{i=1}^{N} \frac{Z_I}{|\mathbf{R}_I - \mathbf{r}_i|}. \tag{2.5}$$

As much as the above approximation significantly reduces the complexity of our problem, it gives no solution for the many-body electron problem. Solving the above equation for the ground state (lowest state) results in the ground state energy of the system. A formally exact way of obtaining the ground state energy is given by the Density Functional Theory, discussed in the next chapter.

2.2 Density Functional Theory

The basic idea, later used to derive the very successful Density Functional Theory (DFT), was introduced in 1927 by L.H.Thomas[17] and E.Fermi[18]. They proposed an alternative representation of a many electron system where the full electron density was the fundamental variable of the many-body problem. The simple *Thomas-Fermi* model describes atoms as negatively charged electron clouds around nuclei in a six-dimensional phase space. The proposed total energy was constructed using the known expressions for kinetic, exchange and correlation energies of a homogeneous electron gas and applied on local density contributions. That way, the total energy had contributions (α =kinetic, exchange, correlation) from local densities at every point in space:

$$E_\alpha[\rho] = \int \rho(\mathbf{r}) \varepsilon_\alpha[\rho(\mathbf{r})] d\mathbf{r}. \tag{2.6}$$

The approximation of only accounting for local density contributions is called the *local density approximation* (LDA, or including spin, L(S)DA). In the above expression the energy has a functional dependence on the electronic density. The same idea is used in DFT, where it is proved that the ground state energy can be expresses exclusively in terms of the electron density.

More than 30 years after Thomas and Fermi introduced their model, Hohenberg and Kohn developed DFT[19].

Theorem 1: The external potential is univocally determined by the electronic density, besides a trivial additive constant.

Theorem 2: The ground state energy of an electron system is a universal functional of the ground state electronic density.

By 'external potential' one considers the potential originating from the static nucleai, plus any applied potential. The second theorem introduces an energy functional,

which has a minimum at the true ground state density and the value is the ground state energy.

However, the theorems can only be used if the many-body density is known. An approach by Kohn and Sham suggested mapping the density of a system of non-interacting electrons onto an interacting system with the same density[20]. Such a non-interacting system is described by the antisymmetric, one-electron orbital wave-functions, and its kinetic energy can be exactly calculated. In other words, the problem of interacting electrons in an external potential is mapped onto a problem of non-interacting electrons in an effective local potential[16]. Obtaining the density and the kinetic energy from the non-interacting system, yields the expression for the energy of the Kohn-Sham system:

$$E_{\mathrm{KS}}[\rho] = \frac{\hbar^2}{m}\sum_{i=1}^{N/2}\langle\phi_i|\nabla^2|\phi_i\rangle + \int \rho(\mathbf{r})v_{\mathrm{ext}}(\mathbf{r})\mathrm{d}^3r + E_{\mathrm{Hartree}} + E_{\mathrm{xc}}[\rho]. \tag{2.7}$$

The first term is the kinetic energy term, the second is the external potential accounting for the electrostatic potential of the nucleai, the third, the Hartree energy, E_{Hartree} is the classical electrostatic interaction corresponding to a charge distribution $\rho(\mathbf{r})$. The electron-electron energy contribution not accounted for by the Hartree term is stored into the so-called exchange-correlation (xc) part, E_{xc},. The latter accounts for the many body nature of the wavefunction and the kinetic correction ignored in the first term due to the non-interacting kinetic approximation.

The introduced formalism is in principle exact, but in practice the exact form of the exchange-correlation part is unknown. Still, different approximations introduced to E_{xc} has made the many-electron problem solvable with a reasonable accuracy.

2.2.1 Exchange-correlation functionals

The first approximation for the exchange-correlation energy in DFT was based on the previously introduced Thomas-Fermi model. The approximation known as the local density approximation assumes the inhomogeneous system to be locally homogeneous and the xc energy is found from the ex energy per particle of a homogeneous electron gas at the given density. The E_{xc} within the LDA has the form of equation 2.8 where the values of $\varepsilon_{xc}[\rho(\mathbf{r})]$ are based on Monte Carlo calculations of the energy of homogeneous electron gases of varying densities[21].

Since LDA is built using a homogeneous electron gas model, it is expected to perform well for systems with relatively homogeneous charge densities (like metals) and have problems with systems having very inhomogenious charge density. Furthermore, LDA fails to cancel the *self-interaction*, so in systems with strongly localized states like molecules and cluster, the exponential decay of the exchange-correction potential in vacuum regions (instead of having attractive $-e^2/r$ behavior) leads to wrong predictions of dissociation limit and ionization energies. Another important failure of LDA, and a general problem in DFT, as will be further discussed in section

2.4, is a huge underestimation of the band gaps, which is a consequence of using the gap-less homogeneous electron gas as a model.

A natural way of improving upon LDA is to include the gradients of the density in the functional. Such approximation an is known as a *generalized gradient approximation*, GGA and the most famous functional within this type is the PBE (Perdew-Burke-Ernzerhof) functional[22]. The variation of density close to the considered point is included into exchange energy by the *enhancement factor*, $F_X[s(\mathbf{r})]$:

$$E_X^{GGA}[\rho] = \int \rho(\mathbf{r})\varepsilon_X^{LDA}[\rho(\mathbf{r})]F_X[s(\mathbf{r})]d\mathbf{r}, \tag{2.8}$$

where $s = |\nabla\rho(\mathbf{r})|/2k_F\rho$ is the dimensionless density gradient.

Within the approximation, the correlation energy is also corrected by a $H[\rho(\mathbf{r}), \nabla\rho(\mathbf{r})]$ term, to fulfill a number of exact conditions.

The introduction of GGA-s is one of the most important advances of DFT and up to now, PBE remains the most used functional in the electronic structure community. However, despite the significant improvements with respect to LDA, there is a limit to the accuracy of PBE. No significant improvements on the estimation of band gaps were achieved and due to the lack of non-locality in the exchange term it still fails for the strongly correlated systems[16].

Several different routes were taken to go beyond the GGA and many new functionals were developed to further improve accuracy of DFT calculations. Often functionals were developed to tackle one specific property so there are currently many specialized functionals with only a single purpose. Few functionals of relevance to the reported work will be introduced later in this chapter.

2.3 Practical implementation of DFT in the GPAW code

The implementation of DFT requires a suitable representation of the wavefunction. Based on the particular problem, different choice of bases function is preferred. The current implementation of GPAW (Grid-based Project Augmented Wave) code[**GPAW**, 14] offers the possibility of expanding the wavefunction in a plane wave basis, on a real space grid[23] or as a linear combination of atomic orbitals (LCAO)[24].

GPAW works in combination with the Atomic Simulation Environment (ASE)[25, 26].

2.3.1 Basis sets in GPAW

In short, plane waves are convenient when dealing with periodic systems enabling fast Fourier transformation between real and reciprocal space. The accuracy of the calculation is determined by the plane wave cutoff. The real space grid is a simple

basis with only one parameter: the grid spacing. It is convenient for both periodic and open boundary conditions in any directions and the only real disadvantage is the egg-box error. The idea behind the LCAO basis set is in constructing a basis of radial functions localized on the atoms allowing faster calculations of large systems. The unoccupied states are represented by polarizing the occupied states. Overall, all three basis sets give reliable results and a choice of the basis set is often governed by the specific problem of interest.

2.3.2 Pseudopotentials and PAW formalism

Even though one can, in principle, include all the electrons in a calculation, one usually only needs the valence electrons to capture interesting chemical and physical properties of the system. The core electrons rarely contribute in chemical bonding or excitations and as such can be approximated, together with the nucleus, with an effective core potential. Such a simplification is called the *pseudopotential* method[27]. Completely loosing information of the core electrons in pseudopotentials has a direct consequence on the shape of the electronic wavefunction. A projected augmented wave (PAW) formalism allows access to the full Kohn-Sham wavefunction while keeping the pseudopotential simplification.

Pseudopotentials are subject to the frozen core approximation which assumes that the core states are localized within the augmentation spheres, and that the core states of the isolated atoms are not changed by the formation of molecules or solids. The number of wavefunctions to be calculated is therefore reduced since only the calculations of valence states are needed. Furthermore, valence electrons are treated non-relativisticly while the pseudopotential includes the full relativistic effects of the core electrons.

The augmented-plane-wave method divides space into atom-centered augmentation spheres inside which the wave functions are taken as some atom-like partial waves, and a bonding region out- side the spheres, where some envelope functions are defined. The partial waves and envelope functions are then matched at the boundaries of the spheres[28]. In the PAW formalism presented by Blöchl[29], a linear transformation of the all-electron wavefunction onto a computationally convenient smooth wave function is constructed. The transformation has no effect outside a cutoff radius and the true wavefunction inside the augmentation sphere is expanded in terms of partial waves.

2.4 Band gap calculations using DFT

The difference between the ionization energy I (energy required to remove the highest valence electron) and electron affinity A (amount of energy spent when an electron is added to the material) of an electronic system is its fundamental band gap. The difference is zero in metals and finite in semiconductors and insulators. The effective

potential which generates the true electron density, the Kohn-Sham potential, $v_{eff}(n)$, is closely related to the ground state energy of the system. The addition or removal of an electron causes a change in the electron density and can be associated with a change in the KS potential (C). The ionization potential and electron affinity for the J electron system are:

$$I(J) = -\epsilon_J(J-\delta), \tag{2.9}$$

$$A(J) = -\epsilon_{J+1}(J+\delta) = -[\epsilon_{J+1}(J-\delta) + C], \tag{2.10}$$

and their difference is then:

$$I(J) - A(J) = \epsilon_{J+1}(J+\delta) - \epsilon_J(J-\delta) \tag{2.11}$$

$$= \epsilon_{J+1}(J) - \epsilon_J(J) + C, \tag{2.12}$$

where ϵ_i are the KS orbital energies and δ is an infinitesimal change. The above shows that the band gap cannot be defined as a difference in KS orbital energies, but a constant C should be added[30]. The same principle is also valid for fractional number of electrons. As the conduction band starts to fill (infinitesimally), the chemical potential $\delta E_v/\delta n(\mathbf{r})$ and the KS orbital energy jump discontinuously from one physical value ($I(J) = -\epsilon_J(J-\delta)$) to another ($A(J) = -\epsilon_{J+1}(J+\delta)$). Therefore, the fundamental gap can be expressed as a discontinuity in the functional derivative[31, 32]. If energy functional has the form as in equation 2.7, the discontinuity can only arise from the kinetic energy and exchange-correlation energy part. Since the kinetic energy is the one of the KS non-interacting system, its functional derivative will result in integer electron orbital energies. This leaves the functional derivative of the xc energy part, resulting in:

$$C = \delta E_{xc}/\delta n(\mathbf{r})|_{j+\delta} - \delta E_{xc}/\delta n(\mathbf{r})|_{j-\delta} \equiv \Delta \tag{2.13}$$

Finally, the fundamental band gap is the sum of the KS gap plus the constant:

$$E_g = \varepsilon_{KS} + \Delta. \tag{2.14}$$

The absence of the derivative discontinuity in LDA and GGA functionals is the main reason for the large underestimation of the obtained band gaps. An estimate of the derivative discontinuity can be included in a simple way. An example of this is the GLLB-SC functional[33]. It is based on the GLLB type exchange[34] and PBEsol[35] correlation. The total effective potential in GLLB-SC has the following form:

$$v_{GLLB-SC}(\mathbf{r}) = 2\varepsilon_{XC}^{PBEsol}(\mathbf{r}) + v_{c,resp}^{PBEsol}(\mathbf{r}) + \sum_{i}^{occ} K_x\sqrt{\varepsilon_r - \varepsilon_i}\frac{|\Psi_i(\mathbf{r})|^2}{\rho(\mathbf{r})}, \tag{2.15}$$

where the first term is the PBEsol exchange-correlation energy density and the second term is the linear correlation response potential ($v_{c,resp}^{PBEsol}(\mathbf{r}) = v^{PBEsol}(\mathbf{r}) - \varepsilon^{PBEsol}(\mathbf{r})$[35]). In the last term, the exchange response potential, the prefactor is derived from the homogeneous electron gas and ε_r is the eigenvalue of the highest occupied orbital. The exchange response approximation employed in the GLLB-SC functional allows deriving the discontinuity from its straightforward dependence on the highest occupied electron state:

$$\Delta_{XC} \approx \sum_{i}^{N} K_x(\sqrt{\varepsilon_{N+1} - \varepsilon_i} - \sqrt{\varepsilon_N - \varepsilon_i}) \int \frac{|\Psi_{N+1}(\mathbf{r})|^2 |\Psi_i(\mathbf{r})|^2}{\rho(\mathbf{r})} d\mathbf{r}. \tag{2.16}$$

The method was implemented in the electronic structure code GPAW and benchmarked versus experiments, other functionals and more accurate many-body methods. The comparison by Castelli et al.[36, 37] is shown in figure 2.1, where the mean absolute error of 0.38 (0.05) eV was found for the GLLB-SC band gaps compared to the state-of-the-art GW method. It is important to emphasize that a GLLB-SC calculation is only two times more expensive than a standard GGA calculation, whereas the cost of the other methods used in comparison can go up to a few orders of magnitude higher.

With a similar computational cost as GLLB-SC, one can obtain band gaps using a modified version of the Becke-Johnson functional, TB09. Becke and Johnson[38] suggested a local potential, known as the optimized effective potential (OEP) for exchange which depends only on total densities. Tran and Blaha modified the effective potential proposed by Becke and Johnson and used the LDA for the correlation part[39]. The final form of the exchange part of TB09 is:

$$V_X^{TB09} = cV_X^{BR}(\mathbf{r}) + (3c - 2)\frac{1}{\pi}\sqrt{\frac{5}{12}}\sqrt{\frac{2t_s(\mathbf{r})}{\rho(\mathbf{r}}}. \tag{2.17}$$

The first term models the Coulomb potential created by the exchange hole, as introduced by Becke and Roussel[39] and t_s is the kinetic energy density, $t_s(\mathbf{r}) = \frac{1}{2}\sum_{i=1}^{N} \Delta\Psi_i^* \cdot \Psi_i$. The parameter c is:

$$c = \alpha + \beta \left(\frac{1}{V_{cell}} \int_{cell} \frac{|\Delta\rho(\mathbf{r}')|}{\rho(\mathbf{r}')} d\mathbf{r} \right)^{1/2}, \tag{2.18}$$

where α and β are fitted to experimental gaps using a least-square procedure. This modification comes with minimal additional computational cost so the method can be used on a wide variety of systems.

An entirely different way of improving the LDA/GGA functionals is to incorporate a portion of exchange from Hartree-Fock (HF) theory[40].

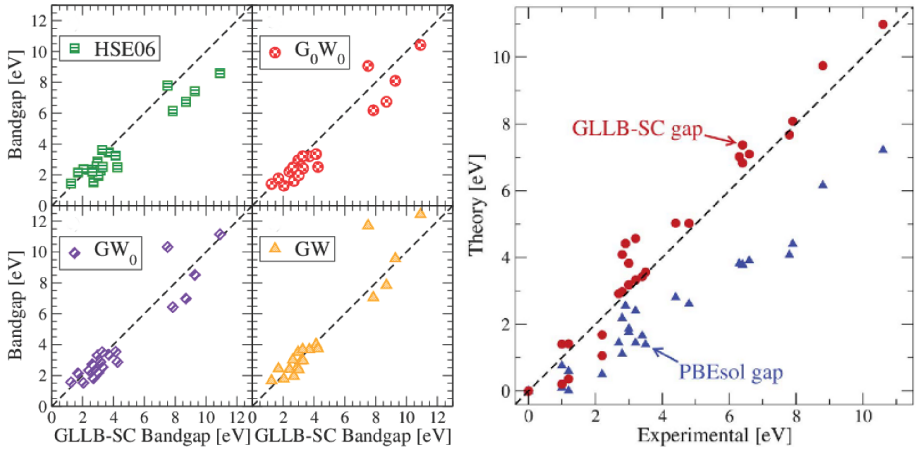

Figure 2.1: a) HSE06, G_0W_0, GW_0, GW band gaps (upper left to bottom right, respectively) as a function of the GLLB-SC gaps. T All the methods except GW underestimate the gaps with respect to the GLLB-SC. b) Comparison between the theoretical and experimental band gap of non-magnetic metal oxides in their most stable structure. Figures from Ref. [36]a) and [37]b).

$$E_X^{HF} = \frac{1}{2}\sum_{i,j}^{occ.} \int \frac{\Phi_i^*(\mathbf{r})\Phi_j^*(\mathbf{r}')\Phi_j(\mathbf{r})\Phi_i(\mathbf{r}')}{|\mathbf{r}-\mathbf{r}'|} d\mathbf{r}d\mathbf{r}'. \tag{2.19}$$

So called *hybrid functionals* are constructed by adding an appropriate fraction of HF to LDA/GGA exchange:

$$E_{XC}^{hyb} = \alpha E_X^{HF} + (1-\alpha)E_X^{GGA} + E_C^{GGA} \tag{2.20}$$

where the coefficient α is chosen or obtained from fitting to some properties in a database. Examples of hybrid functionals are the B3LYP[41], PBE0[42] and HSE[43]. In this work, a HSE hybrid functional is used for band gap calculations. HSE was developed as a faster hybrid functional which made it possible to apply it to larger periodic systems with reasonable computational resources. The functional relies on dividing the exchange interaction into a short and a long term using the error function:

$$\frac{1}{r} = \underbrace{\frac{erfc(\omega r)}{r}}_{\text{short range}} + \underbrace{\frac{erfc(\omega r)}{r}}_{\text{long range}} \tag{2.21}$$

and the strength of the screening is decided by the ω parameter. In the HSE06 version of the functional the value of ω is 0.11 a_0^{-1}. In the GPAW code the HSE06 was implemented only non-self-consistently at the time my results were produced.

The exchange-correlation functionals mentioned above were used in different projects reported in this thesis. The choice of the particular functional will be discussed for each project separately. There is not a single functional that gives the best agreement with experimental values across all classes of materials.

Regarding the computational cost, GLLB-SC and TB09 require roughly the same computational time and resources, while hybrid HSE06, even without the self-consistency implemented is much more expensive.

2.5 Calculating total energies and heats of formation of solid crystals

As for band gaps, accurate approximation to the XC-functional is also important for total energy calculations. When DFT energies are used to calculate properties with chemical accuracy, for example, energy differences of chemical reactions, bonding, etc., inaccuracy in total energies can lead to wrong conclusions.

A great improvement was achieved with the introduction of GGAs, which improve the atomization or cohesive energies of a wide range of molecules and solids, compared to the LDA[44]. Unfortunately, the improvement relies on some cancellation of error, which is system dependent. The self-interaction energy, which is cancelled in HF by the energy from exchange, is not completely cancelled in DFT due to an approximate DFT functional. The errors yielded from the self-interaction energy cancel when calculationg the DFT total energy differences of similar systems. However, this improvement is not systematic but only occurs for similar classes of materials. One of the best examples of the self-interaction error being responsible for wrong prediction of a chemical property is the dissociation of H_2^+, a one electron system where non-zero electron-electron interaction is predicted.

The self-interaction error is partially corrected in hybrid functionals due to the partial inclusion of exact exchange energy. Another possible improvement is including a Hubbard-U potential[45] to increase the localization of electrons. Another improvement of GGAs is to include the Laplacian of the density and/or the kinetic energy density, resulting in so-called meta-GGAs. This will be discussed briefly in the next section.

2.5.1 A brief introduction to meta-GGA exchange correlation functionals

The natural step going beyond the GGAs is the fourth order gradient expansion of the exchange and correlation energy, resulting in the so-called the meta-gemeralized

gradient approximation or meta-GGA. This means including the Laplacian of the electron density ($\nabla^2 n$) or equivalently the kinetic energy density,

$$\tau_\sigma = \frac{1}{2} \sum_{\alpha}^{occup} |\nabla \psi_{\alpha\sigma}(\mathbf{r})|^2, \tag{2.22}$$

where ψ_α are the occupied KS orbitals and σ is the spin index of the electrons. The kinetic energy density is given in terms of the KS orbitals, and the KS orbitals are implicit functionals of the electron density through the KS potential, so the dependency on the density is non-local. Therefore, using the kinetic energy density one can fulfill the slowly varying density expansion to a higher order than for GGA.

The meta-GGA functionals are semi-local and they rely only on the occupied KS orbitals. There is a modest increase in the computational cost of the meta-GGAs compared to the GGAs.

2.5.2 Bayesian Error Estimation ensemble functionals (BEEF)

Raising the question to which extent a calculated quantity is to be trusted, in 2005, Mortensen et all.[46] proposed a scheme for systematic error evaluation in the DFT calculations. The Bayesian Error Estimation ensemble functionals, BEEF, combine machine learning with a Bayesian statistics to generalize the fitting procedure for XC functionals. The ensemble of models or model parameters together with a database of experimental results is used to estimate error bars on model predictions. Within the Bayesian approach, a direct connection between the model, given by a set of parameters, and the data is established. This allows one to ask "given the data what is the best model and what are the uncertainty of the model parameters?"

The proposed model suggests expanding the GGA enhancement factor $F_x(s)$ as:

$$F_x(s) = \sum_{i=1}^{N_p} \Theta_i \left(\frac{s}{s+1}\right)^{2i-2} \tag{2.23}$$

where Θ's are free parameters. The best fit enhancement factor was obtained by minimizing the cost function (here a least-square $C(\Theta) = 1/2 \sum_k (E_k(\Theta) - E_k^{exp})^2$, where $E_k(\Theta)$ is atomization/cohesive energy of system k in the database calculated with the parameters Θ and E_k^{exp} is the experimental atomization/cohesive energy of system k) using three parameters $N_p = 3$.

The key idea is to estimate, for a given calculated observable, the variation of the calculated value of this observable,O, within the ensemble of enhancement factors. This provides an estimate of the error between the best fit value compared to experimental values. The standard deviation of ensemble parameters Θ's (the Bayesian Error Estimate, BEE) can be expressed:

$$\sigma_{BEE}(O) = \sqrt{\frac{1}{N}\sum_{\mu=1}^{N}(O(\Theta^{\mu}) - O_{best-fit})^2} \tag{2.24}$$

Introduction of BEE for prediction of uncertainties in the DFT calculations resulted in developing a family of BEEF functionals: BEEF-vdw[47], enabling to also account for long range van der Waals bonding in materials, meta-BEEF (mBEEF)[48], which as the name indicates, it combines the BEE scheme with the meta-GAA enhancement factor and finally meta-BEEF-vdW[49], which is a combination of the first two.

Finally, a particular member of the BEEF family which played an important role in the work reported in this thesis is the mBEEF functional. The mGGA enhancement factor, a function of reduced density gradient s and the reduced kinetic energy density α, $F_x(s, \alpha)$, is expanded in products of Legendre polynomials,

$$P_{mn} = B_m(t_s)B_n(t_\alpha), \tag{2.25}$$

with the transformations

$$t_s(s) = \frac{2s^2}{q + s^2} - 1 \tag{2.26}$$

and

$$t_\alpha(\alpha) = -\frac{(1-\alpha^2)^3}{1 + \alpha^3 + \alpha^6} \tag{2.27}$$

resulting in

$$F_x(s, \alpha) = \sum_{m=0}^{M}\sum_{n=0}^{N} a_{mn}P_{mn}. \tag{2.28}$$

$M = 7$ so ($\mathrm{M}_{tot} = (\mathrm{M}+1)^2 = 64$) exchange basis functions with expansion coefficients a_{mn}.

This yields a full exchange energy expression:

$$E_{xc} = \sum_{m,n}^{M} a_{mn}E_x^{mn} + E_c^{GGA} \tag{2.29}$$

The correlation energy functional E_c^{GGA} is that of the PBEsol functional. The expansion coefficients a_{mn} are fitted to a database such that the functional performs well

for wide range of properties. The best fit coefficients are used to constitute the main functional.

The error estimate is obtained by using the ensemble of different XC functionals, which is defined by the probability associated to the model δ given the data D. Inspired by the Bayesian statistics, an ensamble of functionals with perturbed coefficients are constructed. The standard deviation of the ensamble is then a good estimate of the uncertainty of the calculation. The ensamble functionals are applied non-self-consistently to converged mBEEF electron density. In practice, a few thousand ensemble functionals suffice for well-converged error estimates.

2.5.3 Using mBEEF functional for calculating chemical properties

As mentioned earlier, accuracy in prediction of chemical properties is not a trivial task for DFT. For example, formation of solid crystals from the elements in their standard state can significantly deviate from the experiments (Stevanović et all. report deviation of 0.25 eV for a set of 252 binary compounds[51]) due to incomplete error cancellation caused by different chemical environments in solid comparing to the standard states. Another issue is determining a degree of matastability of compounds with the same stoichiometry but in different crystal structures. For example, there are cases when one can find several different structures of the same compound within small energy differences so it is hard to claim with a confidence which one is the most stable. Stevanović et all.[51] developed a method which solves the problem by adding corrections to the DFT reference energy. Their scheme, called Fitted Elemental Reference Energy (FERE), calculates corrections by minimizing the root mean square error of the predicted and experimental values. However, FERE may not improve results for the systems not included in the training set.

An alternative is to use a functional from the BEEF family: the mBEEF functional. Without significantly increased computational cost one gets ahold on improved accuracy and also very useful uncertainties allowing to define a degree of confidence in obtained values. Pandey and Jacobsen[50] compared the accuracy of calculated heats of formation of different solids using different functionals. The reported mean absolute error and the standard deviations are significantly improved in mBEEF comparing to other functionals. A comparison between PBE and mBEEF is shown in figure 2.2.

A practical example where uncertainties come handy is shown in figure 2.3. The compound of $ZrMgS_3$ stoichiometry was calculated in several different crystal structures and the goal was to find the lowest energy structure using the total energy per atom difference. The reference is the energy of the lowest structure. Without the uncertainties, one would conclude that $ZrMgS_3$ in $PbPS_3$ prototype is the most stable and others are unstable. However, once the uncertainties are accounted for, three more structures should be considered. In this case, a single, most stable phase, cannot be identified. The same can approach can be applied when investigating stability with respect to the convex hull, where the hull uncertainty is calculated using

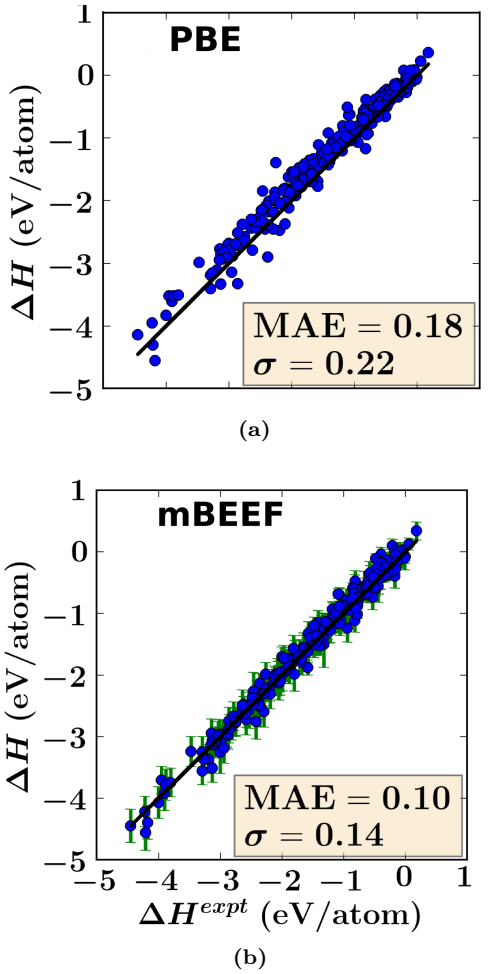

Figure 2.2: Calculated heats of formation with PBE (a) and mBEEF(b) functional. MAE is the mean absolute error and σ is the standard deviation of the difference between calculated and experimental values. Figures from Ref. [50].

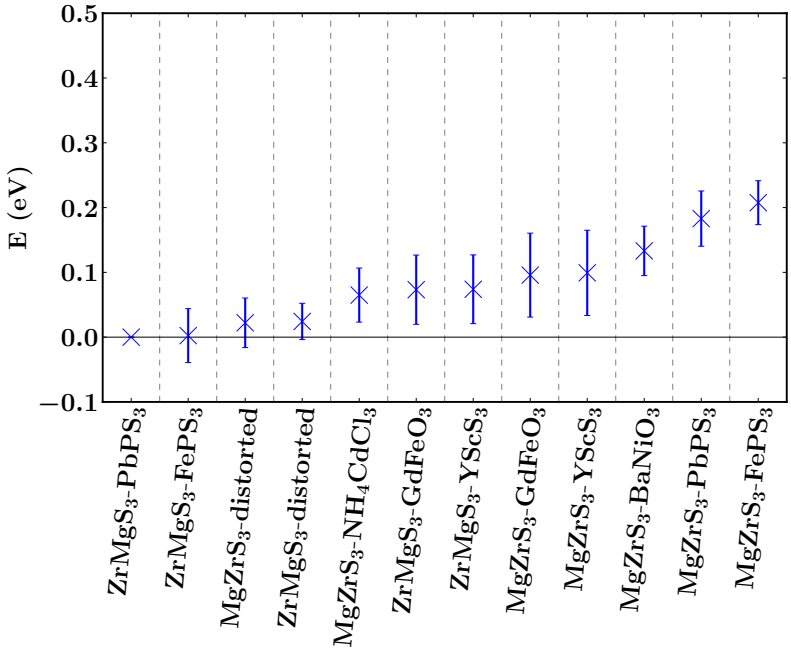

Figure 2.3: Comparison of formation energies for $ZrMgS_3$ compound in several different phases. The uncertainties are calculated with respect to the most stable structure.

the individual uncertainties of the competing compounds.

To summarize, using mBEEF in predicting heats of formation results in higher accuracy comparing to the standard GGAs. The obtained uncertainties in total energy calculations provide insight into degree of metastability in cases with several crystal structures. The work reported in paper III relies on predictive power and accuracy of mBEEF functional, which has shown to be essential in design of new materials.

CHAPTER 3

Methods

DFT is the most convenient and highly reliable method for calculating properties of many different materials in a systematic way, as needed in a screening study. A DFT calculation can be performed only if the is a previous knowledge of the atomic structure, for example candidate material whose properties we want to investigate. However, the inverse, or material design problem, begins with a "wish-list" of properties for a material but no atomic structure. In that case before doing any DFT calculations it is necessary to develop a sensible strategy to tailor the right material. For example, choosing prototype structures for the new material is a way to optimize the process.

3.1 Computational screening techniques

Material properties and therefore the corresponding descriptors can be divided in three groups: i) constituents, ii) crystal structure and iii) electronic properties. It is natural to order the properties in increasing order of their accessibility to calculations. For example, starting with known atomic properties such as electronegativity, valence or toxicity, which do not require new calculations, and continuing with crystal structure, stability or the band gap which need to be accessed by DFT calculations. It is good to organize screening in a way that a large number of materials are removed early in the process before using extensive computer resources. The properties which require more time and resources to calculate should be done for as few as possible materials, and later in the screening process. In other words, one should try to remove as many materials as possible early in the screening giving the opportunity to investigate remaining materials in a better way. One can schematically show the process as a funnel where the number of materials reduces in each step. An example of a screening funnel is shown in figure 3.1 and with small adaptions it can be used for different material design problems. If one performs computational screening on known materials, the steps involving chemical rules can often be skipped since they are only important when used as constraints in design of new materials. Materials design scheme will be discussed in more detail in the next section.

Because of the practical and economical reasons, a screening study may be limited only to materials made out of certain chemical elements. Removing materials containing undesirable constituents is usually done early in the process, unless one is

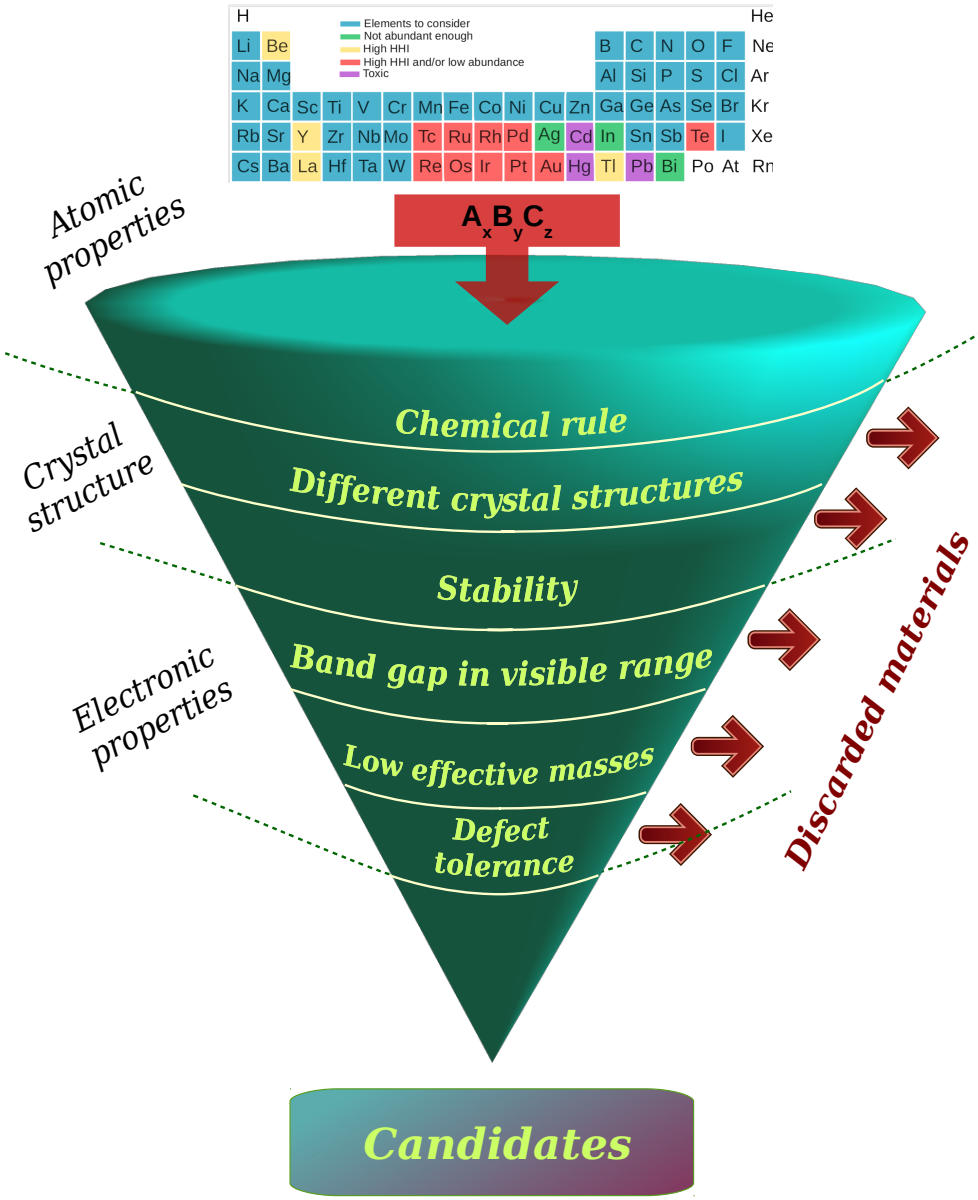

Figure 3.1: Illustration of a step-wise screening procedure using funnel annalogy: initial large number of candidates is reduced every time a new property is investigated. As moving towards the bottom of the funner, the number of candidates decreases, and the cost of the DFT calculations increases.

interested in learning trends and patterns in which case they can be removed at the very end of the screening.

Once the constituents have been selected, the next step is finding the crystal structure and check the thermodynamic stability. The laws of thermodynamics allow for only one globally stable structure for a given chemical stoichiometry. The energy of such a structure, often called the ground state energy, is lower than energies of other phases with the same stoichiometry. In reality, for a given stoichiometry different stable phases may have been experimentally observed, meaning there are one or more stable local minima of energies. Such structures are often synthesized under controlled conditions of pressure and temperature. Regardless if one is investigating known materials or designing new ones, it is crucial that only the stable structures are kept for further investigation. If not experimentally known, this step requires obtaining total energies of materials using the DFT and calculating the thermodynamic stability.

In connection to the physical properties of sunlight absorbers, one investigates electronic properties of materials. Obtaining reliable estimate of the band gaps and effective masses often requires more accurate DFT calculations, so it is done in the last part of the screening. Varying calculation parameters or employing different exchange-correlation functionals may be necessary at this step. Higher accuracy of calculations goes hand-by-hand with higher cost of calculations, sometimes even requiring more accurate, but very expensive methods like the many-body perturbation theory. The increase in computational cost can increase 2-10 times comparing with the standard DFT calculation. The last step in the funnel is tracking down the changes in the electronic properties due to introduction of defects. Calculations are done on a large super-cells, each with a different type of defect. In theory, the same accuracy should be used as for calculating properties of the pristine system, but in reality it is not feasible. Usually the super-cells are treated less strictly because otherwise it would not be feasible to investigate more than just a few compounds. Even at the lower accuracy level one can observe the qualitative influence of defects and draw conclusions. At this point in screening, the number of candidates is hopefully sufficiently reduced so that one can visually inspect each candidate individually in depth.

Finally, using a funnel analogy, the candidates coming out at the end of the funnel are the ones satisfying all the introduced criteria. These candidates require further theoretical and experimental investigation,

3.1.1 Materials design

Design of new, previously unknown materials faces a challenge already at the beginning, because the input to a DFT calculation, chemical species and positions are unknown. Therefore, a great effort has to be made in finding appropriate crystal structures to begin the study on. One usually begins by trying out different chemical elements on different sites in a known crystal structure. Instead of trying out all the possible element combinations, reducing the number of possibilities by applying simple chemical rules like anion-cation distinction or only allowing the sum of va-

lence numbers of the constituents to be zero saves a lot of effort. The latter rule is commonly used when searching for stable semiconductors since materials with sum of valence numbers other than zero are always found to be metallic[52–54]. This is a popular way of investigating whole classes of materials, for example binary zinc-blende semiconductors[55], oxide perovskites[36], organic-inorganic perovskites[56] and many more.

Given a composition, or a set of compositions, has been chosen, the real challenge remains in choosing appropriate crystal structure or structures. Ideally, one would calculate each composition in all known crystal structures and find the most stable one. Of course, such a scenario is unrealistic in practice and there are techniques that allow efficient search through material space. Some of the methods are minima hopping, metadynamics and genetic algorithms, which although efficient, still require significantly more resources than the standard DFT calculations[57–59].

An alternative way is to round up a set of candidate crystal structures, calculate their energies and claim the lowest one to be the ground state. The success of such approach strongly depends on the choice of candidate structures. Often a good place to start is by choosing crystal structures based on known experimental data.

For example, if there are several compounds of the same stoichiometry found in one phase, it is highly likely that there could be even more, yet to be discovered, compounds also stable in the same phase. In general, this approach only works if the constituent elements are substituted in a reasonable way. Position in the periodic table, atomic radius and electronegativity are often useful arguments of why is it a good idea to replace one element with the other[60, 61].

Crystal structure databases containing experimental data such as Inorganic Crystal Structure Database (ICSD)[62] or Crystallography Open Database (COD)[63] are an excellent starting point in narrowing down the choice of structures to investigate. A simple statistical analysis of compounds of a certain stoichiometry in a database yields a data set which can be used as a template in screening.

It is important to emphasize that using only one template structure is not enough: despite the fact it may be the true ground state, exploring only one structure gives no feedback about possible meta-stability of other, possibly valuable compounds. A typical example of such a case are the two allotropes of carbon, graphite and diamond. Both are stable under ambient conditions but the true ground state is graphite. Using it as an argument not to investigate diamond would be a mistake since diamond has shown to be of a great technological importance. Another good example are the three phases of TiO_2, which prepared under different conditions yield materials with different properties[64].

Obtaining knowledge about meta-stable structures is equally important from theoretical and experimental point of view: during material synthesis there is a high chance of obtaining more than one phase, which should be identified. Having information on meta-stable structures allows comparing theoretical and experimental X-ray Diffraction (XRD) and quickly determining crystal structures in the sample.

3.1.2 Databases of materials

Recent advances in screening techniques, data analysis and prediction, together with growing computer resources has resulted in the development of several computational material databases[65] The NOMAD repository[66, 67], AFLOWLIB[68], Materials Project[69], the Open Quantum Materials Database (OQMD)[70], Computational Materials Repository (CMR)[71] and others, together contain several hundreds of thousands of materials and their calculated properties. Easily accessible and systematically obtained data available in the databases is an excellent starting point for many screening, prediction or data mining studies.

3.2 Overview of screening descriptors and criteria

Below there is a detailed overview of all the descriptors included in the screening study. The order in which each descriptor is introduced was elaborated with the funnel approach.

3.2.1 Abundance, cost, toxicity and HHI index

As mentioned in the introduction that one of the downside of some solar cell materials is the toxicity of their constituents. It is no secret that certain chemical elements used

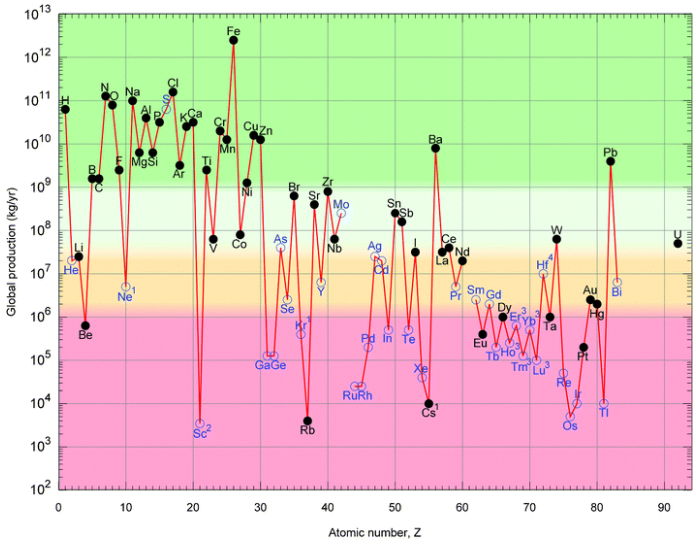

Figure 3.2: Global production of elements in kg/year. Figure from ref.[72] .

in up-to-date solar cells, like As, Cd, Pb, are dangerous or potentially dangerous for human health or harmful for the environment. Having production of clean energy from the sun as a goal, it is only reasonable to do it using harmless materials. Therefore, focusing only on the materials made of non-radioactive or non-toxic elements is important if the material is to be used in devices for mass production.

Furthermore, a large scale production also requires the material to be cheap, so using constituents which are cheap and easy to handle experimentally helps keeping the manufacturing cost lower. Of course, the manufacturing price can fluctuate over time, so one can argue that a better estimate would be the abundance in the Earth's crust. Vesborg and Jaramillo suggested using the global annual production of the element as a key factor since there are cases when not too scarce elements are expensive due to their low production[72]. The yearly global production of different elements is shown in figure 3.2 and according to the reference, a minimum of 33×10^6 kg/year is required for a material to be used in a large scale application.

Another possibility is using the Herfindahl-Hirschman index (HHI), an economic measure which determines how uneven is the production distribution, or simply a measure of the market concentration. It is determined based on several parameters, including the production and cost, but also geo-political aspects and other[73].

3.2.2 Stability

Stability is the most important issue to be addressed when designing new materials. It was already discussed how important it is to find relative stability of different phases and making sure the ground state is obtained. Maybe even more important is determining the stability against the decomposition of material. The former requires knowledge of, in principle, all the relevant competing phases of the same stoichiometry, while the latter is based on knowing all the possible products resulting from

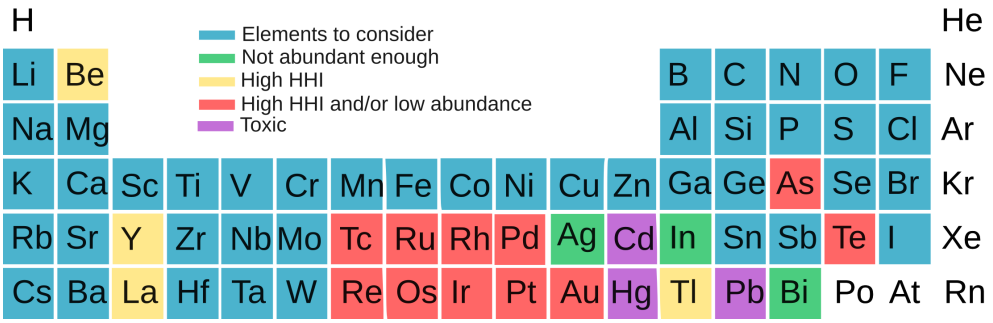

Figure 3.3: Overview of abundance, HHI and toxicity for some elements. Figure from Paper IV .

decomposition of the material. Meaning, if a ternary material is being investigated, it may decompose into combinations of elemental phases (pure elements), binary and ternary compounds of different stoichiometry.

Stability of a material is described by the knowledge of it's free energy of reaction. Since in solids the change in entropy is negligible one can use enthalpy instead of free energy:

The standard enthalpy of formation,

$$\Delta H = \sum \Delta H(products) - \sum \Delta H(reactants)$$

The calculated ground state energies obtained with the DFT are a good approximation in conditions of low temperatures (T∼0K, entropy S∼0) and are to be used to calculate enthalpy of formation. Compound (product) formation is favored when ΔH is negative.

The stability of a compound, as a function of composition, is investigated using the convex hull approach[74]. As shown in figure 3.4, the material should have enthalpy of formation lower than any other structure with the same composition and lower than any linear combination of structures that could result in formation of the material. In other words, the enthalpy of formation versus composition curve, a convex hull, represents the enthalpy of formation of the compound at T=0K. The structures with energies above the convex hull of the same composition are considered unstable and formation of competing materials will be favorable. Competing materials can be found in computational material databases, where some have already built in tool for constructing phase diagrams (like the OQMD or the Materials Project). The similar tool can also be found within the ASE in the |ase.phasediagram| module, used in this work.

In low temperature regime, a DFT total energies are sufficient for constructing the convex hull and determining the stability of the compounds. The previously introduced meta GGA functionals, such as mBEEF, are known for good estimation of heats of formation and moreover provide the corresponding uncertainties of the estimation.

In addition, comparison of several phases of the same stoichiometry is necessary when the ground state is unknown. Calculating total energies using mBEEF exchange-correlation functional provides uncertainties in the calculation due to the approximations in the DFT. The uncertainties can be used to determine the level of meta-stability of different phases. An example of the procedure is shown in section 2.5.3 and applied in the work reported in Paper III.

3.2.3 Electronic properties

The last set of descriptors are defined by the electronic properties of material. Assuming that absorption of photons occurs only at energies higher than the band gap of the material, the simplest descriptor of the efficiency is the size of the gap. As mentioned in the introduction, the ideal single-junction solar cell absorber is predicted

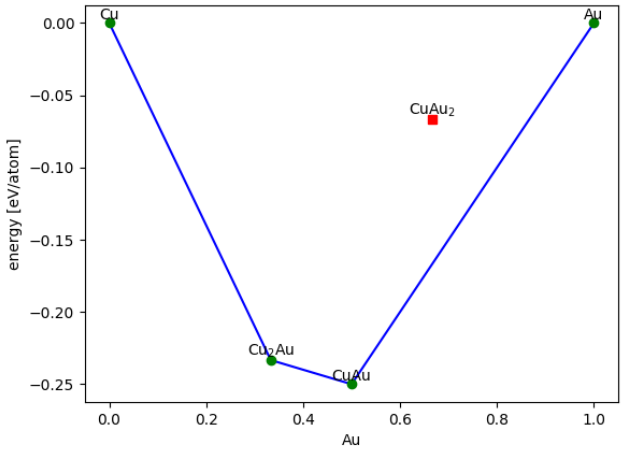

Figure 3.4: Example of the convex hull (blue line) calculated for Cu-Au phase space: the green points correspond to the stable materials and the red points to unstable materials. All the points on the convex hull are stable while the ones above the hull are unstable.

to have a band gap of 1.34 eV whereas currently used materials have band gaps between 1 and 1.5 eV (Si 1.12 eV, GaAs 1.43 eV, CdTe 1.44 eV)[8]. As for the tandem devices, slightly larger band gaps are needed, ideally around 1.7 eV**??**. As the whole operating principle of a device strongly depends on the band gap of the absorber, the same should be predicted with a good accuracy. However, as mentioned in chapter 2, standard DFT tends to underestimate the band gap value. At this point in screening one should consider going beyond standard DFT by employing hybrid functionals or using many-body methods such as GW approximation. All this comes with increased computational cost and is only feasible for materials with smaller unit cells. A possible compromise between accuracy and computational resources in a high-throughput screening can be achieved using the GLLB-SC or TB09 functionals.

In addition to the band gap size, the type of the transition, if the band gap is direct or indirect, can also be used as a descriptor. It is known that in cases when device design only allows a small amount of material, which as a consequence limits the absorption to only direct transitions. In cases where a photoabsorber is thick, the nature of the gap is less relevant (this is due to the fact that one needs phonons for indirect transitions and the phonon density is larger in thicker material). A good example to the discussion above is silicon. It has an indirect band gap so in the solar cells a large amount of material is used. This is also one of the main disadvantages of silicon. For example, organo-metallic perovskite solar cells use around 300 times

less material than the silicon ones[75]. Therefore, device designs with thin-films or nanoparticle absorbers will always require a direct band gap semiconductor. Additionally, one can go even further and include calculations of full absorption spectra.

If one splits the solar energy conversion process into two steps: i) photoabsorption and excitation and ii) charge separation and carrier transport, the band gap is a measure for (partially) describing i). A proper verification of ii) within a high-throughput screening framework is impossible because of the high cost of such calculations. To find more convenient descriptors one can start with the electrical conductivity, $\sigma = n\mu e$ which is a function of carrier concentration n, electronic charge e and carrier mobility μ. Within the simple Drude model, mobility is a function of relaxation time τ and the effective mass of the carriers: $\mu = \frac{q \times \tau}{m^*}$. The relaxation time comes from the scattering processes and obtaining it would require to go beyond the single particle picture. Therefore, only the dependence on effective mass will be used for a rough estimation of mobility: high mobility is expected if the mass is sufficiently low. In general, the effective masses are described by 3×3 tensors. Using the simplest approximation the band edges at the valence band maxima and conduction band minima are parabolic and the effective masses can be obtained by fitting a parabola to the band edges.

A good effective mass evaluation requires dense k-point sampling of the Brillouin zone close to the band extrema, meaning a good quality fitting is required. A dense k-point sampling increases the cost of the DFT calculation so there are proposed schemes to reduce the sampling to only principal direction in the Brillouin zone. Details about applied techniques and their implementation are provided in the next section.

The dependence of carrier mobility on the values of the effective mass is why the masses are used as a descriptor in the screening study. Even though materials with very high mobility, such as GaAs have carrier masses as low as 0.06 m_0[76], a typical upper limit in a screening study is usually up to 1 electron mass unit, m_0.

Material synthesis almost never results with a 100% perfect crystal. Imperfections like vacancies, interstitials or anti-sites are inevitable and often found in small amounts. Such imperfections or defects become important if they influence the electronic properties of the material. Sometimes, defects act as donors or acceptors in material and benefit the semiconductor technology. However, there is also a possibility for defects to have a negative impact on properties of materials. Point defects may introduce states inside the band gap and especially undesirable are the localized states far from the band edges. Lifetime of photoinduced carriers can be significantly reduced due to mid-gap states acting as recombination centers. This will have serious consequence to the device efficiency so materials with trap states are to be avoided. Paper I and the corresponding discussion present different ways of investigating positions of defect states in semiconductors.

3.3 Calculating descriptors in practice using DFT

After giving a general overview of screening descriptors used in my work, in this section I discuss the descriptors which are not obtainable directly from a DFT calculation. Effective masses and defect tolerance investigations require additional calculations and adequate post-processing, which are described in the following subsections.

3.3.1 Fast and efficient effective masses calculations

The photogenerated carriers, electrons and holes reside at the minimum or maximum of the conduction or valence bands, respectively. Close to the band extrema, E versus $\mathbf{k}$ relation appears quadratic, so an obvious first approximation is a parabolic band approximation. The energy-wave-vector relation can be expressed as:

$$E(\mathbf{k}) = \frac{\hbar^2}{2m^*}\mathbf{k}^2 \tag{3.1}$$

yielding the expression for the curvature of the band

$$c = \frac{1}{\hbar^2}\frac{\partial^2}{\partial \mathbf{k}^2}E(\mathbf{k}). \tag{3.2}$$

Because of the equation 3.1 effective mass is than the inverse of the band curvature. For the anisotropic electron/hole energy surface the obtained masses will differ due to the different band curvature in different $\mathbf{k}$ directions. However, if one assumes an isotropic surface, the mass is the same in every direction.

In practice, one can obtain effective mass by fitting a parabola around the valence band maximum (VBM) and conduction band minimum (CBM). Since the band structure in DFT calculation is described by the finite number of k-points, a very dense sampling is required to obtain a good representation of the bands in the vicinity of the extrema. To obtain a trustworthy effective masses on can easily need tens of thousands of k-points when representing the Brillouin zone, which is time and resource consuming and not suitable for a large scale screening study[77]. Therefore, I restricted the dense k-point sampling only to the special path in the Brillouin zone. Setyawan and Curtarolo[78] proposed the coordinates of the high symmetry k-path in the Brillouin zones for 14 Bravais lattices in 7 crystal systems. However, the scheme sets restrictions to the choice of the unit cell of the material. For example, the choice of hexagonal lattice vectors are chosen to yield $\gamma = 120°$ whereas alternatives, like the representation with $\gamma = 60°$ is not included. A tool for converting any unit cell representation to a representation required by Setyawan and Curtarolo is provided in the *SpacegroupAnalyzer* and *HighSymmKpath* modules in the *pymatgen*[79] library which I used.

Figure 3.5a and 3.5b show band structures of the two showcase materials, CdTe and WS_2: CdTe has a fcc structure and the suggested high symmetry path for an fcc

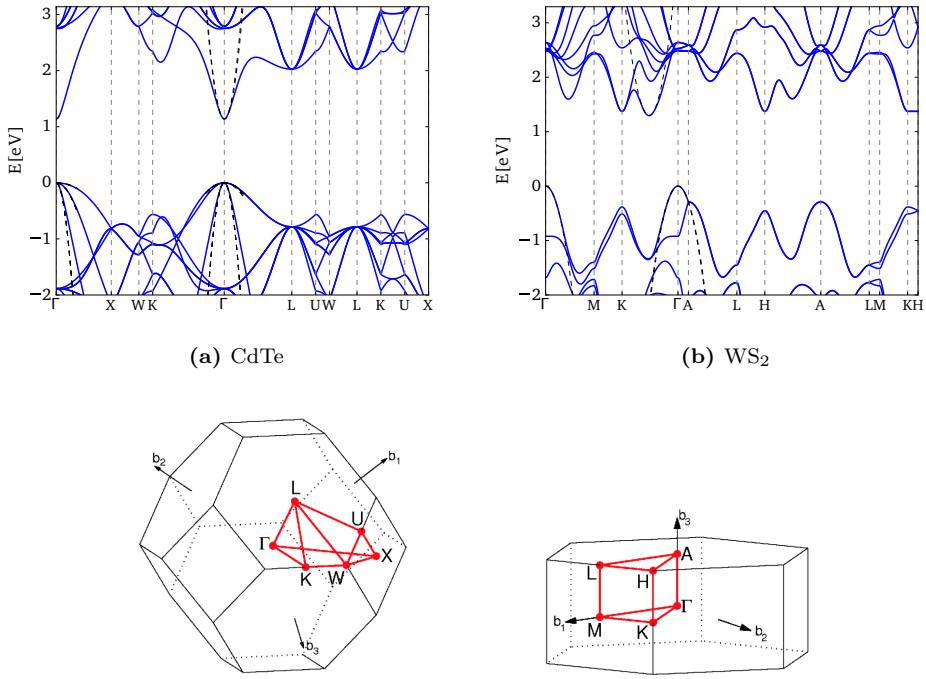

(a) CdTe

(b) WS_2

(c) Suggested path:
Γ-X-W-K-Γ-L-U-W-L-K-U-X

(d) Suggested path:
Γ-M-K-Γ-A-L-H-A-L-M-K-H

Figure 3.5: Band structures of CdTe in the fcc structure,a), and WS_2 in hexagonal structure, b). Calculations were performed using Setyawan and Curtarolo scheme and the fcc and hexagonal Brillouin zone and the high symmetry path used is shown in c) and d), respectively. Black dashed lines represent parabolic fitting to VBM and CBM. In case of band degeneracy at the extrema, a fitting was produced for each band and equivalent number of effective masses obtained.

crystal is shown in figure 3.5c whereas WS_2 has a hexagonal structure and suggested path is shown in figure 3.5d. In case of band degeneracy at the CBM and VBM, there is more than one possible dispersion channel for the carriers. That is the case in the VBM of CdTe, figure 3.5a, there are three degenerate bands with different band curvature and therefore different effective masses. The black dashed line shows parabolic fits for each of the bands involved. On the other hand, no degeneracy was found for the CBM. WS_2 is, unlike CdTe, an indirect band gap material, which can also be seen in the figure, with no degeneracy close to band edges. Calculated hole effective masses for CdTe 2.6, 1.1, 0.86, 0.51 and 0.08 m_0 and the electron effective masses are 0.095 and 0.1 m_0. WS_2 has found to have $0.77m_0$ hole mass and $0.6m_0$ electron mass.

The band structure plots, like the ones in figures 3.5 and 3.6 are projections of the selected path on a single line. This way, bands at the high symmetry points may look continuous. However, since at these points the direction of the path was changed: the path comes from one direction and continues in another direction. These two directions belong to different curvature and should be treated separately. If the band curvature is different in two different directions, the effective masses are also different. An example, the band structure of Mg_3Sb_2 is shown in figure 3.6. The VBM is located at the Γ point and the band path curvature in the K-Γ direction is noticeably different then the curvature in the Γ-A direction. Two separate parabolas were fitted to section in K-Γ direction (red dashed line) and the section in Γ-A direction (green dashed line). The resulting hole effective masses are then 1.1 and 0.09 m_0.

The decision to calculate effective masses only along high symmetry points comes also with some disadvantages, for example, it will fail if the band extrema is not at the chosen path, like the VBM of selenium (see paper V). Despite it, the method has shown to be quite successful and feasible for a large number of compounds. In practice, I have sampled the path in the Brillouin zone with 500 k-points, which is much less than tens of thousands required to evaluate full effective mass tensor. Due to the strict choice of the direction in this method, the masses obtained can be higher than the actual lowest effective mass (in some other direction). We partially account for that by keeping in the screening study materials with slightly higher effective masses than the experimental recommendations. Still, this does not seem to be an issue since most of the candidates have effective masses significantly below the maximum allowed value.

3.3.2 Point defects in material

The unavoidable defects in materials are a cause for poor performance of many semiconductors. Sometimes, even a very small percentage of defects can have an important influence on material's properties. Vacancies, antisites and interstitials of different charge and type, are often objects of scientific investigations in semiconductors. The main concern is whether a point defect will induce new states in the material.

The localized electronic states positioned deep inside the band gap of the semi-

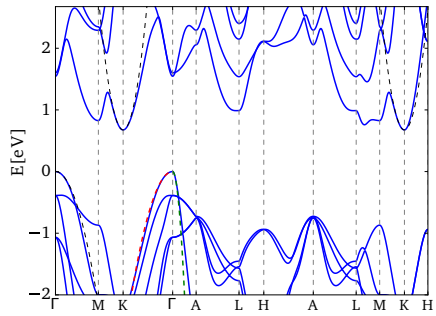

Figure 3.6: Band structure of Mg_3Sb_2: the valence band shows different curvature in the two different directions, K-Γ and Γ-A which yield different effective masses.

conductor can act as scattering centers, reduce carrier mobility and enhance the radiative recombination of photogenerated carriers. As a consequence, the performance of opto-electronic device will be significantly reduced. How much influence a particular defect will have on material performance depends on to what degree does it modify the electronic band structures. The "harmless" defects will introduce states close to band edges (so-called shallow states). The defects are more harmful if the newly introduced states are found deep in the band gap (so-called deep states). One can categorize materials based on position of defect states: materials where defects form deep states are therefore defect sensitive materials while materials only shallow states appear are defect tolerant.

The theoretical modeling of point defects in crystalline materials by means of the DFT has been taken up lots of attention in the past few years. The review by Neugebauer et al.[80] covers in detail identification and characterization of defects using DFT. Based on thermodynamic formalism, formation energies of defects or relative stability of charged states can be identified. However, obtaining reliable results has shown to be problematic due to the lattice geometry and usage of periodic boundary conditions. Firstly, one usually assumes the dilute limit where defect-defect interactions are negligible. Achieving the dilute limit in periodic crystals requires performing calculations in the so-called super-cells (defect surrounded by a few dozen to a few hundred atoms of the host material). Calculating charged defects becomes even more challenging since the electrostatic interaction decays very slowly with increasing super-cell size.

Approaches described in ref. [80] still require significant computational resources and as thorough investigation is not feasible for a large number of materials. Therefore, here I focus only on identification of electronic states due to the neutral vacancies and no in-depth investigation of defects was made.

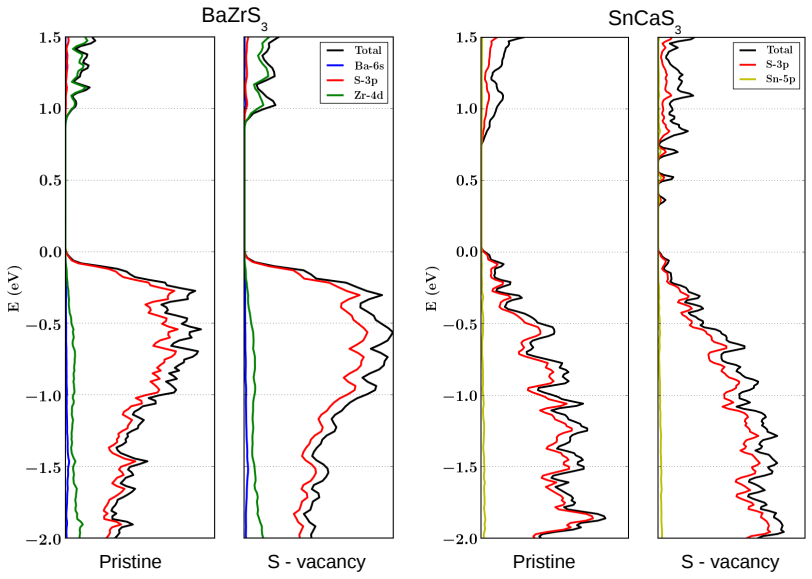

Figure 3.7: Projected and total DOS of $BaZrS_3$ and $SnCaS_3$. Introduction of sulfur vacancy results in additional states in the band gap of $SnCaS_3$ and the material is called defect sensitive. DOS of $BaZrS_3$ does not change significantly and no new states are found so the material is defect tolerant. (Here defect tolerance only implies sulfur vacancy so the procedure should be repeated for other types of defects as well.) Figure from Paper III.

The DFT calculations for the pristine structures and defect super-cell structures were performed using the PBE exchange correlation functional and fixed k-point density. The super-cells with defects were not relaxed since one expects defect to only have local effect on the geometry while the rest of the material keeps the same geometry as the pristine structure. Here I use the density of states (DOS) instead of the band structure to identify possible localized states in the band gap. The size of the band gap is often underestimated due to the PBE exchange correlation functional, but the quantitative nature of defects remains the same[80]. Possible problems may arise for small band gap semiconductors which PBE predicts (almost) metallic.

Figure 3.7 illustrates an example materials with and without defect states in the band gap. Both materials contain sulfur vacancy and in the case of $BaZrS_3$ the DOS around the band gap is almost unchanged, while in case of $SnCaS_3$ new states are present.

This approach is still from ideal since it still requires significant computational resources, which is the main reason why it is always done at the end of the screening process. Finally, the defect analysis employed in this step is only scratching the surface of defect physics of material and additional investigations are often performed for materials of interest, but such work goes beyond the screening study.

CHAPTER 4

Summary of the results

This chapter contains the short summary of the most important results of the papers.

4.1 Paper I: Defect-Tolerant Monolayer Transition Metal Dichalcogenides

In chapter 3 I brought up the issue of imperfections and defects in materials which may have a significant influence on it's electronic properties. In this paper we explain the nature of localized defect states inside the band gap and develop a descriptor to predict appearance of mid-gap, defect induced, states in 2 dimensional(2D) transition metal dichalcogenides.

Firstly, we introduce the connection between the orbital character of the bands and defect tolerance. Based on the orbital character of bands near band edges, one can divide semiconductors into two groups. In general, type i) materials have valence and

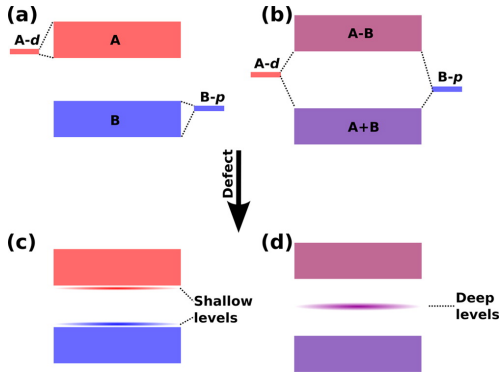

Figure 4.1: (a and b) Nature of the band structures near the band edges for the defect-tolerant and defect-sensitive cases, respectively.(c and d) Shallow and deep levels introduced after the creation of defects. Figure from paper I.

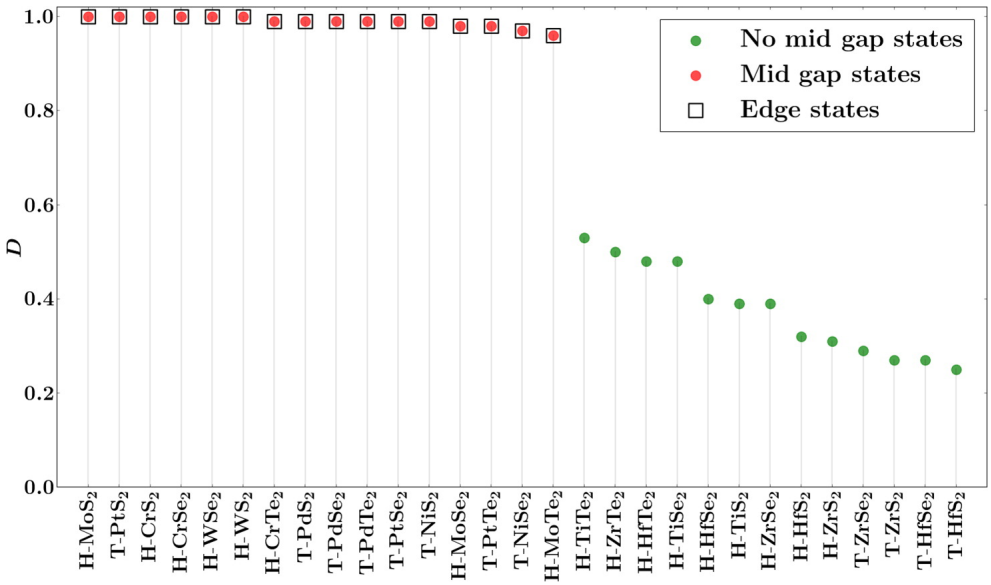

Figure 4.2: Plot showing the compounds (x-axis) and the corresponding D values (y-axis). Red circles indicate the compounds manifesting deep defect states and the green circles indicating the compounds showing no deep defect states after the removal of a chalcogen atom. The black squares represent compounds showing states appearing deep in the band gap after cleaving the monolayer to form nanoribbons. Figure from paper I.

conduction bands composed of orbitals with different character (for instance, HfS_2, shown in figure 2 in the paper, dominantly has sulfur p orbitals close to the valence band edge and hafnium d orbitals close to the conduction band edge). On the other hand, second or type ii) materials have valence and conduction bands composed of bonding and anti-bonding combinations of similar orbitals (an example, also in figure 2 in the paper, is MoS_2 with mixed states in both valence and conduction bands). In the former case, individual orbitals of the different character lie in the band, whereas in the latter case the orbitals lie in the band gap. Removal of an atom leaves behind a dangling bond state, which dependent on the orbital position, will be close to the band edge (tolerant) or in the middle of the band gap (sensitive). The two distinctive cases are illustrated in figure 4.1.

The above is not restricted to 2D metal dichalcogenides but is common for all semiconductors (2D, 3D), also reported in the literature [81]. One can conclude that the key quantity for determining defect tolerance is the orbital character in the vicinity of the band edges. The projected density of states (pDOS) on relevant states (metal

p and chalcogen d in this case) allows determining orbital characters of any material with only one DFT calculation.

The main novelty in the paper is the introduction of quantitative representation of the orbital character: the orbital fingerprint vector.

For a given energy window, the projected density of states onto the atomic orbital, ρ_{ν_i}, (where ν_i's are atom and angular momentum channel) is used to construct the orbital fingerprint vector $|\alpha\rangle$,

$$|\alpha\rangle = c \begin{bmatrix} \rho_{\nu_1} \\ \rho_{\nu_2} \\ \vdots \\ \rho_{\nu_N} \end{bmatrix}, \tag{4.1}$$

and c is the normalization constant.

The orbital fingerprint vector is obtained in the narrow region between the band gap and selected quantity E_n, which is just a distance in eV from the band edge. It gives the quantitative description of orbital character in that region. This infers defining the measure of difference on orbital characters between valence and conduction bands. The measure of distance, normalized orbital overlap (NOO) $D = \langle\alpha|\beta\rangle$ is a quantitative representation of defect tolerance of the material. α and β corresponding to valence and conduction band manifolds, respectively. The materials with different character of valence and conduction bands will result in small D values whereas large D values will be a consequence of identical orbital character. D can take values between 0 and 1, zero for materials with completely different orbital character and one for materials with exactly the same orbital character.

The calculation of D values for 29 TMDs resulted in clear division between defect tolerant and defect sensitive materials. Calculated values, for all the materials, are reported in figure 4.2. To confirm the reliability of NOO, band structure calculations for all pristine monolayers and super-cells with chalcogen vacancy were performed and visually investigated. For all the materials with D values close to one, localized states were found inside the band gap, whereas materials with lower D values did not show deep gap states. Overall, both NOO and direct calculations are in agreement and we report 13 defect tolerant and 16 defect sensitive TMDs.

In addition, the nanoribbons cleaved from TMD monolayers were found to have gap states for defect sensitive monolayers, whereas defect tolerant monolayers did not introduce gap states when cut down to a ribbon. All band structure and pDOS plots for the monolayers and ribbons can be found in the Supporting information of the paper.

In this work, we have investigated chalcogen defects in TMDs and developed a general scheme for predicting formation of gap states due to point defects or edges. More information regarding attempts to generalize the NOO for a wide range of materials, can be found in the Additional Information in chapter 6.1 as it goes beyond the scope of this paper.

4.2 Paper II: II–IV–V_2 and III–III–V_2 Polytypes as Light Absorbers for Single Junction and Tandem Photovoltaic Device

Among the most successful solar cell materials there are few, GaAs, InP and GaInP, which are a combination of III-V group constituents. More materials, like ternary $ZnSnN_2$[82–85] and $ZnSiP_2$[86] containing group V elements, have recently been investigated in the scope of single or tandem solar absorbers. These investigations have served as a motivation to systematically investigate classes of II-IV-V_2 and III-III-V_2 materials as solar absorbers. The selection of elements, for creating materials satisfying the ABX_2 stoichiometry, was made using the valence rules, as shown by the illustration in figure 1 in the paper. We investigate electronic and thermodynamic properties of chalcopyrite, kesterite, and wurtzite polymorphs. The design rule, used in this work, is based on binary semiconductors made of constituents of different ionic character (plus and minus). The anions are always group V elements whereas the cations are combinations of II-IV or III-III elements. Since A and B sites of the three polymorphs are equivalent, the order of AB (or BA) is not relevant in this case.

Beside suggesting good candidates for solar energy harvesting, the additional goal is to explore trends in materials' properties in a class or between classes. The performed investigation is very similar to the screening scheme introduced earlier in chapter 3 and includes investigation of stability, band gaps and carrier effective masses.

Thermodynamic stability of the materials was investigated using the convex hull approach (introduced in the section 3.2). A structure is considered stable if it has energy below or within the uncertainty of the convex hull, and if not, it is expected to dissolve into competing binary or standard phases. We found 32 out of 33 compounds to be thermodynamically stable, the only exception being $CdSiN_2$ (Figure 4 in the paper). The importance of including the uncertainty is seen in the example of $ZnSnN_2$, experimentally synthesized compound which without accounting for the uncertainty would be considered unstable (Figure 4 in the paper).

The band gaps were evaluated using two exchange correlation functionals: GLLB-SC and TB09, both introduced in chapter 2. The trend of decreasing band gaps, as X is moving from N to Sb in the group, is a direct consequence of the domination of X-p states in the valence band maximum. The X-p levels move up in energy as the element electronegativity decreases (N to Sb), which reduces the band gap. The same trend is observed for both binary and ternary compounds (figures 3 and 5 in the paper, respectively) with an exception on tin containing compounds. The exception was further investigated by analyzing the band structures and projected densities of states (pDOS). The anomaly in the conduction band minima, was found in phosphorous containing compounds, where an absence of Zn-s state is likely to be responsible for moving the conduction band higher in energy. More detailed discussion can be found in Results and Discussion section of the paper.

The selection of candidates for solar cell or tandem device materials was based

on the following criteria: i) must be thermodynamically (below the convex hull) and phase stable (have the lowest total energy or within the uncertainty to the most stable phase), ii) must have a band gap between 0.5 and 1.5 eV (small band gap material, SBG) or between 1.5 and 2.1 eV (large band gap material, LBG), and iii) carrier effective masses must be less than 0.7 electron mass units (m_e). Compounds containing toxic elements cadmium or arsenic were never considered as candidates and were only included to observe trends in the group of materials.

Finally, six SBG materials and eight LBG materials were found as promising candidates as photovoltaic absorbers. The search resulted in some already explored materials, for example $ZnSnN_2$ has been successfully synthesized in KT phase and proposed as a PV absorber. The search showed that other two phases of $ZnSnN_2$ should also be considered. $ZnSnP_2$, on the other hand, was found to cover a broader range of band gaps with it's three phases: the ST phase is a SBG candidate whereas the other two are LGB materials.

It is important to explore different, energetically close, polymorphs of the same material since presence of metallic phases is fatal for the light absorption. At the same time, if other polymorphs have interesting electronic properties, different synthesis techniques could be used to obtain desired polymorphs. Energetically close polymorphs and clear trends in electronic properties observed for the materials investigated in this work can be used to further expand materials within the class.

All the data, including crystal structure, band gaps and band structure, effective masses, and stability is provided in an interactive database available through Computational Materials Repository (CMR)[87].

Table 4.1: List of suggested PV candidates and SBG candidates for a tandem device. The experimental values of the band gaps are taken from ref.[76] unless stated otherwise.

Formula	**Structure**	$E_g^{GLLB-SC}$	E_g^{TB09}	$E_g^{Exp.}$	m^*_h	m^*_e
$ZnSiSb_2$	KT	0.78	1.06	-	-0.06	0.10
$ZnSiSb_2$	CP	1.15	1.10	-	-0.28	0.12
$ZnSnN_2$	KT	0.97	1.30	1.1[88]	-0.06	0.10
$ZnSnN_2$	CP	0.79	1.15	-	-0.14	0.08
$ZnSnN_2$	ST	0.94	1.25	-	-0.14	0.10
$ZnSnP_2$	ST	1.39	1.35	-	-0.10	0.13

Table 4.2: List of suggested LBG candidates for a tandem device. The experimental values of the band gaps are taken from ref.[76] unless stated otherwise.

Formula	**Structure**	$E_g^{GLLB-SC}$	E_g^{TB09}	$E_g^{Exp.}$	m^*_h	m^*_e
$GaInN_2$	KT	1.50	1.84	-	-0.13	0.12
$GaInN_2$	CP	1.22	1.62	-	-0.11	0.10
$GaInP_2$	KT	2.16	2.08	-	-0.12	0.16
$GaInP_2$	CP	2.06	2.16	1.83[89]	-0.10	0.11
$ZnGeP_2$	KT	1.73	1.65	-	-0.11	0.20
$ZnSiP_2$	CP	2.20	1.93	2, 2.1[90]	-0.39	0.32
$ZnSnP_2$	KT	1.67	1.61	-	-0.12	0.16
$ZnSnP_2$	CP	1.69	1.75	1.66	-0.10	0.10

4.3 Paper III: Sulfide Perovskites for Solar Energy Conversion Applications: Computational Screening and Synthesis of the Selected Compound $LaYS_3$

Clean fuel production, like solar energy driven water splitting which produces hydrogen is one of the most promising routes toward replacement of fossil fuels with fuels from renewable sources. Unfortunately, current devices are in the development stage and are still coping with problems like efficiency, long time stability and price to be ready for large scale deployment. The suggested device design where instead of absorbing a single photon, one absorbs two, achieving a higher voltage, efficiency can be increased more than three times. Such a design uses who semiconductors in series where the first, large band gap (LBG) semiconductor absorbs higher energy photons and the second, small band gap (SBG) semiconductor absorbs the ones of lower energy. The device is called a tandem device since the two semiconductors work in a tandem. However, their large scale application was held back by the lack of appropriate LBG semiconductors.

Several recent studies showed that some of the ternary sulfides of ABS_3 stoichiometry posses appropriate band gaps and exhibit good absorption properties. Some of the materials are $BaZrS_3$, $SrZrS_3$,[91, 92] $CuTaS_3$[93], $CaZrS_3$ and $SrTiS_3$[92].

In this work we perform a systematic investigation of a whole class of materials with ABS_3 stoichiometry, where A and B are 53 metal cations, yielding to 2809 different combinations. The valence rule, introduced in chapter 3, can be applied here since we are only interested in semiconducting materials and therefore the sum of valence numbers of the constituent elements should be zero. Choosing only A-B combinations that obey the rule reduces the number of combinations to 705.

The selected ABS_3 combinations were initially investigated in a five atom cubic

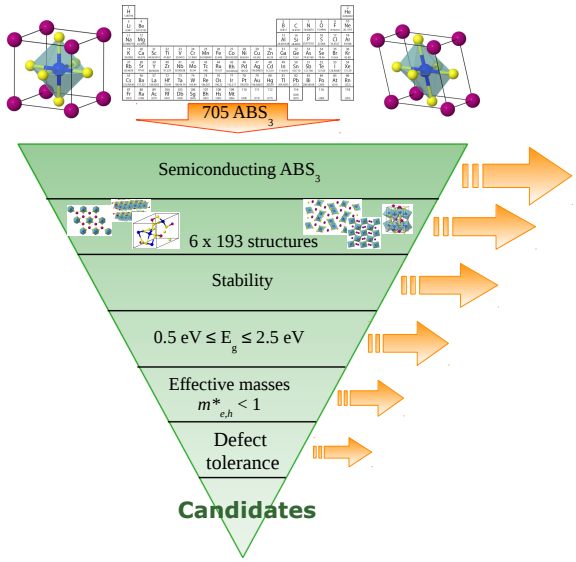

Figure 4.3: Illustration of the screening funnel adopting design criteria used in this work. At each stage, a new criteria is introduced and all materials not satisfying it are removed from further consideration. Figure from paper III.

perovskite and five atom distorted perovskite structure. In the cubic structure, only 15 combinations had non-zero band gap, while in distorted cubic the same was a case for 129 combinations. The combinations found to be metallic in a distorted cubic structure were removed from further investigation. The remaining, semiconducting, compounds were then subject to an extensive screening study based on design criteria discussed in chapter 3. The illustration of design criteria using the funnel analogy is shown in figure 4.4.

Having a reduced number of combinations, the first step is finding the global minimum energy structure. To cope with this nontrivial problem, six most frequent structures of the ABS_3 stoichiometry found in the ICSD were selected as structure prototypes: hexagonal $P6_3/mmc$ structure of $BaNiO_3$, orthorhombic $Pna2_1$ of $YScS_3$, two orthorhombic $Pnma$ structures, $GdFeO_3$ and NH_4CdCl_3/Sn_2S_2, monoclinic $C12/m1$ structure of $FePS_3$ and monoclinic $P1c1$ structure of $PbPS_3$. The crystal structure of these prototypes was used as templates where atoms occupying cation sites were replaced by corresponding A's and B's from the selected combinations.

Total energies obtained after structural relaxation of all the structures in all six prototypes are used to find the most stable structure. Using the mBEEF[48] exchange-correlation functional allows estimating uncertainties in the calculated DFT energies. All the energy differences and uncertainties are calculated with respect to the lowest energy structure in the set of ABS_3 and BAS_3 structures. The convex hull approach (introduced in chapter 3.2.2) was used to calculate stability toward segregation into other known structures or standard states. The pool of reference structures was built using binary and ternary compounds from the OQMD[70] database and the standard states. The stability of different phases is determined using the following criteria: 1) the energy of the structure is lower than the energy of the convex hull (uncertainties included), and 2) the structure is the lowest energy structure or is within 25 meV from the lowest energy structure (both ABS_3 and BAS_3 compounds are included). Given the criteria 2, one includes the room temperature effects since some structures (perovskites) are known to undergo phase transitions at low temperature. If there is more than one structure satisfying the above criteria (1 and 2), it is unclear whether the lowest energy structure is stable or meta-stable. One could, in principle, experimentally obtain a desired phase by choosing appropriate synthesis conditions. Figure 4 in the paper shows three distinctive cases which may occur when applying the above stability criteria.

Some of the compounds ruled stable have already been synthesized and are reported in the ICSD[62] database. We found agreement between calculated and predicted stable prototypes in almost all the cases. Four compounds, however, appear in new structures, which were not part of the screening: $LaYS_3$, $AgTaS_3$, $BiInS_3$ and $CuTaS_3$. All the compounds were calculated in corresponding structures, resulting in low energies so we keep them in the study.

Following down the screening funnel (figure 4.4), only stable (or meta-stable) compounds were further investigated. We access electronic properties by calculating band gaps, and later carrier effective masses of materials. The target values for band gaps are 0.5-1.5 for SBG semiconductors (solar cell absorbers) and 1.5-2.5 for LBG semiconductors (LBG component in the tandem device). The calculations were performed using the GLLB-SC exchange-correlation functional[33, 34]. The selection resulted in 90 structures which were further investigated in the study. Carrier effective masses were calculated using the scheme introduced in section 3.3.1. Since high carrier mobility is directly associated with low effective masses, we restrict selection by keeping only materials with both carrier effective masses lower than one electron mass (m_e). This further reduced number of materials to 42 candidates.

Finally, the sensitivity of materials to point defects was investigated using super-cells for three types of neutral vacancies. The investigation was performed by visually comparing band structures of pristine and super-cell structure for all the candidate materials. Mid-gap states formed due to point defects are unfavorable since they can act as recombination centers and largely reduce material's performance. 27 out of 42 materials form mid-gap states and the cause is always sulfur vacancy. The remaining 15 materials were found defect tolerant, and since they satisfied all the introduced criteria, these materials are our final candidates for good solar cell or tandem device

absorbers.

Identifying properties of different stable phases of a compound is useful once the material is being synthesized. If for a given compound one finds several structures at low energies, there is a chance that synthesis will lead to a sample made out of more than one phase (a small ratio or traces of other phases may be found). In that case, it is beneficial if all the phases have band gaps in relevant range, since existence of, for example metallic phase can lead to recombination losses. Compounds where all the stable phases have band gaps in in range for solar light absorption are reported in bold in table 4.3 and in figure 5 in the paper.

Finally, a perspective candidate, $LaYS_3$, which is a direct band gap material was synthesized in thin-film form by our collaborators. The comparison between experimental x-ray diffraction (XRD) pattern of synthesized film and the simulated XRD pattern was used to identify the $CeTmS_3$ phase of the compound. Besides the agreement in structure, a good match between calculated (1.79 eV) and experimental (2.00 eV) band gaps was also found.

Despite the fact that several properties were not fully investigated in the screening (for example scattering from photons and electrons or the full absorption spectra) the study yielded prospective candidates for solar cell absorbers and LBG absorbers in tandem devices. One of the candidates was successfully synthesized and an agreement between calculations and experiment was obtained for the structure and the band gap. This confirmed the theoretical prediction that $LaYS_3$ could be a good LBG absorber in a tandem water splitting device.

Table 4.3: List of selected candidates based on stability, band gaps, carrier effective masses, and defect tolerance. Compounds where all low-energy structures exhibit band gaps in the range of solar light absorption are indicated in bold. Table reprinted from paper III.

	formula	$E_g^{GLLB-SC}$	$E_{g(direct)}^{GLLB-SC}$	m^*_h	m^*_e	prototype
Ba-Hf	$BaHfS_3$	1.31	1.31	-0.347	0.943	NH_4CdCl_3/Sn_2S_3
Ba-Zr	$BaZrS_3$	2.25	2.25	-0.749	0.426	$GdFeO_3$
Bi-Tl	$BiTlS_3$	1.36	1.98	-0.636	0.309	$FePS_3$
Ca-Hf	$CaHfS_3$	0.99	0.99	-0.336	0.759	NH_4CdCl_3/Sn_2S_3
Ca-Sn	$CaSnS_3$	1.58	1.93	-0.606	0.943	NH_4CdCl_3/Sn_2S_3
Ca-Zr	$CaZrS_3$	1.36	1.36	-0.765	0.884	NH_4CdCl_3/Sn_2S_3
Hf-Sr	$SrHfS_3$	1.12	1.12	-0.327	0.811	NH_4CdCl_3/Sn_2S_3
Hf-Pb	$HfPbS_3$	1.12	1.63	-0.275	0.235	$BaNiO_3$
La-Y	$LaYS_3$	1.79	1.79	-0.670	0.490	$CeTmS_3$
Li-Ta	$TaLiS_3$	1.98	2.00	-0.755	0.985	$FePS_3$
Mg-Zr	$MgZrS_3$	2.21	2.32	-0.718	0.779	distorted
Sb-Y	$SbYS_3$	2.03	2.09	-0.372	0.484	NH_4CdCl_3/Sn_2S_3
Sr-Zr	$SrZrS_3$	1.46	1.46	-0.644	3.115	NH_4CdCl_3/Sn_2S_3
Ta-Tl	$TaTlS_3$	1.15	1.15	-0.297	0.241	distorted
Zn-Zr	$ZrZnS_3$	1.91	1.97	-0.616	0.420	$FePS_3$

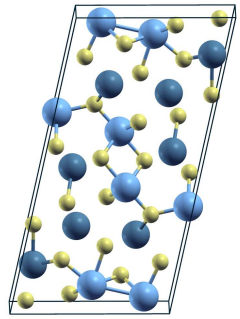

Figure 4.4: Crystal structure of $LaYS_3$ in $CeTmS_3$ phase.

4.4 Paper IV: High-Throughput Assessment of Experimentally Stable Materials for Single Junction and Tandem Photovoltaic Devices

The rapidly growing deployment of PV technology is by far dominated by silicon, whereas other semiconductors, such as GaAs and CdTe have found their application mostly on niche markets. As discussed in the Introduction, all the current PV materials come with flaws which limit their performance. PC technology, on the other hand, is even a step behind the PV because of the lack of suitable absorbers. So-called tandem devices, composed of two photoabsorbers, each conducting one half of the water splitting reaction, can split the task to two materials and obtain required efficiency. However, the lack of suitable candidates for the large band gap (LBG) absorber in the tandem is holding back the progress in PC technology.

Despite the large research effort in finding good PV and PC absorbers, a fairly small number of semiconductors were considerd, when compared to the total number of semiconductors that have been synthesized. In this study, we focus on experimentally known semiconducting compounds and perform an extensive theoretical study to find potential PV and PC absorbers.

The Inorganic Crystal Structure Database (ICSD)[62] has a collection of over 180 000 inorganic compounds. However, the database contains a large number of duplicates and entries with incomplete information. The Open Quantum Materials Database (OQMD)[70] is a computational database which has a selection of unique entries originating from the ICSD. The geometries have been already relaxed using the DFT and several properties have been calculated at the PBE level. This makes it very convenient to use the OQMD entries originating from the ICSD as a initial set for screening. The materials containing toxic or non-abundant elements, as well as the ones containing elements with high Herfindahl-Hirschman index (HHI), are not

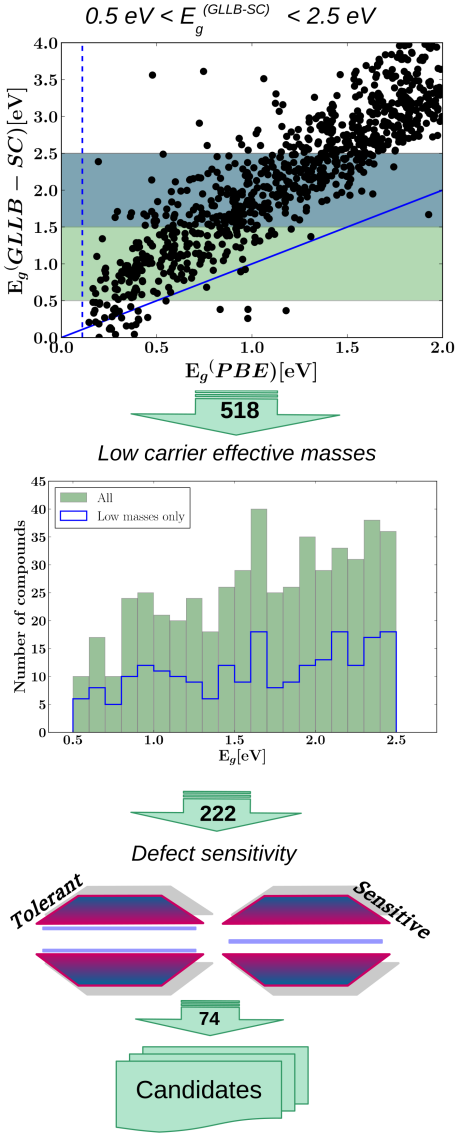

Figure 4.5: Illustration of the step-wise procedure, reprinted form paper IV. Top to bottom: i) Selecting materials with the GLLB-SC calculated band gaps between 0.5 and 2.5 eV. The plot shows the GLLB-SC band gaps versus the PBE band gaps. The blue and green striped areas show the HBG and LBG regions, respectively. ii) Selection of the materials with the carrier effective masses less than one m_e. The histogram of the band gaps of the materials before and after applying the criterion for the effective mass. iii) Selection of the defect tolerant materials: when no mid gap states in the band structure arise as a result of presence of point defects in the crystal, the material is defect tolerant. Number of candidates in each step is written on the arrows.

to be considerd (as motivated in section 3.2.1)

The PBE exchange-correlation (xc) functional severely underestimates the band gaps, but usually predicts correctly whether the material is a metal or a semiconductor. Therefore, on can almost certainly discard all the materials with zero PBE band gap. In addition, we set the upper limit to 2 eV for the PBE band gaps (accounting for the underestimation). The above restrictions result in decreasing the number of interesting materials to 1630. At this stage, we perform a screening study which includes reliable band gap calculations using GLLB-SC xc functional, calculations of carrier effective masses and investigate whether the material is tolerant to the introduction of point defects. The selection process was done using the previously introduced funnel scheme (section 3.2) where in each stage a criteria is introduced and if the obtained values do not satisfy the requirement, the material is no longer considered. This step-wise investigations allows to investigate properties which would normally require unreasonable amount of computer resources, but the reduced number of compounds at each stage makes it feasible.

The first criteria is the band gap in the visible range. Even though GLLB-SC, comparing to PBE, significantly improves band gap prediction, it can still deviate 0.3-0.5 eV from experimental values. To account for it, the range for the band gap for a PV material is set between 0.5 to 1.5 eV, and 1.5 and 2.5 eV for PC material. Carrier effective masses are required to be lower than 1 standard electron mass (m_e). Presence of point defects in materials may introduce new electronic states in the band gap. Such states can act as recombination centers and and harm materials performance. We distinguish two types of materials, based on the type of the new electronic states introduced by the defects: 1) defect tolerant: new electronic states are close to the band edge and play no major role in materials' performance, and 2) defect sensitive: new electronic states are in the middle of the gap and are a potentially terminal for materials performance. The defect tolerance is investigated using the procedure described in section 3.3.2.

Figure 4.5 shows an illustration of step-wise procedure used in this work: introduction of band gap criteria reduces the number of materials to 518, and only 222 of those have low carrier effective masses. In the last stage, materials were investigated for their tolerance to the point defects and the search yielded 74 defect tolerant materials. These 74 materials have satisfied all the introduced criteria in the screening, making it a set of final candidates for PV and PC absorbers. The full list of materials, together with calculated band gaps, carrier effective masses and, if available experimental band gaps, can be found in the table 1 in the manuscript.

A relatively small number of candidates allowed us to investigate few other details for each material. One of the issues is the stability: even though all the materials considered were synthesized, some of them require special conditions, like a high pressure, and may not be stable under ambient conditions. Another thing is phase stability of different polymorphs: there could exist another phase of the compound which is more stable. An example is $CsSnI_3$, a perovskite structure which appears in our list in orthorhombic 'black' and tetragonal phases, but the most stable structure is the orthorhombic 'yellow' phase with the band gap outside of our range (too high).

The search results in several materials which have already been considered for different applications: to name a few, Cs_3Sb was investigated as a photocatode, Cu_2S as a PV absorber and Cu_2O as both PV and PC absorber. The chalcogenide perovskite, $BaZrS_3$, which was also part of the study in Paper III, was found as a promissing candidate in this work as well.

One may notice that some already known PV and PC materials do not appear on the list. We investigated properties required by the descriptors for a small set of known PV and PC materilas, Si, GaAs,CdTe, CdSe, GaP, $CuInSe_2$ and $BiVO_4$, and discussed why they fail to pass our screening study. Firstly, As, Cd, Te and Bi are not on the list of allowed elements due to toxicity or low abundance (see figure 1 in the manuscript). Calculated band gap values are in a reasonable agreement with the experimental ones, with the exception of GaP, where calculated band gap is slightly overestimated, and $BiVO_4$, where the 1 eV difference between calculated and experimental band gaps can be assigned to the thermal effects. Lastly, defect sensitivity removes the remaining candidates, including silicon, which is known to require very high purity in order to perform well.

This exhaustive screening study begins with synthesized materials reported in the ICSD database and after investigating several properties including band gaps and effective masses, results in 74 candidates for PV and PC application. All the candidates are composed of non-toxic, abundant materials with low HHI index, which is directly connected to the final cost of material. A further experimental and more sophisticated theoretical evaluation is required to make sure that a candidate would work optimally in a device.

4.5 Paper V: Trigonal Selenium as Large Band Gap Material in Tandem Photoelectrochemical Devices

Despite selenium being one of the oldest known semiconductors, it has not been used for large scale deployment, like for example silicon. Rapid development of silicon as a solar energy absorber may have postponed the research on selenium, but mainly the cause for it was the low obtained efficiency (5%) comparing to the one of the silicon. The recently obtained 6.5% conversion efficiency is the record for selenium[94]. However, the recent advances in photoelectrochemical (PC) community suggested a tandem device composed of a small and large band gap semiconductors which work in a tandem. Selenium, with its 1.85 eV[76] band gap is an interesting candidate for the large band gap (LBG) absorber.

In this work we explore properties of trigonal selenium and its suitability to serve as a LBG absorber in a tandem device. Some of the previously introduced descriptors (see section 3.2), band gaps, effective masses and defect tolerance are also used in this work.

The crystal structure of selenium is a hexagonal lattice in which the atoms are arranged in spiral rods. The rods are oriented along the c axis of the cell. Such a

geometry suggests weak bonding between individual chains. However, our work shows the presence of covalent like bonding between the rods. The same was previously reported by Joannopoulos et al.[95]. In addition we explore the connection between the geometry and the opto-electronic properties.

We report calculated band gap values obtained with Density Functional Theory (DFT) and quasi particle G_0W_0 approximation. The DFT results in 1.71 eV (1.93 eV direct) and 1.86 eV(2.28 eV direct) using GLLB-SC[34] and HSE06[43] functionals, respectively. Calculated G_0W_0 quasi-particle band gap is slightly lower, 1.71 eV (1.98 eV direct). Obtained carrier effective masses are sufficiently low (0.166 m_e for holes and 0.123 m_e for electrons; m_e is the standard electron mass) suggesting high mobilities of both electrons and holes.

Optical properties are another indication of the type of bonding among neighboring rods. The electronic band structure shows larger dispersion in directions parallel to the rods. The absorption spectrum was obtained using the Random Phase Approximation (RPA) and solving the Bethe-Salpeter equation (BSE). The obtained spectra shows roughly three times stronger absorption in direction parallel to the rods. This goes hand by hand with the observations from the band structure and more in depth analysis suggests that the lowest transitions correspond to transitions within a rod. However, the transitions perpendicular to the rods are not negligible and suggest that selenium behaves more like a quasi-1D bulk semiconductor than a one dimensional material.

In addition, material's sensitivity toward introduction of point defects was investigated using the procedure described in section 3.3.2. Except the selenium vacancy, we also investigated tellurium and oxygen antisite. Our study shows that both selenium vacancy and oxygen antisite introduce mid gap states, whereas tellurium antisite is harmless with no new states in the band gap.

Finally, based on the appropriate band gap and low effective masses, selenium is a good candidate for a LBG PC absorber. Issues my arise due to mid gap states introduced by selenium vacancy or oxygen antisite, and therefore additional defect investigation is necessary.

This work is a collaboration between us and an experimental group at DTU Physics. The results presented here are only the theoretical part of the project.

CHAPTER 5

Papers

5.1 Paper I:Defect-Tolerant Monolayer Transition Metal Dichalcogenides

NANO LETTERS

Letter

pubs.acs.org/NanoLett

Defect-Tolerant Monolayer Transition Metal Dichalcogenides

Mohnish Pandey,[†] Filip A. Rasmussen,[†] Korina Kuhar,[†] Thomas Olsen,[†] Karsten W. Jacobsen,[†] and Kristian S. Thygesen*[,†,‡]

[†]Center for Atomic-Scale Materials Design (CAMD), Department of Physics, Technical University of Denmark, DK-2800 Kongens Lyngby, Denmark

[‡]Center for Nanostructured Graphene (CNG), Department of Physics, Technical University of Denmark, DK-2800 Kongens Lyngby, Denmark

Supporting Information

ABSTRACT: Localized electronic states formed inside the band gap of a semiconductor due to crystal defects can be detrimental to the material's optoelectronic properties. Semiconductors with a lower tendency to form defect induced deep gap states are termed defect-tolerant. Here we provide a systematic first-principles investigation of defect tolerance in 29 monolayer transition metal dichalcogenides (TMDs) of interest for nanoscale optoelectronics. We find that the TMDs based on group VI and X metals form deep gap states upon creation of a chalcogen (S, Se, Te) vacancy, while the TMDs based on group IV metals form only shallow defect levels and are thus predicted to be defect-tolerant. Interestingly, all the defect sensitive TMDs have valence and conduction bands with a very similar orbital composition. This indicates a bonding/antibonding nature of the gap, which in turn suggests that dangling bonds will fall inside the gap. These ideas are made quantitative by introducing a descriptor that measures the degree of similarity of the conduction and valence band manifolds. Finally, the study is generalized to nonpolar nanoribbons of the TMDs where we find that only the defect sensitive materials form edge states within the band gap.

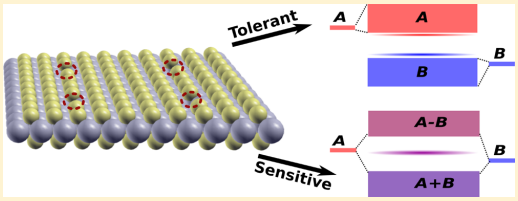

KEYWORDS: *Defect tolerance, density functional theory, descriptor, fingerprint, nanoribbon, 2D materials*

Single layers of semiconducting transition metal dichalcogenides (TMDs) are presently attracting much attention due to their unique optoelectronic properties which include direct−indirect band gap transitions,[1−4] valley selective spin−orbit interactions,[5,6] high charge carrier mobilities,[7−9] and strong light−matter interactions arising from large oscillator strengths and tightly bound excitons.[10,11] Another attractive feature of the two-dimensional (2D) materials is the fact that their electronic properties can be readily tuned, e.g., by applying strain,[12] electrostatic gating,[13,14] or by van der Waals heterostructure engineering.[15−17] In parallel with this development new 2D materials are continuously being discovered. For example, monolayers and multilayers of $MoTe_2$, $NbSe_2$, $NiTe_2$, TaS_2, $TaSe_2$, TiS_2, WS_2, WSe_2, and ZrS_2 have recently been synthesized or isolated by exfoliation.[18]

One of the main performance limiting factors of optoelectronics devices such as photo detectors, light-emitting diodes, solar cells, and field effect transistors is the presence of crystal defects in the active semiconductor material. Such defects can act as local scattering centers which reduce the mobility of charge carriers and enhance the nonradiative recombination of photoexcited electron−hole pairs. The effectiveness of a defect to scatter charge carriers, trap excitons, and induce recombination between electrons and holes depends crucially on the way the defect modifies the electronic structure around the band edges; in particular whether or not, it introduces localized states inside the band gap (deep gap states). On the other hand, defect states lying close, i.e., on the order of k_BT, to the conduction or valence band edges (shallow defect states) might enhance the charge carrier concentration and thereby the conductivity.[19] Depending on the extent of localization of a defect state it might affect the mobility as well. The materials where defects introduce deep gap states are termed defect-sensitive, while the materials where no or only shallow levels appear are called defect-tolerant.

There have been several experimental[20,21] and theoretical[22] studies of defects and their influence on the electronic properties of few-layer MoS_2—the most well-studied of the TMDs. These studies indicate that S vacancies are the most common type of defects and that they lead to the formation of localized states inside the band gap. The sulfur vacancies are believed to be the main reason for the low mobility observed in back gated field effect transistors based on chemical vapor deposition (CVD) grown MoS_2, which is usually 1−2 orders of magnitude lower than the theoretical limit set by phonon scattering.[7,8] In contrast, mobilities very close to the theoretical limit were recently measured in van der Waals heterostructure devices where a high-quality mechanically exfoliated MoS_2

Received: November 5, 2015
Revised: March 29, 2016
Published: March 30, 2016

DOI: 10.1021/acs.nanolett.5b04513
Nano Lett. 2016, 16, 2234−2239

monolayer was encapsulated into hexagonal boron nitride and contacted by graphene electrodes.[9] Defect-induced deep gap states are also responsible for the ultrafast nonradiative recombination of photoexcited excitons in MoS_2 which limits the quantum efficiency of CVD grown TMDs to <0.01.[23−25] Indeed, it was recently demonstrated that chemical passivation of the dangling bonds around the S vacancies in MoS_2 increases the photoluminescence quantum efficiency to almost unity.[26,27] However, defects and impurity doping can also be used constructively. For example, p-type conductivity in MoS_2, which is otherwise naturally n-doped, has been recently explored via niobium doping which introduces shallow acceptor levels near the valence band edge.[28,29] Defect states in monolayer WSe_2[30] and hBN[31] have recently been shown to act as single photon emitters with exciting opportunities for quantum technology. Engineering of the chemical activity of monolayer MoS_2 for the hydrogen evolution reaction was recently demonstrated via tuning the concentration of sulfur vacancies.[32]

In this Letter, we systematically explore the tolerance of monolayer TMDs to chalcogen vacancies. Using ab initio methods we calculate band structures of 29 monolayer semiconducting TMDs with and without chalcogen vacancies. The compounds have been selected from a 2D materials database which contains different electronic properties calculated from first-principles DFT and GW methods.[33,34] The correlation between the tendency of TMDs to form deep gap states and the orbital character of the valence and conduction band is established via a simple descriptor, the normalized orbital overlap (NOO), which is calculated from the projected density of states of the pristine system. We find that deep gap states are introduced for all the TMDs based on group VI and group X metals whose valence and conduction bands have similar orbital character (NOO close to 1) while no states or only shallow states are introduced for the other materials which have different orbital composition of their conduction and valence bands (NOO significantly less than 1). Additionally, we explore nanoribbons of all the TMDs and find that cleaving of the monolayer along a nonpolar direction of the defect tolerant TMDs induces only shallow states in the band gap as opposed to the nanoribbons of defect sensitive TMDs which all have metallic edge states.

All density functional theory (DFT) calculations were performed with the GPAW electronic structure code.[35] The wave functions are expanded on a real space grid with a grid spacing of 0.18 Å, and we use the PBE exchange-correlation (xc)-functional.[36] All of the pristine structures have been relaxed until the forces on each atom were below 0.05 eV/Å. Structures with chalcogen vacancies were modeled using a 3 × 3 supercell; see Figure 1.

In this work we base our analysis of defect states on the PBE single-particle band structures. This may seem as a drastic oversimplification as the PBE is known to underestimate the band gap of semiconductors, and its description of localized states is also problematic due to self-interaction errors which tend to push occupied levels up in energy. However, due to the large number of systems investigated here, and because we are interested in the qualitative features of the band structure, i.e., whether or not the vacancies introduce localized states in the gap, rather than the absolute energies of band edges and gap states, we rely on the PBE band structures in the present work. As discussed below we find that the PBE results are qualitatively fully consistent with the more rigorous Slater−Janak theory.

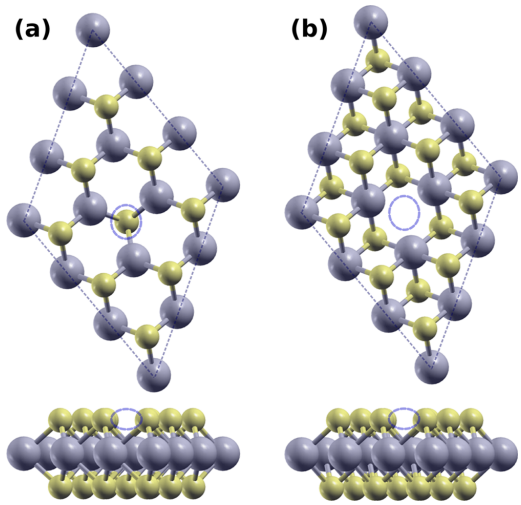

Figure 1. (a) Top and sideview of a prototypical structure of a metal dichalcogenide in the 2H structure used for the defect calculations. The unit cell is shown by the dotted lines. The defect structure is created by making a chalcogen vacancy as indicated by a blue ellipse. (b) Similar figure as (a) for the 1T structure.

The standard way to analyze defect energy levels in semiconductors is based on total energy calculations for supercells containing the defect in different charge states. This procedure is, however, not straightforward. For example, it does not overcome the PBE band gap problem, and thus the correct band edge positions must be inferred from experiments or more accurate calculations such as the GW method.[37] Moreover, the slow convergence of the total energy of a charged supercell with the cell size implies that some kind of energy correction scheme must be applied to achieve meaningful numbers, and there is no unique solution to this problem.[38−43] Alternatively, Slater−Janak (SJ) transition state theory may be used to obtain the defect levels without the need to compare total energies of differently charged systems.[44,45] The SJ method exploits that the Kohn−Sham eigenvalues are related to the derivative of the total energy E with respect to the occupation number η_i of the respective orbital,

$$\frac{\partial E[N]}{\partial \eta_i} = \varepsilon_i \tag{1}$$

Assuming that the eigenvalue for the highest occupied state ε_H varies linearly with the occupation number (this is in fact a very good approximation), the electron affinity level can be obtained as

$$E^{N+1} - E^N = \int_0^1 \varepsilon_H(\eta)\mathrm{d}\eta = \varepsilon_H\left(\frac{1}{2}\right) \tag{2}$$

Thus, one obtains the electron affinity level (ionization potential) as the highest unoccupied (lowest occupied) single-particle eigenvalue of the system with 0.5 electron added to (removed from) the supercell. The SJ model has previously been shown to predict semiconductor defect levels

DOI: 10.1021/acs.nanolett.5b04513
Nano Lett. 2016, 16, 2234−2239

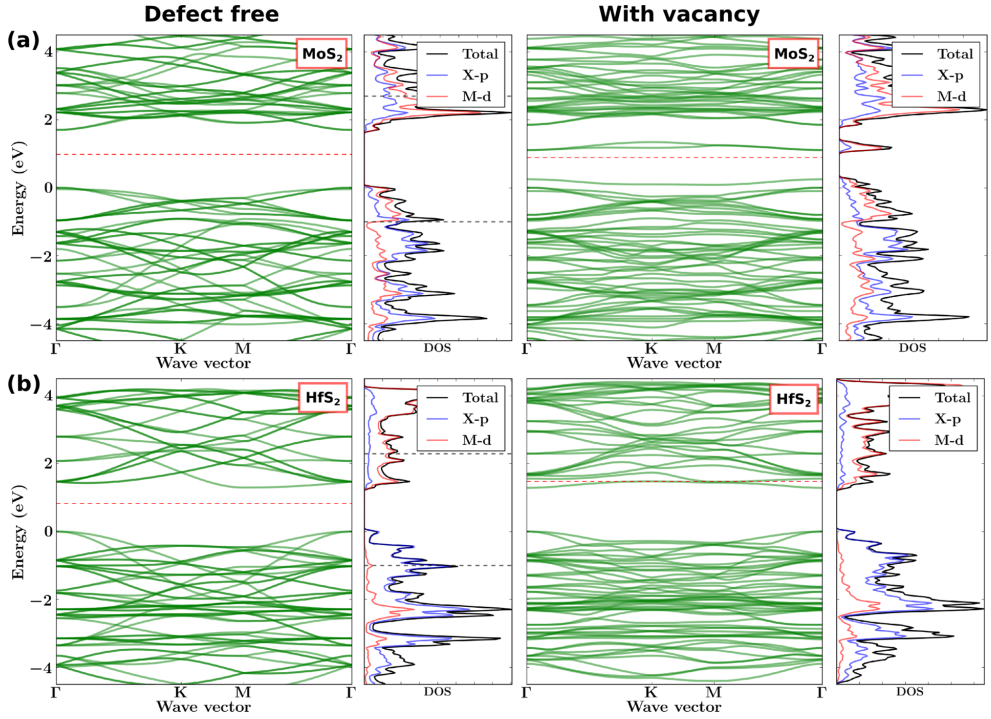

Figure 2. (a)PBE band structures, the DOS, and the PDOS on the chalcogen p-orbitals and metal d-orbitals of the monolayer 2H-MoS_2 in its pristine form (left) and with an S vacancy (right). For comparison, the band structure is plotted for 3 × 3 supercell for the pristine as well as the defect structure. The energy levels have been aligned to the valence band maximum of the pristine monolayer. (b) Similar figure as (a) for 1T-HfS_2.

in good agreement with the results obtained from more elaborate total energy difference schemes.[46]

For all 29 TMDs, we have applied the SJ method to compute the ionization potential and electron affinity levels of a 3 × 3 supercell containing a chalcogen vacancy. For consistency the systems have been structurally relaxed with the added ±0.5 electron in the supercell. The results do not differ qualitatively from those derived from the PBE band structure of the neutral supercells. In particular, the two methods predict the same set of materials to be defect tolerant and defect sensitive, respectively. However, there are small differences between the two approaches. Taking MoS_2 as an example, the neutral PBE spectrum shows an occupied defect level positioned around 0.2 eV above the top of the valence band; see Figure 2a. After removal of 0.5 electron, the self-consistent PBE spectrum no longer shows this defect level (see Figure S68 in the Supporting Information). This indicates that the PBE description places the occupied defect level too high in energy which is most likely due to the PBE self-interaction error. Interestingly, PBE total energy difference calculations find the defect state below the valence band maximum in agreement with the SJ calculation.[22] However, this disagreement with the neutral PBE spectrum does not affect the conclusions regarding the defect tolerance of MoS_2 because both PBE and SJ consistently predict the presence of unoccupied defect levels at around 0.7 eV below the conduction band minimum (see Figure 2a) which again agrees with calculations based on total energy differences.[22]

We mention that PBE+U calculations were also performed for all the TMDs with U values ranging from 0 to 4 eV. However, the band gaps of the group VI and group X TMDs were found to decrease with increasing U leading to unphysical small band gaps for typical U values. Based on these findings, we do not consider PBE+U to be more accurate than PBE for the considered class of TMDs.

Figure 2a shows the PBE band structures, the total density of states (DOS), and the projected density of states (PDOS) on the chalcogen p-orbitals and metal d-orbitals of 2H-MoS_2 in its pristine form (left) and with an S vacancy (right). The three narrow bands inside the band gap (one just above the valence band edge and two almost degenerate bands just above the band gap center) are formed by dangling Mo d bonds localized around the S vacancy. From the PDOS it is seen that the valence band maximum (VBM) and conduction band minimum (CBM) have very similar orbital characters indicating that they consist of bonding and antibonding combinations of sulfur p and metal d states, respectively. We note that the finite size of the supercell (3 × 3) is responsible for the small dispersion of the deep gap states. We have found that applying a 4 × 4 supercell does not change the conclusions.

Figure 2b shows a similar plot as Figure 2a for 1T-HfS_2. In contrast to 2H-MoS_2, this compound largely conserves its electronic structure around the band edges, and no defect state is introduced. Additionally, the DOS plot shows that the states near the VBM are mostly dominated by the chalcogen p states

DOI: 10.1021/acs.nanolett.5b04513
Nano Lett. 2016, 16, 2234−2239

whereas the CBM edge states mainly consist of the metal d states.

The above examples indicate that the orbital character of the valence/conduction bands are crucial for the tendency to form deep gap states. Based on the above picture the materials can be categorized in two classes; one with conduction and valence bands composed of bonding and antibonding combinations of similar orbitals, the other with valence and conduction bands composed of orbitals with distinctly different character; see Figure 3. This picture also agrees with previous works on defect tolerance in semiconductors.[47] The correspondence between the orbital character of the bands and the defect tolerance can be understood from elementary chemical bond theory. In the case of similar orbital character of the valence and conduction bands, the former will have bonding character, and the latter will have the antibonding character. This implies that the energy of the individual orbitals should lie inside the band gap; see Figure 3b. Thus, the creation of a vacancy leaves a dangling bond state corresponding to one of the orbitals lying deep in the band gap. On the other hand, different orbital characters of the valence and conduction bands suggests that these bands are formed by orbitals lying outside the band gap, and therefore dangling bond states should not fall inside the gap. To quantify the orbital character of the electronic states in a given energy window from E_1 to E_2 we introduce the orbital fingerprint vector,

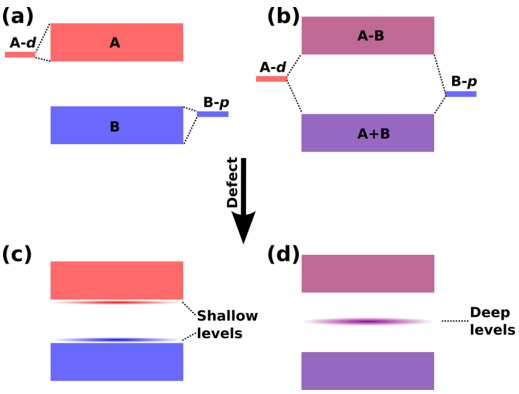

Figure 3. (a and b) Nature of the band structures near the band edges for the defect-tolerant and defect-sensitive cases, respectively. In all of the TMDs studied here, the states near the band edges primarily have contributions from the metal d states and chalcogen p states. In the defect tolerant case, the nature of the bands near the band edges are significantly different, whereas in the defect-sensitive case, they are of mixed nature. (c and d) Shallow and deep levels introduced after the creation of defects.

$$|\alpha\rangle = c\begin{bmatrix}\rho_{\nu_1}\\ \rho_{\nu_2}\\ \vdots\\ \rho_{\nu_N}\end{bmatrix} \tag{3}$$

where c is a normalization constant, the ν_i's are (a, l) pairs where "a" and "l" denote the atom and angular momentum channel, respectively; and $\rho_{\nu i}$ is the projected density of states onto the atomic orbital $\phi_{\nu i}$ integrated over the energy window,

$$\rho_{\nu_i} = \sum_n \int_{E_1}^{E_2} |\langle\psi_n|\phi_{\nu_i}\rangle|^2 \delta(E - E_n)\, dE \tag{4}$$

Using the orbital fingerprint vector, we can define the normalized orbital overlap (NOO) between two manifolds of bands located in the energy windows E_1^v to E_2^v and E_1^c to E_2^c as

$$D = \langle\alpha|\beta\rangle \tag{5}$$

where α and β correspond to the valence and conduction band manifolds. By taking the two energy windows to lie around the

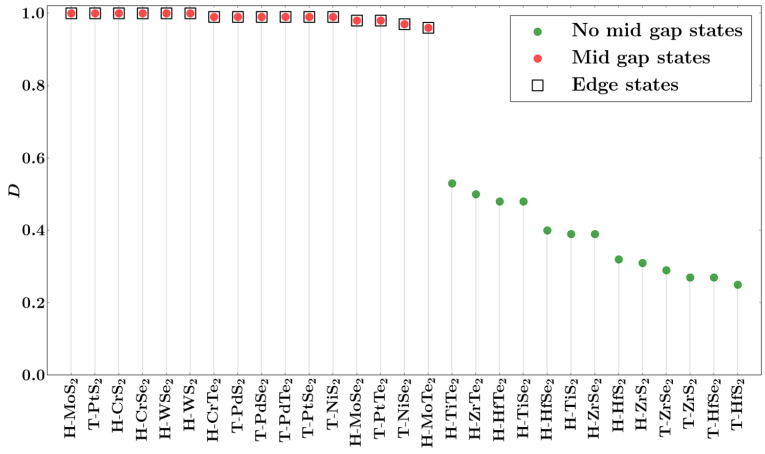

Figure 4. Plot showing the compounds (y-axis) and the corresponding D values (x-axis). Red circles indicate the compounds manifesting deep defect states and the green circles indicating the compounds showing no deep defect states after the removal of a chalcogen atom. The black squares represent compounds showing states appearing deep in the band gap after cleaving the monolayer to form nanoribbons. Cr, Mo, and W dichalcogenides are group-IV; Ti, Zr, and Hf dichalcogenides are group-VI, and Ni, Pd, and Pt dichalcogenides are group-X.

DOI: 10.1021/acs.nanolett.5b04513
Nano Lett. 2016, 16, 2234−2239

VBM and CBM, respectively, we have a measure of the difference in average orbital character around the valence and conduction band edges. We note that $D = 0$ for materials with completely different character of the valence and conduction bands, while $D = 1$ for materials with identical orbital character at the valence and conduction bands.

We have computed D (with an energy window of 1 eV above/below the conduction/valence band extrema) for a set of 29 monolayer TMDs; see Figure 4. We have carried out band structure calculations like the ones shown in Figure 2 for all 29 TMDs (see Supporting Information). For all of the materials with $D \sim 1$ we find localized states inside the band gap. In contrast all of the materials with D significantly less than 1 do not show deep gap states. The compounds exhibiting deep defect states after the removal of a chalcogen atom are shown with red circles in the Figure 4, whereas the compounds where no deep gap states are introduced after a chalcogen atom is removed are marked with green circles. This clearly shows that the NOO between the valence and conduction band manifolds represent a reliable and quantitative descriptor for the degree of defect tolerance of the TMDs. We stress that this rule should apply to the case of vacancies, crystal distortions, or other perturbations whose effect is to distort the intrinsic bonding. On the other hand, in the case of impurity atoms, the presence of deep gap states depends also on the energy of the atomic orbitals of the impurity atom relative to the band edges.

The clear division of 29 TMDs into defect-tolerant and defect-sensitive materials can be understood from Figure 5. The

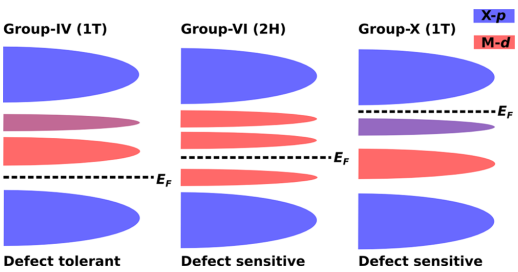

Figure 5. Sketch showing the filling of the electronic levels of the different groups of the transition metal dichalcogenides. The TMDs of group-IV are defect-tolerant, whereas the TMDs of group-VI X are defect-sensitive. The chalcogen p states are shown in blue and the metal d states in red. The regions with mixed color have mixed p and d character.

splitting of the levels, the relative contribution of the chalcogen-p and metal-d, and the position of the Fermi level decides the value of the descriptor. For example, in the 1T phase the position of the Fermi level in group-4 TMDs leads to the VBM having chalcogen-p and the CBM having metal-d character hence leading to defect tolerance. On the other hand, filling up of more levels in group-10 compounds places the Fermi level in such a way that the VBM and CBM states have dominant chalcogen-p character (for example, see SI for PDOS of NiS_2) resulting in similar orbital fingerprint vectors consequently leading to defect sensitivity. A similar argument can be applied to the compounds of group-6 in the 2H structure.

Additionally, we also calculated the band structure of nanoribbons cleaved from the monolayer TMDs. As recently explained, TMD nanoribbons cleaved along a polar direction will manifest metallic edge states due to the presence of a dipole across the ribbon.[48] However, cleaving the monolayer along a nonpolar direction can introduce edge states due to the formation of dangling bonds thus having a close resemblance to the case of a monolayer with a vacancy where the shallow/deep levels arise due to the presence of dangling bonds. Therefore, we expect that the arguments for the monolayers with vacancies will also be applicable for the edges in the nanoribbons.

Figure 6a and b show the structure of the nonpolar nanoribbons of the 2H and 1T structures, respectively, used

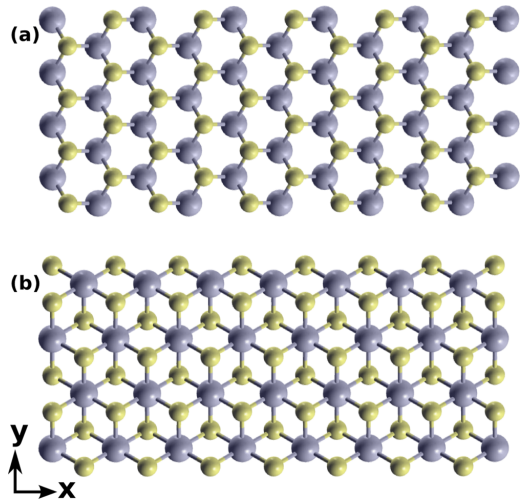

Figure 6. (a) Structure of a nanoribbon of the 2H structure cleaved along the nonpolar direction. The edges of the nanoribbons lie along the x-axis with a finite width along the y-axis; (b) a nanoribbon cleaved from the 1T structure.

for the analysis of the edge states. The edges of the nanoribbons are directed along the horizontal axis. In Figure 4 the nanoribbons supporting edge states (lying deep) in the band gap are shown with open squares. The figure consistently shows that only the defect sensitive TMDs form edge states deep in the band gap, whereas the defect tolerant TMDs form only shallow, or no, edge states in the band gap (see Supporting Information for the band structure). This indicates that the analysis based on the NOO descriptor is rather general and should be applicable to other system with imperfections involving dangling bonds. We are currently investigating the descriptor and possible generalizations of it for different classes of semiconductors.

In summary, we have explored the sensitivity of the band structure of 2D TMDs toward chalcogen vacancies. Our analysis shows that the tendency of the materials to form localized states within the band gap strongly depends on the similarity of the orbital character of the states near the conduction and valence band. These ideas were made quantitative by introducing a simple descriptor based on the projected density of states at the conduction and valence band edges. For a set of 29 semiconducting TMDs, we found a clear correlation between the size of this descriptor and the presence of deep gap states induced by a chalcogen vacancy or by the formation of a one-dimensional edge. The idea of identifying

DOI: 10.1021/acs.nanolett.5b04513
Nano Lett. 2016, 16, 2234−2239

defect-tolerant materials based on a quantitative descriptor measuring valence and conduction band state similarity is completely general. In particular it does not depend on the dimensionality of the material and should be useful both as general concept and as a tool for computational prediction of defect-tolerant compounds.

■ ASSOCIATED CONTENT

Supporting Information

The Supporting Information is available free of charge on the ACS Publications website at DOI: 10.1021/acs.nanolett.5b04513. The 2H and 1T structures used for the analysis can be accessed at http://cmr.fysik.dtu.dk.

Band structures of 29 TMDs monolayers in the pristine and defect forms and the band structure of the nonpolar nanoribbons; the plot of the descriptor for different energy windows; and the effect of relaxation and charging of the systems (PDF)

■ AUTHOR INFORMATION

Corresponding Author

*E-mail: thygesen@fysik.dtu.dk.

Notes

The authors declare no competing financial interest.

■ ACKNOWLEDGMENTS

The authors acknowledge support from the Danish Council for Independent Research's Sapere Aude Program, Grant No. 11-1051390. The Center for Nanostructured Graphene is sponsored by the Danish National Research Foundation, Project DNRF58.

■ REFERENCES

(1) Mak, K. F.; Lee, C.; Hone, J.; Shan, J.; Heinz, T. F. *Phys. Rev. Lett.* **2010**, *105*, 136805.
(2) Splendiani, A.; Sun, L.; Zhang, Y.; Li, T.; Kim, J.; Chim, C.-Y.; Galli, G.; Wang, F. *Nano Lett.* **2010**, *10*, 1271−1275.
(3) Zeng, H.; Liu, G.-B.; Dai, J.; Yan, Y.; Zhu, B.; He, R.; Xie, L.; Xu, S.; Chen, X.; Yao, W. *Sci. Rep.* **2013**, *3*, 01608.
(4) Zhang, C.; Johnson, A.; Hsu, C.-L.; Li, L.-J.; Shih, C.-K. *Nano Lett.* **2014**, *14*, 2443−2447.
(5) Cao, T.; Wang, G.; Han, W.; Ye, H.; Zhu, C.; Shi, J.; Niu, Q.; Tan, P.; Wang, E.; Liu, B.; et al. *Nat. Commun.* **2012**, *3*, 887.
(6) Mak, K. F.; He, K.; Shan, J.; Heinz, T. F. *Nat. Nanotechnol.* **2012**, *7*, 494−498.
(7) Kaasbjerg, K.; Thygesen, K. S.; Jacobsen, K. W. *Phys. Rev. B: Condens. Matter Mater. Phys.* **2012**, *85*, 115317.
(8) Kaasbjerg, K.; Thygesen, K. S.; Jauho, A.-P. *Phys. Rev. B: Condens. Matter Mater. Phys.* **2013**, *87*, 235312.
(9) Cui, X.; Lee, G.-H.; Kim, Y. D.; Arefe, G.; Huang, P. Y.; Lee, C.-H.; Chenet, D. A.; Zhang, X.; Wang, L.; Ye, F.; et al. *Nat. Nanotechnol.* **2015**, *10*, 534−540.
(10) Britnell, L.; Ribeiro, R. M.; Eckmann, A.; Jalil, R.; Belle, B. D.; Mishchenko, A.; Kim, Y.-J.; Gorbachev, R. V.; Georgiou, T.; Morozov, S. V.; et al. *Science* **2013**, *340*, 1311−1314.
(11) Bernardi, M.; Palummo, M.; Grossman, J. C. *Nano Lett.* **2013**, *13*, 3664−3670.
(12) Conley, H. J.; Wang, B.; Ziegler, J. I.; Haglund, R. F.; Pantelides, S. T.; Bolotin, K. I. *Nano Lett.* **2013**, *13*, 3626−3630.
(13) Liu, Q.; Li, L.; Li, Y.; Gao, Z.; Chen, Z.; Lu, J. *J. Phys. Chem. C* **2012**, *116*, 21556−21562.
(14) Rostami, H.; Moghaddam, A. G.; Asgari, R. *Phys. Rev. B: Condens. Matter Mater. Phys.* **2013**, *88*, 085440.
(15) Gao, G.; Gao, W.; Cannuccia, E.; Taha-Tijerina, J.; Balicas, L.; Mathkar, A.; Narayanan, T. N.; Liu, Z.; Gupta, B. K.; Peng, J.; et al. *Nano Lett.* **2012**, *12*, 3518−3525.
(16) Geim, A. K.; Grigorieva, I. V. *Nature* **2013**, *499*, 419−425.
(17) Andersen, K.; Latini, S.; Thygesen, K. S. *Nano Lett.* **2015**, *15*, 4616−4621.
(18) Chhowalla, M.; Shin, H. S.; Eda, G.; Li, L.-J.; Loh, K. P.; Zhang, H. *Nat. Chem.* **2013**, *5*, 263−275.
(19) Wen, X.; Feng, Y.; Huang, S.; Huang, F.; Cheng, Y.-B.; Green, M.; Ho-Baillie, A. *J. Mater. Chem. C* **2016**, *4*, 793.
(20) McDonnell, S.; Addou, R.; Buie, C.; Wallace, R. M.; Hinkle, C. L. *ACS Nano* **2014**, *8*, 2880−2888.
(21) Qiu, H.; Xu, T.; Wang, Z.; Ren, W.; Nan, H.; Ni, Z.; Chen, Q.; Yuan, S.; Miao, F.; Song, F.; et al. *Nat. Commun.* **2013**, *4*, 2642.
(22) Komsa, H.-P.; Krasheninnikov, A. V. *Phys. Rev. B: Condens. Matter Mater. Phys.* **2015**, *91*, 125304.
(23) Wang, H.; Zhang, C.; Rana, F. *Nano Lett.* **2015**, *15*, 339−345.
(24) Lopez-Sanchez, O.; Lembke, D.; Kayci, M.; Radenovic, A.; Kis, A. *Nat. Nanotechnol.* **2013**, *8*, 497−501.
(25) Ross, J. S.; Klement, P.; Jones, A. M.; Ghimire, N. J.; Yan, J.; Mandrus, D. G.; Taniguchi, T.; Watanabe, K.; Kitamura, K.; Yao, W.; et al. *Nat. Nanotechnol.* **2014**, *9*, 268−272.
(26) Lu, J.; Carvalho, A.; Chan, X. K.; Liu, H.; Liu, B.; Tok, E. S.; Loh, K. P.; Neto, A. H. C.; Sow, C. H. *Nano Lett.* **2015**, *15*, 3524−3532.
(27) Amani, M.; Lien, D.-H.; Kiriya, D.; Xiao, J.; Azcatl, A.; Noh, J.; Madhvapathy, S. R.; Addou, R.; KC, S.; Dubey, M.; et al. *Science* **2015**, *350*, 1065−1068.
(28) Suh, J.; Park, T.-E.; Lin, D.-Y.; Fu, D.; Park, J.; Jung, H. J.; Chen, Y.; Ko, C.; Jang, C.; Sun, Y.; et al. *Nano Lett.* **2014**, *14*, 6976−6982.
(29) Wan, H.; Xu, L.; Huang, W.-Q.; Zhou, J.-H.; He, C.-N.; Li, X.; Huang, G.-F.; Peng, P.; Zhou, Z.-G. *RSC Adv.* **2015**, *5*, 7944−7952.
(30) Chakraborty, C.; Kinnischtzke, L.; Goodfellow, K. M.; Beams, R.; Vamivakas, A. N. *Nat. Nanotechnol.* **2015**, *10*, 507−511.
(31) Tran, T. T.; Bray, K.; Ford, M. J.; Toth, M.; Aharonovich, I. *Nat. Nanotechnol.* **2015**, *11*, 37−41.
(32) Li, H.; Tsai, C.; Koh, A. L.; Cai, L.; Contryman, A. W.; Fragapane, A. H.; Zhao, J.; Han, H. S.; Manoharan, H. C.; Abild-Pedersen, F.; et al. *Nat. Mater.* **2015**, *15*, 48−53.
(33) Rasmussen, F. A.; Thygesen, K. S. *J. Phys. Chem. C* **2015**, *119*, 13169−13183.
(34) https://cmr.fysik.dtu.dk/ (accessed July 31, 2015).
(35) Enkovaara, J.; Rostgaard, C.; Mortensen, J. J.; Chen, J.; Dułak, M.; Ferrighi, L.; Gavnholt, J.; Glinsvad, C.; Haikola, V.; Hansen, H. A.; et al. *J. Phys.: Condens. Matter* **2010**, *22*, 253202.
(36) Perdew, J. P.; Burke, K.; Ernzerhof, M. *Phys. Rev. Lett.* **1996**, *77*, 3865−3868.
(37) Huser, F.; Olsen, T.; Thygesen, K. S. *Phys. Rev. B: Condens. Matter Mater. Phys.* **2013**, *88*, 245309.
(38) Leslie, M.; Gillan, N. J. *J. Phys. C: Solid State Phys.* **1985**, *18*, 973.
(39) Makov, G.; Payne, M. C. *Phys. Rev. B: Condens. Matter Mater. Phys.* **1995**, *51*, 4014−4022.
(40) Lany, S.; Zunger, A. *Phys. Rev. B: Condens. Matter Mater. Phys.* **2008**, *78*, 235104.
(41) Freysoldt, C.; Neugebauer, J.; Van de Walle, C. G. *Phys. Rev. Lett.* **2009**, *102*, 016402.
(42) Komsa, H.-P.; Rantala, T. T.; Pasquarello, A. *Phys. Rev. B: Condens. Matter Mater. Phys.* **2012**, *86*, 045112.
(43) Schultz, P. A. *Phys. Rev. Lett.* **2000**, *84*, 1942−1945.
(44) Gallino, F.; Pacchioni, G.; Di Valentin, C. *J. Chem. Phys.* **2010**, *133*, 144512.
(45) Chakrabarty, A.; Patterson, C. H. *J. Chem. Phys.* **2012**, *137*, 054709.
(46) Li, Y.; Sanna, S.; Schmidt, W. G. *J. Chem. Phys.* **2014**, *140*, 234113.
(47) Zakutayev, A.; Caskey, C. M.; Fioretti, A. N.; Ginley, D. S.; Vidal, J.; Stevanovic, V.; Tea, E.; Lany, S. *J. Phys. Chem. Lett.* **2014**, *5*, 1117−1125.
(48) Gibertini, M.; Marzari, N. *Nano Lett.* **2015**, *15*, 6229−6238.

DOI: 10.1021/acs.nanolett.5b04513
Nano Lett. 2016, 16, 2234−2239

5.2 Paper II: II–IV–V_2 and III–III–V_2 Polytypes as Light Absorbers for Single Junction and Tandem Photovoltaic Device

THE JOURNAL OF PHYSICAL CHEMISTRY C

Article

pubs.acs.org/JPCC

II–IV–V_2 and III–III–V_2 Polytypes as Light Absorbers for Single Junction and Tandem Photovoltaic Devices

Mohnish Pandey,*[†,‡] Korina Kuhar,[†,‡] and Karsten W. Jacobsen[†]

[†]CAMD, Department of Physics, Technical University of Denmark, DK-2800 Kongens Lyngby, Denmark

ABSTRACT: Recent experiments on II–IV–V_2 type nitrides and phosphides have shown that these materials are potential candidates as photovoltaic absorbers. The materials space for such light absorbers can be expanded by elemental substitution of the different species, and thanks to the small energy difference of the polymorphs, the space can be extended by tuning the atomic structure as well. Using electronic structure calculations, we explore chalcopyrite, kesterite, and wurtzite polymorphs of II–IV–V_2 and III–III–V_2 materials for light absorption especially in the visible range. Based on the thermodynamic stability, band gap, and charge carrier effective masses, we discuss the posssibility for the materials containing nontoxic elements to act as PV absorbers. Additionally, the systematic mapping of the materials space provides trends in thermodynamic and electronic properties which can be exploited further to tune these properties via elemental substitution and/or alloying.

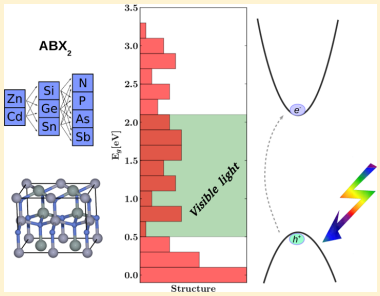

INTRODUCTION

The world's heavy dependence on fossil fuels for energy production has led to the current situation with severe climate challenges. Therefore, it is of utmost importance to provide viable alternative energy resources with solar energy being one of them. Solar energy can be harnessed in different ways, for example, photoelectrochemical water splitting, thermoelectrics, solar cells, etc.[1−4] However, harvesting solar energy in an efficient and economical way requires identification and design of new light-absorbing materials.

Currently, photovoltaics (PV) is an active area of research to harvest solar energy. One of the biggest advantages of the PV technology is that it offers a direct route for light-to-electricity conversion. The semiconductors used in single-component PV devices and the small band gap (SBG) semiconductors of tandem devices should have a band gap of ∼1 eV for an efficient light absorption along with other desired properties like stability, low charge carrier recombination rates, high mobility of carriers, etc.[5] On the other hand, the large band gap (LBG) component of two-photon tandem devices for water-splitting using sunlight requires a band gap of ∼2 eV[5] in addition to the properties mentioned above. A large body of work has been carried out on ternary and quaternary semiconductors for PV because of the possibilities of element substitution, alloying, and phase engineering to tune the thermodynamic and electronic properties of these materials.[6−9] Among the ternary semiconductors, $ZnSnN_2$ has recently gained attention due to a few promising experiments showing its visible light absorption for PV.[7,9,10] A phosphide of a similar class, $ZnSiP_2$, has been demonstrated in a recent experiment as a potential candidate in a silicon tandem PV device.[11] Additionally, it has been reported that a wide span of band gaps can be obtained in these materials by cation disordering and crystal structure modification which enhances their suitability for different PV applications.[7−10,12−14]

The above studies suggest that there is a large potential in these classes of materials for PV and tandem devices thus requiring further exploration to find suitable candidates. The compounds we consider are derived by elemental substitution in $ZnSnN_2$, resulting in a set of compounds with the ABX_2 stoichiometry, where possible A, B, and X are A = Al, Ga, Zn, Cd; B = Ga, In, Ge, Sn, Si; and X = N, P, As, Sb. The selection of elements is shown in Figure 1. In cases where the elements at site A and site B belong to the same group, the order AB is equivalent to order BA since the sites A and B are equivalent by symmetry. The incorporation of toxic elements like cadmium and arsenic in the list above is mainly for analyzing the trend in thermodynamic or electronic properties. The compounds containing these elements are excluded from the final list of suggested PV absorbers.

The structural types are chosen using a design rule in which binary semiconductors with ionic character are used as a skeleton for constructing ternary and quaternary structures through cation substitution.[15] Based on this design principle, we explore the kesterite (KT) and stannite (ST) phases of the orthorhombic wurtzite structure and the chalcopyrite (CP) phase of the zincblende polymorph; see Figure 2.[16,17] The local environments present in the chosen structures are not very different, and this results in similar thermodynamic stability of the different structures. However, their band gaps may differ noticeably thus providing a flexibility to tune the band gap range.[18,19] We also investigate the stability of different compounds by comparing their formation energies with the

Received: July 27, 2017
Published: August 4, 2017

DOI: 10.1021/acs.jpcc.7b07437
J. Phys. Chem. C 2017, 121, 17780−17786

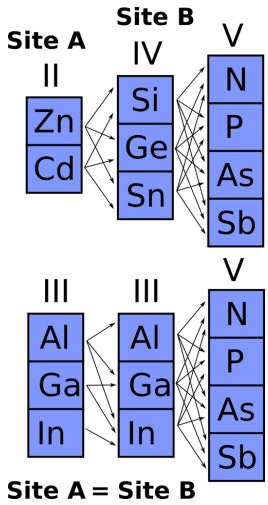

Figure 1. Selection of elements for sites A, B, and X. In cases where the elements at site A and site B belong to the same group, the order AB is equivalent to order BA since the sites A and B are equivalent in terms of symmetry.

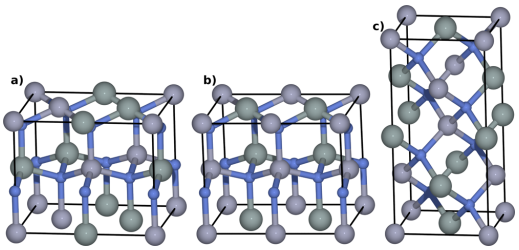

Figure 2. Polytypes of $ZnSnN_2$. (a) Wurtzite–kesterite (KT). (b) Wurtzite–stannite (ST). (c) Zincblende–chalcopyrite (CP). Blue, green, and gray spheres represent the nitrogen, tin, and zinc atoms, respectively.

energy of the convex hull calculated from competing phases. In order to get an accurate estimate of the relative thermodynamic stability of the different phases, we calculate relative energies including uncertainties. Additionally, the size of the band gap for visible light absorption and the magnitudes of the carrier effective masses for high mobility are also calculated. Following the procedure above, we identify new candidates which might be potentially relevant for PV and tandem devices along with a few already known materials.

COMPUTATIONAL DETAILS

The electronic structure calculations are performed with density functional theory using the projector augmented wave (PAW)[20] description as implemented in the GPAW code.[21,22] The lattice constants of the structures are calculated using the PBEsol functional which gives better results as compared to other semilocal functionals.[23] The wave functions are expanded in a plane-wave basis with an energy cutoff of 800 eV. A k-point mesh of $7 \times 7 \times 7$ for the KT and ST structures and $7 \times 7 \times 5$ for the CP structure is used for the sampling of the Brillouin zone using the Monkhorst–Pack scheme.[24] All the structures are optimized until the forces are converged to 0.05 eV/Å or below. For the calculation of the heat of formation along with the uncertainties, a recently developed meta generalized gradient approximation (meta-GGA) functional mBEEF[25] is used which has been recently shown to predict heats of formation accurately.[26] The band gaps are calculated using the semilocal GLLB-SC functional[27,28] which explicitly takes the derivative discontinuity into account and the modified version of the Becke–Johnson exchange potential[29] by Tran and Blaha.[30] Previous works on the comparison of the GLLB-SC and TB09 with the many-body G_0W_0 show that both the functionals give good prediction of the band gaps in intermediate band gap regime, the regime we are interested in.[31,32] Addtionally, we calculate the band gap of the few tin-, antimony-, and cadmium-containing compounds with spin–orbit coupling and find that the band gap changes by less than 0.1 eV which is negligible compared to the error in the calculations we are taking into account. Therefore, it can be safely ignored without affecting the conclusions.

RESULTS AND DISCUSSION

As a preliminary step to reduce the number of compounds to be explored, we consider the stability of compounds with respect to the standard states of the constituent elements, i.e., standard heat of formation (ΔH). A positive value of ΔH implies thermodynamic instability and that the compound cannot be synthesized under standard conditions. This consideration rules out the antimonides of the III–III–Sb_2 type, which all have positive ΔH values. Selecting the elements as shown in Figure 1, along with the fact that the order AB is equivalent to BA in cases where the elements at site A and site B belong to the same group, results in 33 compounds in each phase with negative values of ΔH. For the purpose of comparison and understanding trends, we also calculate the band gaps of III–V compounds in the wurtzite and zincblende structures as shown in Figure 3.

Using the approach described above, we present the properties of the 33 compounds in three prototypes, KT, ST, and CP, in Figure 4 and Figure 5. In most of the cases, the three prototypes of a single compound differ in energy by 50 meV/atom or less. The uncertainties in the calculated energies are estimated by taking the structure with the minimum energy as the reference and using the mBEEF ensemble on the energy differences. For example, if KT is the minimum energy structure of a given compound, then the uncertainty of the energy difference between ST and KT, and between CP and KT, is calculated. As a general trend, the ST structure has the highest energy in most of the cases, whereas CP and KT are thermodynamically more stable and in many cases have energy differences which are within the calculated uncertainties. Furthermore, the thermodynamic stability of a compound also requires that it does not segregate into other compounds. This aspect of thermodynamic stability is explored via the commonly used convex hull approach. In this approach the energy of the convex hull is calculated using a pool of competing structures which contains the standard states of the constituent elements and relevant binary compounds. For a compound to be stable it should have an energy less than or equal to the energy of the convex hull. We calculate the energy of the convex hull along with the uncertainty for all the compounds using mBEEF and taking the competing structures and reference phases from the OQMD database.[33]

DOI: 10.1021/acs.jpcc.7b07437
J. Phys. Chem. C 2017, 121, 17780–17786

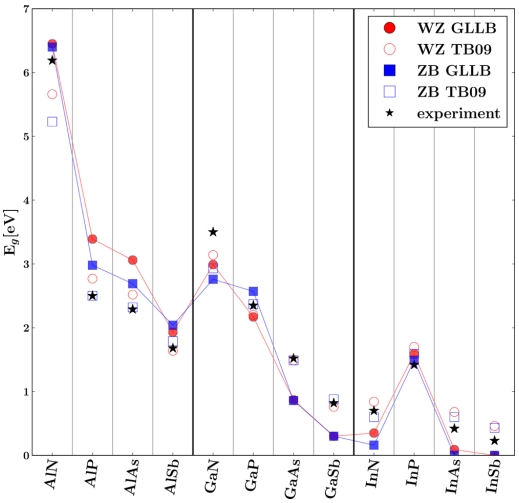

Figure 3. Calculated band gaps using the GLLB-SC functional (filled markers) and TB09 (hollow markers). The figure shows a general trend that the band gap decreases in moving down the column from N to Sb. The good agreement of the calculated band gaps with the band gaps reported in experiments justifies the employment of GLLB-SC and TB09 functional to calculate the band gap of the ternary compounds for potential PV candidates. The experimental values of the band gap shown in the plot correspond to the zincblende structure except in the cases for AlN, GaN, and InN where the values are for the wurtzite structure.

The energies of the 33 compounds in the three structures with respect to the convex hull are shown in Figure 4. It can be noted that the uncertainty of the convex hull is generally considerably larger than for the KT/ST/CP structures. This is because the hull includes structures which are more different than the KT/ST/CP structures, and the energy differences are therefore more difficult to predict. The figure clearly shows that all the compounds except $CdSiN_2$ have the energy below the convex hull or within the uncertainty of the same. Therefore, we predict that all the compounds except $CdSiN_2$ are potentially stable. We note that the experimentally observed $ZnSnN_2$ is close to instability in this approach.

The calculated band gap values of all the compounds in the three phases together with the reported experimental values for some of the CP structures[34] are shown in Figure 5. The obtained band gap values for the 33 structures in all the prototypes span a range of ∼0−5 eV. Despite the large variation in the band gap of different compounds, some general trends in the variation can be observed. First, compounds in ST structures appear to have slightly lower band gaps compared to their KT and CP polymorphs with the latter two often having almost the same band gaps. Second, an almost monotonic decrease of the band gap as X goes from N to Sb is observed. The orbital character of the valence band explains this trend. Figure 6 shows the band structure of $ZnSnN_2$, $ZnSnP_2$, $ZnSnAs_2$, and $ZnSnSb_2$. The projected density of states (PDOS) for all the compounds mentioned above shows that the states near the valence band minimum (VBM) are dominated by the p-states of N, P, As, or Sb. Therefore, as the electronegativity of the elements decreases, the p-levels move up in energy which eventually lifts the valence band; therefore, the band gap decreases. In the present case, the electronegativity decreases in moving down the column from N to Sb, and therefore, the band gap also decreases in that order. The correlation between the electronegativity and band gap has also been established previously for a set of binary compounds which is also shown in Figure 3.[35]

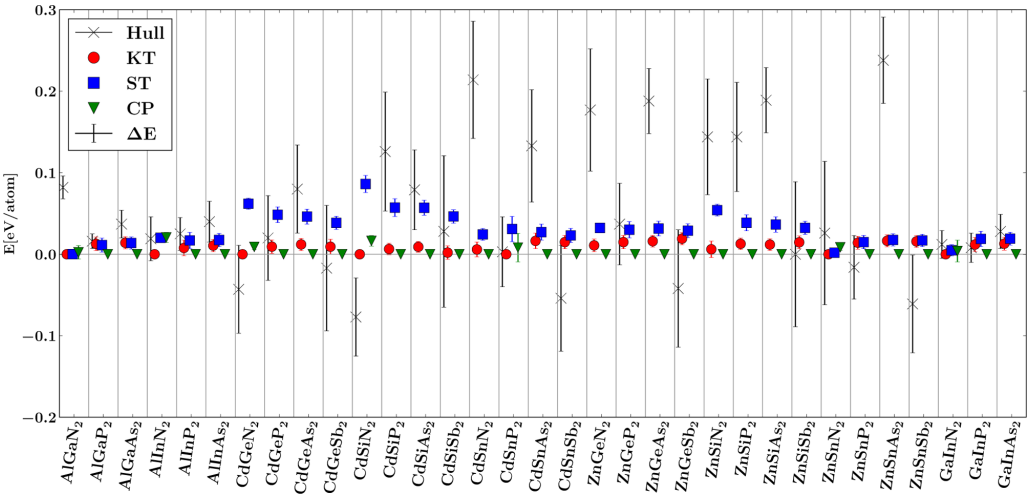

Figure 4. MBEEF total energies and corresponding uncertainties. The energy of the convex hull is represented with × and the uncertainty Δ*E*. The energy of the most stable phase of the different compounds is taken as the zero of the energy. The figure shows that all the compounds except $CdSiN_2$ lie below or close to the convex hull when the uncertainties are taken into account. This implies an unlikely dissociation of the compounds to the competing phases, and they can therefore be regarded as metastable. The large uncertainties in the convex hull arise from the fact that the chemical environments of the species involved in creating the hull are significantly different from the bulk solids KT/ST/CP.

DOI: 10.1021/acs.jpcc.7b07437
J. Phys. Chem. C 2017, 121, 17780−17786

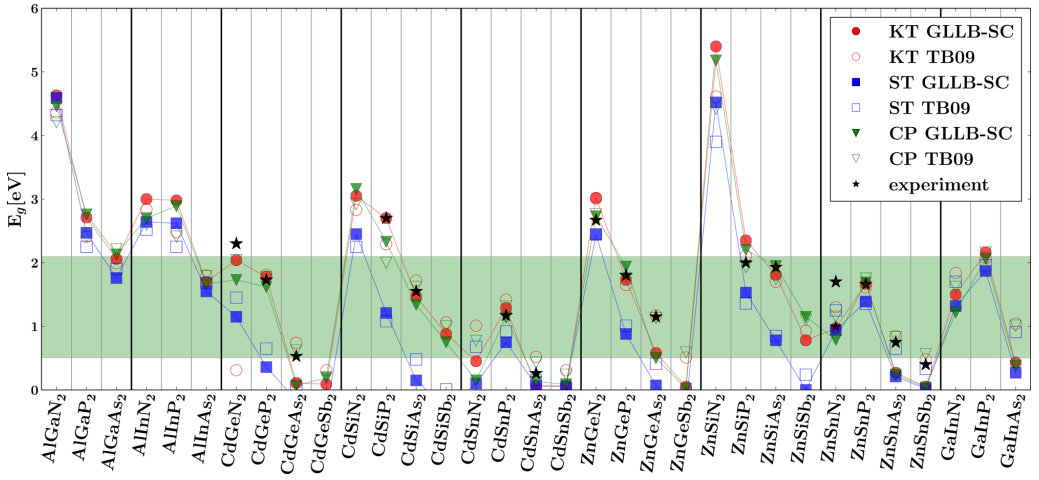

Figure 5. Calculated band gaps using GLLB-SC functional (filled markers) and TB09 (hollow markers). The figure shows a general trend that the band gap decreases in moving down the column from N to Sb. However, in some cases the behavior of nitrides is very different from the P, As, and Sb group. This mainly stems from the fact that the character of the bottom of the conduction band in the case of "outliers" differs significantly in nitrides as compared to the compounds containing P, As, or Sb. The calculated band gaps agree reasonably well with the experimental values in most of the cases and different functionals; i.e., TB09 and GLLBSC give similar results except in a few cases, e.g., $CdGeN_2$. Thick vertical lines are shown to divide the compounds into $AB(N, P, As, Sb)_2$ group where "AB" is a particular combination of cations.

However, the trend described above shows anomalous behavior in going from N to P for the tin-containing compounds. In order to find a possible explanation for this behavior, we analyze the band structure and PDOS of $ZnSn(N, P, As, Sb)_2$; see Figure 6. The figure shows that the valence bands of all the compounds have similar behavior as far as the dispersion of the band structure and nature of the states comprising the VBM are concerned, and their characters are mainly dominated by the p-states of N, P, As, or Sb. Therefore, the anomalous behavior mainly arises from the conduction band. The figure shows that to some extent the CBMs of $ZnSn(N, As, Sb)_2$ look similar. The CBM of these compounds has a special characterstic of having a highly dispersive isolated band significantly separated from the other bands in the conduction band manifold. The band mainly contains Sn-s, (N, As, Sb)-p states, and Zn-s states, although it is bit difficult to see in the case of $ZnSnSb_2$ because of the diminishing band gap. As opposed to the compounds in the $ZnSn(N, As, Sb)_2$ class, $ZnSnP_2$ (or $CdSnP_2$) shows significantly different behavior. First, it lacks the isolated dispersive band in the conduction band as compared to the other compounds in $ZnSn(N, As, Sb)_2$ class. Second, the states near the CBM have negligible contribution from the Zn-s states. The absence of Zn-s states might be responsible for pushing up of the conduction band which leads to anomalous behavior of the phosphides compared to the group containing N, As, and Sb.

In order to consider a semiconductor as a potential PV absorber or to act as a SBG material in a tandem device, we take a broad window of 0.5−1.5 eV for the band gap. Similarly, a window of 1.5−2.1 eV is chosen for the LBG material in a tandem device. The decision to use such a wide range was made because the materials used as an inspiration, $ZnSnN_2$ and $ZnSiP_2$, have gaps of ∼1.5 and ∼2.0, respectively, but on the other hand, the calculated values may deviate from the experimental values by ∼0.5 even with accurate functionals. To test the accuracy of the predictions of two functionals used for the band gap calculations, GLLB-SC and TB09, we also include the experimental data of the systems reported in ref 34 if available. In the region of low gaps, TB09 gives higher values, often matching very well with the experimental band gaps, while in the case of the large gaps (3.5 eV or more) TB09 values are lower than GLLB-SC. Unfortunately, lack of experimental data in that region prevents us from concluding which functional gives better estimation. However, in the band gap region of our interest both the functionals give similar values which are also close to the experimental values in most of the cases. There are 60 materials (26 different ABX_2 combinations in one or more prototypes) which have the band gap in the range of 0.5−2.1 eV (green region in Figure 5). Based only on the size of the band gap, these compounds represent a preliminary set of possible PV absorbers.

The list of 60 light absorbers highlighted above is based only on the size of the band gap which is not the only criterion a semiconductor has to meet in order to act as a good PV/SBG and LBG material. One additional criterion which can be easily accessed is the charge carrier effective masses. Low effective mass enhances the charge carrier mobility which is essential for low recombination losses. Calculated carrier effective masses are shown in Figure 7 where hole masses are the ones with a minus sign and electron masses with a plus sign. The masses are calculated by fitting a parabola along a high-symmetry direction in the Brillouin zone. The threshold for both carrier effective masses being lighter than 0.7 electron mass units (m_e) is chosen as a criteria for a suitable PV materials, shown in green in Figure 7. The cases in which there are valleys with different effective masses, we select the lowest of all the absolute value of the masses. The figure clearly shows that the majority of the calculated effective masses are lower than 0.7 m_e with the exceptions of mostly hole masses of the ST structures.

DOI: 10.1021/acs.jpcc.7b07437
J. Phys. Chem. C 2017, 121, 17780−17786

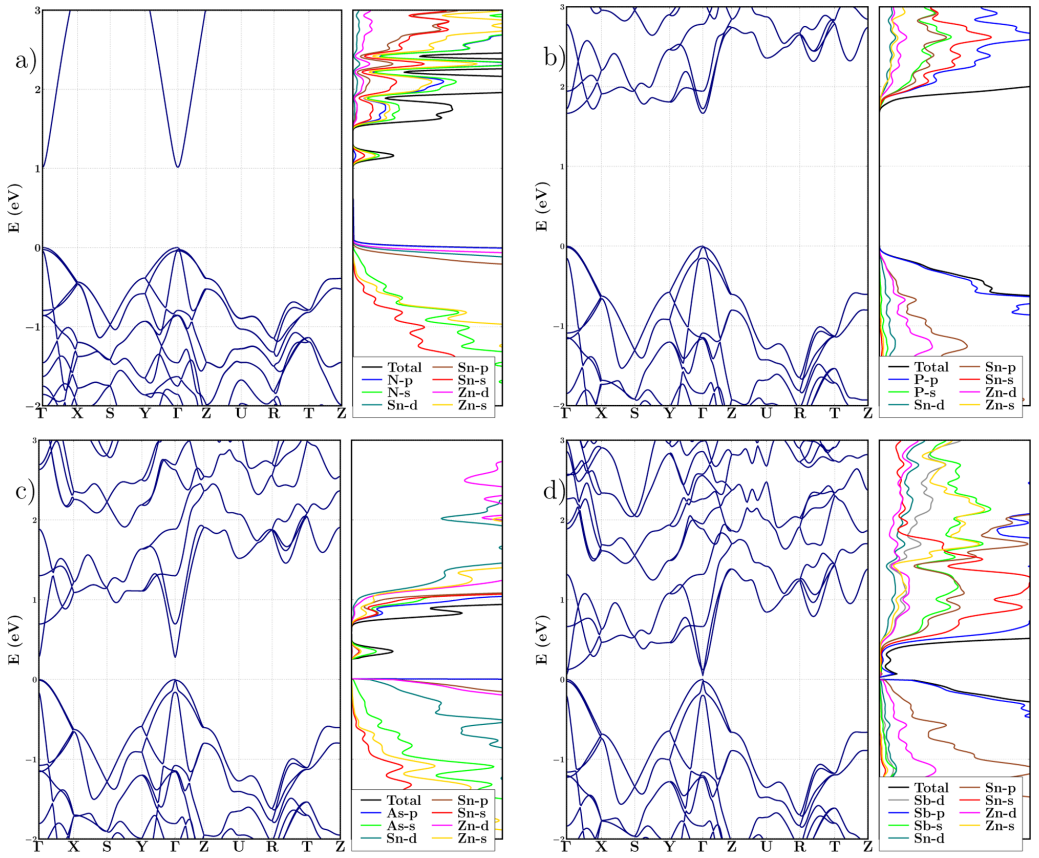

Figure 6. (a–d) Projected density of states and band structures of $ZnSnN_2$, $ZnSnP_2$, $ZnSnAs_2$, and $ZnSnSb_2$, respectively. The zero of the energy is taken as the energy of the top of the valence band. The band structure of $ZnSn(N, As, Sb)_2$ looks similar to only slight differences whereas a distinctive feature of the band structure of $ZnSnP_2$ is the absence of a highly dispersive isolated band. In addition to the similarity in the band structure, $ZnSn(N, As, Sb)_2$ share the common characteristic of having similar nature of the states composing CBM and VBM. The VBM mainly is comprised of (N, As, Sb)-p states whereas Sn-s and (N, As, Sb)-p states and Zn-s states dominate the CBM. The nature of the states involved in the VBM of $ZnSnP_2$ is similar to $ZnSn(N, As, Sb)_2$, i.e., P-p states, whereas the CBM has negligible contribution from the Zn-s states. This makes $ZnSnP_2$ behave significantly different from $ZnSn(N, As, Sb)_2$.

Taking into account the stability, band gaps, effective masses, and toxicity, we can further narrow down the list of possible PV/SBG and LBG candidates. For example, $ZnSnSb_2$ in different phases is ruled out because of instability with respect to the convex hull. On the other hand, heavy electron mass rules out the CP phase of $ZnGeP_2$. Considering the analysis above and removing the compounds containing Cd and As due to toxicity, 14 materials (7 different ABX_2 combinations in 1 or more prototypes) seem to be promising PV/SBG and LBG absorbers. The list of the PV/SBG and LBG candidates is provided in Table 1 and Table 2, respectively.

Among the candidates in Table 1 and Table 2 only $ZnSiSb_2$ (KT) and $ZnGeP_2$ (KT) have indirect band gaps whereas the other candidates are direct band gap semiconductors. The CP phase of $ZnSiSb_2$ has been computationally explored as a possible thermoelectric material;[37] however, to the best of our knowledge the possibility of this compound to act as a PV absorber has not been considered before. It is interesting to note that all three phases of $ZnSnN_2$ qualify as good PV absorbers with the KT phase already having been synthesized, characterized, and proposed as a potential PV absorber in previous work.[7] The occurrence of $ZnSnN_2$ in all three phases stresses the importance of exploring different polymorphs of the same material which are energetically close. In such cases, if all the competing phases are semiconducting having band gaps in the desired range, then having a polymorphic sample might not affect the light absorption of the material. However, if one (or more) of the competing phase(s) turns out to be metallic, then the polymorphism of the sample will have a detrimental effect on the light absorption. Therefore, it is necessary to assess the optical properties of the different phases apriori. Interestingly, the presence of $ZnSnP_2$ in both tables shows that the different phases of it span a band gap range which might be useful for single junction as well as tandem PV devices. The optical properties of the CP structure of $ZnSnP_2$ have been explored in previous works; however, our results show that

DOI: 10.1021/acs.jpcc.7b07437
J. Phys. Chem. C 2017, 121, 17780–17786

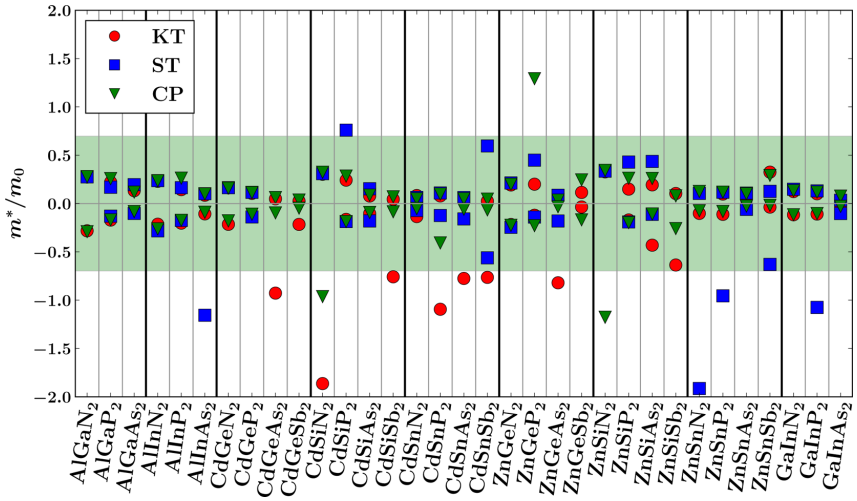

Figure 7. Effective masses for electrons and holes. The negative sign is due to the orientation of the parabola fitted to the top of the valence band; therefore, hole masses have negative sign. Similarly, electron masses have positive sign. Green area is the limit of "light masses". Thick vertical lines are shown to divide the compounds into AB(N, P, As, Sb)$_2$ group where "AB" is a particular combination of cations.

Table 1. List of Suggested PV Candidates and SBG Candidates for a Tandem Device[a]

formula	structure	$E_g^{GLLB-SC}$	E_g^{TB09}	E_g^{exp}	m^*_h	m^*_e
$ZnSiSb_2$	KT	0.78	1.06		−0.09	0.10
$ZnSiSb_2$	CP	1.15	1.10		−0.26	0.08
$ZnSnN_2$	KT	0.97	1.30	1.1[7]	−0.10	0.11
$ZnSnN_2$	CP	0.79	1.15		−0.07	0.13
$ZnSnN_2$	ST	0.94	1.25		−0.10	0.11
$ZnSnP_2$	ST	1.39	1.35		−0.10	0.13

[a]The experimental values of the band gaps are taken from ref 34. unless stated otherwise.

Table 2. List of Suggested LBG Candidates for a Tandem Device[a]

formula	structure	$E_g^{GLLB-SC}$	E_g^{TB09}	E_g^{exp}	m^*_h	m^*_e
$GaInN_2$	KT	1.50	1.84		−0.12	0.12
$GaInN_2$	CP	1.22	1.62		−0.12	0.13
$GaInP_2$	KT	2.16	2.08		−0.10	0.11
$GaInP_2$	CP	2.06	2.16	1.83[36]	−0.10	0.12
$ZnGeP_2$	KT	1.73	1.65		−0.12	0.20
$ZnSiP_2$	CP	2.20	1.93	2, 2.1[11]	−0.26	0.20
$ZnSnP_2$	KT	1.67	1.61		−0.11	0.10
$ZnSnP_2$	CP	1.69	1.75	1.66	−0.08	0.12

[a]The experimental values of the band gaps are taken from ref 34. unless stated otherwise.

there is a potential in the other phases of $ZnSnP_2$ not only for single junction but for tandem devices as well. The importance of polymorphism is reflected in $GaInN_2$ and $GaInP_2$ also where the multiple phases are photoactive. Additionally, finding an already explored CP phase of $GaInP_2$ as a potential PV absorber with the approach we adopt consolidates our conclusion for the other phases.[36]

In conclusion, we have explored the different polymorphs of II−IV−V_2 and III−III−V_2 type semiconductors as potential light absorbers for PV and tandem PV devices. Careful thermodynamic and electronic structure analysis based on heat of formation, relative stability, band gaps, carrier effective masses, and toxicity results in 14 potential light absorbers. Additionally, we also propose that owing to the small energy differences of the different polymorphs phase engineering of these materials can be employed relatively easily to control their electronic properties and expand the materials space for PV and tandem PV applications. The systematic mapping of the materials space provides trends in thermodynamic and electronic properties which can be exploited further to tune these properties via elemental substitution and/or alloying.

AUTHOR INFORMATION

Corresponding Author

*E-mail: mohpa@fysik.dtu.dk.

ORCID

Mohnish Pandey: 0000-0002-1715-0617

Author Contributions

‡These authors contributed equally to this work.

Notes

The authors declare no competing financial interest.

All the data of band gaps, effective masses, and stability is provided in an interactive database. The web address of the database is https://cmrdb.fysik.dtu.dk/?project=abx2.

ACKNOWLEDGMENTS

This work was partly supported by a research grant (9455) from VILLUM FONDEN.

REFERENCES

(1) Vayssierres, L. *On Solar Hydrogen and Nanotechnology*; John Wiley and Sons (Asia) Pvt. Ltd, 2009.

(2) Chamberlain, G. Organic Solar Cells: A Review. *Sol. Cells* **1983**, *8*, 47−83.

(3) Ni, M.; Leung, M. K.; Leung, D. Y.; Sumathy, K. A Review and Recent Developments in Photocatalytic Water-splitting Using TiO_2 for

DOI: 10.1021/acs.jpcc.7b07437
J. Phys. Chem. C 2017, 121, 17780−17786

Hydrogen Production. *Renewable Sustainable Energy Rev.* **2007**, *11*, 401−425.
(4) Schmidt-Mende, L.; Fechtenkötter, A.; Müllen, K.; Moons, E.; Friend, R. H.; MacKenzie, J. D. Self-Organized Discotic Liquid Crystals for High-Efficiency Organic Photovoltaics. *Science* **2001**, *293*, 1119−1122.
(5) Seger, B.; Castelli, I. E.; Vesborg, P. C. K.; Jacobsen, K. W.; Hansen, O.; Chorkendorff, I. 2-Photon Tandem Device for Water Splitting: Comparing Photocathode First Versus Photoanode First Designs. *Energy Environ. Sci.* **2014**, *7*, 2397−2413.
(6) Wang, C.; Chen, S.; Yang, J.-H.; Lang, L.; Xiang, H.-J.; Gong, X.-G.; Walsh, A.; Wei, S.-H. Design of I_2−II−IV−VI_4 Semiconductors through Element Substitution: The Thermodynamic Stability Limit and Chemical Trend. *Chem. Mater.* **2014**, *26*, 3411−3417.
(7) Fioretti, A. N.; Zakutayev, A.; Moutinho, H.; Melamed, C.; Perkins, J. D.; Norman, A. G.; Al-Jassim, M.; Toberer, E. S.; Tamboli, A. C. Combinatorial Insights into Doping Control and Transport Properties of Zinc Tin Nitride. *J. Mater. Chem. C* **2015**, *3*, 11017−11028.
(8) Narang, P.; Chen, S.; Coronel, N. C.; Gul, S.; Yano, J.; Wang, L.-W.; Lewis, N. S.; Atwater, H. A. Bandgap Tunability in Zn(Sn,Ge)N_2 Semiconductor Alloys. *Adv. Mater.* **2014**, *26*, 1235−1241.
(9) Feldberg, N.; Aldous, J. D.; Linhart, W. M.; Phillips, L. J.; Durose, K.; Stampe, P. A.; Kennedy, R. J.; Scanlon, D. O.; Vardar, G.; Field, R. L.; et al. Growth, Disorder, and Physical Properties of $ZnSnN_2$. *Appl. Phys. Lett.* **2013**, *103*, 042109.
(10) Lahourcade, L.; Coronel, N. C.; Delaney, K. T.; Shukla, S. K.; Spaldin, N. A.; Atwater, H. A. Structural and Optoelectronic Characterization of RF Sputtered $ZnSnN_2$. *Adv. Mater.* **2013**, *25*, 2562−2566.
(11) Martinez, A. D.; Warren, E. L.; Gorai, P.; Borup, K. A.; Kuciauskas, D.; Dippo, P. C.; Ortiz, B. R.; Macaluso, R. T.; Nguyen, S. D.; Greenaway, A. L.; et al. Solar Energy Conversion Properties and Defect Physics of $ZnSiP_2$. *Energy Environ. Sci.* **2016**, *9*, 1031−1041.
(12) Veal, T. D.; Feldberg, N.; Quackenbush, N. F.; Linhart, W. M.; Scanlon, D. O.; Piper, L. F. J.; Durbin, S. M. Band Gap Dependence on Cation Disorder in $ZnSnN_2$ Solar Absorber. *Adv. Ener. Mater.* **2015**, *5*, 1501462.
(13) Chen, S.; Narang, P.; Atwater, H. A.; Wang, L.-W. Phase Stability and Defect Physics of a Ternary $ZnSnN_2$ Semiconductor: First Principles Insights. *Adv. Mater.* **2014**, *26*, 311−315.
(14) Senabulya, N.; Feldberg, N.; Makin, R. A.; Yang, Y.; Shi, G.; Jones, C. M.; Kioupakis, E.; Mathis, J.; Clarke, R.; Durbin, S. M. Stabilization of Orthorhombic Phase in Single-Crystal $ZnSnN_2$ Films. *AIP Adv.* **2016**, *6*, 075019.
(15) Chen, S.; Walsh, A.; Luo, Y.; Yang, J.-H.; Gong, X. G.; Wei, S.-H. Wurtzite-Derived Polytypes of Kesterite and Stannite Quaternary Chalcogenide Semiconductors. *Phys. Rev. B: Condens. Matter Mater. Phys.* **2010**, *82*, 195203.
(16) Goodman, C. H. L. A New Group of Compounds with Diamond Type (Chalcopyrite) Structure. *Nature* **1957**, *179*, 828−829.
(17) Jaffe, J. E.; Zunger, A. Theory of the Band-gap Anomaly in ABC_2 Chalcopyrite Semiconductors. *Phys. Rev. B: Condens. Matter Mater. Phys.* **1984**, *29*, 1882−1906.
(18) Wang, J.-J.; Hu, J.-S.; Guo, Y.-G.; Wan, L.-J. Wurtzite $Cu_2ZnSnSe_4$ Nanocrystals for High-performance Organic-inorganic Hybrid Photodetectors. *NPG Asia Mater.* **2012**, *4*, e2.
(19) Yeh, C.-Y.; Wei, S.-H.; Zunger, A. Relationships between the Band Gaps of the Zinc-Blende and Wurtzite Modifications of Semiconductors. *Phys. Rev. B* **1994**, *50*, 2715.
(20) Kresse, G.; Joubert, D. From Ultrasoft Pseudopotentials to the Projector Augmented-wave Method. *Phys. Rev. B: Condens. Matter Mater. Phys.* **1999**, *59*, 1758−1775.
(21) Enkovaara, J.; Rostgaard, C.; Mortensen, J. J.; Chen, J.; Dułak, M.; Ferrighi, L.; Gavnholt, J.; Glinsvad, C.; Haikola, V.; Hansen, H. A.; et al. Electronic Structure Calculations with GPAW: A Real-space Implementation of the Projector Augmented-wave Method. *J. Phys.: Condens. Matter* **2010**, *22*, 253202.
(22) Larsen, A.; et al. The Atomic Simulation Environment—A Python library for Working with Atoms. *J. Phys.: Cond. Mater.* **2017**, *29*, 273002.
(23) Perdew, J. P.; Ruzsinszky, A.; Csonka, G. I.; Vydrov, O. A.; Scuseria, G. E.; Constantin, L. A.; Zhou, X.; Burke, K. Restoring the Density-Gradient Expansion for Exchange in Solids and Surfaces. *Phys. Rev. Lett.* **2008**, *100*, 136406.
(24) Monkhorst, H. J.; Pack, J. D. Special Points for Brillouin-Zone Integrations. *Phys. Rev. B* **1976**, *13*, 5188.
(25) Wellendorff, J.; Lundgaard, K. T.; Jacobsen, K. W.; Bligaard, T. mBEEF: An Accurate Semi-local Bayesian Error Estimation Density Functional. *J. Chem. Phys.* **2014**, *140*, 144107.
(26) Pandey, M.; Jacobsen, K. W. Heats of Formation of Solids with Error Estimation: The mBEEF Functional with and without Fitted Reference Energies. *Phys. Rev. B: Condens. Matter Mater. Phys.* **2015**, *91*, 235201.
(27) Gritsenko, O.; van Leeuwen, R.; van Lenthe, E.; Baerends, E. J. Self-consistent Approximation to the Kohn-Sham Exchange Potential. *Phys. Rev. A: At., Mol., Opt. Phys.* **1995**, *51*, 1944.
(28) Kuisma, M.; Ojanen, J.; Enkovaara, J.; Rantala, T. T. Kohn-Sham Potential with Discontinuity for Band Gap Materials. *Phys. Rev. B: Condens. Matter Mater. Phys.* **2010**, *82*, 115106.
(29) Tran, F.; Blaha, P. Accurate Band Gaps of Semiconductors and Insulators with a Semilocal Exchange-Correlation Potential. *Phys. Rev. Lett.* **2009**, *102*, 226401.
(30) Becke, A. D.; Johnson, E. R. A Simple Effective Potential for Exchange. *J. Chem. Phys.* **2006**, *124*, 221101.
(31) Waroquiers, D.; Lherbier, A.; Miglio, A.; Stankovski, M.; Poncé, S.; Oliveira, M. J. T.; Giantomassi, M.; Rignanese, G.-M.; Gonze, X. Band Widths and Gaps from the Tran-Blaha Functional: Comparison with Many-Body Perturbation Theory. *Phys. Rev. B: Condens. Matter Mater. Phys.* **2013**, *87*, 075121.
(32) Castelli, I. E.; Hüser, F.; Pandey, M.; Li, H.; Thygesen, K. S.; Seger, B.; Jain, A.; Persson, K. A.; Ceder, G.; Jacobsen, K. W. New Light-Harvesting Materials Using Accurate and Efficient Bandgap Calculations. *Adv. Ener. Mater.* **2015**, *5*, 1400915.
(33) Saal, J. E.; Kirklin, S.; Aykol, M.; Meredig, B.; Wolverton, C. Materials Design and Discovery with High-Throughput Density Functional Theory: The Open Quantum Materials Database (OQMD). *JOM* **2013**, *65*, 1501−1509.
(34) Madelung, O. *Semiconductors Data Handbook*; Springer: Berlin, 2004; pp 815−835.
(35) Quarto, F. D.; Sunseri, C.; Piazza, S.; Romano, M. C. Semiempirical Correlation between Optical Band Gap Values of Oxides and the Difference of Electronegativity of the Elements. Its Importance for a Quantitative Use of Photocurrent Spectroscopy in Corrosion Studies. *J. Phys. Chem. B* **1997**, *101*, 2519−2525.
(36) Gu, J.; Yan, Y.; Young, J. L.; Steirer, K. X.; Neale, N. R.; Turner, J. A. Water Reduction by a p-$GaInP_2$ Photoelectrode Stabilized by an Amorphous TiO_2 Coating and a Molecular Cobalt Catalyst. *Nat. Mater.* **2016**, *15*, 456−460.
(37) Sreeparvathy, P. C.; Kanchana, V.; Vaitheeswaran, G. Thermoelectric Properties of Zinc Based Pnictide Semiconductors. *J. Appl. Phys.* **2016**, *119*, 085701.

DOI: 10.1021/acs.jpcc.7b07437
J. Phys. Chem. C 2017, 121, 17780−17786

5.3 Paper III: Sulfide Perovskites for Solar Energy Conversion Applications: Computational Screening and Synthesis of the Selected Compound $LaYS_3$

The publication is submitted.

Sulfide Perovskites for Solar Energy Conversion Applications: Computational Screening and Synthesis of the Selected Compound $LaYS_3$

Korina Kuhar, ‡[a] **Andrea Crovetto,**‡[b] **Mohnish Pandey,**[a] **Kristian S. Thygesen,**[a,c] **Brian Seger,**[b] **Peter Vesborg,**[b] **Ole Hansen,**[b,d] **Ib Chorkendorff,**[b] **and Karsten W. Jacobsen***[a]

Received Xth XXXXXXXXXX 20XX, Accepted Xth XXXXXXXXX 20XX

First published on the web Xth XXXXXXXXXX 200X

DOI: 10.1039/b000000x

One of the key challenges in photoelectrochemical water splitting is to identify efficient semiconductors with band gaps of the order of ∼2 eV to operate as the large-band-gap component in water splitting tandem devices. Here, we address this challenge by extensive computational screening of ternary sulfides followed by synthesis and confirmation of the properties of one of the most promising materials. The screening focusses on materials with ABS_3 composition taking both perovskite and non-perovskite structures into consideration, and the material selection is based on descriptors for thermodynamic stability, light absorption, charge mobility, and defect tolerance. One of the most promising candidates identified is $LaYS_3$. This material was synthesized directly in thin-film form demonstrating its stability, crystal structure, light absorption, and strong photoluminescence. These data confirms its potential applicability in tandem photoelectrochemical devices for hydrogen production.

1 Introduction

Efficient harvesting of solar energy is urgently needed to tackle the growing energy demand and deleterious effects of the large scale consumption of fossil fuels. Different routes are actively being explored for the conversion of solar energy to other forms, for example electricity, or chemical or thermal fuels[1–5]. This work focuses on photoelectrochemical production of fuels such as hydrogen through light-induced splitting of water.

In 1972 Fujishima and Honda demonstrated that direct light-driven water splitting was possible[6], and since then a number of water splitting materials have been identified[7]. However, due to the large band gap required to split water with a single photon, the solar-to-hydrogen efficiency of such a device is currently below 1% and numerical modeling shows that the efficiency cannot exceed 11% even under optimistic assumptions[8] and probably no more than 5-8% can be realized in practice[9–11]. These estimates can be easily verified using freely available numerical modeling tools[12,13].

A solution to this problem is to use two photons instead of one to obtain the required voltage. This requires a so-called tandem device with two semiconductors, one with a large band gap (LBG) to absorb the most energetic photons, and one with a small band gap (SBG) to absorb the photons of lower energy, operating in series to boost the voltage. Modeling shows that with an optimal combination of light absorbers such a device can, in principle, be as efficient as 25-29% depending on the estimates of catalytic efficiencies, Ohmic losses etc.[9,10,14,15], while efficiencies of up to about 21% should be realistic considering all real-world losses[8]. In the past two decades the record for highest solar-to-hydrogen efficiency for tandem devices has consistently been held by III-V (GaAs family) devices[16–18] and recently, record efficiencies have risen above 16%[19] for monolithic photoelectrochemical devices. These devices, however, are all prone to corrosion in electrolyte even in conjunction with protection layers[20] and contain the scarce elements Ga and In for which it is an open question whether supplies can scale to TW-level deployment[21].

As an alternative to the III/V systems, modeling suggests that Si is an excellent choice as the SBG semiconductor with its 1.1 eV band gap. Many of the integration issues that previously plagued Si such as mitigating corrosion issues without effecting charge transport has now been resolved[22–24]. One of the largest outstanding problems is to find an efficient LBG semiconductor with a band gap of 1.6-2.0 eV to match Si

† Electronic Supplementary Information (ESI) available: [details of any supplementary information available should be included here]. See DOI: 10.1039/b000000x/

‡ These authors contributed equally to this work.

[a] *CAMD, Department of Physics, Technical University of Denmark, DK - 2800 Kongens Lyngby, Denmark; E-mail: kwj@fysik.dtu.dk*

[b] *SurfCat, Department of Physics, Technical University of Denmark, DK - 2800 Kgs. Lyngby, Denmark.*

[c] *Center for Nanostructured Graphene (CNG), Department of Physics, Technical University of Denmark, DK - 2800 Kongens Lyngby, Denmark.*

[d] *DTU Nanotech, Technical University of Denmark, DK - 2800 Kongens Lyngby, Denmark.*

in a tandem device[25]. Researchers have investigated several such materials including WO_3[26], $BiVO_4$[27], GaP[28], F_2O_3[29], Cu_2O[30], a-Si[31], a-SiC[32], CdSe[33], GaInP[16], metal-organic perovskites[34,35], and most recently $Cu_2BaSn(S,Se)_4$[36], but, with the latter as a possible exception, they all have problems related to non-optimal band gaps, instability, poor charge transport, or they are made from non-abundant elements.

Significant computational screening investigations of water splitting materials have been performed for oxides, oxynitrides, and oxyfluorides in perovskite or perovskite-derived structures or based on the Inorganic Crystal Structure Database (ICSD)[37–44], but so far no break-through materials have resulted from these screenings. The oxides tend to have too large band gaps with very anodic valence band maxima (VBM) with respect to the water redox level resulting in large internal voltage loss in the device. However, both of the aforementioned issues can be resolved by substituting oxygen with sulfur, which reduces the band gap along with making the VBM more cathodic thus bringing it closer to the water redox level[45]. The original motivation for the focus on oxides is their stability under the strongly oxidizing conditions of oxygen evolution, but the use of protection layers lends hope that less stable materials such as sulfides could work as photoabsorbers since they are protected from the electrolyte.

Here we investigate the possibility of ternary sulfides in the ABS_3 stoichiometry as LBG semiconductors. This class of materials has seen intense interest the last couple of years mostly in the context of PV solar cells. $CuTaS_3$ has been synthesized exhibiting good absorption properties[46]. Perera et al.[47] have synthesized $BaZrS_3$, $CaZrS_3$, $SrTiS_3$, and $SrZrS_3$ using high temperature sulfurization of the corresponding oxides. Most recently Niu et al.[48] also synthesized and characterized $BaZrS_3$ and $SrZrS_3$, the latter one in two different phases. Furthermore, Meng et al.[49] have investigated the alloy system $BaZr_{1-x}Ti_xS_3$ suggesting tunability of the band gap. Two computational studies have suggested materials with appropriate band gaps for single-cell PV application: the study by Sun et al.[50] investigates nine sulfides and nine selenides and suggests that $CaTiS_3$ and $BaZrS_3$ (and the selenides $CaZrSe_3$ and $CaHfSe_3$) have relevant PV band gaps, while Ju et al.[51] also investigate nine ABS_3 sulfides (and a similar number of selenides and oxides) and points to $SrSnS_3$ as a potential PV light absorber.

In the following we shall present a comprehensive screening of ABS_3 compounds where we initially consider all 2809 combinations of 53 A-metal atoms and 53 B-metal atoms. The screening funnel is illustrated in Figure 1. Based on valence considerations the initial number of compounds is reduced to 705 distinct ABS_3 combinations, which are investigated in a distorted perovskite structure to identify the ones which are semiconductors. The heats of formation of the compounds are investigated in an additional six crystal structures and the possibility of segregation is assessed by considering all reactions where the compounds disintegrate into one- or two-element constituents. The band gaps are calculated with the so-called GLLB-SC functional and only materials with visible-light absorption remain in the funnel. The electron and hole mobilities are considered through calculation of the effective band curvature. Finally, the defect tolerance of the compounds are investigated by determining whether or not the introduction of vacancies gives rise to electronic states in the band gap.

Our screening study results in a short list of potential LBG photo-absorbers along with some potential PV materials. We synthesize and investigate one of the most promising LBG photo-absorbers, $LaYS_3$, and show that it does indeed have the predicted crystal structure and band gap. Photoluminescence experiments confirm that any potential defect state is not contributing to deep gap recombination sites.

2 Computational Details

The electronic structure calculations are performed using Density Functional Theory (DFT) in the Projector Augmented Wave (PAW) formalism[52] as implemented in the electronic structure code GPAW[53]. The calculations are controlled using the Atomic Simulation Environment[54]. The cell and atomic relaxations are performed using the PBEsol functional which gives better estimates of lattice constants compared to other semi-local functionals[55]. The wavefunctions are expanded in a plane-wave basis with an energy cutoff of 800 eV. The sampling of the Brillouin zone is performed using the Monkhorst-Pack scheme[56]. The k-point mesh is $7\times7\times7$ for the systems in the cubic, distorted cubic and orthorhombic ($Pna2_1$) structures, $6\times3\times6$ for the systems in the monoclinic structure, and $4\times3\times4$ for the orthorhombic *Pnma* structure. Finer k-point meshes are adopted for the calculation of band structures and effective masses. All the structures are optimized until the forces are converged to 0.05 eV/Å or below. The heat of formation calculations, together with the corresponding uncertainties, have been calculated using the meta generalized gradient approximation functional mBEE[57], which has been shown to give good predictions of the heat of formation in comparison with experiments[58]. For the mBEEF calculations the wavefunctions are described on a real space grid. The band gaps and band structures are calculated using the more accurate semi-local GLLB-SC functional[59,60]. The GLLB-SC functional with similar computational cost as the other semi-local functionals predicts band gaps which are quite close to the predictions of more computationally demanding many-body-perturbation-theory calculations (GW) and hybrid functionals[42]. Spin-orbit coupling was included in the calculations for materials containing elements with atomic number (Z) higher than 56.

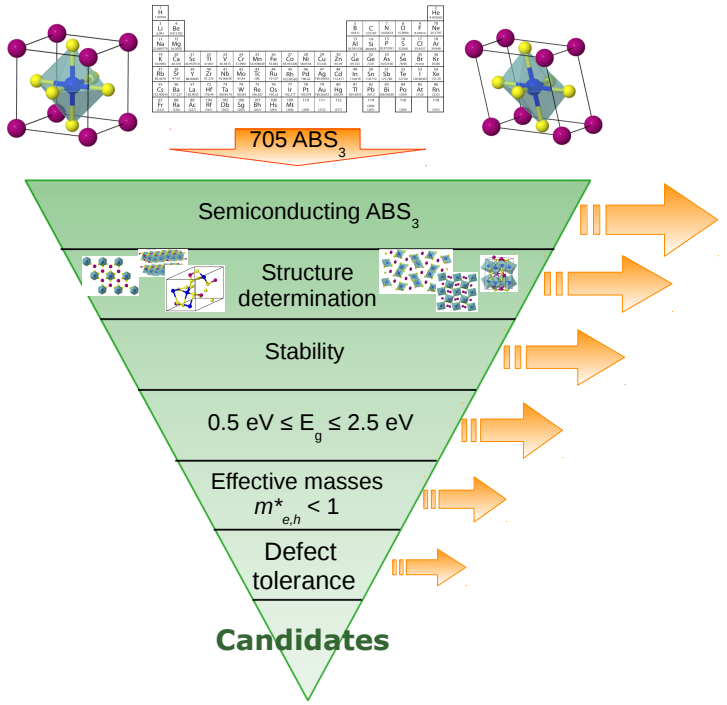

Fig. 1 Sketch of the screening funnel. The different design criteria lead to a gradual reduction in the number of candidate materials.

3 Experimental Details

$LaYS_3$ thin films are produced in two synthesis steps. The first is deposition of LaY thin-film precursors on a fused silica substrate by co-sputtering of La and Y metallic targets from magnetron sources with RF and DC power respectively. The power densities on each target are tuned to obtain a La/Y atomic ratio close to 1 in the precursors, as measured by energy dispersive x-ray spectroscopy (EDX) after deposition. The second step is sulfurization of the LaY precursors in a quartz tube furnace with a 70 sccm flow of 5% H_2S in Ar at atmospheric pressure. The precursors are sulfurized for 10 hours at 1000°C, with ramp rates of 10°C/min (up) and 5°C/min (down).

The elemental composition of both the thin film precursors and the sulfurized thin film is characterized in a FEI Quanta 200 FEG scanning electron microscope (SEM) equipped with an EDX detector (X-Max^N 50, Oxford Instruments). A beam voltage of 8 kV is sufficient to reliably determine the intensity of the *L* x-ray lines of La and Y without penetrating into the fused silica substrate. Complementary characterization of composition is performed by x-ray photoemission spectroscopy (XPS) using a Thermo Scientific K-Alpha instrument with monochromatized Al K_α x-ray source at 1486.68 eV. Before acquiring the XPS spectrum, the sample surface is cleaned of its native oxide by in-situ ion beam etching. Elemental composition is determined using the following lines: La 3d, Y 3p, S 2s, and O 1s. Identification of the crystal structure of the sulfurized film is done through analysis of x-ray diffraction patterns (XRD) obtained with a PANalytical Empyrean diffractometer in the Bragg-Brentano measurement configuration using Cu K_α radiation. As a reference for XRD phase analysis, the unit cell details of each possible $LaYS_3$ structural prototype calculated in this work are entered as input in the program GDIS[61]. The program simulates the powder XRD patterns of the different prototypes, which are used as a reference to assign experimental XRD peaks to a certain prototype.

The band gap of the sulfurized film is estimated based on its absorption coefficient, which is in turn extracted by spectroscopic ellipsometry in the visible-UV range using a J.A. Woollam M-2000 rotating compensator ellipsometer. The (unknown) optical functions of the $LaYS_3$ compound are fitted to a Kramers-Kronig consistent b-spline function with 3 nodes/eV. Thickness and roughness of the $LaYS_3$ film are also fitted, whereas the optical functions of the fused silica substrate are obtained from a separate ellipsometry measurement on the bare substrate. This method has been described in detail before for films of other sulfide materials on glass[62,63]. Steady-state photoluminescence (PL) spectra are measured at room temperature with an Accent RPM2000 system at an excitation wavelength of 405 nm and power density 1 W/mm^2.

4 Results and Discussion

4.1 Computational Screening

In order for a material to possess a band gap it has to obey the valence rule which requires that the valences (with sign) of the cations and anions add up to zero. A few exceptions to the valence rule exists under extreme conditions of temperature and/or pressure but violation of the rule under normal physical conditions is very unlikely[64]. Therefore, as a starting point we impose the valence rule on the selection of cations A and B so that the sum of oxidation states of the cations should be 6 corresponding to the value of -6 from the three sulfur anions. As a result, the selection of A and B cations (lanthanides except lanthanum and actinides excluded) gives 705 distinct ABS_3 combinations. However, imposing the valence rule is not sufficient for a compound to be stable and have a non-zero band gap and we therfore proceed as follows: we first carry out the structural relaxation of the ABS_3 compounds in a perfectly symmetric five atom cubic unit cell retaining the unit cell symmetry during relaxation. Thereafter, the same set of compounds are relaxed by breaking the cubic symmetry of the unit cell in order to see the effect of symmetry breaking on the energies and band gaps. Interestingly, only 15 out of the 705 combinations in the perfectly cubic structure have non-zero band gaps. However, breaking the symmetry has a significant effect on the band gaps and results in the identification of 56 compounds where both the ABS_3 and BAS_3 distorted structures exhibit a gap and 73 compounds where only one of the two distorted structures show a gap. In 8 cases the two-component systems A_2S_3 exhibit a gap, but we shall not investigate these further here. An overview of the band gap values for the compounds in the distorted structure is shown in Figure 2.

The set of $56+73=129$ compounds provides a good starting point for identifying compounds which might be semiconducting in other non-cubic structures; however, finding global energy minimum structures of 129 compounds is a challenging task. Therefore, we decided to rely on the frequency of the crystal structures of compounds of ABS_3 stoichiometry occurring in the experimental data reported in ICSD[65,66]. Selecting the database entries of ABS_3 stoichiometry (ignoring the lanthanides and actinides in the entry) shows that most of the compounds crystallize in only a few prototypes. The six most frequently occurring prototypes are (see Figure 3): (1) Hexagonal *P6$_3$/mmc* structure of $BaNiO_3$. This is a perovskite with face sharing octahedra. (2) Orthorhombic *Pna2$_1$* structure of $YScS_3$. A perovskite with corner sharing octahedra. (3) Orthorhombic *Pnma* structure of $GdFeO_3$ (similar to the the black structure of $CsSnI_3$). This is a perovskite with corner sharing octahedra. (4) another orthorhombic *Pnma* structure of NH_4CdCl_3/Sn_2S_3 or the so-called "needle-like" structure

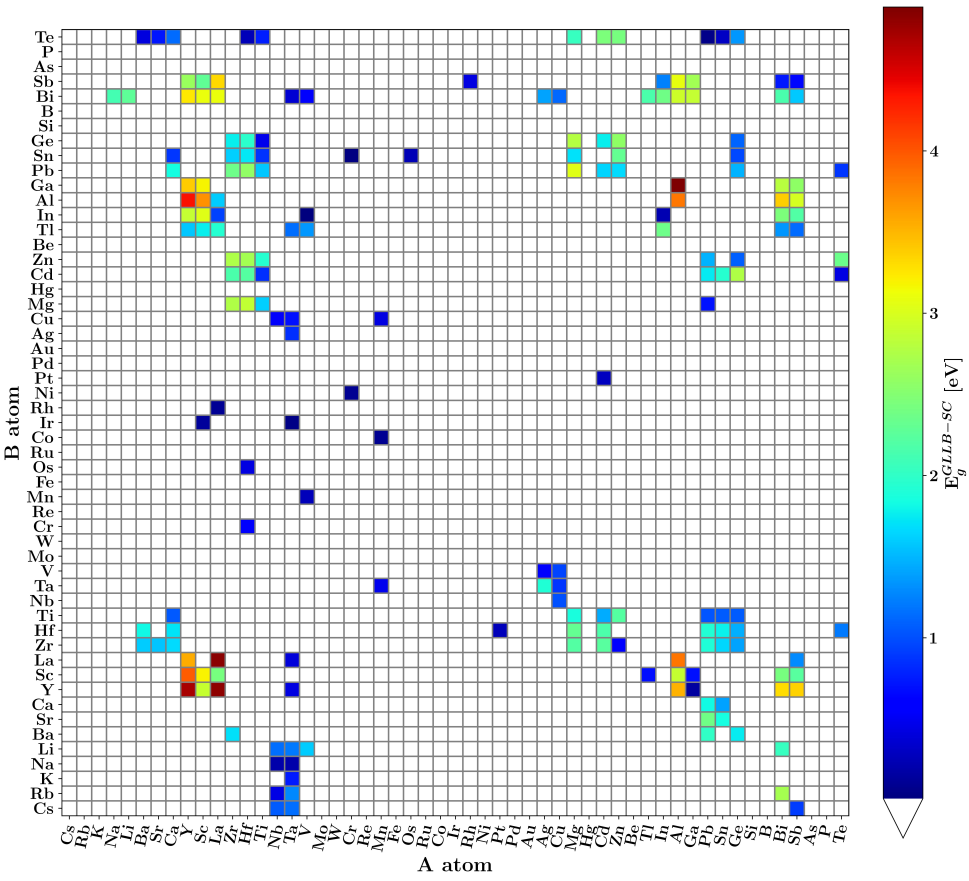

Fig. 2 Calculated band gap values using the GLLB-SC functional for the distorted 5-atom unit cell. Most of the materials do not have a band gap because the valences do not add up to zero. 129 compounds exhibit a band gap in the distorted 5-atom unit cell.

(similar to the yellow structure of $CsSnI_3$). In this perovskite the octahedra share edges. (5) monoclinic *C12/m1* structure of $FePS_3$. This is a layered perovskite with edge sharing octahedra. (6) monoclinic *P1c1* structure of $PbPS_3$. It is worth mentioning that we are not limiting ourselves to explore only perovskite structures, which are recognized by having octahedra containing B cations in their centers and non-metal atoms in their corners, but we also consider the structure $PbPS_3$ which is not a perovskite. This non-perovskite structure is chosen due to the high frequency of occurrence in the ICSD. For convenience we hereafter refer to all the structures as perovskites.

The prototypes introduced above represent the initial structures for the sulfide perovskites. Using the crystal structure of the prototypes as templates the atomic sites are substituted with A's and B's from our previously determined compounds. In the 56 cases where both the ABS_3 and BAS_3 exhibit gaps in the distorted structure, we investigate both AB permutations, while in the 73 cases with only one of the AB combinations showing a gap in the distorted structure we only investigate the relevant permutation. The number of atoms in the unit cell of the $BaNiO_3$ type structure is 10 whereas the other prototypes have 20 atoms in the unit cell. The structures are subsequently completely relaxed with respect to the unit cell and the atomic positions. The initial structures contain small symmetry-breaking displacements, which mean that in some cases the structures change considerably during relaxation. In order to obtain a correct classification of the final structures, we monitor potential changes of the space groups using the spglib-library[67]. Within a reasonable tolerance most of the lowest-energy structures have unchanged symmetry. Some exceptions are systems initially in the distorted *P1* structure, which often during relaxation obtain a higher, but still mostly quite low, degree of symmetry. In one case, the $MnTaS_3$ compound, the symmetry of the distorted perovskite increases to the *R3* space group. About one third of the compounds initially in the $YScS_3$ structure ($Pna2_1$) increase their symmetry to *Pnma*. The character of this structure is further investigated using feature vectors and a metric which describe local atomic structures in crystals[68]. It turns out that the $YScS_3$ structure in these cases has relaxed into the $GdFeO_3$ structure. Among the lowest energy structures this transformation happens for $BaHfS_3$ and $BaZrS_3$. Two compounds, $CdHfS_3$ and $TeHfS_3$, obtain the lowest energy by distorting the $BaNiO_3$ prototype so that the symmetry is reduced from $P6_3/mmc$ to $P2_1m$.

The structural optimizations result in total energies of all the compounds in the different structures, which can be compared to find the most stable structure with the lowest energy per atom. In order to get not only an estimate of the energy differences but also their uncertainties we employ the technique of Bayesian error estimation in the mBEEF functional[69]. The reference energy for a given compound is taken as the energy of the lowest-energy structure from the set of the obtained ABS_3 and BAS_3 structures. Thereafter, the energy differences and uncertainties are calculated with respect to this reference energy. Additionally, the stability of compounds is also calculated with respect to competing phases consisting of elemental, binary, and ternary phases, where the elemental phases are the standard states of the elements, and the binary and ternary phases are the sulfides of one ($A_\alpha S_\beta$, $B_\gamma S_\delta$ type) and two ($A_\mu B_\nu S_\varepsilon$ type) elements, respectively. The pool of competing phases is taken as the stable compounds in the Open Quantum Materials Database (OQMD)[70]. The pool consists of the elementary phases of the elements and 208 compounds. Their structures are re-optimized with the PBEsol functional and their energies calculated with mBEEF.

The stability versus segregation of a given ABS_3 compound is determined by constructing the convex energy hull in the A-B-S space. The elemental phases are placed in the corners of a triangle defining a plane (with, say, $z = 0$) and the z-coordinate of the remaining phases are their standard heats of formation. The in-plane positions of the compounds with respect to the elemental phases are given by their stoichiometry. By considering all triangles obtained by connecting three of the points the so-called convex hull, which includes all triangles with maximal stability, can be constructed.

In constructing the hull, the compounds with the ABS_3 compositions are not included and we refer to the energy of the hull at this composition as simply the hull energy. The phase ABS_3 is unstable if the hull energy (E_{hull}) is lower than the energy of ABS3 (E_{ABS_3}). Additionally, the Bayesian error estimates of the hull energy (ΔE_{hull}) is calculated in the same manner as described before. The comparison of E_{hull} and E_{ABS_3} (along with the uncertainties) gives a robust criterion to assess the low-temperature stability of ABS_3.

Besides comparing the energies of different structures of ABS_3 with the convex hull we also compare their relative energies in order to address potential (meta-)stability. The NH_4CdCl_3/Sn_2S_3 structure turns out to be the most common lowest energy structure whereas the cubic and $BaNiO_3$ structures are rarely the most stable one. The remaining structures have roughly equal frequency of appearance as the lowest energy structure.

With respect to stability of the different phases, three different situations can be identified. They are illustrated for some selected compounds in Figure 4. 1) The convex hull has the lowest energy even when the uncertainty is taken into account. If this is the situation the ABS_3 compound cannot be expected to be stable in any of the suggested structures and should therefore be discarded. This is for example the case with $HfTeS_3$ as seen in Figure 4. 2) Several structures and/or the convex hull are within the uncertainties of the lowest energy structure or have an energy of less than 25 meV above the lowest energy structure. In this case it is unclear whether the compound in the lowest energy structure is stable and/or metastable even

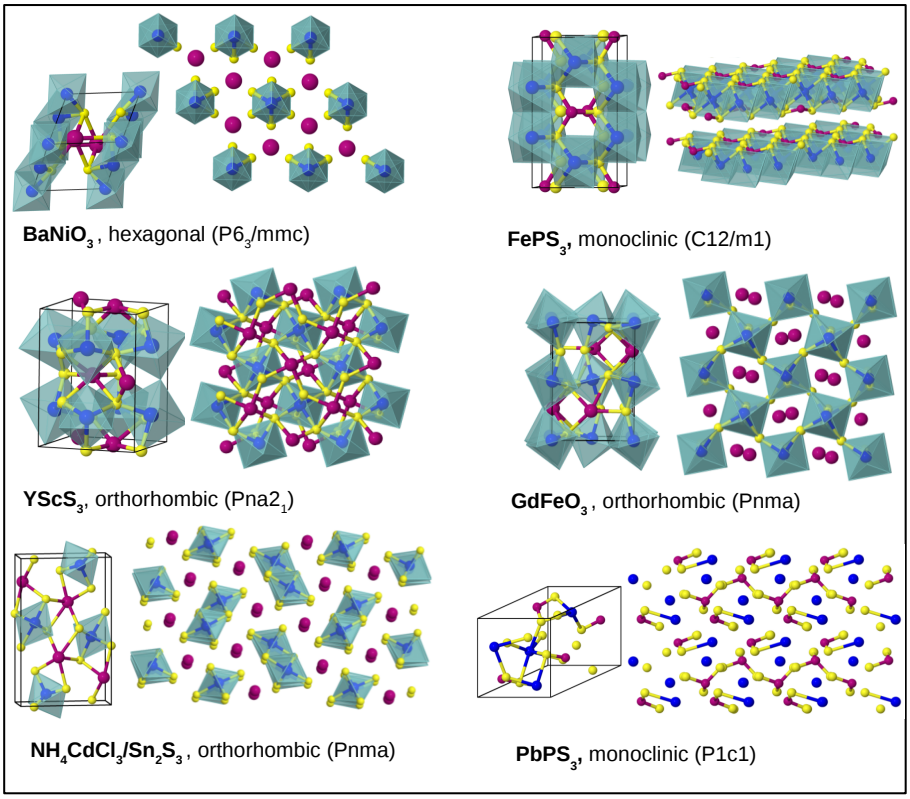

Fig. 3 The most common prototypes in the ICSD[65,66] for ABS_3 materials. We investigate all compounds in these six structures plus the cubic and the distorted cubic structures.

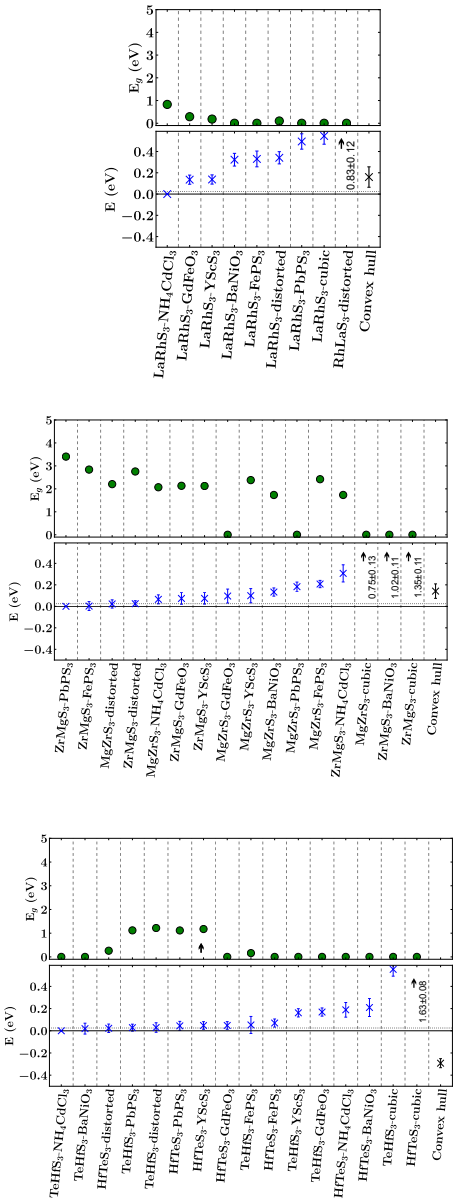

Fig. 4 Comparison of formation energies, E, and band gaps, E_g, of different phases for a selection of compounds. The energy error bars are calculated relative to the most stable ABS_3 structure. For some compounds, like $LaRhS_3$ (top left panel) there is a single structure significantly more stable than the other structures and the convex hull. In other cases, like $ZrMgS_3$ (top right panel), several structures have energies within the uncertainties of the calculations and might be (meta-)stable. In such cases it is useful to check the corresponding band gaps for all the (meta-)stable structures. Finally, in cases, like $TeHfS_3$ (bottom panel), all the investigated phases are unstable relative to the convex hull and the compounds do therefore not need to be considered further.

at low temperatures. The perovskites often exhibit symmetry breaking phase transitions at moderate temperatures, but the prediction of the complete phase diagram would require a detailed study of the entropic contributions to the free energy. Such studies have been carried out for for example $BaTiO_3$ [71] and to some extent for $CsSnI_3$ [72]. An extensive study of perovskite phase stability in sulfides including some discussion of thermal effects due to phonons can be found in Ref. 73. By choosing an appropriate synthesis route the phase formation can to some extent be controlled, and it might be possible to form non-equilibrium phases which for all practical purposes are stable. We therefore keep the compounds in this class for further studies. An example is $ZrMgS_3$, as shown in Figure 4. 3) A single structure has a significantly lower energy compared to all the other structures and the convex hull. We take a compound to be in this class if the energy of the most stable structure is lower than the competing energies minus the error bar and if there are no other structures within 25 meV. The 25 meV leaves some space for entropic effects at room temperature. The compounds in this class are the potentially most promising ones since the room temperature phase can be predicted with considerable certainty. The compound $LaRhS_3$ illustrates this case in Figure 4. Overall, we find 75 different ABS_3 compositions in 155 structures to be further investigated.

At this stage of the screening we check if any of these compounds have been experimentally synthesized according to ICSD, and in which structures. For example, $BaZrS_3$ (ICSD 23288), $PbZrS_3$ (ICSD 2439) and $SrZrS_3$(ICSD 23287) appear in ICSD in the structures the calculations show to have the lowest energy. $LaScS_3$ (ICSD 641844) and $YScS_3$ (ICSD 23422) appear experimentally in the $YScS_3$ prototype with $Pna2_1$ symmetry. This structure is already included in our investigations, but the calculations find $LaScS_3$ to be slightly more stable in the $GdFeO_3$ structure and $YScS_3$ to be slightly more stable in the $PbPS_3$ structure. We observe a similar situation with $CaZrS_3$ and $CaHfS_3$, both reported in the ICSD in the $GdFeO_3$ structure, but the calculations show $PbPS_3$ structure to be the most stable one. However, in all four cases the energy differences are smaller than the calculated error bars on the energy differences. $SnSrS_3$ (ICSD 651032) is reported in the ICSD in the NH_4CdCl_3/Sn_2S_3 structure, but the structure was synthesized under high pressure. The calculations on the other hand, predict $GdFeO_3$ to be the lowest energy structure.

Four compounds appear in entirely new structures in ICSD: $LaYS_3$, $AgTaS_3$, $BiInS_3$ and $CuTaS_3$. The $BiInS_3$-structure (ICSD 290195) is not the result of an experimental structure determination but comes from a computational study. However, we confirm that it has a low energy and include it in the further studies. $CuTaS_3$ appears in a genuinely new prototype (ICSD 43272), which is a 'needle-like' perovskite and different from the NH_4CdCl_3/Sn_2S_3 structure we identify. Calculations on the $CuTaS_3$ structure confirm that it is more stable than the NH_4CdCl_3/Sn_2S_3 structure. $CuTaS_3$ was recently synthesized[46], and the band gap measured to around 1 eV in good agreement with our calculated value for this structure of 0.98 eV.

The ICSD reports the $LaYS_3$ in the $CeTmS_3$ prototype. Calculating the energy of this structure, we find that it is the most stable one, while we also find the NH_4CdCl_3/Sn_2S_3 structure within the calculational uncertainty. In the $CeTmS_3$ we calculate a direct band gap of 1.79 eV close to the direct band gap of 1.87 eV calculated in the NH_4CdCl_3/Sn_2S_3 structure.

Our main focus is on identifying LBG materials for water splitting. However, the screening approach is also of relevance for identification of PV materials. The known successful solar cell materials have band gaps around 1 eV as a balance between the number of photons absorbed and the energy gain per photon. Considering the approximate nature of the band gap calculations, we therefore focus on materials with band gaps in the range 0.5-1.5 eV as candidates for solar cell absorbers. The semiconductors in the water splitting devices and tandem solar cells are required to have a wider band gap, around 2 eV, if incorporated as a LBG component in a tandem device, so here we choose a range of 1.5-2.5 eV as the target for our candidates. The selection is performed based on the calculated GLLB-SC gaps. In most cases the gaps are indirect, but for some systems the gaps are direct. The latter ones are particularly relevant for thin photo-absorbers because of the higher absorbance.

The result of the selection based on band gap is shown in Fig. 5. Overall 90 compounds with 57 different ABS_3 compositions fall within the relevant gap ranges and will proceed to the next step in the selection procedure. Compounds in the NH_4CdCl_3/Sn_2S_3 structure are the most common ones while there are no cubic compounds and only two compounds in the $BaNiO_3$ structure. Three different cases can be identified.

1) A given compound has one structure which is significantly more stable than the competing phases and which has a band gap in the relevant range. A compound where this is the case is indicated in the figure with a circle around the symbol and the name of the compound is written in bold. An example is $LaYS_3$.

2) A compound has several structures at low energies, but they all have gaps in the interesting ranges. In this case several symbol for the gaps will appear in the figure and the name of the compound is written in bold. This is, for example, the case for $BaZrS_3$, where the $GdFeO_3$ structure has the lowest energy with a band gap of 2.3 eV, and the distorted structure has also a low energy and a band gap of 1.6 eV.

3) Finally, a compound might have one or more low-energy structures with relevant band gaps, but it also has low-energy structures with gaps outside the range (for example metallic). These cases show up in Fig. 5 with their names written in or-

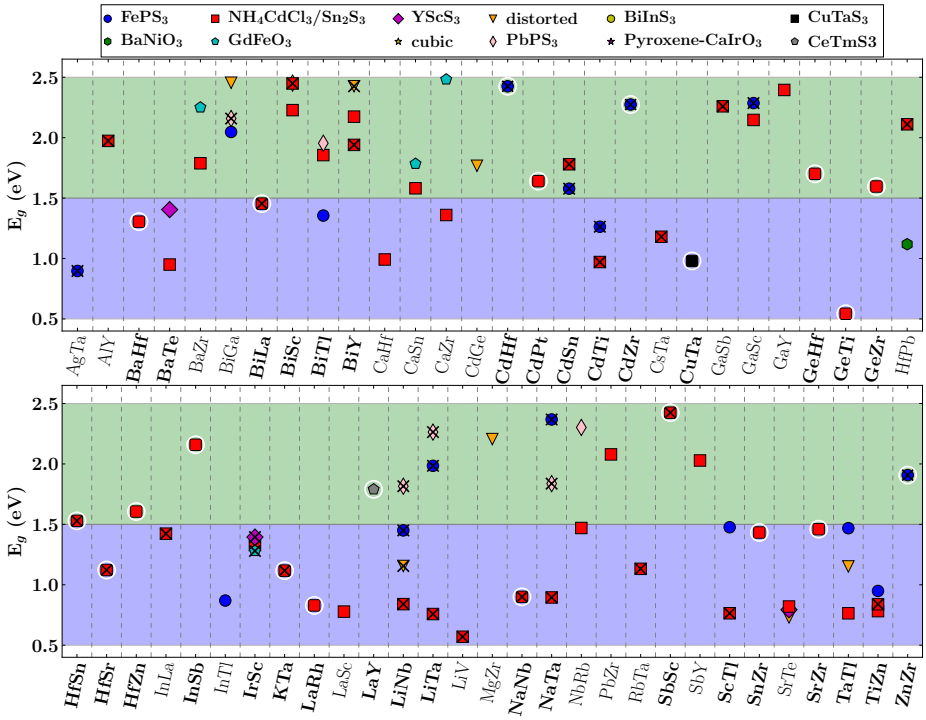

Fig. 5 All the stable compounds, according to the procedure described in the caption of Fig. 4, with the corresponding band gaps in the region relevant for solar cells (0.5-1.5 eV) and water splitting (1.5-2.5 eV) application. All the band gap values were calculated using the GLLB-SC functional. Markers with crosses on top indicate that the chemical formula should be read in reverse, instead of AB (written on the x-label), it is BA. The cases where one structure is considered significantly more stable than the competing phases are indicated with a circle around the symbol, whereas compositions where all stable structures have a band gap size relevant for either PV or PEC are written in bold.

dinary non-bold font. A complete overview of the energies and band gaps for all the different compounds and structures can be found in the supplementary material. The data are furthermore available at the Computational Materials Repository (CMR)[74,75] and at the NoMaD repository[76].

Appropriate photoabsorption alone is not sufficient for a material to perform well in a PV or PEC device, so it is important to address the issues occurring after the photon has been absorbed and the carriers have been generated. Ideally, the carriers (electrons and holes) would separate and generate current, but if a large part of carriers recombine almost immediately all the energy is lost. The recombination probability is smaller for carriers with higher mobilities, and it can be used as a targeted property in the screening procedure. Carrier mobility is difficult to calculate, but effective mass, which is in relation with the mobility as $\propto 1/\mu$, can easily be obtained from a DFT calculation. Carrier effective masses were obtained by fitting a parabola to the top of the valence band and bottom of the conduction band of the material. Band structures are calculated along the high-symmetry points as suggested by Setyawan and Curtarolo[77]. We further consider candidates with the absolute values of the effective masses of both carriers smaller than 1 electron mass (because of the orientation of the fitted parabola we use negative signs for hole masses and positive signs for electron masses). This criterion leads to a further reduction in the number of candidate materials to 36 different ABS_3 compositions in 42 structures.

In Table 1 we report the calculated effective masses of the 42 selected candidates together with the calculated band gaps and the type of band gap. We find 18 compounds and structures with a direct band gap, and they are mostly in one of the orthorhombic structures NH_4CdCl_3/Sn_2S_3, $GdFeO_3$ and $YScS_3$. The 42 compounds (composition+structure) with desirable electronic properties are now passed on to the next step in the screening procedure which considers defects.

Defects in a material are often limiting its optoelectronic performance because point defects in crystals may introduce additional states inside the band gap. These additional gap states may act as recombination centers and reduce the charge separation efficiency. Whether the formation of point defects will be detrimental for the photovoltaic performance of a material, depends on the position of the additional states: materials with defect states deep inside the band gap are called defect sensitive, while the ones with defect states inside the bands or close to the band edges are called defect tolerant.

We explore the defect tolerance of the selected candidates by performing defect calculations on the supercells for three types of atomic vacancies: A atom, B atom and S vacancy. Defects were created in a 2x2x2 (3x3x3 for the distorted and cubic prototypes) supercells. The calculations for both the pristine and defect structures were carried out using the PBE exchange correlation functional and the wavefunctions were expanded in an LCAO (dzp) basis set. The k-point mesh was chosen to scale with the system size: pristine structures were calculated with a dense 14x14x14 mesh, while the mesh for the supercells was reduced to 7x7x7. In the cases of the supercells of the distorted and cubic structures (3x3x3 supercells), the k-point mesh was further decreased to 5x5x5. Due to limitations of computer time, relaxations were not performed, and the spectral analysis was carried out based on the PBE band structure. More accurate results could in principle be obtained with GW band structures, but this is again very computationally demanding and is a subject of future work. The approach here has previously been applied and compared favorably to the more rigorous Slater-Janak method for transition metal

Table 1 Candidates selected based on stability, band gaps 0.5 - 2.5 eV and carrier effective masses smaller than 1 electron mass. Compounds, where all low-energy structures exhibit band gaps in the range 0.5-2.5 eV, are indicated in bold. The formulas of the materials with direct band gaps are underlined.

	formula	$E_g^{GLLB-SC}$	$E_{g(direct)}^{GLLB-SC}$	m^*_h	m^*_e	prototype
Ag - Ta	$TaAgS_3$	0.90	0.97	-0.272	0.606	$FePS_3$
Ba - Hf	$\underline{BaHfS_3}$	1.31	1.31	-0.347	0.943	NH_4CdCl_3/Sn_2S_3
Ba - Te	$\underline{BaTeS_3}$	1.40	1.40	-0.208	0.317	$YScS_3$
	$BaTeS_3$	0.95	1.21	-0.480	0.343	NH_4CdCl_3/Sn_2S_3
Ba - Zr	$\underline{BaZrS_3}$	2.25	2.25	-0.749	0.426	GdFeO3
Bi Ga	$\underline{BiGaS_3}$	2.05	2.47	-0.826	0.448	$FePS_3$
	$BiGaS_3$	2.45	2.76	-0.682	0.197	distorted
Bi - Sc	$BiScS_3$	2.45	2.72	-0.470	0.799	$PbPS_3$
Bi - Tl	$BiTlS_3$	1.36	1.98	-0.636	0.309	$FePS_3$
Ca - Hf	$\underline{CaHfS_3}$	0.99	0.99	-0.336	0.759	NH_4CdCl_3/Sn_2S_3
Ca - Sn	$\underline{CaSnS_3}$	1.58	1.93	-0.606	0.943	NH_4CdCl_3/Sn_2S_3
Ca Zr	$\underline{CaZrS_3}$	2.48	2.48	-0.222	0.413	GdFeO3
	$\underline{CaZrS_3}$	1.36	1.36	-0.369	0.800	NH_4CdCl_3/Sn_2S_3
Cd - Ge	$\underline{CdGeS_3}$	1.77	1.77	-0.606	0.227	distorted
Cd - Sn	$\underline{SnCdS_3}$	1.58	1.58	-0.585	0.151	$FePS_3$
Cd - Ti	$TiCdS_3$	1.26	1.39	-0.351	0.550	$FePS_3$
Cd - Zr	$ZrCdS_3$	2.27	2.39	-0.421	0.455	$FePS_3$
Ga - Sb	$SbGaS_3$	2.26	2.29	-0.590	0.900	NH_4CdCl_3/Sn_2S_3
Ga Sc	$\underline{GaScS_3}$	2.15	2.15	-0.318	0.322	NH_4CdCl_3/Sn_2S_3
	$\underline{ScGaS_3}$	2.29	2.40	-0.710	0.551	$FePS_3$
Ga - Y	$\underline{GaYS_3}$	2.39	2.39	-0.544	0.903	NH_4CdCl_3/Sn_2S_3
Ge - Ti	$\underline{GeTiS_3}$	0.54	0.61	-0.250	0.680	NH_4CdCl_3/Sn_2S_3
Hf - Pb	$HfPbS_3$	1.12	1.63	-0.275	0.235	BaNiO3
Hf - Sr	$\underline{SrHfS_3}$	1.12	1.12	-0.327	0.811	NH_4CdCl_3/Sn_2S_3
In - La	$\underline{LaInS_3}$	1.42	2.30	-0.574	0.830	NH_4CdCl_3/Sn_2S_3
In - Sb	$\underline{InSbS_3}$	2.16	2.16	-0.429	0.170	NH_4CdCl_3/Sn_2S_3
In - Tl	$\underline{InTlS_3}$	0.87	0.87	-0.612	0.138	$FePS_3$
La - Sc	$\underline{LaScS_3}$	0.78	0.78	-0.408	0.464	NH_4CdCl_3/Sn_2S_3
La - Y	$\underline{LaYS_3}$	1.79	1.79	-0.670	0.490	$CeTmS_3$
Li - Ta	$TaLiS_3$	1.98	2.00	-0.755	0.985	$FePS_3$
Mg - Zr	$MgZrS_3$	2.21	2.32	-0.718	0.779	distorted
Na - Ta	$TaNaS_3$	2.37	2.39	-0.396	0.490	$FePS_3$
Sb - Sc	$ScSbS_3$	2.42	2.57	-0.387	0.352	NH_4CdCl_3/Sn_2S_3
Sb - Y	$SbYS_3$	2.03	2.09	-0.372	0.484	NH_4CdCl_3/Sn_2S_3
Sc - Tl	$ScTlS_3$	1.48	1.65	-0.798	0.402	$FePS_3$
Sr Te	$\underline{SrTeS_3}$	0.79	0.79	-0.258	0.294	$YScS_3$
	$\underline{SrTeS_3}$	0.82	1.01	-0.404	0.202	NH_4CdCl_3/Sn_2S_3
Sr - Zr	$\underline{SrZrS_3}$	1.46	1.46	-0.345	0.790	NH_4CdCl_3/Sn_2S_3
Ta - Tl	$\underline{TaTlS_3}$	1.15	1.15	-0.297	0.241	distorted
	$TaTlS_3$	1.47	1.15	-0.866	0.608	$FePS_3$
Ti - Zn	$TiZnS_3$	0.95	1.03	-0.236	0.444	$FePS_3$
Zn - Zr	$ZrZnS_3$	1.91	1.97	-0.616	0.420	$FePS_3$

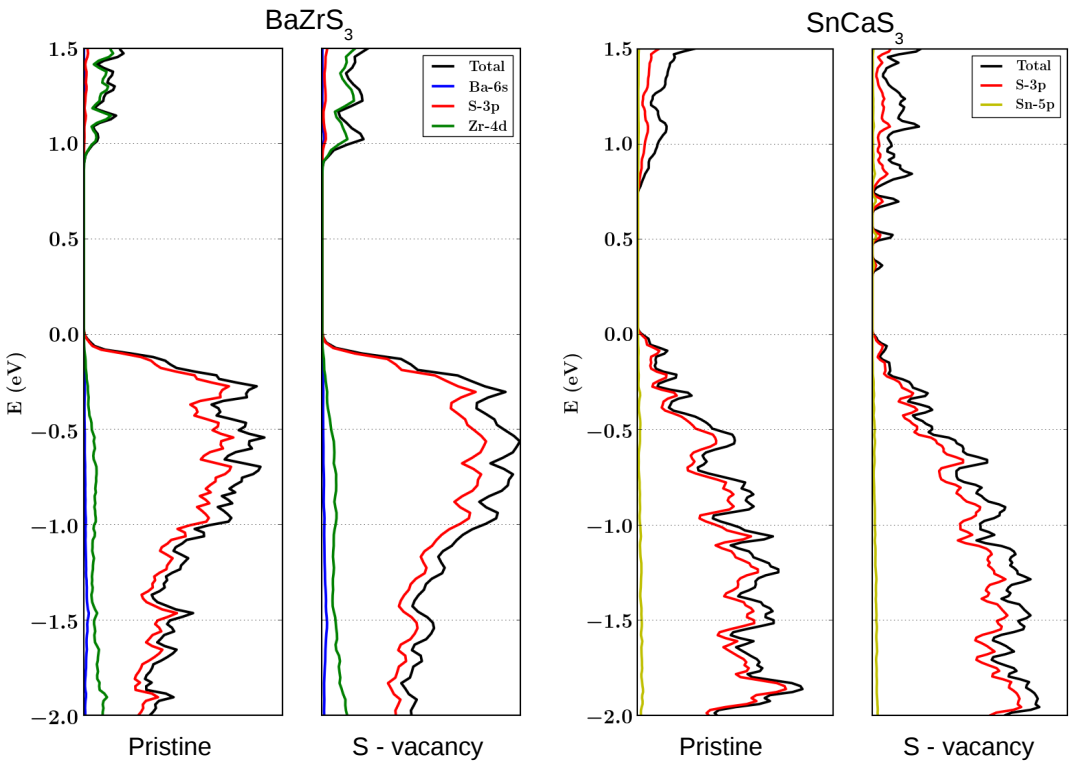

Fig. 6 Projected and total density of states for $BaZrS_3$ ($GdFeO_3$ structure)(left) and $SnCaS_3$ (NH_4CdCl_3/Sn_2S_3 structure)(right) with and without a sulfur vacancy. In the case of $BaZrS_3$ the introduction of a vacancy does not give rise additional states inside the band gap, while in the case of $SnCaS_3$, deep states are found within the band gap.

dichalcogenides[78,79].

We identify the defect sensitive materials by calculating the band structure and the electronic density of states (DOS). The presence of a deep lying state in the gap shows up as a contribution to the DOS in the region of the band gap. Fig, 6 illustrates this for a sulfur vacancy in the two cases $BaZrS_3$, where there are no gap states, and $SnCaS_3$, where states in the gap are present. In the cases where deep gap states appear they are always caused by sulfur vacancies while the cation vacancies do not seem to introduce deep gap states.

We identify 15 out of the 42 candidate materials to be tolerant to vacancies. This set of 15 materials, summarized in Table: 2, is the final output of the screening and we suggest them as a potential materials for solar energy conversion application. Some of the materials mentioned in Table: 2 have also been studied in previous experimental and theoretical works. For example, band gap tuning and the defect properties of $BaZrS_3$ have been explored by Meng *et. al* and Sun *et. al*[50,80]. The band gap reported for $BaZr_3$ in different studies varies in range from 1.7-1.9 eV which agrees reasonably well with our calculated value[47,48]. Interestingly, our defect analysis based on the band structure identifies $BaZrS_3$ as tolerant towards vacancy defects and the total energy based defect calculations by Meng *et. al* also predicts only shallow level defects in the material. Similarly, our calculated value of the band gap of $SrZrS_3$ agree well with the reported experimental value of 1.53 eV by Niu et al.[48]. However, there are also some differences in our predicted set of candidates as compared to the predictions by Ju *et. al* and Sun *et. al*. For example, $SrSnS_3$ and $CaTiS_3$ are discarded from our proposed list of materials. According to our calculations the most stable structure of $SrSnS_3$, and the only one in our stability threshold, is $GdFeO_3$ with a gap of only 0.1 eV. However, Ju *et. al* did not explore $GdFeO_3$ as a possible prototype which explains the difference in our results. Similarly, we find that the lowest energy structure of $CaTiS_3$ is the needle-like with a band gap of 0.2 eV which is too small as per our criteria. On the other hand, some of the compounds we find are not reported in other studies because we do not impose the constraint of Goldschmidt tolerance factor in the selection of elements, because Goldschmidt's criterion is after all only an empirical rule and developed mainly for oxides. $CuTaS_3$, which was recently studied by Heo *et al.*[46], is removed from our final list because of too large effective masses.

Finally, the set of suggested candidates consists of eight direct band gap materials, $BaZrS_3$ in the $GdFeO_3$ structure, $BaHfS_3$, $CaHfS_3$, $CaZrS_3$, $SrZrS_3$ and $SrHfS_3$ in the NH_4CdCl_3/Sn_2S_3 structure, $TaTlS_3$ in distorted structure and $LaYS_3$ in $CeTmS_3$ structure. All but $TaTlS_3$ happen to be in one of the three orthorhombic structures. Furthermore, in cases where the material can be found in more than one stable phase, there is a risk that some of the other phases are metallic. Since the energy differences are small, there is a concern that during material synthesis, one will obtain (partially or fully) the metallic structure of the compound, which would be fatal for the material's PV performance. Out of our candidates, the metallic competing structures only appear in the case of Ba-Zr ($BaZrS_3$ and $ZrBaS_3$), where two metallic $ZrBaS_3$ structures, $YScS_3$ and $PbPS_3$ have energies within the calculational uncertainty. In the next section we proceed through synthesis of $LaYS_3$, one of the most promising candidates in Table 2.

Table 2 List of selected candidates based on stability, band gaps, carrier effective masses, and defect tolerance. Compounds where all low-energy structures exhibit band gaps in the range of solar light absorption are indicated in bold.

	formula	$E_g^{GLLB-SC}$	$E_{g(direct)}^{GLLB-SC}$	m^*_h	m^*_e	prototype
Ba-Hf	$BaHfS_3$	1.31	1.31	-0.347	0.943	NH_4CdCl_3/Sn_2S_3
Ba-Zr	$BaZrS_3$	2.25	2.25	-0.749	0.426	$GdFeO_3$
Bi-Tl	$BiTlS_3$	1.36	1.98	-0.636	0.309	$FePS_3$
Ca-Hf	$CaHfS_3$	0.99	0.99	-0.336	0.759	NH_4CdCl_3/Sn_2S_3
Ca-Sn	$CaSnS_3$	1.58	1.93	-0.606	0.943	NH_4CdCl_3/Sn_2S_3
Ca-Zr	$CaZrS_3$	1.36	1.36	-0.765	0.884	NH_4CdCl_3/Sn_2S_3
Hf-Sr	$SrHfS_3$	1.12	1.12	-0.327	0.811	NH_4CdCl_3/Sn_2S_3
Hf-Pb	$HfPbS_3$	1.12	1.63	-0.275	0.235	$BaNiO_3$
La-Y	$LaYS_3$	1.79	1.79	-0.670	0.490	$CeTmS_3$
Li-Ta	$TaLiS_3$	1.98	2.00	-0.755	0.985	$FePS_3$
Mg-Zr	$MgZrS_3$	2.21	2.32	-0.718	0.779	distorted
Sb-Y	$SbYS_3$	2.03	2.09	-0.372	0.484	NH_4CdCl_3/Sn_2S_3
Sr-Zr	$SrZrS_3$	1.46	1.46	-0.644	3.115	NH_4CdCl_3/Sn_2S_3
Ta-Tl	$TaTlS_3$	1.15	1.15	-0.297	0.241	distorted
Zn-Zr	$ZrZnS_3$	1.91	1.97	-0.616	0.420	$FePS_3$

4.2 Synthesis of $LaYS_3$

According to our results, the structure with the lowest energy of $LaYS_3$ is the $CeTmS_3$ structure. We attempt to synthesize $LaYS_3$ in thin film form, which is more relevant for actual devices than the powder form. The La/Y atomic ratio is checked after sputter deposition of the LaY precursor films. Averaging EDX measurements from three random spots yields La/Y $= 1.01 \pm 0.01$ as desired. After sulfurization, the (La+Y)/S ratio is 0.70 according to EDX and 0.66 according to XPS, which is consistent with the ratio of 0.67 expected for a stoichiometric $LaYS_3$ film. Residual oxygen is quantified by EDX and XPS as 7% and 9% of the total atomic concentration, respectively. The thickness of the sulfurized film is 550 nm according to ellipsometry.

As discussed in the Experimental Details, theoretical XRD patterns based on the relaxed structure of each $LaYS_3$/$YLaS_3$ prototype are employed to index experimental peaks. The only existing experimental XRD reference among those compounds is a powder sample studied in the 1970s, which was identified as $LaYS_3$ in the $CeTmS_3$ prototype (ICSD 641874)[82]. The main peaks of this previous experimental pattern are very close (within 0.2°) to those of our theoretical XRD pattern for the same prototype (Figure S3, supplementary material). The measured XRD pattern of our sulfurized

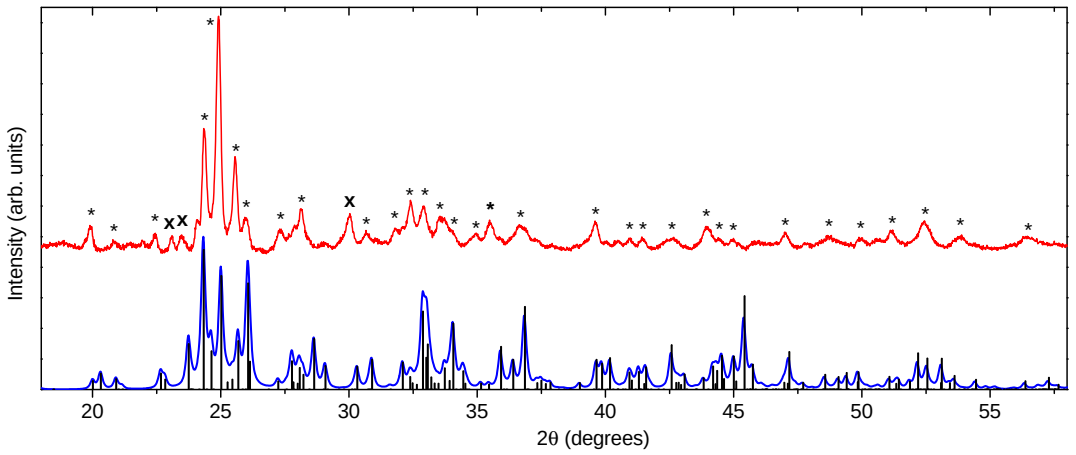

Fig. 7 Top plot (red): experimental XRD pattern of the synthesized film. Bottom plot (blue): theoretical XRD pattern of $LaYS_3$ in the $CeTmS_3$ prototype, assuming random orientation and $0.2°2\theta$ broadening. Vertical lines (black): theoretical XRD peak positions and relative intensities of $LaYS_3$ in the $CeTmS_3$ prototype assuming random orientation. Due to the very large number of low-intensity peaks predicted for this structure, theoretical peaks having intensity less than 1/25 the most intense peak at 24.3° are not visualized in the figure and are disregarded in the analysis. The * and **x** symbols indicate experimental peaks located within $0.2°2\theta$ and $0.3°2\theta$ of a theoretical peak, respectively.

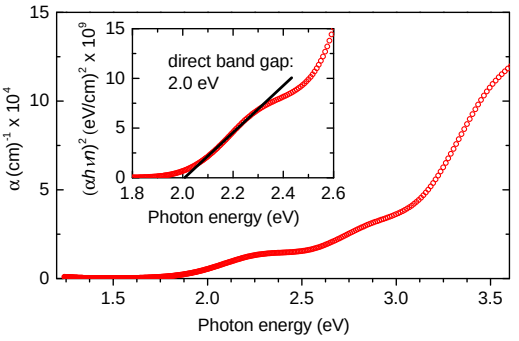

Fig. 8 Main plot: absorption coefficient of $LaYS_3$ according to spectroscopic ellipsometry. Inset: Determination of the value of the direct band gap from absorption coefficient and refractive index[81], both extracted by spectroscopic ellipsometry.

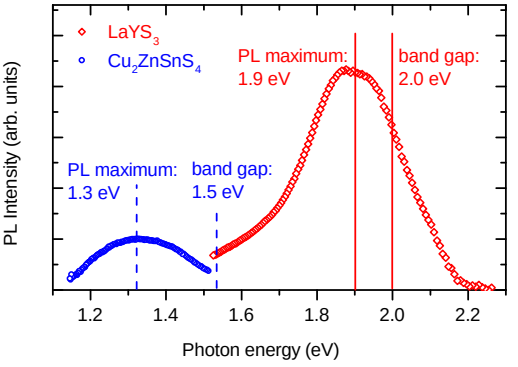

Fig. 9 Photoluminescence spectra of $LaYS_3$ (red) and Cu_2ZnSnS_4 (blue) thin films. The scale is the same for both spectra. The solid (dashed) vertical lines indicate the PL peak position and band gap of $LaYS_3$ (Cu_2ZnSnS_4).

film is shown in Figure 7, together with the simulated pattern of $LaYS_3$ ($CeTmS_3$ structure). Among the 35 peaks identified in the XRD pattern, 32 are within a distance of $0.2°2\theta$ from a major peak expected by theory, and the remaining 3 are within $0.3°2\theta$. By visualizing the XRD pattern over a broader 2θ range, a few other low-intensity peaks can be identified (Figure S3, supplementary material). They can all be indexed to the $CeTmS_3$ structure. It must be noted that some major peaks expected for a randomly oriented $LaYS_3$ powder with the $CeTmS_3$ structure are absent in the measured XRD pattern of our thin film. This can tentatively be explained by texturing of the film, i.e., the tendency of some crystal planes of $LaYS_3$ to grow parallel to the substrate plane.

Further confirmation that the $LaYS_3$ structure with the $CeTmS_3$ prototype is the main constituent of the film is given by analysis of its absorption coefficient α, shown in Figure 8. All the lowest-energy structures of $LaYS_3$ and $YLaS_3$ are predicted to have direct band gaps (Fig. S1, supplementary material). For a direct band gap material, linear extrapolation of $(\alpha h\nu n)^2$ against $h\nu$ is expected to yield the band gap[81]. In the above expressions $h\nu$ is the photon energy and n is the refractive index, which is simply derived from α through the Kramers-Kronig relationship. This procedure yields a band gap of 2.0 eV, as shown in the inset of Figure 8. The value is within the calculation error for both the $CeTmS_3$ structure of $LaYS_3$ (calculated band gap: 1.79 eV) and the NH_4CdCl_3/Sn_2S_3 structure of both $LaYS_3$ and $YLaS_3$ (calculated band gap: 1.87 eV). However, the two NH_4CdCl_3/Sn_2S_3 structures can be excluded due to their incompatibility with the measured XRD pattern (Figure S3, supplementary material). The band gaps of all other possible structures of $LaYS_3$ and $YLaS_3$ are incompatible with the experimental band gap.

To give a preliminary assessment on whether $LaYS_3$ can be potentially used as a photoabsorber, a steady-state PL spectrum is measured (Figure 9). Considering the value of the absorption coefficient of $LaYS_3$ at the PL excitation wavelength (Figure 8), a PL analysis depth of 250 nm is derived. Therefore, the PL measurement probes recombination properties in the bulk of the film. In an ideal semiconductor the PL peak position should be centered on the band gap, as electrons from the conduction band minimum recombine radiatively with holes from the valence band maximum. However, in polycrystalline semiconductors used in thin-film solar cells the PL peak is often observed at a lower energy than the band gap energy (Stokes shift). An example is Cu_2ZnSnS_4 (CZTS), where the PL peak is systematically shifted by 100-200 meV with respect to the band gap energy, even in solar cells with efficiency above 10%[83]. This can be due to trap- and tail states caused by impurities or native defects. To make a meaningful comparison, Figure 9 shows the PL spectrum of the $LaYS_3$ film together with the PL spectrum of a fully sulfurized Cu_2ZnSnS_4 film that was later processed into a solar cell with 5.2% conversion efficiency[84]. The PL acquisition parameters were the same for both materials. In the Cu_2ZnSnS_4 film, the PL peak is located 200 meV below its band gap[84]. On the other hand, the PL peak in our $LaYS_3$ film is centered at 1.9 eV, which is 100 meV lower than the band gap extracted from ellipsometry (Figure 8). We also note that the related binary compound La_2S_3 has a much larger offset of 600 meV between its band gap (2.7 eV) and its PL peak position (2.1 eV)[85]. The above discussion indicates that $LaYS_3$ could be a successful high-band gap photoabsorber for tandem water splitting devices.

5 Conclusions

In the current study we have explored different polymorphs of sulfur perovskites with ABS_3 stoichiometry as potential light absorbers for solar energy conversion - in particular as the large band gap material for a tandem photoelectrode. As compared to oxide perovskites explored in previous works, sulfur perovskites tend to have smaller band gaps pertinent for visible light absorption. Our results are based on a systematic screening procedure using a chain of simple descriptors. The procedure takes into account stability (through the formation energy), light absorption (the band gap), mobility (effective masses), and defect sensitivity (defects states in the gap). The outcome is a list of promising candidate materials as PV and PEC light absorbers. Among them, $LaYS_3$ is synthesized as a thin film for the first time, showing excellent agreement with the calculated structure and direct band gap. Additionally, a preliminary study by photoluminescence hints towards favorable defect properties in $LaYS_3$ thin films, which is also consistent with the computational results for defect sensitivity in that material. The screening procedure is certainly not complete. Several properties are not fully accounted for by the descriptors. One example is the mobility, where the electron or hole effective mass only describe one aspect of the mobility. A deeper understanding and a more accurate calculation would require consideration of scattering from phonons, electron, and impurities beyond what can be achieved in a screening study. However, the excellent agreement with experimental data from our synthesized $LaYS_3$ compound and from the already known compounds lends credibility to the approach. Further experimental studies will be undertaken to capitalize on these findings and investigate their full potential including schemes for protection and interfacing.

Acknowledgement

This work was supported by a research grant (9455) from VILLUM FONDEN. The Center for Nanostructured Graphene is sponsored by the Danish National Research Foundation,

Project DNRF103. The project also received funding from the European Unions Horizon 2020 research and innovation programme under Grant Agreement No. 676580 with The Novel Materials Discovery (NOMAD) Laboratory, a European Center of Excellence and the Danish Council for Independent Research (DFF-4005-00463).

References

1 L. Vayssierres, *On Solar Hydrogen and Nanotechnology*, John Wiley and Sons (Asia) Pvt. Ltd, 2009.
2 G. Chamberlain, *Sol. Cells*, 1983, **8**, 47–83.
3 M. Ni, M. K. Leung, D. Y. Leung and K. Sumathy, *Renewable Sustainable Energy Rev.*, 2007, **11**, 401 – 425.
4 L. Schmidt-Mende, A. Fechtenktter, K. Mllen, E. Moons, R. H. Friend and J. D. MacKenzie, *Science*, 2001, **293**, 1119–1122.
5 A. M. Kolpak and J. C. Grossman, *Nano Lett.*, 2011, **11**, 3156–3162.
6 A. Fujishima and K. Honda, *Nature*, 1972, **238**, 37–38.
7 T. Hisatomi, J. Kubota and K. Domen, *Chem. Soc. Rev.*, 2014, **43**, 7520–7535.
8 P. C. K. Vesborg and B. Seger, *Chemistry of Materials*, 2016, **28**, 8844–8850.
9 S. Hu, C. Xiang, S. Haussener, A. D. Berger and N. S. Lewis, *Energy & Environmental Science*, 2013, **6**, 2984.
10 M. F. Weber and M. J. Dignam, *International Journal of Hydrogen Energy*, 1986, **11**, 225–232.
11 J. Y. Kim, G. Magesh, D. H. Youn, J.-W. Jang, J. Kubota, K. Domen and J. S. Lee, *Scientific reports*, 2013, **3**, 37.
12 M. Dumortier, S. Tembhurne and S. Haussener, *Energy Environ. Sci.*, 2015, **8**, 3614–3628.
13 B. Seger, O. Hansen and P. C. K. Vesborg, *Solar RRL*, 2017, **1**, e201600013.
14 L. C. Seitz, Z. Chen, A. J. Forman, B. A. Pinaud, J. D. Benck and T. F. Jaramillo, *Chemsuschem*, 2014, **7**, 1372–1385.
15 R. E. Rocheleau and E. L. Miller, *International Journal of Hydrogen Energy*, 1997, 771–782.
16 O. Khaselev and J. A. Turner, *Science*, 1998, **280**, 425.
17 E. Verlage, S. Hu, R. Liu, R. J. R. Jones, K. Sun, C. Xiang, N. S. Lewis and H. A. Atwater, *Energy Environ. Sci.*, 2015, **8**, 3166–3172.
18 M. M. May, H.-J. Lewerenz, D. Lackner, F. Dimroth and T. Hannappel, *Nature Communications*, 2015, **6**, 8286.
19 J. L. Young, M. A. Steiner, H. Döscher, R. M. France, J. A. Turner and T. G. Deutsch, *Nature Energy*, 2017, **2**, 17028.
20 R. J. Britto, J. D. Benck, J. L. Young, C. Hahn, T. G. Deutsch and T. F. Jaramillo, *The Journal of Physical Chemistry Letters*, 2016, **7**, 2044–2049.
21 P. C. K. Vesborg and T. F. Jaramillo, *RSC Advances*, 2012, **2**, 7933.
22 B. Seger, T. Pedersen, A. B. Laursen, P. C. K. Vesborg, O. Hansen and I. Chorkendorff, *Journal of the American Chemical Society*, 2013, **135**, 1057–1064.
23 S. Hu, M. R. Shaner, J. A. Beardslee, M. Lichterman, B. S. Brunschwig and N. S. Lewis, *Science*, 2014, **344**, 1005–1009.
24 B. Mei, T. Pedersen, P. Malacrida, D. Bae, R. Frydendal, O. Hansen, P. C. K. Vesborg, B. Seger and I. Chorkendorff, *The Journal of Physical Chemistry C*, 2015, **119**, 15019–15027.
25 J. H. Montoya, L. C. Seitz, P. Chakthranont, A. Vojvodic, T. F. Jaramillo and J. K. Nørskov, *Nature Materials*, 2016, **16**, 70–81.
26 M. R. Shaner, K. T. Fountaine, S. Ardo, R. H. Coridan, H. A. Atwater and N. S. Lewis, *Energy & Environmental Science*, 2014, **7**, 779–790.
27 L. Han, F. F. Abdi, R. van de Krol, R. Liu, Z. Huang, H.-J. Lewerenz, B. Dam, M. Zeman and A. H. M. Smets, *Chemsuschem*, 2014, **7**, 2832–2838.
28 B. Kaiser, D. Fertig, J. Ziegler, J. Klett, S. Hoch and W. Jaegermann, *ChemPhysChem*, 2012, **13**, 3053–3060.
29 K. Sivula, F. Le Formal and M. Gratzel, *Chemsuschem*, 2011, **4**, 432–449.
30 A. Paracchino, V. Laporte, K. Sivula, M. Gratzel and E. Thimsen, *Nature Materials*, 2011, **10**, 456–461.
31 Y. Lin, C. Battaglia, M. Boccard, M. Hettick, Z. Yu, C. Ballif, J. W. Ager and A. Javey, *Nano Letters*, 2013, **13**, 5615–5618.
32 I. A. Digdaya, L. Han, T. W. F. Buijs, M. Zeman, B. Dam, A. H. M. Smets and W. A. Smith, *Energy & Environmental Science*, 2015, **8**, 1585–1593.
33 E. S. Smotkin, S. Cervera-March, A. J. Bard, A. Campion, M. A. Fox, T. Mallouk, S. E. Webber and J. M. White, *The Journal of Physical Chemistry*, 1987, **91**, 6–8.
34 E. Edri, S. Kirmayer, M. Kulbak, G. Hodes and D. Cahen, *Journal of Physical Chemistry Letters*, 2014, **5**, 429–433.
35 F. Fumagalli, S. Bellani, M. Schreier, S. Leonardi, H. C. Rojas, A. Ghadirzadeh, G. Tullii, A. Savoini, G. Marra, L. Meda, M. Gratzel, G. Lanzani, M. T. Mayer, M. R. Antognazza and F. Di Fonzo, *Journal of Materials Chemistry A*, 2016, **4**, 2178–2187.
36 D. Shin, E. Ngaboyamahina, Y. Zhou, J. T. Glass and D. B. Mitzi, *Journal of Physical Chemistry Letters*, 2016, **7**, 4554–4561.
37 I. E. Castelli, T. Olsen, S. Datta, D. D. Landis, S. Dahl, K. S. Thygesen and K. W. Jacobsen, *Energy Environ. Sci.*, 2012, **5**, 5814–5819.
38 I. E. Castelli, D. D. Landis, K. S. Thygesen, S. Dahl, I. Chorkendorff, T. F. Jaramillo and K. W. Jacobsen, *Energy & Environmental Science*, 2012, **5**, 9034.
39 Y. Wu, P. Lazic, G. Hautier, K. Persson and G. Ceder, *Energy & Environmental Science*, 2012, **6**, 157–168.
40 I. E. Castelli, J. M. Garcia-Lastra, F. Hüser, K. S. Thygesen and K. W. Jacobsen, *New Journal Of Physics*, 2013, **15**, 105026.
41 B. Seger, I. E. Castelli, P. C. K. Vesborg, K. W. Jacobsen, O. Hansen and I. Chorkendorff, *Energy Environ. Sci.*, 2014, **7**, 2397–2413.
42 I. E. Castelli, F. Hser, M. Pandey, H. Li, K. S. Thygesen, B. Seger, A. Jain, K. A. Persson, G. Ceder and K. W. Jacobsen, *Adv. Ener. Mater.*, 2015, **5**, 1400915.
43 I. E. Castelli, K. S. Thygesen and K. W. Jacobsen, *J. Mater. Chem. A*, 2015, **3**, 12343–12349.
44 I. E. Castelli, K. Kuhar, M. Pandey and K. W. Jacobsen, in *Theoretical Modeling of Organohalide Perovskites for Photovoltaic Applications*, ed. G. Giorgi and K. Yamashita, CRC Press, 2017, pp. 1–38.
45 K. Zhang and L. Guo, *Catal. Sci. Technol.*, 2013, **3**, 1672–1690.
46 J. Heo, L. Yu, E. Altschul, B. E. Waters, J. F. Wager, A. ZUNGER and D. A. Keszler, *Chemistry Of Materials*, 2017, **29**, 2594–2598.
47 S. Perera, H. Hui, C. Zhao, H. Xue, F. Sun, C. Deng, N. Gross, C. Milleville, X. Xu, D. F. Watson, B. Weinstein, Y.-Y. Sun, S. Zhang and H. Zeng, *Nano Energy*, 2016, **22**, 129–135.
48 S. Niu, H. Huyan, Y. Liu, M. Yeung, K. Ye, L. Blankemeier, T. Orvis, D. Sarkar, D. J. Singh, R. Kapadia and J. Ravichandran, *Advanced Materials*, 2017, **29**, 1604733.
49 W. Meng, B. Saparov, F. Hong, J. Wang, D. B. Mitzi and Y. Yan, *Chemistry of Materials*, 2016, **28**, 821–829.
50 Y.-Y. Sun, M. L. Agiorgousis, P. Zhang and S. Zhang, *Nano Letters*, 2015, **15**, 581–585.
51 M.-G. Ju, J. Dai, L. Ma and X. C. Zeng, *Advanced Energy Materials*, 2017, **2**, 1700216.
52 G. Kresse and D. Joubert, *Phys. Rev. B*, 1999, **59**, 1758–1775.
53 J. Enkovaara, C. Rostgaard, J. J. Mortensen, J. Chen, M. Dułak, L. Ferrighi, J. Gavnholt, C. Glinsvad, V. Haikola, H. A. Hansen and *et al*, *J. Phys.: Condens. Matter*, 2010, **22**, 253202.
54 S. R. Bahn and K. W. Jacobsen, *Computing in Science and Engineering*, 2002, **4**, 56–66.

55 J. P. Perdew, A. Ruzsinszky, G. I. Csonka, O. A. Vydrov, G. E. Scuseria, L. A. Constantin, X. Zhou and K. Burke, *Phys. Rev. Lett.*, 2008, **100**, 136406.

56 H. J. Monkhorst and J. D. Pack, *Phys. Rev. B*, 1976, **13**, 12.

57 J. Wellendorff, K. T. Lundgaard, K. W. Jacobsen and T. Bligaard, *J. Chem. Phys.*, 2014, **140**, 144107.

58 M. Pandey and K. W. Jacobsen, *Phys. Rev. B*, 2015, **91**, 235201.

59 O. Gritsenko, R. van Leeuwen, E. van Lenthe and E. J. Baerends, *Phys. Rev. A*, 1995, **51**, 1944.

60 M. Kuisma, J. Ojanen, J. Enkovaara and T. T. Rantala, *Phys. Rev. B*, 2010, **82**, 115106.

61 S. Fleming and A. Rohl, *Zeitschrift für Kristallographie - Crystalline Materials*, 2009, **220**, 580–584.

62 A. Crovetto, R. Chen, R. B. Ettlinger, A. C. Cazzaniga, J. Schou, C. Persson and O. Hansen, *Solar Energy Materials and Solar Cells*, 2016, **154**, 121–129.

63 A. Crovetto, A. Cazzaniga, R. B. Ettlinger, J. Schou and O. Hansen, *Thin Solid Films*, 2015, **582**, 203–207.

64 W. Zhang, A. R. Oganov, A. F. Goncharov, Q. Zhu, S. E. Boulfelfel, A. O. Lyakhov, E. Stavrou, M. Somayazulu, V. B. Prakapenka and Z. Konopkova, *Science*, 2013, **342**, 1502–1505.

65 G. Bergerhoff, R. Hundt, R. Sievers and I. D. Brown, *J. Chem. Inf. Comput. Sci.*, 1983, **23**, 66–69.

66 *Inorganic Crystal Structure Database (ICSD)*, `https://icsd.fiz-karlsruhe.de`.

67 *Spglib*, `https://atztogo.github.io/spglib/`, accessed 2017-01-13.

68 K. T. Schütt, H. Glawe, F. Brockherde, A. Sanna, K. R. Müller and E. K. U. Gross, *Physical Review B*, 2014, **89**, 205118.

69 J. J. Mortensen, K. Kaasbjerg, S. L. Frederiksen, J. K. Nørskov, J. P. Sethna and K. W. Jacobsen, *Physical Review Letters*, 2005, **95**, 216401–4.

70 J. E. Saal, S. Kirklin, M. Aykol, B. Meredig and C. Wolverton, *JOM*, 2013, **65**, 1501–1509.

71 W. Zhong, D. Vanderbilt and K. M. Rabe, *Physical Review Letters*, 1994, **73**, 1861.

72 C. E. Patrick, K. W. Jacobsen and K. S. Thygesen, *Physical Review B*, 2015, **92**, 201205.

73 J. A. Brehm, J. W. Bennett, M. R. Schoenberg, I. Grinberg and A. M. Rappe, *Journal Of Chemical Physics*, 2014, **140**, 224703.

74 D. D. Landis, J. S. Hummelshøj, S. Nestorov, J. Greeley, M. Dulak, T. Bligaard, J. K. Nørskov and K. W. Jacobsen, *Computing in Science and Engineering*, 2012, **14**, 51.

75 `https://cmr.fysik.dtu.dk`.

76 `http://nomad-repository.eu`.

77 W. Setyawan and S. Curtarolo, *Comput. Mater. Sci.*, 2010, **49**, 299–312.

78 M. Pandey, F. A. Rasmussen, K. Kuhar, T. Olsen, K. W. Jacobsen and K. S. Thygesen, *Nano Lett.*, 2016, **16**, 2234–2239.

79 F. Gallino, G. Pacchioni and C. Di Valentin, *Journal Of Chemical Physics*, 2010, **133**, 144512.

80 W. Meng, B. Saparov, F. Hong, J. Wang, D. B. Mitzi and Y. Yan, *Chem. Mater.*, 2016, **28**, 821–829.

81 F. Stern, *Solid State Physics*, 1963, **15**, 299–408.

82 D. Carré, J. Flahaut, P. Khodadad, P. Laruelle, N. Rodier and V. Van Tien, *Journal of Solid State Chemistry*, 1973, **7**, 321–336.

83 C. Yan, K. Sun, J. Huang, S. Johnston, F. Liu, B. P. Veettil, K. Sun, A. Pu, F. Zhou, J. A. Stride, M. A. Green and X. Hao, *ACS Energy Letters*, 2017, **2**, 930–936.

84 A. Cazzaniga, A. Crovetto, C. Yan, K. Sun, X. Hao, J. Ramis Estelrich, S. Canulescu, E. Stamate, N. Pryds, O. Hansen and J. Schou, *Solar Energy Materials and Solar Cells*, 2017, **166**, 91–99.

85 R. Mauricot, J. Dexpert-Ghys and M. Evain, *Journal of Luminescence*, 1996, **69**, 41–48.

5.4 Paper IV: High-Throughput Computational Assessment of Previously Synthesized Semiconductors for Photovoltaic and Photoelectrochemical Devices.

The publication is in preparation.

High-Throughput Computational Assessment of Previously Synthesized Semiconductors for Photovoltaic and Photoelectrochemical Devices.

Korina Kuhar,[†] Mohnish Pandey,[†] Kristian S. Thygesen,[†,‡] and Karsten W. Jacobsen[*,†]

†*Computational Atomic-scale Materials Design (CAMD), Department of Physics, Technical University of Denmark, DK - 2800 Kongens Lyngby, Denmark*

‡*Center for Nanostructured Graphene (CNG), Department of Physics, Technical University of Denmark, DK - 2800 Kongens Lyngby, Denmark*

E-mail: kwj@fysik.dtu.dk

Abstract

Using computational screening we identify materials with potential use as light absorbers in photovoltaic or photoelectrochemical devices. The screening focuses on compounds of up to three different chemical elements, which are abundant and non-toxic. A prescreening is carried out based on information from the ICSD and OQMD databases. The light absorption, carrier mobility, defect tolerance, and stability of the materials are assessed by a set of simple computational descriptors. The identified 74 materials include a variety of pnictogenides, chalcogenides, and halogenides. Several recently investigated light absorbers such as $CsSnI_3$, $CsSnBr_3$, and $BaZrS_3$ appear on the list.

Introduction

The increasing demand for energy to supply the growing human population has led to large-scale consumption of fossil fuels. As a result, the emission of greenhouse gases into the atmosphere is having detrimental effects on the environment. Therefore, it is an urgent requirement to explore fossil-free energy resources. One of the most promising such resources is the solar energy. Although, solar energy may not be able to fully substitute the fossil fuels in the near future, it has the potential to alleviate the environmental problems if used at a global scale. There are numerous ways to harvest the solar energy, to name a few; photovoltaics (PV), photoelectrochemical (PEC) generation of hydrogen or other chemicals, and thermal fuels.[1–5] These technologies are still not fully developed and significant efforts are required for their large-scale deployment.

Solid-state PV and PEC processes rely on materials which absorb the solar photons, generate electrons and holes, and conduct them to surfaces to participate in chemical processes or deliver electric current. For a material to work in a reasonable way, these processes must all be carried out efficiently. The PV technology relies predominantly on silicon as an absorber[6–8] in addition to a few other semiconductors such as GaAs, CdTe, InP, GaInP, CIGS

and hybrid perovskites.[6,7,9–11] The deployment of PV technology is rapidly growing, while the PEC technology has not been realized yet mainly due to the lack of materials which can efficiently harvest visible light and use the generated electron-hole pair to for example split water. However, numerous materials have been explored for PEC, to name a few; TiO_2, CdS, Bi_2S_3, Sb_2S_3,WO_3, ZnO and Fe_2O_3.[12,13] Despite numerous attempts, an analog of silicon for PEC has not been found yet. In order to address the challenges hampering the PEC technology alternative strategies are continuously being explored. One such strategy is to integrate existing silicon PV devices into PEC units. In these “tandem" devices two semiconductors with different band gaps (one of them being for example the silicon) are used as photoanode and photocathode, each conducting one half of the water-splitting reaction.[14–16]

Despite the considerable research efforts the number of semiconductors, which have been explored for PV or PEC, is still small compared to the number of semiconductors, which have been synthesized. Therefore, a systematic investigation of the properties of already known semiconductors may reveal new interesting materials for PV or PEC application. However, performing experimental investigation of all relevant properties for thousands of materials is a daunting task, and this is where computational screening approaches may play a role.

In the past few years, publicly available databases with calculated properties of hundreds of thousands of materials have been established.[17–23] However, some of the properties like band gaps or charge carrier effective masses, which are relevant to PV and PEC applications, are either not reported or the reported values are not very accurate due to limitations of the methods used. In the present work, we use the data reported in the Open Quantum Materials Database (OQMD)[17,18] and then take a step further to calculate relevant electronic properties of already synthesized materials. The criteria we use to screen the materials are based on the toxicity and abundance of constituent elements, thermodynamic stability, band gap in the visible spectrum, high charge carrier mobility, and small tendency of the materials to exhibit defect-mediated mid-gap states in the band gap. Based on the criteria, we suggest new candidates which can potentially act as PV and PEC light absorbers.

Computational Details

The electronic structure calculations are performed using Density Functional Theory (DFT) in the Projector Augmented Wave (PAW) formalism[24] as implemented in the electronic structure code GPAW[25,26] with the ASE interface.[27,28] The wave functions, electron density and the effective potential are expanded on a real space grid with a grid spacing of 0.18 Å. The sampling of the Brillouin zone is performed using the Monkhorst-Pack scheme.[29] The k-point density is chosen to be 5 points $Å^{-1}$, and finer k-point meshes are adopted for the calculation of band structures and effective masses. The band gaps and band structures are calculated using the more accurate semi-local Gritsenko, van Leeuwen, van Lenthe and Baerends potential (GLLB) improved for solids (-SC) potential which includes an explicit estimation of the derivative discontinuity.[30,31] The GLLB-SC functional with similar computational cost as the other semi-local functionals predicts band gaps which are quite close to the predictions of more computationally demanding many-body-perturbation-theory calculations and hybrid functionals.[32] Spin-orbit coupling was included in the calculations for materials containing elements with atomic number (Z) higher than 56. Investigation of defect properties was done with the PBE exchange correlation functional.[33]

Results and Discussion

The Inorganic Crystal Structure Database[34] is a library of over 180000 inorganic compounds, where most of the compounds have been experimentally synthesized. The OQMD database is a computational materials database, which contains information about a large fraction of the crystal structures present in the ICSD. In the following we shall take as the starting point the materials in OQMD which originates from the ICSD. This limitation to the materials that appear in both ICSD and OQMD has several advantages: 1) As mentioned by-far most of the materials in ICSD have been synthesized, so this means that they can be considered stable or at least meta-stable. We do therefore not investigate material stability any further

in the screening process, which saves considerable computer time. However, in the final stage of the screening we return to the stability issue, because some of the compounds have been synthesized only under extreme conditions. 2) In ICSD many materials appear several times as duplicates, but these have been removed in the OQMD. 3) The materials in OQMD have already been structurally optimized within the DFT framework using the PBE functional so that atomic forces and stresses vanish. This is convenient for further computational investigation. 4) Several properties like the band gaps of the compounds have already been calculated at the PBE-level, which we shall also exploit.

The initial download from the OQMD contained 28,566 compounds to be considered [1]. These compounds are uniquely identified by their ICSD numbers, which are also provided in the OQMD database. We shall here limit ourselves to compounds of up to three elements of which there are 22,807.

We now begin a screening funnel, where we gradually remove compounds, which do not seem promising according to a list of criteria. The first step in the funnel is to restrict ourselves to compounds, which are made of only abundant and non-toxic elements for which an open market exists. We use the analysis by Gaultois *et al.*,[35] which is based on the crustal abundance of the elements and the so-called Herfindahl-Hirschman index (HHI) as a measure of the concentration or monopoly-character of the resources and the market. A priority list of elements based on these criteria are shown in Figure 1 and the resulting elements are also indicated in blue in the table of elements in Figure 2.

The abundance and toxicity criteria for the elements lead to a reduction in the number of compounds from 22,807 to 7,241. In the next step in the screening funnel we benefit from the fact that the Kohn-Sham band gaps have already been calculated and reported in the OQMD database using the PBE functional. It is well known that band gaps calculated with the PBE are severely underestimated, so we therefore use these band gaps only in a semi-quantitative way. We first discard all compounds without a PBE band gap, i.e the compounds which

[1] We acquired the dataset from the OQMD database around October 2014. At that time the ICSD-entries in the OQMD included systems with up to 35 atoms in the primitive unit cell.

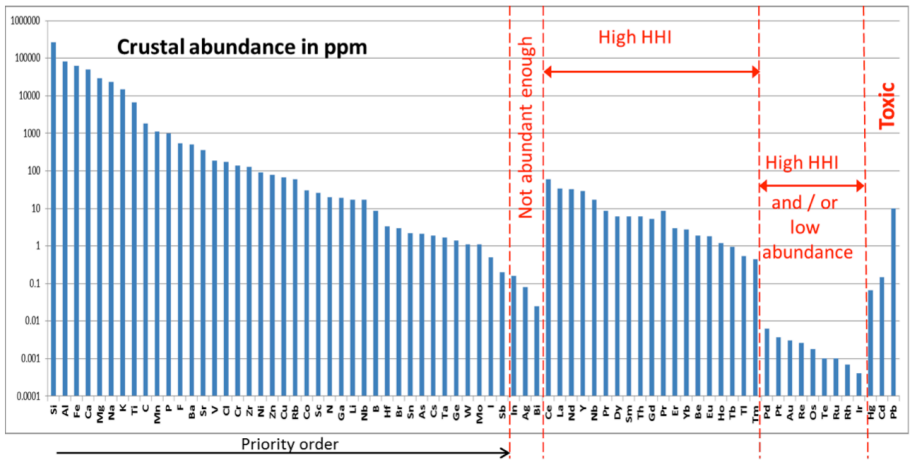

Figure 1: The list of elements to be considered in the screening study based on crustal abundance and the Herfindahl-Hirschman index (HHI).[35]

according to PBE are metallic. It should be noted that some compounds, for example several oxides, are in reality semiconductors or insulators despite a vanishing PBE band gap because of strong correlation effects. Such compounds are therefore not included in the screening. Additionally, we exploit the underestimation of the PBE band gaps to discard materials which have PBE band gaps higher than 2.0 eV. The optimal band gap for single junction PV devices is $\sim$1 eV, which we shall refer to as a small band gap (SBG), whereas the tandem devices require for their large band gap component (LBG) a band gap of $\sim$2.0 eV.[16] This leads us to focus on materials with band gaps between 0.5 eV and 2.5 eV. It is quite unlikely that a material with a PBE band gap of more than 2 eV does in fact have an experimental band gap of less than 2.5 eV, so these materials are discarded. The number of candidate materials is reduced to 1630 by this step. The procedure is schematically shown in Figure 2.

We now move on to consider a proper evaluation of the band gaps of the materials. As mentioned above, the PBE functional severely underestimates the band gaps and cannot therefore be used for realistic prediction. The underestimation has two reasons: the first is that PBE is only a crude approximation to the exact DFT functional, and the second is that the Kohn-Sham gap does not agree with the true fundamental band gap even with the exact functional. The so-called GLLB-SC functional improves on both of these problems.[30,31] It has an improved Kohn-Sham potential compared to semi-local functionals like PBE, leading to more correct Kohn-Sham band gaps, and it includes an explicit evaluation of the so-called derivative discontinuity, which corrects the Kohn-Sham gap to obtain the fundamental gap. The GLLB-SC functional gives a reasonable estimate of the band gaps within $\approx 0.3 - 0.5$ eV as demonstrated in previous work with comparisons to experiment and to G_0W_0 and HSE06 calculated band gaps.[32]

The GLLB-SC functional has convergence issues and maybe also more fundamental problems for magnetic systems, and we therefore concentrate on the spin-paired semiconductors. This reduces the number of candidate materials from 1,630 to 929. This is a significant re-

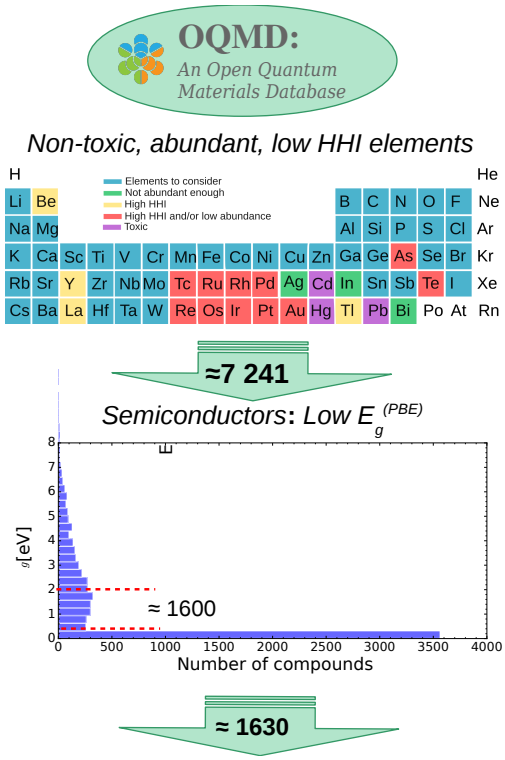

Figure 2: Flow of data selection process: Entries are extracted from the OQMD database (22,807 that originate from the ICSD with up to three elements), only entries containing non-toxic, abundant and low HHI elements are to be considered further. Furthermore, the number of candidates is additionally decreased by selecting only semiconducting materials with 0 eV$< \mathrm{E}_g^{PBE} \leq 2$ eV, containing up to three elements resulting in 1,630 candidates.

duction and it would be interesting in future work to investigate also the 701 spin-polarized compounds. In Figure 3(a) we show the GLLB-SC calculated values of the band gaps versus the PBE band gaps. The figure clearly shows that the GLLB-SC band gaps are larger than the PBE calculated values in most cases and that it is unlikely that materials with a PBE band gap above 2 eV could have a GLLB-SC band gap in the relevant range. Based on the GLLB-SC predicted band gaps we identify 323 LBG and 195 SBG materials for further consideration.

Efficient transport of the generated charge carriers after light absorption is required for low losses in a PV/PEC material. The losses mainly arise due to recombination of charge carriers, which can potentially be prevented if the charges separate and move apart fast enough after their generation. Therefore, high mobilities are a prerequisite for efficient charge transport and should dampen the losses due to recombination. Several mechanisms can limit the carrier mobilities including scattering by phonons, electrons, or defects, but direct calculation of the scattering times associated with these different mechanism is difficult and computationally demanding in particular for large systems. However, independent of the scattering mechanism and the scattering life time, the mobilities are inversely proportional to the effective charge carrier masses, and we shall therefore use the effective electron and hole masses as descriptors for the mobilities.

The carrier effective masses are obtained by fitting a parabola to the top of the valence band and bottom of the conduction band of the band structure. The band structures are calculated along the high-symmetry band path as suggested by Setyawan and Curtarolo.[36] At high-symmetry points where the band path changes directions, parabolic fits are made on both sides of the symmetry point. We choose an upper limit for both the effective electron and hole masses to be one standard electron mass. Figure 3 (b) shows a combined histogram of all the materials with band gaps in the relevant range (green) and the ones with low effective masses (blue). This step decreases the number of materials from 518 (with appropriate band gap) to 222 materials, which additionally satisfy the criterion for the

effective mass.

Figures4 and 5 show the band gaps of the binary and ternary PV and PEC materials satisfying the criteria introduced so far. The selection process so far identifies several materials which are well-known light absorbers such as ZnS, ZnS_2, FeS_2, $CsSnI_3$ and, $ZnSiP_2$. This, to some extent, validates our approach. At the end of the screening process, we shall consider other well-known light absorbers, which do not appear as candidates and discuss the reasons for this.

The final step in the screening funnel takes defect properties into account. Defects can be detrimental to the performance of semiconductors as PV/PEC materials. For example, the defects present in FeS_2 act as recombination centers, which severely deteriorates its performance.[37] Generally, presence of different defects like vacancies, substitutional defects, and impurities may give rise to new electronic states in the band gap, which reduces the photo-absorption or they act as recombination centers.[38] The materials exhibiting this kind of behavior are commonly termed "defect-sensitive", whereas semiconductors which only show nominal change in their electronic structure upon introducing defects are termed "defect-tolerant".[38–40]

In the following we aim to identify the defect-tolerant materials by explicit calculation of the electronic structure in the presence of defects. Ideally, defect calculations require large supercells with different charge state along with careful incorporation of electrostatic corrections to the electronic structure and energies.[41–45] However, such accurate defect calculations are computationally too demanding for a screening study like the present one, and, furthermore, we are not aiming to study defect properties in detail, but only to determine whether a given material is defect tolerant or not.

We limit ourselves to study vacancy defects in their neutral states by creating one defect in repeated 2×2×2 (or 3×3 ×3 if the pristine unit cell was smaller than 5 atoms) supercells. Vacancies for all the constituent elements are investigated. The density of states (DOS) is then calculated in the defect supercell without relaxing the atomic structure after defects

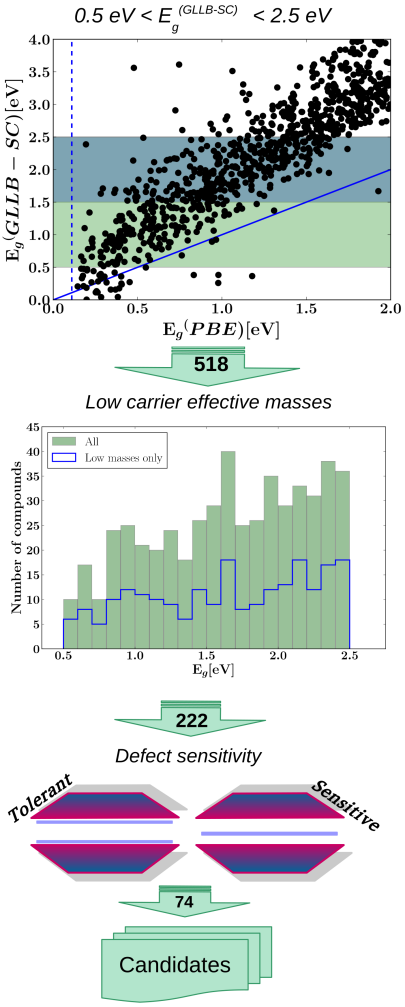

Figure 3: Schematic view of the step-wise inclusion of new descriptors. a) Selecting materials with the GLLB-SC calculated band gaps in the range between 0.5 and 2.5 eV. The plot shows the GLLB-SC band gaps versus the PBE band gaps. The blue and green striped areas show the HBG and LBG regions, respectively. b) Selection of the compounds with the carrier effective masses less than one standard electron mass. The histogram of the band gaps of the materials before and after applying the criterion for the effective mass. c) Selection of the defect tolerant materials. Defect tolerance refers to the situation when no mid gap states in the band structure arise as a result of presence of point defects in the crystal. Numbers written on the arrows represent the number of candidates in each step.

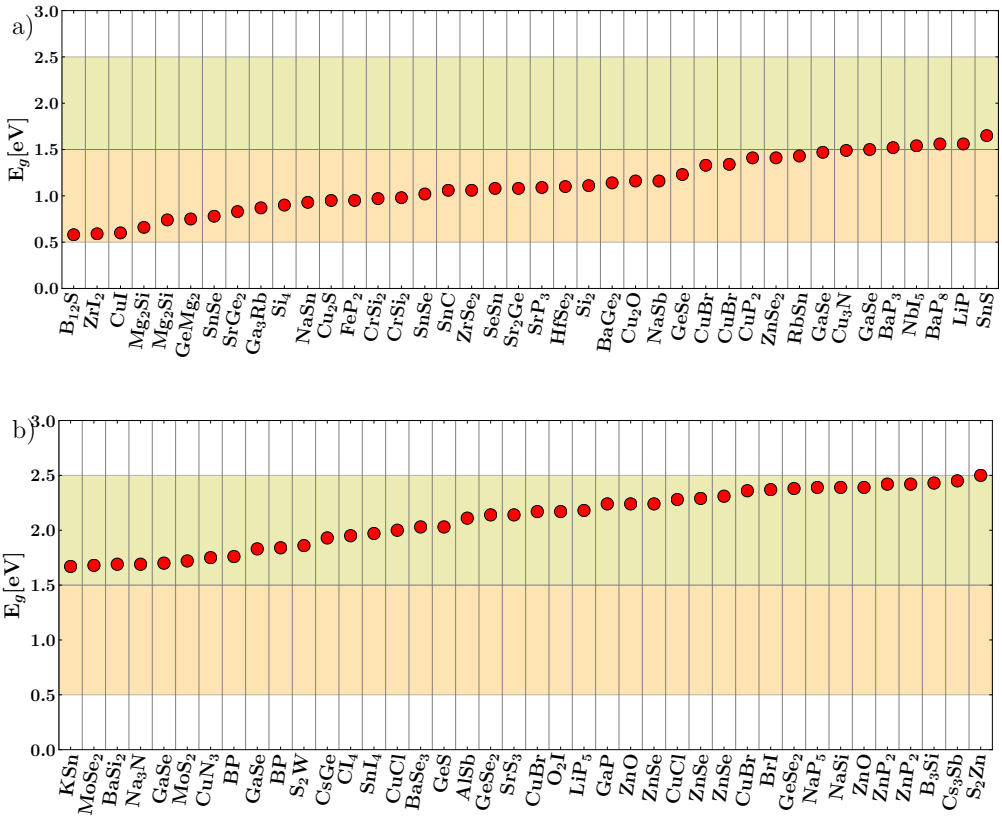

Figure 4: Calculated band gaps of binary systems satisfying the screening criteria for abundance, non-toxicity, light absorption, and mobility. Orange and yellow areas represent LBG and HBG regions, respectively. Table with numerical values and ICSD codes can be found in the supplementary material.

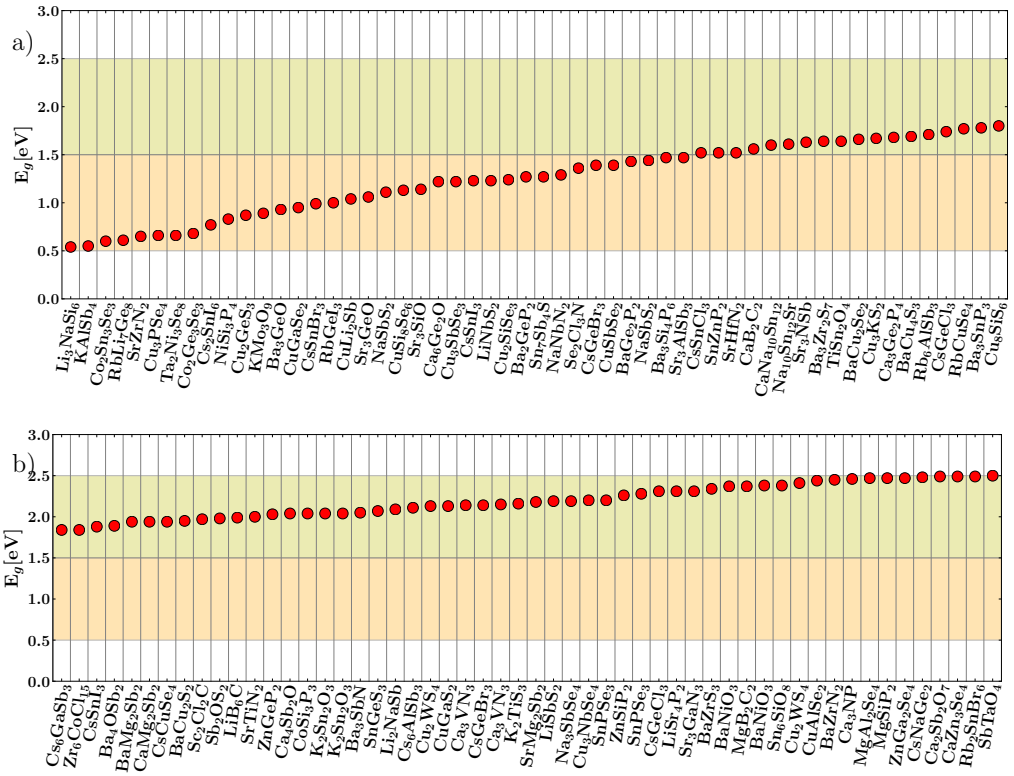

Figure 5: Calculated band gaps of ternary systems satisfying the screening criteria for abundance, non-toxicity, light absorption, and mobility. Orange and yellow regions represent LBG and HBG regions, respectively. Table with numerical values and ICSD codes can be found in the supplementary material.

are introduced. The calculations are performed using the LCAO-mode of GPAW with a dzp basis set.[46] If the resultant DOS resembles the DOS of the pristine structure i.e. there are no mid-gap states in the band gap (or only shallow states near the band edges), we consider the material as defect-tolerant. This approach does not rule out that other kinds of defects can in fact harm the photoelectric performance, but at least it removes from the screening funnel the ones where the vacancies lead to mid-gap states.

This completes the screening funnel and the resulting candidates are shown in Table 1. In the following we shall discuss these materials and some of their properties in more detail.

Table 1: Final list of suggested PV and PEC candidates including the calculated band gaps and effective masses, and, if available, experimental band gaps. The energies of the compounds with respect to the convex hulls ΔH_{hull} (eV/atom) are also reported. A large positive value of ΔH_{hull} implies that the compound may not be stable under normal conditions. Compounds with $\Delta H_{hull} > 0.05$ eV are shown in parenthesis. The corresponding ICSD numbers of all the compounds are provided in Table 1 of the Supplementary Information. For the compounds labelled by asterisks the investigations of defect sensitivities are inconclusive, because the PBE/LCAO gaps are too narrow to allow for a clear distinction between mid-gap and shallow states.

Formula	$E_g^{GLLB-SC}$	$E_{g(direct)}^{GLLB-SC}$	m^*_h	m^*_e	$E_g^{exp.}$	ΔH_{hull}
Al_2MgSe_4*	2.47	2.47	0.379	0.211	-	0.01
$(B_{12}S)$*	0.58	0.75	0.401	0.294	-	0.41
Ba_3P_4	1.07	1.07	0.945	0.974	1.6[47]	0.00
Ba_3SbN	2.05	2.05	0.181	0.247	-	0.00
Ba_5Sb_4	0.94	1.27	0.661	0.361	-	0.00
Ba_4SnP_4	1.78	1.79	0.318	0.471	-	0.01
BaCaSn	0.88	0.88	0.339	0.73	-	0.00
BaLiP	1.98	1.98	0.161	0.161	-	0.00
$BaZrN_2$	2.45	2.45	0.38	0.277	-	0.00
$BaZrS_3$	2.34	2.34	0.351	0.425	1.8[48,49]	0.00
Ca_3NP	2.46	2.46	0.206	0.288	-	0.00

Continued on next page

Table 1 – continued from previous page

Formula	$E_g^{GLLB-SC}$	$E_{g(direct)}^{GLLB-SC}$	m^*_h	m^*_e	$E_g^{exp.}$	ΔH_{hull}
CaLiSb	1.36	1.36	0.132	0.404	-	0.00
Cs_2SnI_6*	0.77	0.77	0.835	0.256	1.3 [50]	0.00
Cs_3Sb	2.45	2.75	0.758	0.232	1.6(300K) [51]	0.00
Cs_6AlSb_3	2.11	2.21	0.906	0.276	-	0.00
Cs_6GaSb_3	1.84	1.94	0.99	0.289	-	0.00
$CsCuSe_4$	1.94	2.01	0.475	0.256	-	0.00
CsGe Cl_3	2.31	2.31	0.268	0.285	-	0.00
$CsNaGe_2$	2.48	2.51	0.353	0.506	-	0.00
$CsSnBr_3$	0.99	0.99	0.089	0.078	1.26 [52]	0.00
$CsSnI_3$ (B)	1.23	1.23	0.104	0.061	1.3 (GW 1.3) [53,54]	0.00
$CsSnI_3$	1.88	1.88	0.121	0.094	-	0.00
(CuI)	0.6	1.39	0.706	0.362	-	0.07
(Cu_3N)	1.49	2	0.236	0.207	1.5 [55]	0.24
Cu_2S	0.95	0.95	0.259	0.153	1.2 [51]	0.01
Cu_3SbSe_3	1.22	1.27	0.522	0.438	1.68 [56]	0.03
Cu_8SiSe_6	1.13	1.15	0.464	0.189	1.33 [57]	0.05
Cu_2GeS_3	0.87	0.87	0.26	0.157	-	0.00
Cu_2O	1.16	1.16	0.251	0.776	2.17 [51]	0.00
Cu_3KS_2	1.67	1.74	0.359	0.395	-	0.00
$CuAlSe_2$	2.44	2.44	0.217	0.156	-	0.00
$CuGaS_2$	2.13	2.13	0.234	0.187	2.53 [58]	0.00
CuKSe*	1.44	1.44	0.103	0.131	-	0.00
$CuSbSe_2$	1.39	1.59	0.77	0.557	1.2 [59]	0.00
Ga_2Se_3	2.02	2.02	0.214	0.164	1.9 [51]	0.00
Hf_3N_4	2.39	2.39	0.27	0.372	1.8 [60]	0.00
K_2P_3	1.89	1.91	0.786	0.993	-	0.00

Continued on next page

Table 1 – continued from previous page

Formula	$E_g^{GLLB-SC}$	$E_{g(direct)}^{GLLB-SC}$	m^*_h	m^*_e	$E_g^{exp.}$	ΔH_{hull}
$K_2Sn_2O_3$	2.04	2.04	0.222	0.15	-	0.00
KMo_3O_9	0.89	0.96	0.965	0.639	-	0.00
KZnSb*	0.88	1.01	0.061	0.089		0.01
Li_2NaSb	2.09	3.38	0.131	0.24	-	0.00
Li_3NaSi_6	0.54	0.6	0.314	0.412	-	0.00
LiP	1.56	1.84	0.424	0.578	-	0.00
LiSrN*	1.64	2.19	0.916	0.276	-	0.00
LiSrP	2.29	2.59	0.375	0.653	-	0.00
LiZnN	1.52	1.52	0.128	0.163	1.9[61,62]	0.00
Mg_2Si*	0.66	0.66	0.192	0.574	-	0.00
Mg_3Sb_2*	1.1	1.91	0.103	0.231	1.1[63]	0.00
Mg_2Ge	0.75	1.67	0.084	0.219	0.74[51]	0.00
NaBaP	2.22	2.22	0.209	0.25	-	0.00
$NaNbN_2$*	1.29	1.94	0.23	0.523	-	0.00
NbI_5	1.54	1.59	0.853	0.372	-	0.00
O_2I	2.17	2.69	0.721	0.771	-	0.02
Rb_2SnBr_6	2.49	2.49	0.816	0.368	-	0.00
Rb_6AlSb_3	1.71	1.79	0.95	0.239	-	0.00
$RbGeI_3$	1	1	0.088	0.07	-	0.03
$RbLi_7Ge_8$*	0.61	0.67	0.708	0.476	-	0.00
RbSn	1.43	1.43	0.624	0.281	-	0.00
$SnPSe_3$	2.2	2.33	0.724	0.675	-	0.00
Sr_2Ge	1.08	1.08	0.125	0.606	-	0.00
Sr_3 $AlSb_3$	1.47	1.47	0.586	0.443	-	0.00
Sr_3GaN_3	2.31	2.37	0.625	0.266	-	0.00
Sr_3GeO	1.06	1.06	0.103	0.168	-	0.00

Continued on next page

Table 1 – continued from previous page

Formula	$E_g^{GLLB-SC}$	$E_{g(direct)}^{GLLB-SC}$	m^*_h	m^*_e	$E_g^{exp.}$	ΔH_{hull}
Sr_3SbN	1.63	1.63	0.192	0.184	1.15[64]	0.00
Sr_3SiO	1.14	1.14	0.144	0.188	-	0.00
$SrGe_2$	0.83	1.01	0.518	0.482	-	0.00
SrS_3	2.14	2.14	0.936	0.706	-	0.00
$SrZrN_2$	0.65	1.31	0.259	0.319	-	0.00
(ZnS_2)	2.5	2.83	0.474	0.456	2.5 (2.7 GW)[65]	0.08
$(ZnSe_2)$	1.41	1.65	0.204	0.568	$1.56G_0W_0$,1.7GW[65]	0.15
Zr_3N_4	2.13	2.13	0.316	0.379	2.1-2.3[66]	0.05
ZrI_2*	0.59	0.71	0.907	0.373	0.1[67]	0.00
ZrNI*	0.92	0.92	0.287	0.365	-	0.00
$ZrSe_2$*	1.06	1.91	0.285	0.284	1.2,1.6[68]	0.00

However, before doing so, we shall return to the issue of material stability. By far, most of the materials in ICSD have been experimentally synthesized and can therefore be regarded as stable or at least meta-stable. However, some of the materials are synthesized under extreme conditions of pressure or temperature and are therefore not necessarily stable under normal conditions. These materials might therefore decompose into competing phases, which are more stable. This issue can be assessed by the convex hull construction from the formation energies. The convex hull value at a given chemical composition is obtained by minimizing the linear combination of energies of all possible phases constrained to the given composition. If the compound lies significantly above the hull it is an indication of a potential problem with the stability under normal conditions. This might be due to high pressure/temperature synthesis, but can also be caused by other problems with the ICSD entry.

The relative stabilities, ΔH_{hull}, of the compounds with respect to the convex hull are shown in 1. The data are obtained directly from the OQMD database. If ΔH_{hull} is zero for a particular compound, then the compound is most likely stable under normal conditions

whereas a large positive value imply possible instability. The compounds with ΔH_{hull} above 50 meV are shown in parenthesis. For example is CuI in a high-pressure phase, while both $B_{12}S$ and Cu_3N have warnings associated with them in the ICSD indicating a potential problems with the crystal determination for these compounds.

Some of the candidates reported in Table 1 have been previously explored for different applications. For example, Cs_3Sb has been investigated experimentally and theoretically as a photocathode.[69–71] We note that De'Munari et al.[72] report a phase transition occurring at around 260 K which could explain the mismatch between the calculated (2.45 eV) and the experimental (1.6 eV at 300K[51]) band gap values for this particular compound. Furthermore, Wu *et al.* explored Cu_2S nanocrystals for PV application[73] whereas Cu_3SbSe_3 and LiBC have been explored as potential thermoelectric and high temperature superconductor, respectively.[56,74–77] Cu_2O has been investigated both in a PV[78] and PEC[79] context. Additionally, attempts have been made to make solar cells out of the ternary compounds of copper, $CuSbSe_2$ and Cu_8Se_6Si.[57,80]

A few of the identified perovskites have been explored actively in recent years. For example, we find $CsSnBr_3$ and $CsSnI_3$ as PV semiconductors having the band gap of $\sim$1.3 eV.[52,81] However, the poor stability of $CsSnX_3$ perovskites in moisture or air prevents them from being used as absorbers in PV devices. However, recent suggestions to improve the air stability of the above mentioned perovskites propose Cs_2SnI_6 as a derivative of $CsSnI_3$ which in addition to having improved stability also has high absorption coefficient;[82] we also find Cs_2SnI_6 as one of the possible PV candidates. Two phases of $CsSnI_3$ satisfy the criteria: the orthorhombic so called 'black' phase (1.32 eV band gap) and the tetragonal phase (1.88 eV band gap). However, the most stable $CsSnI_3$ phase, the orthorhombic 'yellow' phase, was not part of the study due to a too high PBE band gap (experimental band gap is 2.6 eV[83]).

In addition to the halogen perovskites, the chalcogen perovskite $BaZrS_3$ has been explored intensively in the last few years as a possible high band gap absorber for water splitting with a band gap of 1.8 eV.[48,84] As 1 shows, the screening also identifies $BaZrS_3$ as a potential

candidate for PEC application.

Table 2: Calculated properties of known solar energy conversion materials.

Formula	$E_g^{GLLB-SC}$	$E_{g(direct)}^{GLLB-SC}$	m^*_h	m^*_e	$E_g^{exp.}$	defect tolerant
CdSe	1.52	1.52	0.093	0.103	1.73	no
CdTe	1.59	1.59	0.080	0.096	1.43	no
GaAs	0.85	0.85	0.039	0.049	1.42	yes
GaP	2.57	2.81	0.095	0.144	2.3	no
GaInP	1.78	1.78	0.099	0.126	1.81[9]	no
Si	1.11	3.06	0.108	0.559	1.12	no
$CuInSe_2$	1.45	1.45	0.191	0.114	1.01	yes
$BiVO_4$	3.71	3.71	0.463	0.577	2.4-2.5[85]	no

The above discussion shows that a few relevant descriptors when used in conjunction lead to a tremendous reduction in the materials space, and that several already known promising materials result from the screening. This provides some credibility to the approach. To shed further light on the screening procedure we now briefly discuss a small set of already known PV and PEC materials, which do not appear on the list, and their descriptor values. The materials we consider are Si, GaAs, CdTe, CdSe, GaP, $CuInSe_2$ and $BiVO_4$.

The calculated band gaps and effective masses for these materials are shown in Table 2. They all have energy gaps in either the PV or PEC region in reasonable agreement with experimental values, except for GaP and $BiVO_3$. The band gap of GaP exceeds the 2.5 eV limit by only 0.07 eV, while the discrepancy between the calculated and experimental band gaps for $BiVO_3$ is of the order 1 eV. Wiktor *et al.*[86] have studied the electronic properties of $BiVO_3$ in great detail and find that for this particular material the thermal and zero-point fluctuations lead to a very significant reduction of the calculated band gap by as much as 0.6 - 0.9 eV bringing the calculated gap in considerably better agreement with the experimental value. However, calculation of the thermal effects involve a very time-consuming simulation, which cannot be performed for all compounds in a screening study. All of the effective masses are below the limit of one electron mass used in the screening.

Most of the materials in Table 2 are removed from the screening funnel already at the first step, because As, Bi, Cd, In, and Te are not on the list of accepted chemical elements.

GaP is removed because of the band gap slightly above 2.5 eV and would also otherwise have been removed because of defect sensitivity. Last but not least silicon is removed because of defect sensitivity.

Conclusions

In this work we have focussed on identifying light-absorbing materials for PV and PEC applications taking already synthesized semiconductors of up to three different elements as presented in ICSD as a starting point. Using a set of simple descriptors in a screening funnel the number of compounds is reduced to only 74 candidate materials.

It should be noted that even though the number of semiconductors considered here is measured in the thousands, it still only represents a small fraction of the full space of stable or meta-stable materials. The rather brute-force approach used here, where in principle all materials are investigated, cannot be expected to be applicable to the much larger space of available materials. New approaches based on statistical learning will have to be developed in order to efficiently scan many different crystal structures with different compositions to test for stability.

The descriptors applied in the present work also need to be refined and new descriptors have to be developed for high-throughput screenings. The calculations of the band gaps presented here have rather large uncertainties associated with them, and it is a real challenge to include for example thermal effects as discussed in the case of $BiVO_3$. Furthermore, the band gap itself is only a rough measure of the light absorption properties and even though more sophisticated approaches like time-dependent DFT and the Bethe-Salpeter equations exist, they are still too computationally time-consuming to be applied to many thousand materials.

Defects and interfaces play a major role in optoelectronic device performance, and the present study only addresses the defect issue at the most basic level. Only vacancy defect

are studied and only at the level of semi-local functionals. Many other intrinsic defects can be of importance and a more accurate determination of electronic levels in the band gap require treatments at the non-local DFT or GW level.

Any screening study potentially includes both false-positives and true-negatives and the present study is no exception. There could be many reasons that a material appearing in Table 1, would not work optimally in a real device. However, we think that materials not appearing in the list hardly can be expected to be well-functioning. There might be a few "outliers" where the descriptors fail, but in general the descriptors are conservative. If, for example, the band gap is not in the proper range poor performance can be expected. Similarly if the carrier masses are large, the mobility is expected to be limited and charge extraction will be difficult.

Acknowledgement

Discussions with Gilles Dennler and Andrea Crovetto are gratefully acknowledged. The authors acknowledge VILLUM FONDEN for financial support with research grant number 9455. The Center for Nanostructured Graphene is sponsored by the Danish National Research Foundation, Project DNRF103.

References

(1) Vayssierres, L. *On Solar Hydrogen and Nanotechnology*; John Wiley and Sons (Asia) Pvt. Ltd, 2009.

(2) Chamberlain, G. Organic Solar Cells: A Review. *Sol. Cells* **1983**, *8*, 47–83.

(3) Ni, M.; Leung, M. K.; Leung, D. Y.; Sumathy, K. A Review and Recent Developments in Photocatalytic Water-splitting Using TiO_2 for Hydrogen Production. *Renewable Sustainable Energy Rev.* **2007**, *11*, 401 – 425.

(4) Schmidt-Mende, L.; Fechtenkötter, A.; Müllen, K.; Moons, E.; Friend, R. H.; MacKenzie, J. D. Self-Organized Discotic Liquid Crystals for High-Efficiency Organic Photovoltaics. *Science* **2001**, *293*, 1119–1122.

(5) Kolpak, A. M.; Grossman, J. C. Azobenzene-Functionalized Carbon Nanotubes As High-Energy Density Solar Thermal Fuels. *Nano Lett.* **2011**, *11*, 3156–3162.

(6) Green, M. A. Thin-film solar cells: review of materials, technologies and commercial status. *Journal of Materials Science: Materials in Electronics* **2007**, *18*, 15–19.

(7) Green, M. A.; Emery, K.; Hishikawa, Y.; Warta, W.; Dunlop, E. D. Solar cell efficiency tables (Version 45). *Progress in Photovoltaics: Research and Applications* **2015**, *23*, 1–9, PIP-14-274.

(8) Glunz, S. W.; Preu, R.; Biro, D. In *Comprehensive Renewable Energy*; Sayigh, A., Ed.; Elsevier: Oxford, 2012; pp 353–387, DOI: 10.1016/B978-0-08-087872-0.00117-7.

(9) Polman, A.; Knight, M.; Garnett, E. C.; Ehrler, B.; Sinke, W. C. Photovoltaic materials: Present efficiencies and future challenges. *Science* **2016**, *352*, aad4424.

(10) Kayes, B. M.; Nie, H.; Twist, R.; Spruytte, S. G.; Reinhardt, F.; Kizilyalli, I. C.; Higashi, G. S. *27.6 percent Conversion efficiency, a new record for single-junction solar cells under 1 sun illumination*; 2011 37th IEEE Photovoltaic Specialists Conference, 2011.

(11) First Solar Achieves Efficiency, Durability Milestones (NASDAQ:FSLR). `http://investor.firstsolar.com/releasedetail.cfm?ReleaseID=895118`.

(12) Walter, M. G.; Warren, E. L.; McKone, J. R.; Boettcher, S. W.; Mi, Q.; Santori, E. A.; Lewis, N. S. Solar Water Splitting Cells. *Chemical Reviews* **2010**, *110*, 6446–6473.

(13) Li, Y.; Zhang, J. Hydrogen generation from photoelectrochemical water splitting based on nanomaterials. *Laser & Photonics Reviews* **2010**, *4*, 517–528.

(14) Zhang, K.; Ma, M.; Li, P.; Wang, D. H.; Park, J. H. Water Splitting Progress in Tandem Devices: Moving Photolysis beyond Electrolysis. *Advanced Energy Materials* **2016**, *6*, n/a–n/a.

(15) Brillet, J.; Yum, J.-H.; Cornuz, M.; Hisatomi, T.; Solarska, R.; Augustynski, J.; Graetzel, M.; Sivula, K. Highly efficient water splitting by a dual-absorber tandem cell. *Nature Photonics* **2012**, *6*, 824–828.

(16) Seger, B.; Castelli, I. E.; Vesborg, P. C. K.; Jacobsen, K. W.; Hansen, O.; Chorkendorff, I. 2-Photon Tandem Device for Water Splitting: Comparing Photocathode First Versus Photoanode First Designs. *Energy Environ. Sci.* **2014**, *7*, 2397–2413.

(17) Saal, J. E.; Kirklin, S.; Aykol, M.; Meredig, B.; Wolverton, C. Materials Design and Discovery with High-Throughput Density Functional Theory: The Open Quantum Materials Database (OQMD). *JOM* **2013**, *65*, 1501–1509.

(18) Kirklin, S.; Saal, J. E.; Meredig, B.; Thompson, A.; Doak, J. W.; Aykol, M.; Rühl, S.; Wolverton, C. The Open Quantum Materials Database (OQMD): assessing the accuracy of DFT formation energies. *npj Computational Materials* **2015**, *1*, npjcompumats201510.

(19) Jain, A.; Ong, S. P.; Hautier, G.; Chen, W.; Richards, W. D.; Dacek, S.; Cholia, S.; Gunter, D.; Skinner, D.; Ceder, G. et al. The Materials Project: A materials genome approach to accelerating materials innovation. *APL Materials* **2013**, *1*, 011002.

(20) Curtarolo, S.; Setyawan, W.; Hart, G. L.; Jahnatek, M.; Chepulskii, R. V.; Taylor, R. H.; Wang, S.; Xue, J.; Yang, K.; Levy, O. et al. AFLOW: An automatic framework for high-throughput materials discovery. *Computational Materials Science* **2012**, *58*, 218 – 226.

(21) Landis, D. D.; Hummelshøj, J. S.; Nestorov, S.; Greeley, J.; Dulak, M.; Bligaard, T.;

Nørskov, J. K.; Jacobsen, K. W. The Computational Materials Repository. *Computing in Science and Engineering* **2012**, *14*, 51.

(22) `https://cmr.fysik.dtu.dk`.

(23) `http://nomad-repository.eu`.

(24) Kresse, G.; Joubert, D. From Ultrasoft Pseudopotentials to the Projector Augmented-wave Method. *Phys. Rev. B* **1999**, *59*, 1758–1775.

(25) Mortensen, J. J.; Hansen, L. B.; Jacobsen, K. W. Real-space grid implementation of the projector augmented wave method. *Physical Review B* **2005**, *71*, 35109.

(26) Enkovaara, J.; Rostgaard, C.; Mortensen, J. J.; Chen, J.; Dułak, M.; Ferrighi, L.; Gavnholt, J.; Glinsvad, C.; Haikola, V.; Hansen, H. A. et al. Electronic Structure Calculations with GPAW: A Real-space Implementation of the Projector Augmented-wave Method. *J. Phys.: Condens. Matter* **2010**, *22*, 253202.

(27) Bahn, S. R.; Jacobsen, K. W. An Object-Oriented Scripting Interface to a Legacy Electronic Structure Code. *Computing in Science and Engineering* **2002**, *4*, 56–66.

(28) Larsen, A.; Mortensen, J.; Blomqvist, J.; Castelli, I. E.; Christensen, R.; Dulak, M.; Friis, J.; Groves, M.; Hammer, B.; Hargus, C. et al. The Atomic Simulation Environment - A Python library for working with atoms. *Journal of Physics Condensed Matter* **2017**,

(29) Monkhorst, H. J.; Pack, J. D. Special Points for Brillouin-zone Integrations. *Phys. Rev. B* **1976**, *13*, 12.

(30) Gritsenko, O.; van Leeuwen, R.; van Lenthe, E.; Baerends, E. J. Self-consistent Approximation to the Kohn-Sham Exchange Potential. *Phys. Rev. A* **1995**, *51*, 1944.

(31) Kuisma, M.; Ojanen, J.; Enkovaara, J.; Rantala, T. T. Kohn-Sham Potential with Discontinuity for Band Gap Materials. *Phys. Rev. B* **2010**, *82*, 115106.

(32) Castelli, I. E.; Hüser, F.; Pandey, M.; Li, H.; Thygesen, K. S.; Seger, B.; Jain, A.; Persson, K. A.; Ceder, G.; Jacobsen, K. W. New Light-Harvesting Materials Using Accurate and Efficient Bandgap Calculations. *Adv. Ener. Mater.* **2015**, *5*, 1400915.

(33) Perdew, J. P.; Burke, K.; Ernzerhof, M. Generalized Gradient Approximation Made Simple. *Phys. Rev. Lett.* **1996**, *77*, 3865–3868.

(34) Bergerhoff, G.; Hundt, R.; Sievers, R.; Brown, I. D. The Inorganic Crystal Structure Data Base. *J. Chem. Inf. Comput. Sci.* **1983**, *23*, 66–69.

(35) Gaultois, M. W.; Sparks, T. D.; Borg, C. K. H.; Seshadri, R.; Bonificio, W. D.; Clarke, D. R. Data-Driven Review of Thermoelectric Materials: Performance and Resource Considerations. *Chemistry of Materials* **2013**, *25*, 2911–2920.

(36) Setyawan, W.; Curtarolo, S. High-throughput electronic band structure calculations: challenges and tools. *Comput. Mater. Sci.* **2010**, *49*, 299–312.

(37) Shukla, S.; Xing, G.; Ge, H.; Prabhakar, R. R.; Mathew, S.; Su, Z.; Nalla, V.; Venkatesan, T.; Mathews, N.; Sritharan, T. et al. Origin of Photocarrier Losses in Iron Pyrite (FeS2) Nanocubes. *ACS Nano* **2016**, *10*, 4431–4440, PMID: 26962638.

(38) Zakutayev, A.; Caskey, C. M.; Fioretti, A. N.; Ginley, D. S.; Vidal, J.; Stevanovic, V.; Tea, E.; Lany, S. Defect Tolerant Semiconductors for Solar Energy Conversion. *The Journal of Physical Chemistry Letters* **2014**, *5*, 1117–1125.

(39) Pandey, M.; Rasmussen, F. A.; Kuhar, K.; Olsen, T.; Jacobsen, K. W.; Thygesen, K. S. Defect-Tolerant Monolayer Transition Metal Dichalcogenides. *Nano Lett.* **2016**, *16*, 2234–2239.

(40) Walsh, A.; ZUNGER, A. Instilling defect tolerance in new compounds. *Nature Publishing Group* **2017**, *16*, 964–967.

(41) Lany, S.; Zunger, A. Assessment of correction methods for the band-gap problem and for finite-size effects in supercell defect calculations: Case studies for ZnO and GaAs. *Phys. Rev. B* **2008**, *78*, 235104.

(42) Freysoldt, C.; Neugebauer, J.; Van de Walle, C. G. Fully *Ab Initio* Finite-Size Corrections for Charged-Defect Supercell Calculations. *Phys. Rev. Lett.* **2009**, *102*, 016402.

(43) Komsa, H.-P.; Rantala, T. T.; Pasquarello, A. Finite-size supercell correction schemes for charged defect calculations. *Phys. Rev. B* **2012**, *86*, 045112.

(44) Schultz, P. A. Charged Local Defects in Extended Systems. *Phys. Rev. Lett.* **2000**, *84*, 1942–1945.

(45) Goyal, A.; Gorai, P.; Peng, H.; Lany, S.; Stevanović, V. A computational framework for automation of point defect calculations. *Comput. Mater. Sci.* **2017**, *130*, 1–9.

(46) Larsen, A. H.; Vanin, M.; Mortensen, J. J.; Thygesen, K. S.; Jacobsen, K. W. Localized atomic basis set in the projector augmented wave method. *Physical Review B* **2009**, *80*, 195112.

(47) Ropp, R. C. *Encyclopedia of the Alkaline Earth Compounds*; Newnes, 2012; Google-Books-ID: yZ786vEild0C.

(48) Niu, S.; Huyan, H.; Liu, Y.; Yeung, M.; Ye, K.; Blankemeier, L.; Orvis, T.; Sarkar, D.; Singh, D. J.; Kapadia, R. et al. Bandgap Control via Structural and Chemical Tuning of Transition Metal Perovskite Chalcogenides. *Advanced Materials* **2017**, *29*, n/a–n/a.

(49) 2.08 eV obtained with HSE06 functional.

(50) Wang, A.; Yan, X.; Zhang, M.; Sun, S.; Yang, M.; Shen, W.; Pan, X.; Wang, P.; Deng, Z. Controlled Synthesis of Lead-Free and Stable Perovskite Derivative Cs2SnI6 Nanocrystals via a Facile Hot-Injection Process. *Chemistry of Materials* **2016**, *28*, 8132–8140.

(51) Madelung, O. *Semiconductors Data Handbook*; Springer: Berlin, 2004; pp 815–835.

(52) Moghe, D.; Wang, L.; Traverse, C. J.; Redoute, A.; Sponseller, M.; Brown, P. R.; Bulović, V.; Lunt, R. R. All vapor-deposited lead-free doped CsSnBr3 planar solar cells. *Nano Energy* **2016**, *28*, 469–474.

(53) Huang, L.-y.; Lambrecht, W. R. L. Electronic band structure, phonons, and exciton binding energies of halide perovskites CsSnCl3, CsSnBr3, and CsSnI3. *Physical Review B* **2013**, *88*, 165203.

(54) Yu, C.; Chen, Z.; Wang, J. J.; Pfenninger, W.; Vockic, N.; Kenney, J. T.; Shum, K. Temperature dependence of the band gap of perovskite semiconductor compound CsSnI3. *Journal of Applied Physics* **2011**, *110*, 063526–063526.

(55) Kim, K. J.; Kim, J. H.; Kang, J. H. Structural and optical characterization of Cu3N films prepared by reactive RF magnetron sputtering. *Journal of Crystal Growth* **2001**, *222*, 767 – 772.

(56) Fernández, A. M.; Turner, J. A. Preparation and photocharacterization of Cu–Sb–Se films by electrodeposition technique. *Solar Energy Materials and Solar Cells* **2003**, *79*, 391–399.

(57) Brammertz, G.; Vermang, B.; ElAnzeery, H.; Sahayaraj, S.; Ranjbar, S.; Meuris, M.; Poortmans, J. Fabrication and characterization of ternary Cu8SiS6 and Cu8SiSe6 thin film layers for optoelectronic applications. *Thin Solid Films* **2016**, *616*, 649 – 654.

(58) Tell, B.; Shay, J. L.; Kasper, H. M. Electrical Properties, Optical Properties, and Band Structure of $CuGaS_2$ and $CuInS_2$. *Phys. Rev. B* **1971**, *4*, 2463–2471.

(59) Colombara, D.; Peter, L. M.; Rogers, K. D.; Painter, J. D.; Roncallo, S. Formation of CuSbS2 and CuSbSe2 thin films via chalcogenisation of Sb–Cu metal precursors. *Thin Solid Films* **2011**, *519*, 7438–7443.

(60) Yablonskikh, M.; Dzivenko, D.; Bourguille, J.; Riedel, R.; Magnano, E.; Parmigiani, F.; Zerr, A. Electronic structure and band gap of oxygen bearing c-Zr3N4 and of c-Hf3N4 by soft X-ray spectroscopy. *physica status solidi (a)* **2014**, *211*, 835–842.

(61) Kuriyama, K.; Kato, T.; Tanaka, T. Optical band gap of the filled tetrahedral semiconductor LiZnN. *Phys. Rev. B* **1994**, *49*, 4511–4513.

(62) Kuriyama, K.; Taguchi, R.; Kushida, K.; Ushiyama, K. Growth and band gap of the filled tetrahedral semiconductor LiZnN. *Journal of Crystal Growth* **1999**, *198*, 802 – 805.

(63) Watson, L. M.; Marshall, C. A. W.; Cardoso, C. P. On the electronic structure of the semiconducting compounds Mg 3 Bi 2 and Mg 3 Sb 2. *Journal of Physics F: Metal Physics* **1984**, *14*, 113.

(64) Gäbler, F.; Kirchner, M.; Schnelle, W.; Schwarz, U.; Schmitt, M.; Rosner, H.; Niewa, R. (Sr3N)E and (Ba3N)E (E = Sb, Bi): Synthesis, Crystal Structures, and Physical Properties. *Zeitschrift für anorganische und allgemeine Chemie* **2004**, *630*, 2292–2298.

(65) Olsson, P.; Vidal, J.; Lincot, D. Ab initio study of II–(VI) 2 dichalcogenides. *Journal of Physics: Condensed Matter* **2011**, *23*, 405801.

(66) Johansson, B.; Hentzell, H.; Harper, J.; Cuomo, J. Higher nitrides of hafnium, zirconium, and titanium synthesized by dual ion beam deposition. *J. Mater. Res.* **1986**, *1*, 442–451.

(67) Guthrie, D. H.; Corbett, J. D. Synthesis and structure of an infinite-chain form of ZrI2 (α). *Journal of Solid State Chemistry* **1981**, *37*, 256 – 263.

(68) Moustafa, M.; Zandt, T.; Janowitz, C.; Manzke, R. Growth and band gap determination of the ZrS_xSe_{2-x} single crystal series. *Phys. Rev. B* **2009**, *80*, 035206.

(69) Kalarasse, L.; Bennecer, B.; Kalarasse, F. Optical properties of the alkali antimonide semiconductors Cs3Sb, Cs2KSb, CsK2Sb and K3Sb. *Journal of Physics and Chemistry of Solids* **2010**, *71*, 314–322.

(70) Spicer, W. E. Photoemissive, Photoconductive, and Optical Absorption Studies of Alkali-Antimony Compounds. *Phys. Rev.* **1958**, *112*, 114–122.

(71) Wei, S.-H.; Zunger, A. Electronic structure of M_3^{I}Sb-type filled tetrahedral semiconductors. *Phys. Rev. B* **1987**, *35*, 3952–3961.

(72) De'Munari, G. M.; Mambriani, G.; Giusiano, F. Photoemissive Yield of Cs3Sb Photocathode and Its Dependence on Temperature. *Review of Scientific Instruments* **1967**, *38*, 1128–1132.

(73) Wu, Y.; Wadia, C.; Ma, W.; Sadtler, B.; Alivisatos, A. P. Synthesis and Photovoltaic Application of Copper(I) Sulfide Nanocrystals. *Nano Letters* **2008**, *8*, 2551–2555.

(74) Lazicki, A.; Yoo, C.-S.; Cynn, H.; Evans, W. J.; Pickett, W. E.; Olamit, J.; Liu, K.; Ohishi, Y. Search for superconductivity in LiBC at high pressure: Diamond anvil cell experiments and first-principles calculations. *Phys. Rev. B* **2007**, *75*, 054507.

(75) Rosner, H.; Kitaigorodsky, A.; Pickett, W. E. Prediction of High T_c Superconductivity in Hole-Doped LiBC. *Phys. Rev. Lett.* **2002**, *88*, 127001.

(76) Caputo, R. Exploring the structure-composition phase space of lithium borocarbide, LixBC for x [less-than-or-equal] 1. *RSC Adv.* **2013**, *3*, 10230–10241.

(77) Miao, R.; Yang, J.; Jiang, M.; Zhang, Q.; Cai, D.; Fan, C.; Bai, Z.; Liu, C.; Wu, F.; Ma, S. First-principles study of superconductivity in the hole self-doped LiB1.1C0.9. *Journal of Applied Physics* **2013**, *113*, 133910.

(78) Briskman, R. N. A Study of Electrodeposited Cuprous-Oxide Photovoltaic Cells. *Solar Energy Materials and Solar Cells* **1992**, *27*, 361–368.

(79) Liu, Y.; Yang, G.; Zhang, H.; Cheng, Y.; Chen, K.; Peng, Z.; Chen, W. Enhanced visible photocatalytic activity of Cu2O nanocrystal/titanate nanobelt heterojunctions by a self-assembly process. *RSC Advances* **2014**, *4*, 24363–24368.

(80) Welch, A. W.; Baranowski, L. L.; Zawadzki, P.; Lany, S.; Wolden, C. A.; Zakutayev, A. CuSbSe 2 photovoltaic devices with 3% efficiency. *Applied Physics Express* **2015**, *8*, 082301.

(81) Song, T.-B.; Yokoyama, T.; Aramaki, S.; Kanatzidis, M. G. Performance Enhancement of Lead-Free Tin-Based Perovskite Solar Cells with Reducing Atmosphere-Assisted Dispersible Additive. *ACS Energy Letters* **2017**, *2*, 897–903.

(82) Qiu, X.; Cao, B.; Yuan, S.; Chen, X.; Qiu, Z.; Jiang, Y.; Ye, Q.; Wang, H.; Zeng, H.; Liu, J. et al. From unstable CsSnI3 to air-stable Cs2SnI6: A lead-free perovskite solar cell light absorber with bandgap of 1.48 eV and high absorption coefficient. *Solar Energy Materials and Solar Cells* **2017**, *159*, 227 – 234.

(83) da Silva, E. L.; Skelton, J. M.; Parker, S. C.; Walsh, A. Phase stability and transformations in the halide perovskite $CsSnI_3$. *Phys. Rev. B* **2015**, *91*, 144107.

(84) Meng, W.; Saparov, B.; Hong, F.; Wang, J.; Mitzi, D. B.; Yan, Y. Alloying and Defect Control within Chalcogenide Perovskites for Optimized Photovoltaic Application. *Chemistry of Materials* **2016**, *28*, 821–829.

(85) Cooper, J. K.; Gul, S.; Toma, F. M.; Chen, L.; Glans, P.-A.; Guo, J.; Ager, J. W.; Yano, J.; Sharp, I. D. Electronic Structure of Monoclinic BiVO4. *Chemistry of Materials* **2014**, *26*, 5365–5373.

(86) Wiktor, J.; Reshetnyak, I.; Ambrosio, F.; Pasquarello, A. Comprehensive modeling of the band gap and absorption spectrum of BiVO4. *Physical Review Materials* **2017**, *1*, 022401.

5.5 Paper V: Trigonal Selenium as a Large Band Gap Material in Tandem Photoelectrochemical Devices

The publication is in preparation

Trigonal Selenium as a Large Band Gap Material in Tandem Photoelectrochemical Devices

Korina Kuhar, Mohnish Pandey, Thomas Olsen, and Karsten W. Jacobsen*

Center for Atomic-scale Materials Design (CAMD), Department of Physics, Technical University of Denmark, DK - 2800 Kongens Lyngby, Denmark

E-mail: kwj@fysik.dtu.dk

*To whom correspondence should be addressed

Introduction

Selenium (Se, Z=34, Greek *selene* meaning "Moon") is one of the oldest known semiconductors. Even though Selenium very early showed promising photoelectric properties, being the first material to show photoelectric effect,[1] no usage of Selenium in commercial purposes has been reported. The lack of practical application is probably the reason why Selenium was not extensively studied, unlike for example, silicon or germanium, other well known elemental semiconductors.

A recently introduced strategy for achieving higher efficiency using tandem photovoltaic(PV) and photoelectrochemical(PC) devices, has resulted in increased interest in high band gap semiconductors. A simple device design assumes two semiconductors, a small band gap (SBG) semiconductor, like for example silicon, and the large band gap (LBG)) working in a tandem. However, the main challenge remains finding a suitable LBG material.

For a long time the record conversion efficiency of selenium was only 5%[2] and it was only lately that a redesigned selenium device was introduced and a new efficiency record of 6.5%[3] was obtained. In light of the recent result and with high demand for LBG semiconductors, we explore properties of trigonal selenium and its suitability to serve as a LBG absorber in a tandem device.

Selenium is a simple amorphous semiconductor which crystallizes in a trigonal crystal system of hexagonal family (spacegroup number 152). Even though the literature reports several different phases of selenium (α,[4] β[5] and γ[6] monoclinic phases) and several other phases obtained by applying high pressure[7] the trigonal form is the only one thermodynamically stable at the ambient conditions.

The hexagonal unit cell, a= 4.366 Å, c=4.954 Å, α=β = 90 , γ = 120 contains three atoms in a primitive cell. The atoms are arranged in spiral rods oriented along the c axis of the cell, with one rod at the center of hexagonal structure and one at each corner of a hexagon. The geometry suggests that single rods are held together only by a week, possibly weak van der Waals type, interaction. That would further imply that single selenium rods

should show similar properties as the bulk selenium.

However, Joannopoulos et al.[8] investigated the structure of selenium and found some covalent-like bonding between the rods. In this work we investigate electronic and optical properties of trigonal selenium using electronic structure methods. We also investigate the connection between a 1D-like geometry and electronic and optical properties of the material. Finally, our conclusion is in agreement with the reference above; even though many properties are predominantly arising from single rods, significant contribution comes from the interaction between the neighboring rods. As a result, selenium cannot be classified as purely bulk semiconductor or a 1D van der Waals type one, but rather a mixture of both.

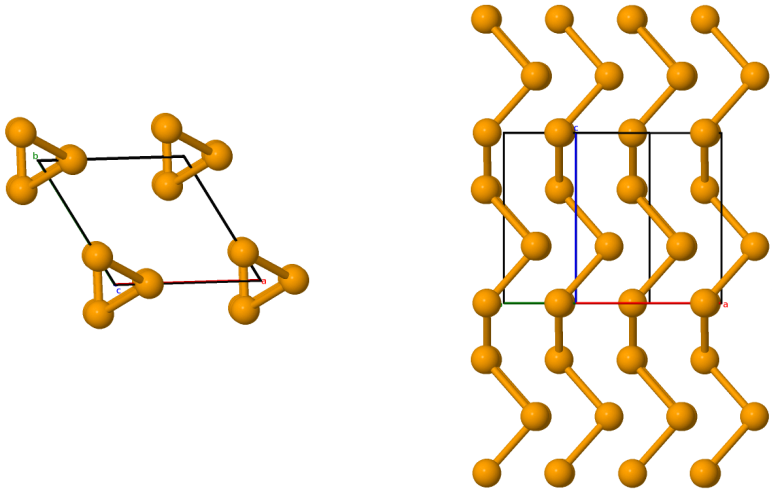

Figure 1: Crystal structure of trigonal Selenium: the one dimensional spiral rods are extending in the c-axis direction (right). The view from the top (left) shows the arrangement of rods in the corners of hexagonal primitive cell.

Computational details

Electronic structure calculations were performed using the GPAW code.[9] The band structure and effective mass calculations are performed using Density Functional Theory (DFT)

in the Projector Augmented Wave (PAW) formalism.[10] The wavefunctions are expanded in a plane-wave basis with an energy cutoff of 800 eV. The sampling of the Brillouin zone is performed using the Monkhorst-Pack scheme.[11] A 7×7×7 k-point mesh was used for band gap calculations, whereas band structure and effective masses required finer meshes. For calculating electronic properties, band gap, band structure and effective masses, a more accurate, semi-local GLLB-SC exchange-correlation functional[12] was employed because of it's high accuracy and similar computational cost as other semi-local functionals.[13,14] Additionally, band gap was also evaluated using a hybrid HSE06 functional.[15]

The LDA eigenvalues and wave functions, used as the input in the G_0W_0 calculations,[16,17] were calculated with a plane wave basis cutoff energy of 800 eV and a 6×6×6 k-point mesh. For the initial investigation of the convergence with respect to the plane wave cutoff and number of unoccupied bands used, the dielectric function and the correlation self-energy were calculated using cutoffs of 150, 200 and 250 eV and extrapolated to infinite cutoff using the standard $1/E_{cut}^{3/2}$ dependence. Frequency integration in the self-energy is evaluated on the real axis using a logarithmic grid.

The optical spectra with and without the excitonic effects are calculated solving the Bethe-Salpeter equation[18] and in the random-phase approximation (RPA, independent-particle picture), respectively.[19,20]

The calculations with point defects were performed on 3×3×3 super-cells using the PBE functional and the LCAO-mode of GPAW with a dzp basis set.[21]

Results

Selenium is an indirect band gap semiconductor with a small difference between direct and indirect band gap. Experiments report 1.85 eV for the indirect and 1.95 for the direct band gap.[22] Similar values are obtained theoretically, where the GLLB-SC and HSE06 functionals result band gaps of 1.71 eV (1.93 eV direct) and 1.86 eV(2.28 eV direct), respectively. G_0W_0

quasi-particle band gap is slightly lower, 1.71 eV (1.98 eV direct). Electronic band structure along the hexagonal high-symmetry band path with and without spin-orbit coupling is shown in Figure 2 (left). One can see how the red dashed lines (where spin orbit was included) are on top of the blue solid lines (where spin-orbit coupling was not included), meaning that the effect of spin orbit coupling has an insignificant influence on the size of the band gap. It does, however, split the spin degeneracy due to the lack of inversion symmetry in the trigonal structure. The small difference between indirect and direct band gap is clearly visible from the band structure. However, the absolute valence band maximum (VBM) and conduction band minimum (CBM) are not on the high-symmetry path illustrated in Figure 2 (left). VBM is found slightly off the L-H path, while CBM is close to the H point. The Brillouin zone and positions of VBM and CBM is shown in Figure 2 (right). The obtained band structure shows larger dispersion along the directions parallel to the rods, especially in segments H-K and L-M, which is a direct consequence of the quasi 1D geometry of selenium.

In connection to the mobility of photo-excited carriers, we calculate the carrier effective masses. Using the dense k-point sampling around VBM and CBM we are able to extract effective masses by fitting parabolas in the three directions around VBM and CBM. Since we are interested in room temperature effects, we include in the fit a region up to 25 meV from the band extremes (25 meV $\approx$ 290 K). The resulting hole effective masses are 0.527, 0.519 and 0.166 m_e (m_e is the standard electron mass) and electron effective masses 0.127, 0.123 and 0.137 m_e.

Figure 3 shows the optical properties perpendicular and along the rods, respectively. The blue line is the optical spectra without the excitonic effects, calculated in the random-phase approximation (RPA, independent-particle picture) and the green line is the spectra obtained with BSE, which includes the electron-hole interactions.

The first peak observed in the optical spectra in the direction perpendicular to the selenium rods (Figure 3, left) can be assigned to transitions from the highest occupied band. This single band is isolated in the directions perpendicular to the rods, including the L-H

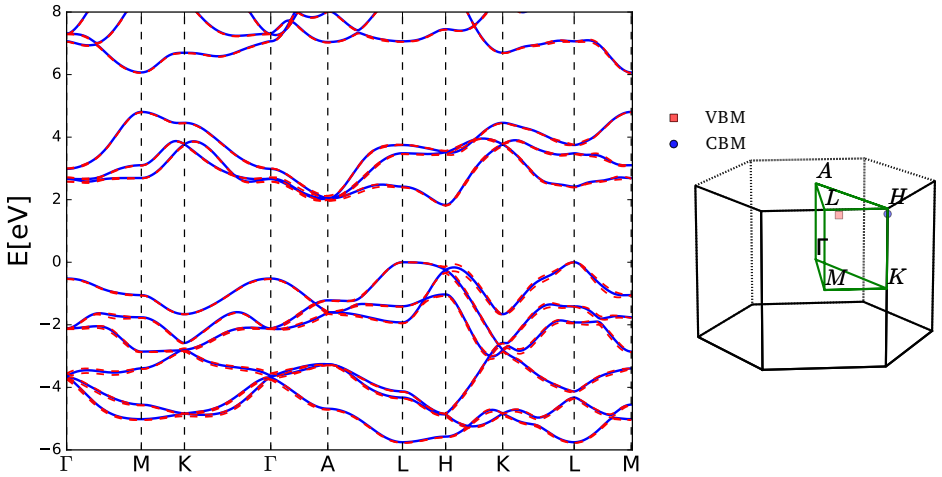

Figure 2: Calculated band structure along the high-symmetry band path with (red dashed lines) and without (blue solid lines) spin orbit coupling(left). Brillouin zone of Selenium with the high symmetry points and path. Valence band maximum (VBM) and conduction band minimum (CBM) are off the path (right).

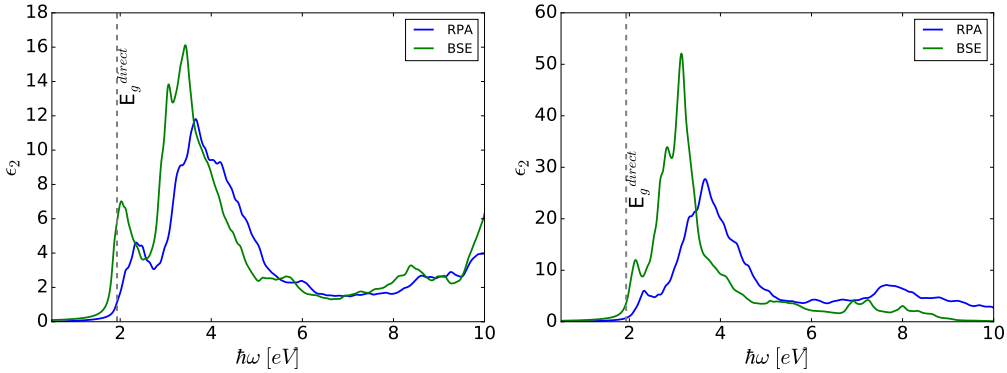

Figure 3: Optical spectra perpendicular (left) and along (right) Se rod direction obtained with BSE (green) and RPA (blue). The vertical lines mark direct band gap position, calculated with GLLB-SC functional.

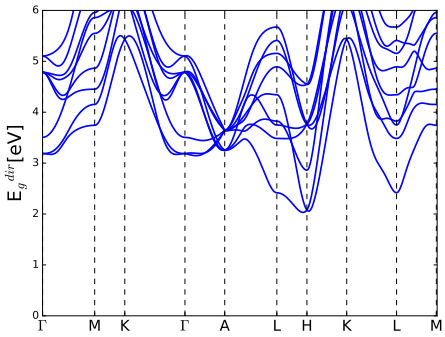

Figure 4: Energy difference between lowest unoccupied and highest occupied bands along the high-symmetry path in the Brillouin zone.

section, where the lowest direct band gap is located. Therefore, the transitions originating from the two highest occupied band in L-H region will result in an isolated peak of lower intensity. The second, higher and broader peak, is result of transitions originating from remaining regions perpendicular to the rods (Γ-M-K-Γ, A-L-H), where the value of direct band gap is at least 3 eV, together with contributions from the next two highest occupied bands. The direct band gap values along the high-symmetry paths are shown in Figure 4. The offset between the RPA and BSE excitonic peaks is the exciton binding energy and in this case is found to be 0.18 eV.

The optical spectra along the direction of the selenium rods is shown in Figure 3, right. The intensity of the spectrum is roughly three times higher when comparing to the spectra in the direction perpendicular to the selenium rods. This comes as a consequence of the strong hybridization along the rods, also seen in the H-K region which has the strongest dispersion of the entire band structure. The region around H and L points, according to the Figure 4, is most likely the origin of transitions forming the first, small peak in the absorption spectrum.

The exciton binding energy is increased and here it results 0.28 eV.

Despite the spectral differences in the two directions, the absence of the sharp, isolated

excitonic peak suggests that the material behaves more like other bulk semiconductors and less like a low-dimensional material.

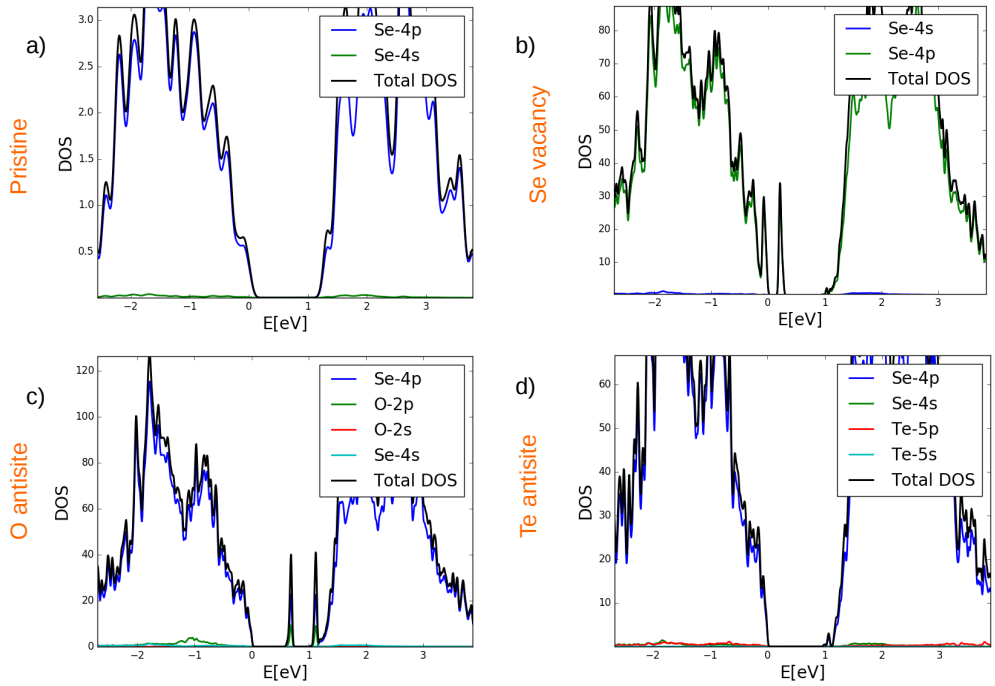

Figure 5: Density of states of pristine selenium structure (a), structure with selenium vacancy (b), oxygen antisite (c) and tellurium antisite(d). Selenium vacancy and oxygen antisite introduce mid-gap states whereas tellurium antisite does not seem to have a significant effect on the band structure.

The sensitivity of the electronic properties of the material due to introduction of point defects was investigated for selenium vacancy and oxygen and tellurium antisites. The calculations were performed on 3×3×3 super-cells, each super-cell containing one type of defects. The Figure 5 shows the changes in the total density of states in the area close to the band gap. Selenium vacancy and oxygen antisite introduce a mid-gap state while the tellurium antisite has almost no effect on the density of states. Since the mid-gap states

act as recombination centers and lead to the loss of photo-excited electrons, they should be avoided. Therefore, presence of selenium vacancies or having oxygen impurity on a selenium site is unwanted since the material cannot "tolerate" their presence. However, there seems to be no problem with tellurium antisites since no mid-gap states are visible.

Conclusion

The reported work suggests that trigonal selenium has suitable band gap and sufficiently low effective masses to perform well as a LBG absorber in a tandem photoelectrochemical device. Problems such as carrier recombination may arise due to point vacancies or oxygen antisites, since both are shown to introduce mid-gap states. Also, additonal investigation, including charged defects may be necessary. Furthermore we investigate optical absorption along and perpendicular to the direction of selenium rods. Our results suggest that selenium has a quasi-1D structure, with the bonding between the neighboring rods significantly strong that a material cannot be called purely 1D.

References

(1) Guarnieri, M. More Light on Information [Historical]. *IEEE Industrial Electronics Magazine* **2015**, *9*, 58–61.

(2) Nakada, T.; Kunioka, A. Polycrystalline Thin-Film TiO 2 /Se Solar Cells. *Japanese Journal of Applied Physics* **1985**, *24*, L536.

(3) Todorov, T. K.; Singh, S.; Bishop, D. M.; Gunawan, O.; Lee, Y. S.; Gershon, T. S.; Brew, K. W.; Antunez, P. D.; Haight, R. Ultrathin high band gap solar cells with improved efficiencies from the world's oldest photovoltaic material. *Nature Communications* **2017**, *8*, 682.

(4) Cherin, P.; Unger, P. Refinement of the crystal structure of -monoclinic Se. *Acta Crys-*

tallographica Section B: Structural Crystallography and Crystal Chemistry **1972**, *28*, 313–317.

(5) Marsh, R. E.; Pauling, L.; McCullough, J. D. The crystal structure of selenium. *Acta Crystallographica* **1953**, *6*, 71–75.

(6) Foss, O.; Janickis, V. Crystal structure of -monoclinic selenium. *Journal of the Chemical Society, Dalton Transactions* **1980**, *0*, 624–627.

(7) Keller, R.; Holzapfel, W. B.; Schulz, H. Effect of pressure on the atom positions in Se and Te. *Phys. Rev. B* **1977**, *16*, 4404–4412.

(8) Joannopoulos, J. D.; Schlüter, M.; Cohen, M. L. Electronic structure of trigonal and amorphous Se and Te. *Phys. Rev. B* **1975**, *11*, 2186–2199.

(9) Enkovaara, J.; Rostgaard, C.; Mortensen, J. J.; Chen, J.; Dułak, M.; Ferrighi, L.; Gavnholt, J.; Glinsvad, C.; Haikola, V.; Hansen, H. A.; *et al*, Electronic Structure Calculations with GPAW: A Real-space Implementation of the Projector Augmented-wave Method. *J. Phys.: Condens. Matter* **2010**, *22*, 253202.

(10) Kresse, G.; Joubert, D. From Ultrasoft Pseudopotentials to the Projector Augmented-wave Method. *Phys. Rev. B* **1999**, *59*, 1758–1775.

(11) Monkhorst, H. J.; Pack, J. D. Special Points for Brillouin-zone Integrations. *Phys. Rev. B* **1976**, *13*, 12.

(12) Gritsenko, O.; van Leeuwen, R.; van Lenthe, E.; Baerends, E. J. Self-consistent Approximation to the Kohn-Sham Exchange Potential. *Phys. Rev. A* **1995**, *51*, 1944.

(13) Castelli, I. E.; Olsen, T.; Datta, S.; Landis, D. D.; Dahl, S.; Thygesen, K. S.; Jacobsen, K. W. Computational screening of perovskite metal oxides for optimal solar light capture. *Energy & Environmental Science* **2012**, *5*, 5814–5819.

(14) Castelli, I. E.; Hüser, F.; Pandey, M.; Li, H.; Thygesen, K. S.; Seger, B.; Jain, A.; Persson, K. A.; Ceder, G.; Jacobsen, K. W. New Light-Harvesting Materials Using Accurate and Efficient Bandgap Calculations. *Advanced Energy Materials* **2015**, *5*, n/a–n/a.

(15) Heyd, J.; Scuseria, G. E.; Ernzerhof, M. Hybrid functionals based on a screened Coulomb potential. *The Journal of Chemical Physics* **2003**, *118*, 8207–8215.

(16) Strinati, G.; Mattausch, H. J.; Hanke, W. Dynamical aspects of correlation corrections in a covalent crystal. *Phys. Rev. B* **1982**, *25*, 2867–2888.

(17) Hüser, F.; Olsen, T.; Thygesen, K. S. Quasiparticle GW calculations for solids, molecules, and two-dimensional materials. *Phys. Rev. B* **2013**, *87*, 235132.

(18) Salpeter, E. E.; Bethe, H. A. A Relativistic Equation for Bound-State Problems. *Phys. Rev.* **1951**, *84*, 1232–1242.

(19) Furche, F. Molecular tests of the random phase approximation to the exchange-correlation energy functional. *Phys. Rev. B* **2001**, *64*, 195120.

(20) Olsen, T.; Thygesen, K. S. Random phase approximation applied to solids, molecules, and graphene-metal interfaces: From van der Waals to covalent bonding. *Phys. Rev. B* **2013**, *87*, 075111.

(21) Larsen, A. H.; Vanin, M.; Mortensen, J. J.; Thygesen, K. S.; Jacobsen, K. W. Localized atomic basis set in the projector augmented wave method. *Physical Review B* **2009**, *80*, 195112.

(22) Madelung, O. *Semiconductors Data Handbook*; Springer: Berlin, 2004; pp 815–835.

CHAPTER 6

Additional information

This chapter provides additional information and details on the papers and methods used to produce published results. In addition, some unpublished results related to the work presented are also included in this chapter.

6.1 Paper I:Defect-Tolerant Monolayer Transition Metal Dichalcogenides

The descriptor introduced in the paper works very well for 2D metal dichalcogenides, which has been confirmed by visually investigating band structures of pristine and defect materials. The natural step forward at this point is going beyond the well defined material class and using the descriptor on different 2- and 3D systems.

We used a set of 18 bulk semiconductors and insulators to test the performance of the NOO descriptor introduced in the paper. Calculations for each material in the pristine structure and a supercell structure containing a point vacancy have been performed using the DFT. The changes in the band structure were investigated for both possible vacancies by comparing the density of states of pristine and supercell structures. This allows categorizing materials into defect tolerant (no deep states were found in the band gap) and defect sensitive (deep state were found in the band gap). The observed conclusions were then compared with the results obtained using the NOO descriptor.

Figure 6.1 shows calculated values of descriptor D for 18 materials investigated. Materials without the mid-gap states (tolerant) are plotted in green and materials showing mid-gap states are plotted in red. The predicted D values are more disperse in this case, comparing to the values ontanied for the TMDs, as reported in the publication. There is no clear separation between the high and low D values. Furthermore, the descriptor seems to predict well only in cases of very high D values (>0.8). From the pDOS of the investigated materilas, one can often see contributions from several different states (3 or 4) to the total DOS close to the band edge, unlike the only two states found in TMDs. This becomes an even larger problem if one goes to ternary or higher order compounds, where contirbutions from many different states are expected. Furthermore, the descriptor will fail in cases where the states deeper in the band are responsible for formation of the dangling bonds and mid gap states.

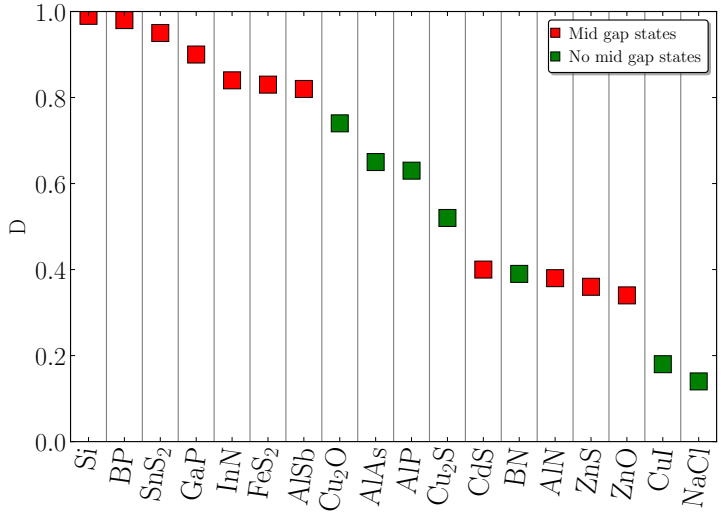

Figure 6.1: NNO descriptor values (D) for investigated bulk compounds. Red squares indicate the compounds manifesting deep defect states and the green squares indicating the compounds showing no deep defect states after the introduction of a vacancy. The energy window of 2eV was used for calculating D.

This short analysis shows that the description behind the NOO is too simple to sucessfully predict defect tolerance for materials whose pDOS is much different comparing to the pDOS of the TMDs. However, within this analysis we have not found an example of a false negative (for D>0.8) but several fake positives. This indicates that there could be some room for improvements but this is beyond the scope of this work.

In conclusion, when it comes to different materials with different types of interatomic bondings in crystals, one still has to use the standard, visual, way to investigate defect sensitivity. Unfortunatelly, calculations for large supercells are then necessary, increasing of the cost of the process. Hence, defect investigations as part of screening projects are performed late in the process on a small number of candidates.

6.2 Paper II: II–IV–V_2 and III–III–V_2 Polytypes as Light Absorbers for Single Junction and Tandem Photovoltaic Device

6.2.1 Calculated and experimental band gaps for II-IV-V_2 compounds

In section 2.4 I have discussed the well known failiure of the DFT: the band gap problem. In this work, I have the opportunity to compare results obtained using functionals introduced in section 2.4 with the experimental values. All the band gaps were calculated using two functionals, GLLB-SC and TB09, which give a good trade of between cost and accuracy. Here we were able to make a direct comparison between calculated and experimantally obtained band gap values for 16 semiconductors (numerical values can be found in the publication). Within the range of interest (0.5-2.1 eV), both functionals give similar results and are in a good agreement with the experiments.

In figure 6.2 calculated versus experimental band gap values are shown. For the reported set, TB09 functional gives higher values than GLLB-SC functional, the mean absolute error (MAE) of the difference between calculations and experiments is 0.17 for the TB09 and 0.3 for the GLLB-SC. However, this was only evaluated for small band gaps. GLLB-SC functional gives higher values in the region of higher gaps (Figure 5 in the paper), but the lack of experimental data prevents us from testing the accuracy. In this particular case, TB09 has shown to give values closer to the experimental ones, in our region of interest which is between 0.5 and 2.1 eV. However, one cannot claim that TB09 is overall a better functional, it only give better agreement with experiments in this particular case. Also, one should keep in mind that the work here is restricted on particular material class and more diverse data set is necessary in order to draw conclusions about functional performance.

6.2.2 Carrier effective masses for III-III-V_2 compounds

Aside from the carrier effective masses of II-IV-V_2 compounds reported in the publication, here we report them also for the III-III-V_2 compounds. Carrier effective masses were calculated using the procedure reported in the manuscript for all 11 compounds in two structures, wurtzite and zinckblende. The only exceptions not included are both structures of InSb and ZB phase of InAs, which are predicted metallic (using GLLB-SC functional). The carrier effective masses of the remining materials are all within the light mass limit, illustrated with the green area in figure 6.3.

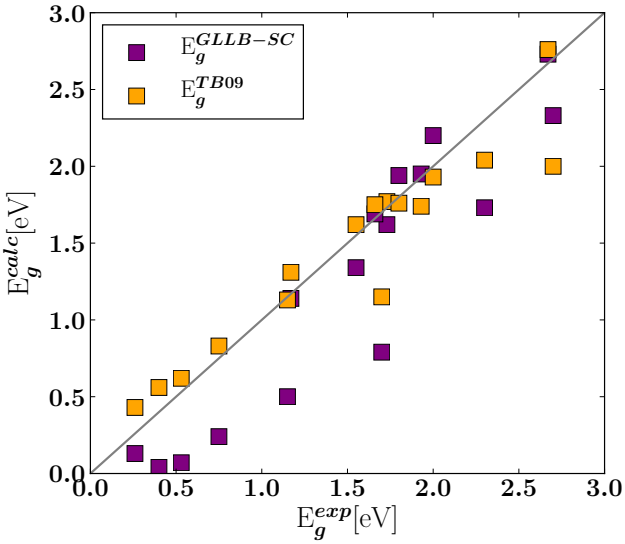

Figure 6.2: Experimental versus calculated values of the band gaps. Calculated values are obtained with both GLLB-SC (purple) and TB09 (orange) functional. The x=y line is plotted in gray. The mean absolute error of the difference between calculated and experimental values is 0.3 for the GLLB-SC and 0.17 for TB09 functional.

6.3 Paper III: Sulfide Perovskites for Solar Energy Conversion Applications: Computational Screening and Synthesis of the Selected Compound $LaYS_3$

The thorough study such as this one results in the large amount of calculated data. Several crystal structures calculated for each compound result in over 1 600 different materials. Adding the information about stability, prototypes, band gaps, effective masses and other, the amount of data gets sufficently large that one needs appropriate tools for quick search and data analysis. We store our data in ASE database ($|ase.db|$) format, which comes as part of the standard ASE installation.

The database is organized ina away that each row contains information for one material. The standard ASE *Atoms* object is fully stored, which includes the crystal structure, magnetic moments, charge, and, if available, the name of the calculator. Furthermore, one creates key-value pairs, as columns in the table, to store the cus-

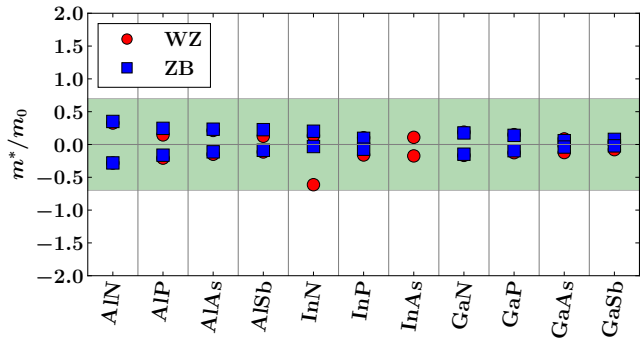

Figure 6.3: Calculated effective masses for electrons and holes. The signs correspond to the orientation of the parabola fitted to the top of the valence band (holes) and bottom of the conduction band (electrons).

tomized data.

The database of ABS_3 compounds used in this work has 12 additional key-value pairs, as shown in figure 6.4. The *ABS3_name* keyword stands for empirical formula of the compound (different prototypes have different structural formulas) and the *prototype* keyword reffers to the structural prototype of the material, as obtained from the ICSD database. Properties obtained in relation to the stability of material are the total energy (*total_en*), energy difference between the energy of the material and the energy of the most stable structure, together with the corresponding uncertainty (*E_relative_perAtom* and *E_uncertainty_perAtom*, respectively, both in eV/atom). The position of the convex hull with respect to the lowest structure is stored as *E_hull*, and the uncertainty of the convex hull is accordingly *E_uncertainty_hull*. Electronic prperties include band gaps, calculated with PBEsol and GLLB-SC functionals (*PBEsol_gap*, *GLLB_ind* and *GLLB_dir*) and electron, *m_e*, and hole, *m_h*, effective masses. However, due to the screening procedure described earlier, the set of calculated properties is not complete for all the materials. The materials which were removed from the study at the earlier stage will have less properties reported.

The database is accessible through the command line, where one can query the data set and manipulate key-value pairs. The interface to the python programming language allows advanced data manipulation using python tools such as numpy or matplotlib. A more user friendly interface, using the web browser, is also available but allows only querying the data.

Once the publication is accepted by the journal, the database will be available through the CMR home page[87].

Items	Value	Unit
ABS3_name	CuTaS3	
E_hull	0.0543837556	
E_relative_perAtom	0.0	
E_uncertanty_hull	0.0538847752716	
E_uncertanty_perAtom	0.0	
GLLB_dir	0.970	
GLLB_ind	0.980	
PBEsol_gap	0.340	
ASE-calculator name	gpaw	
Charge	0.000	|e|
Total energy	-1679.700	eV
m_e	2.340	
m_h	-1.130	
Mass	1362.696	au
prototype	CuTaS3	
total_en	-1679.700	

Figure 6.4: An example of customized key-value pairs for the $CuTaS_3$. The *Items* column contains the short name of the properties available and the *value* column their corresponding values. In addition, one can add the physical units for each property. Data in this format is available using the *ase.db* web interface.

CHAPTER 7

Additional results and implementation

In this chapter I report on an implementation and results which did not result in a scientific publication.

The motivation behind this work comes from the recent significant interest in novel, atomically thin materials. Starting with the 2004 discovery of graphene[96], the first two dimensional (2D) material, to now, when we witness an explosion in demand for new low dimensional materials. So far, various applications of not only 2D, but also one dimensional (1D) and zero dimensional (0D) materials have been suggested, such as battery electrodes, catalysis and photo-catalysis, sensor development and electronics to name a few[97, 98].

Here we propose a computational technique to identify bulk structures which possess a low-dimensional atomic structure. The technique was applied on a large data set available in a experimental materials database (ICSD).

7.1 Unraveling low-dimensional structure of experimentally known compounds

An interesting property of low dimensional materials is the ability to weakly bond to each other or to a bulk structure. This is due to weak van der Waals (vdW) forces holding the two materials together. The heterostructure made by stacking single layer sheets on top of one another allow the surfaces of materials to interact through vdW forces. The resulting stack is an artificial material of a chosen structure, where the strong covalent bonds maintain the in plane stability, and weak vdW forces keep the heterostructure together. On the other hand, there is a group of materials that are natural heterostructures, where the “bulk” material is actually a combination of different low-dimensional constituents held together by the vdW forces. Since it is well known that 2D materials can be exfoliated from the layered bulk compounds, identifying materials which are natural heterostructures is the fastest route to a discovery of new stable monolayers. The same approach holds for other low dimensional systems,

where 1D nano-ribbons, nano-wires and nano-rods, or 0D fullerenes, small organic molecules and quantum dots can be obtained from the "parent" heterostructure.

Here I present an algorithm for identifying the lower dimensional nature of the experimentally known compounds. It is based on a scaling number of atomic clusters with the increasing cell size. The method was applied on the materials in the Inorganic Crystal Structure Database (ICSD)[62] and used to classify crystal structures based on the dimensionality of their structural constituents. The algorithm was written in *python* programming language and is expected to be implemented in the new version of the Atomic Simulation Environment (ASE)[25, 26].

7.1.1 Different low-dimensional structure types

Materials databases contain a large number of materials, most of which are bulk. However, a significant number of "hidden", natural van der Waals-like structures have not yet been explored in a systematic manner. Such structures also possess great diversity, from simple stacking of 2D layers along a major crystal axis (figure 7.1a, to complex lower dimensional or multi-dimensional structures without a simple rule of repetition.

Figure 7.1 shows three examples: i) a layered structure with layers stacked along a principal crystal axis (figure 7.1a), ii) a structure with 1D rod-like constituents (figure 7.1b) and iii) a structure composed of 0D dots (figure 7.1c). In each of these cases the parent structure can be described as a system of low-dimensional atomic clusters where the distances between clusters are significantly larger than the usual distances between the neighboring atoms.

An example of the more complex, but fairly common situation is illustrated in figure 7.2 on an example of Na_2GeO_{10}. Layers are buckled and spread in a wavy manner, corrugating to the neighboring layers as they bend. $FeO_{16}S_2Zn$, the second example (figure 7.2b) contains unusual 1D rods arranged in different orientations.

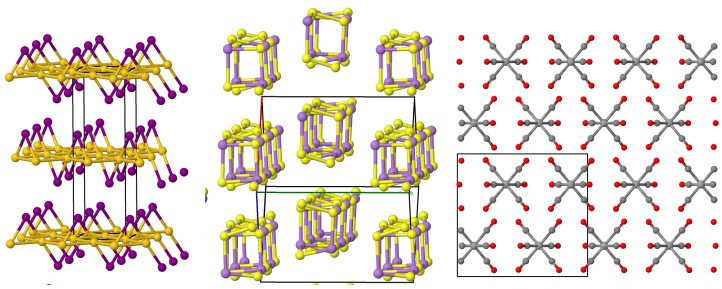

(a) **(b)** **(c)**

Figure 7.1: Example of materials containing layered (2D) a), rod-like (1D) b) and 0D c) constituents. All materials are real examples from ICSD database.

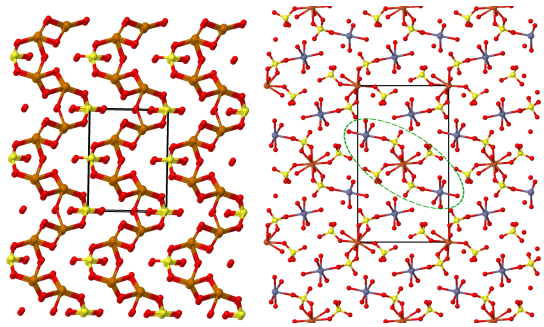

(a) (b)

Figure 7.2: Low dimensional nature of Na_2GeO_{10} a) and $FeO_{16}S_2Zn$ b). The green ellipse in b) highlights a single 1D rod.

Such an unusual example gives only a small taste of the complexity and variety of low-dimensional systems.

Characteristics such as variation in the spacing between the atomic clusters, cluster corrugation, clusters spread in different directions, or a heterostructure being a mixture of different low-dimensional constituents (for example 2D and 1D), make systematic identification of low-dimensional constituents from the bulk "parents" a nontrivial problem. Our approach contains a single algorithm able to cope with all these issues, which successfully classifies materials based on the dimensionality of the constituents.

7.1.2 Overview of the algorithm

What is visually a trivial task, like identifying 2D, 1D and 0D nature of the structures in figure 7.1, is much more complicated for a computer whose only input are atomic coordinates of the atoms.

The first part of the algorithm is based on identifying atomic clusters in a unit cell. The clusters are built using the |*ase.neighborlist*|[99] module: two atoms belong to the same cluster if they are neighbors or there exists a path from one to another through nearest neighbors. Mathematically, for atoms to be in the same cluster, they must satisfy the transitivity property of the equivalence class: for every three elements a, b, and c in a class, if a $\sim$ b and b $\sim$ c, then a $\sim$ c.

However, the definition of neighbors is not strictly defined, since different species in the different chemical environment form bonds of different lengths. Still, a good way to begin is by using the covalent radii of the species. After a series of tests, a restriction R for considering atoms to be neighbors is chosen as the sum of their covalent radii r_c plus a threshold t of 25-35% ($R = r_c \cdot (1 + t)$).

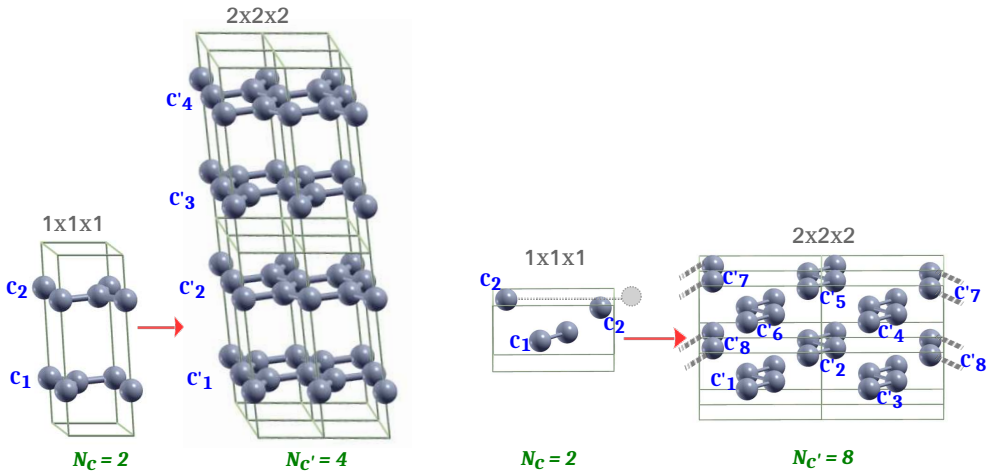

Figure 7.3: Examples of the scaling relations in the number of atomic clusters for compounds with 2D and 1D constituents. N_c is a number of clusters in a primitive and $N_{c'}$ is a number of clusters in a 2×2×2 super-cell. Clusters in the primitive cells are labeled c_i and in the super-cell c'_i. The structure in a) is obviously 2D-like, and the number of clusters doubles when going from the primitive cell to a 2×2×2 super-cell. It is more difficult to visualize the two primitive and eight super-cell chains in the structure in b) since the bonds in clusters c_2, c'_7 and c'_8 are not directly visible but are the consequence of the periodic boundary conditions.

The second part is based on the scaling of the number of clusters in the primitive cell and the 2×2×2 super-cell. If N_c is the number of clusters found in the primitive cell, $N_{c'}$ the number of clusters found in 2×2×2 super-cell and D the dimensionality of the of the constituents, one can write:

$$\frac{N_{c'}}{N_c} = 2^{3-D}. \tag{7.1}$$

For example, if the compound is a 3D bulk ($D = 3$), then all the atoms belong to the same cluster and therefore N_c=1. Repeating the cell will make no difference and only one cluster will be found, $N_{c'}$=1. Solving equation 7.1.2 one gets $D = 3$. The illustration in figure 7.3 shows how the rule is applied to 2D and 1D systems. Figure 7.3a is a layered 2D structure with two clusters in the primitive cell and four in the 2×2×2 super-cell (the number of clusters is increased only in the vertical direction). The factor of two, resulting from $\frac{N_{c'}}{N_c} = \frac{4}{2}$ results in $D = 2$ when solving equation 7.1.2; the structure is therefore two dimensional. Similarly, the primitive cell of the

structure in the figure 7.3b has two clusters (the two top atoms belong to the same cluster due to the periodic boundary conditions) and the corresponding 2×2×2 super-cell has eight clusters in total, resulting in $D = 1$. From here, the generalization to zero dimensional systems, where $\frac{N_{c'}}{N_c} = 8$ and therefore $D = 0$ is straightforward.

The method is not bound to purely 3D, 2D, 1D and 0D structures: a simple extension allows identifying complex mixed-dimensional compounds containing different low-dimensional constituents. Cases where $\frac{N_{c'}}{N_c} \neq 1, 2, 4, 8$ indicate a presence of more than one type of constituents. The dimensionality is then determined by treating each cluster in the primitive cell separately: N_c is then always one (one cluster at the time) and different values of Nc' will correspond to different constituents, depending on how many new clusters of the same type are found in 2×2×2 super-cell.

Such a general approach works on systems of different size and complexity and the only inputs required are the positions of all the atoms and the size of the unit cell. However, the method is purely based on material's geometry and cannot give any prediction on the feasibility of the exfoliation or the stability the low-dimensional constituents. The extracted constituents should be re-valuated using electronic structure methods such as DFT.

7.1.3 Results

The ICSD database contains 184 699[1] crystal structures in total, but roughly half of the entries (93 555) either contain incomplete information or contain atomic positions with partial occupancy. These entries are of no use to us and therefore will not be considered in the study.

We apply the algorithm for determining the low dimensional nature of the crystal constituents on the remaining 91 144 entries. The 3D bulk structure is by far the most common. We find between 79 623 to 81 486 bulk materials in our set (the number is dependent on the choice the threshold in definition of neighbor list restriction R). The 2D, 1D and 0D structures are found in 8 193 to 9 525 entries and the rest are mixed dimensional structures. Figure 7.4 shows distribution of different low-dimensional structures in the total ICSD database. The sensitivity of the algorithm to the choice of the restriction R was also investigated. The number of structures in each group does not significantly change if the threshold is increased up to 15%. The two distinct cases are shown in figure 7.5. The increase in R results in a slight increase in the number on 3D structures, which is expected, since the inclusion of more neighbors results in expansion of the atomic cluster. However, the number if 2D structures is not significantly smaller since some structures, previously being recognized as 1D or 0D, are now identified as 2D. Overall, slightly varying the R value will have effect on structures with sensitive geometry but will not introduce significant changes in the distribution of low-dimensional structures. Visual investigation also showed that there is no ideal R value for this problem (usually system dependent), instead one

[1]The database was obtained sometime in 2016

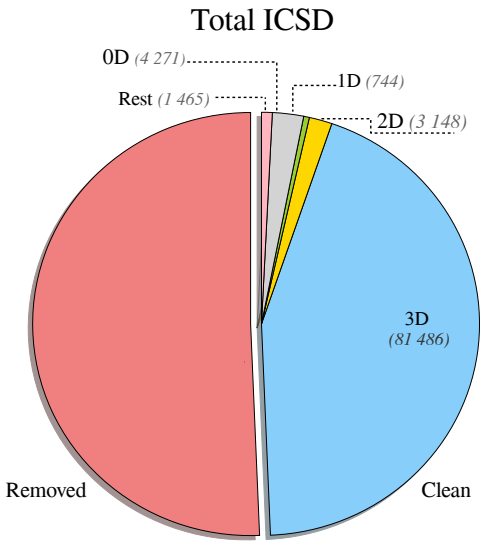

Figure 7.4: Distribution of structures in the ICSD database: more than half of the entries are discarded due to incomplete structure information or atomic positions with partial occupancy. The remaining entries are dominantly 3D bulk structures, while the rest is distributed between 2D, 1D, 0D and mixed-dimensional structures. Overall, only around 6.2% of all the entries (or 12.4% of the usable entries) are made of low dimensional constituents. The R value is set to 1.35.

should do additional inspections once the set of interest is small enough to make it feasible.

Another issue of the ICSD database is a large number of duplicate structures. The *StructureMatcher* module in the *pymatgen*[79] library enables crystal structure comparison and was used here to remove majority of the duplicate entries. Since the definition of duplicate within the *StructureMatcher* depends on the choice of parameters for bond, lattice vector and angle tolerance, the distorted structures that do not fall within assigned thresholds will not be recognized as duplicates. A possible solution to these problem is relaxation of the structures using the DFT and applying the *StructureMatcher* on relaxed geometries. However, that goes beyond the scope of this work where we focus only on ICSD geometries.

Removal of duplicate structures resulted in 2 146 unique entries with 2D constituents and 710 entries with 1D constituents. These structures were further investigated in terms of structural prototypes, as provided in the ICSD. However, 804 2D structures and 438 1D structure have no prototype information so cannot be clas-

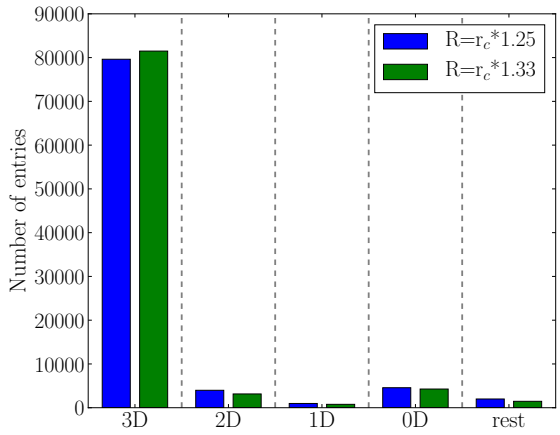

Figure 7.5: Distribution of selected ICSD structures on 3D, 2D, 1D, 0D and mixed-D structures. The dependence on the atomic neighbor list restriction R shows that, by increasing the R value, the number of 3D identified structures increases and the number of low-dimensional structures decreases.

sified. Overall, 617 different prototypes for the layered structures (structures with 2D constituents) and 160 different prototypes for the rod structures (structures with 1D constituents) are found. Figure 7.6 shows the distribution of the most common layered prototypes: CdI_2 group is the most common one when a small R value is used, but does not appear for larger Rs. However, this is a well known layered structure since some experimentally known monolayers have been exfoliated from heterostructure with this prototype (ex. PbI_2[100] or HfS_2[101]). The two MoS_2 prototypes, 3R and 4H, are merely a different stacking of the same, so-called 2H monolayer. The other phase of 2D MoS_2, the so-called 1T phase has the same structure as monolayer CdI_2, however the corresponding layered structure is not experimentally reported in the ICSD. Among other structures we find well known prototypes such as $FePS_3$, a layered system which forms octahedrons similar to those in perovskite structure (Fe atom in the middle and S atoms on the corners of the octahedrons), Bi_2Te_3, SmSI, FeOCl, TiS_3 amongst others. A few examples are shown in figure 7.7. The majority of common prototypes, as shown in figure 7.6 are represented with a similar number of structures regardless of the R value. The few exceptions, where the high R value has not found any layered structure in a prototype, are CdI_2, Delafossite-$NaCrS_2$, FeOCl and Brucite-Mg(OH). In each case, a recognizable layered geometry is present and the 2D constituents are distinguished when visualized.

A similar analysis was performed for the rod structures. The most frequent pro-

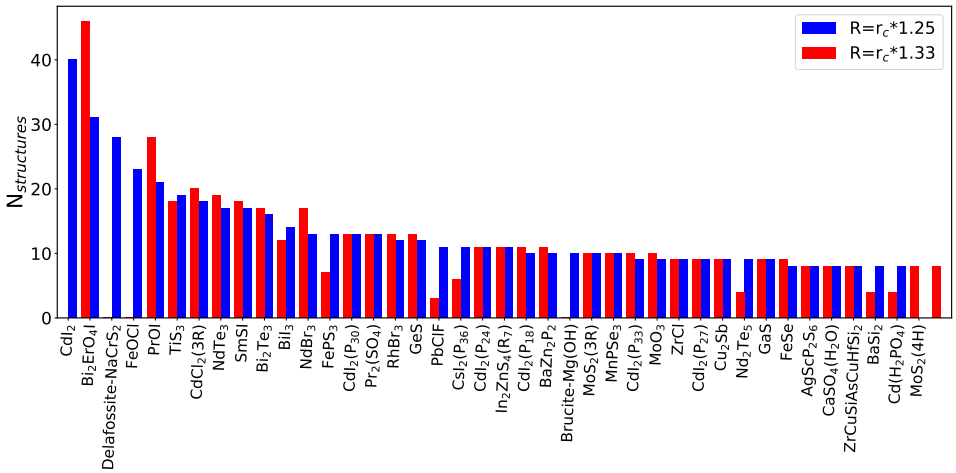

Figure 7.6: Most common layered structure prototypes obtained by this search. The sensitivity to the choice of the R value is also investigated: for the set in the figure, smaller R values result in more prototypes, all of which have been visually identified as belonging to layered structures.

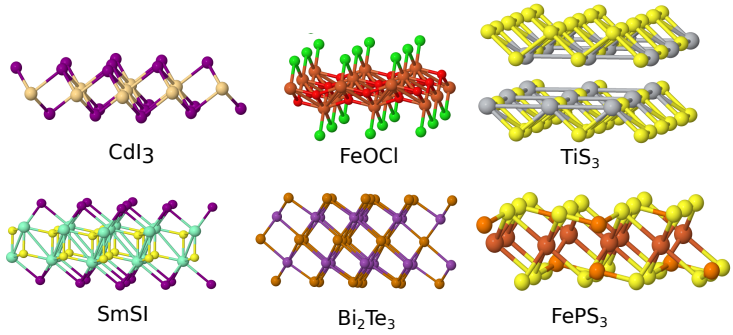

Figure 7.7: Examples of monolayers of some of the most common layered prototypes: CdI_3, FeOCl, TiS_3 (two layers since the structure has a translational symmetry), SmSI, Bi_2Te_3 and $FePS_3$.

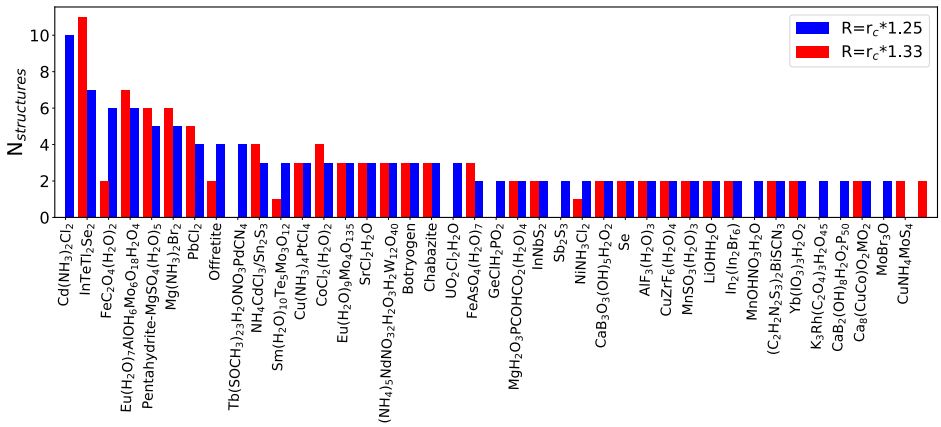

Figure 7.8: Most common rod structure prototypes obtained by this search. The sensitivity to the choice of the R value is similar to the case of the layered structures: smaller R values give more prototypes.

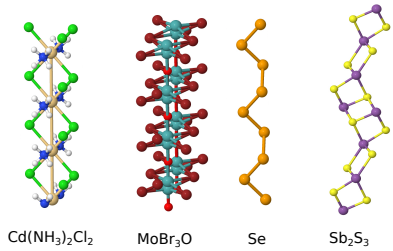

Figure 7.9: Examples of single rods of four rod prototypes. The first example, $Cd(NH_3)_2Cl_2$ is only found when a low R value is used (Figure 7.8) but clearly has a rod-like structure. Other examples are $MoBr_3O$, elemental selenium and Sb_2S_3.

totypes are illustrated in figure 7.8. The same pattern of vanishing prototypes for a large value of R was observed. The prototypes in question were visually investigated, and in all cases a rod structure was found. Such an example, $Cd(NH_3)_2Cl_2$, is illustrated in figure 7.9. The figure also shows other examples of successfully identified 1D constituents, one of them being the trigonal ground state of selenium made of loosely connected spiral rods.

The brief analysis reported above only scratched the surface of the diverse world of low-dimensional heterostructures. As mentioned, there is a large number of possibly interesting but poorly represented layered and rod prototypes which require further attention. The extension to 0D and mixed-dimensional structures is also an obvious step forward. One of the other possible applications of the algorithm is in structural relaxation or genetic algorithms, which are often useful to capture changes is dimensionality of the constituents of the structure.

7.1.4 Conclusion

We have successfully developed an algorithm for systematic classification of materials based on the type of their low dimensional constituents. The algorithm can cope even with structures with varying spacing between the atomic clusters, structures with corrugated clusters or clusters spreading in different directions. The simple approach relies on the material's geometry and defines the clusters of atoms and scaling of numbers of clusters when going from primitive cell to a super-cell. This approach cannot replace the full DFT study since it gives no information on exfoliation energies. It can, however, be used as prior to the DFT study and help decrease the number of structures to consider. Here we show application of the method on the entries in the ICSD database where it successfully identifies experimentally known heterostructures and produces an exhaustive list of potential candidates for exfoliation. The results obtained using this method can serve as a starting point for a screening study or for building a database of low-dimensional materials.

CHAPTER 8

Conclusion

Discovering new materials using computational screening can be a daunting task without a good strategy. This work has been concerned with finding new excellent photovoltaic (PV) and photoelectrochemical (PC) materials, which, must have the following properties: efficient light absorption and carrier separation, low production cost and they should be non-toxic or harmful for the environment. The screening strategy applied here relies on using the correct descriptors for the properties mentioned above. The descriptors were choosen to be: band gap in the visible range, low carrier effective masses and no electronic mid-gap states due to point defects. Additionally, materials are required to be composed of elements that are abundant, non-toxic and come with a low HHI index.

Most of the materials investigated here have not been synthesized yet, which imposes an additional criteria; stability. Whether the material is stable with respect to the decomposition into competing phases is investigated using the convex hull approach. Another issue, phase stability, can be a tricky task in cases where the crystal structure is not known. In that case a search for the ground state of materials was done by investigating known prototypes of the same stoichiometry as the material of interest and finding the structure with lowest energy.

A step-wise procedure, where at each step a new criteria is introduced, and materials not satisfying the criteria are removed from the study, has shown to successfully cope with the task of finding new PV and PC materials. The order in which a descriptor appears in the study depends on the complexity and cost of the calculation needed to obtain it. This way, the "easy" descriptors are introduced earlier and obtained for many materials while the "difficult" ones are added later and are obtained only for a handful of materials.

Our studies resulted in several candidate materials for photovoltaics and photoelectrochemical production of hydrogen. Several of the promissing semiconductors have already been already synthesized, and they satisfy all the criteria introduced. Some of those, like for example Cu_2S, Cu_2O, $CuSbSe_2$, $CsSnI_3$, $ZnSnN_2$, $ZnSiP_2$, $BaZrS_3$ and others, have already been investigated for PV or PC application. Others require additional theoretical and experimental investigation. Also, we discovered new, previously unknown materials which possess all the desired properties. Even though we investigated the stability of the compounds, issues may rise due to non-ideal experimental conditions, thermal effects or metastability of several phases. In my opinion, it is crucial to work closely with the experimentalist as they can point

out individual issues regarding materials of interest. For example, one will face problems when trying top deposit some metals together with sulfur. An example of such a collaboration can be found paper III, where a successful cohesion of experimental and theoretical work resulted in synthesis of $LaYS_3$, a promissing large band gap semiconductor for photoelectrochemical water splitting. A matching crystal structure was obtained as well as good agreement between theoretical and experimental band gap.

In the future, the increasing computational resources available will allow more similar studies. One should keep in mind though that quality and not quantity is what makes good science and reliable results, meaning computers should not be used blindly. Instead, one should focus on improving current methods and make sure that the fundamental science is adequatelly represented. On way to achieve that is by introducing better descriptors. For example, more work can be done on investigating the effect of defects, which will require additional computational resources.

Interesting discussions with the experimentalists put light on practical issues which I have not been fully aware of before, such as previously mentioned problem of depositing some elements together with sulfur. Also, several important questions, mainly regarding stability and metastability of different phases of the compounds, arised from the collaboration and solving those was a great addition to the project. A close collaboration and exchange of knowledge between the theory and experiment is the best strategy toward a sucessfully searching for better energy conversion materials.

Bibliography

[1] José Goldemberg et al., editors. *World energy assessment: energy and the challenge of sustainability*. New York, NY: United Nations Development Programme, 2000.

[2] Nathan S. Lewis and Daniel G. Nocera. "Powering the planet: Chemical challenges in solar energy utilization". en. In: *Proceedings of the National Academy of Sciences* 103.43 (October 2006), pages 15729–15735. DOI: 10.1073/pnas.0603395103.

[3] *Solar power passes 1% global threshold*. June 2015.

[4] Guohua Jiang, Tao Chen, and Qiang Yang. *Photocatalytic Materials*. en. Research article. DOI: 10.1155/2012/186948. 2012.

[5] William Shockley and Hans J. Queisser. "Detailed Balance Limit of Efficiency of p-n Junction Solar Cells". In: *Journal of Applied Physics* 32.3 (March 1961), pages 510–519. DOI: 10.1063/1.1736034.

[6] Albert Polman et al. "Photovoltaic materials: Present efficiencies and future challenges". en. In: *Science* 352.6283 (April 2016), aad4424. DOI: 10.1126/science.aad4424.

[7] Martin A. Green et al. "Solar cell efficiency tables (Version 45)". en. In: *Progress in Photovoltaics: Research and Applications* 23.1 (January 2015), pages 1–9. DOI: 10.1002/pip.2573.

[8] Andrew Rex and Stephen Thornton. "Modern Physics for Scientists and Engineers (Fourth Edition)". In: *All Faculty Scholarship* (January 2013).

[9] M. F. Weber and M. J. Dignam. "Splitting water with semiconducting photoelectrodes—Efficiency considerations". In: *International Journal of Hydrogen Energy* 11.4 (January 1986), pages 225–232. DOI: 10.1016/0360-3199(86)90183-7.

[10] M. C. Hanna and A. J. Nozik. "Solar conversion efficiency of photovoltaic and photoelectrolysis cells with carrier multiplication absorbers". In: *Journal of Applied Physics* 100.7 (October 2006), page 074510. DOI: 10.1063/1.2356795.

[11] Mary D. Archer and James R. Bolton. "Requirements for ideal performance of photochemical and photovoltaic solar energy converters". In: *The Journal of Physical Chemistry* 94.21 (October 1990), pages 8028–8036. DOI: 10.1021/j100384a011.

[12] Sophia Haussener et al. “Simulations of the irradiation and temperature dependence of the efficiency of tandem photoelectrochemical water-splitting systems”. en. In: *Energy & Environmental Science* 6.12 (2013), pages 3605–3618. DOI: 10.1039/C3EE41302K.

[13] Brian Seger et al. “2-Photon tandem device for water splitting: comparing photocathode first versus photoanode first designs”. In: *Energy & Environmental Science* 7.8 (2014), pages 2397–2413. DOI: 10.1039/c4ee01335b.

[14] *The Projector Augmented-wave Method*. 2017. URL: https://wiki.fysik.dtu.dk/gpaw/ (visited on August 17, 2017).

[15] M Born and R Oppenheimer. “Zur Quantentheorie der Molekeln”. In: *Annalen der Physik* 389 (1927), pages 457–484. DOI: 10.1002/andp.19273892002.

[16] Jorge Kohanoff. *Electronic Structure Calculations for Solids and Molecules*. Cambridge, 2006.

[17] L. H. Thomas. “The calculation of atomic fields”. In: *Mathematical Proceedings of the Cambridge Philosophical Society* 23.5 (1927), pages 542–548. DOI: 10.1017/S0305004100011683.

[18] E Fermi. “Statistical method to determine some properties of atoms”. In: *Rend. R. Acc. Naz. dei Lincei* 6.1 (1927), pages 602–607.

[19] P. Hohenberg and W. Kohn. “Inhomogeneous Electron Gas”. In: *Phys. Rev.* 136 (3B November 1964), B864–B871. DOI: 10.1103/PhysRev.136.B864.

[20] W. Kohn and L. J. Sham. “Self-Consistent Equations Including Exchange and Correlation Effects”. In: *Physical Review* 140.4A (1965), A1133–A1138. DOI: 10.1103/PhysRev.140.A1133.

[21] D. M. Ceperley and B. J. Alder. “Ground State of the Electron Gas by a Stochastic Method”. In: *Phys. Rev. Lett.* 45 (7 August 1980), pages 566–569. DOI: 10.1103/PhysRevLett.45.566.

[22] John P. Perdew, Kieron Burke, and Matthias Ernzerhof. “Generalized Gradient Approximation Made Simple”. In: *Phys. Rev. Lett.* 77 (1996), pages 3865–3868.

[23] J. J. Mortensen, L. B. Hansen, and K. W. Jacobsen. “Real-space grid implementation of the projector augmented wave method”. In: *Phys. Rev. B* 71 (3 January 2005), page 035109. DOI: 10.1103/PhysRevB.71.035109.

[24] A. H. Larsen et al. “Localized atomic basis set in the projector augmented wave method”. In: *Phys. Rev. B* 80 (19 November 2009), page 195112. DOI: 10.1103/PhysRevB.80.195112.

[25] *Atomistic Simulation Environment*. 2017. URL: https://wiki.fysik.dtu.dk/ase/ (visited on August 17, 2017).

[26] Ask Hjorth Larsen et al. “The atomic simulation environment—a Python library for working with atoms”. In: *Journal of Physics: Condensed Matter* 29.27 (2017), page 273002.

[27] David Vanderbilt. “Soft self-consistent pseudopotentials in a generalized eigenvalue formalism”. In: *Phys. Rev. B* 41 (11 April 1990), pages 7892–7895. DOI: 10.1103/PhysRevB.41.7892.

[28] Karsten Rostgaard. *The Projector Augmented-wave Method*. 2010. URL: https://wiki.fysik.dtu.dk/gpaw/_downloads/paw_note.pdf (visited on August 17, 2017).

[29] P. E. Blöchl. “Projector augmented-wave method”. In: *Phys. Rev. B* 50 (24 December 1994), pages 17953–17979. DOI: 10.1103/PhysRevB.50.17953.

[30] John P. Perdew et al. “Understanding band gaps of solids in generalized Kohn–Sham theory”. en. In: *Proceedings of the National Academy of Sciences* 114.11 (March 2017), pages 2801–2806. DOI: 10.1073/pnas.1621352114.

[31] John P. Perdew and Mel Levy. “Physical Content of the Exact Kohn-Sham Orbital Energies: Band Gaps and Derivative Discontinuities”. In: *Phys. Rev. Lett.* 51 (20 November 1983), pages 1884–1887. DOI: 10.1103/PhysRevLett.51.1884.

[32] John P. Perdew. “Density functional theory and the band gap problem”. en. In: *International Journal of Quantum Chemistry* 30.3 (September 1986), pages 451–451. DOI: 10.1002/qua.560300314.

[33] M. Kuisma et al. In: *Phys. Rev. B* 82.11 (September 2010), page 115106. DOI: 10.1103/PhysRevB.82.115106.

[34] O. Gritsenko et al. “Self-consistent Approximation to the Kohn-Sham Exchange Potential”. In: *Phys. Rev. A* 51 (1995), page 1944.

[35] John P. Perdew et al. “Restoring the Density-Gradient Expansion for Exchange in Solids and Surfaces”. In: *Phys. Rev. Lett.* 100 (2008), page 136406.

[36] Ivano E. Castelli et al. “Computational screening of perovskite metal oxides for optimal solar light capture”. en. In: *Energy & Environmental Science* 5.2 (January 2012), pages 5814–5819. DOI: 10.1039/C1EE02717D.

[37] Ivano E. Castelli et al. “New Light-Harvesting Materials Using Accurate and Efficient Bandgap Calculations”. en. In: *Advanced Energy Materials* 5.2 (January 2015), n/a–n/a. DOI: 10.1002/aenm.201400915.

[38] Axel D. Becke and Erin R. Johnson. “A simple effective potential for exchange”. In: *The Journal of Chemical Physics* 124.22 (June 2006), page 221101. DOI: 10.1063/1.2213970.

[39] Fabien Tran and Peter Blaha. “Accurate Band Gaps of Semiconductors and Insulators with a Semilocal Exchange-Correlation Potential”. In: *Phys. Rev. Lett.* 102 (22 June 2009), page 226401. DOI: 10.1103/PhysRevLett.102.226401.

[40] Attila Szabo and Neil S Ostlund. *Modern quantum chemistry : introduction to advanced electronic structure theory*. English. Mineola, N.Y. : Dover Publications, 1996.

[41] Axel D. Becke. “Density-functional thermochemistry. III. The role of exact exchange”. In: *The Journal of Chemical Physics* 98.7 (April 1993), pages 5648–5652. DOI: 10.1063/1.464913.

[42] Carlo Adamo and Vincenzo Barone. “Toward reliable density functional methods without adjustable parameters: The PBE0 model”. In: *The Journal of Chemical Physics* 110.13 (March 1999), pages 6158–6170. DOI: 10.1063/1.478522.

[43] Jochen Heyd, Gustavo E. Scuseria, and Matthias Ernzerhof. “Hybrid functionals based on a screened Coulomb potential”. In: *The Journal of Chemical Physics* 118.18 (April 2003), pages 8207–8215. DOI: 10.1063/1.1564060.

[44] John P. Perdew et al. “Atoms, molecules, solids, and surfaces: Applications of the generalized gradient approximation for exchange and correlation”. In: *Phys. Rev. B* 46 (11 September 1992), pages 6671–6687. DOI: 10.1103/PhysRevB.46.6671.

[45] Burak Himmetoglu et al. “Hubbard-corrected DFT energy functionals: The LDA+U description of correlated systems”. In: *International Journal of Quantum Chemistry* 114.1 (2014), pages 14–49. DOI: 10.1002/qua.24521.

[46] J. J. Mortensen et al. “Bayesian Error Estimation in Density-Functional Theory”. In: *Phys. Rev. Lett.* 95 (21 November 2005), page 216401. DOI: 10.1103/PhysRevLett.95.216401.

[47] Jess Wellendorff et al. “Density functionals for surface science: Exchange-correlation model development with Bayesian error estimation”. In: *Phys. Rev. B* 85 (23 June 2012), page 235149. DOI: 10.1103/PhysRevB.85.235149.

[48] Jess Wellendorff et al. “mBEEF: An accurate semi-local Bayesian error estimation density functional”. In: *The Journal of Chemical Physics* 140.14 (April 2014), page 144107. DOI: 10.1063/1.4870397.

[49] Keld T. Lundgaard et al. “mBEEF-vdW: Robust fitting of error estimation density functionals”. In: *Phys. Rev. B* 93 (23 June 2016), page 235162. DOI: 10.1103/PhysRevB.93.235162.

[50] Mohnish Pandey and Karsten W. Jacobsen. “Heats of formation of solids with error estimation: The mBEEF functional with and without fitted reference energies”. In: *Phys. Rev. B* 91 (23 June 2015), page 235201. DOI: 10.1103/PhysRevB.91.235201.

[51] Vladan Stevanovi ć et al. “Correcting density functional theory for accurate predictions of compound enthalpies of formation: Fitted elemental-phase reference energies”. In: *Phys. Rev. B* 85 (11 March 2012), page 115104. DOI: 10.1103/PhysRevB.85.115104.

[52] I. E. Castelli and K. W. Jacobsen. “Designing rules and probabilistic weighting for fast materials discovery in the Perovskite structure”. en. In: *Modelling and Simulation in Materials Science and Engineering* 22.5 (2014), page 055007. DOI: 10.1088/0965-0393/22/5/055007.

[53] Ivano E. Castelli et al. “Stability and bandgaps of layered perovskites for one- and two-photon water splitting”. en. In: *New Journal of Physics* 15.10 (2013), page 105026. DOI: 10.1088/1367-2630/15/10/105026.

[54] Anubhav Jain et al. “Performance of genetic algorithms in search for water splitting perovskites”. en. In: *Journal of Materials Science* 48.19 (October 2013), pages 6519–6534. DOI: 10.1007/s10853-013-7448-9.

[55] Yin Wang et al. “Electronic structure of III-V zinc-blende semiconductors from first principles”. In: *Physical Review B* 87.23 (June 2013), page 235203. DOI: 10.1103/PhysRevB.87.235203.

[56] Marina R. Filip and Feliciano Giustino. “Computational Screening of Homovalent Lead Substitution in Organic–Inorganic Halide Perovskites”. In: *The Journal of Physical Chemistry C* 120.1 (January 2016), pages 166–173. DOI: 10.1021/acs.jpcc.5b11845.

[57] A. Laio and M. Parrinello. “Escaping free-energy minima”. In: *Proceedings of the National Academy of Sciences* 99.20 (September 2002), pages 12562–12566. DOI: 10.1073/pnas.202427399.

[58] Stefan Goedecker. “Minima hopping: An efficient search method for the global minimum of the potential energy surface of complex molecular systems”. In: *The Journal of Chemical Physics* 120.21 (June 2004), pages 9911–9917. DOI: 10.1063/1.1724816.

[59] Artem R Oganov and Colin W Glass. “Crystal structure prediction using ab initio evolutionary techniques: principles and applications.” English. In: *Journal of Chemical Physics* 124.24 (June 2006), page 244704. DOI: 10.1063/1.2210932.

[60] Christopher C. Fischer et al. “Predicting crystal structure by merging data mining with quantum mechanics”. en. In: *Nature Materials* 5.8 (August 2006), pages 641–646. DOI: 10.1038/nmat1691.

[61] Anubhav Jain et al. “A high-throughput infrastructure for density functional theory calculations”. In: *Computational Materials Science* 50.8 (June 2011), pages 2295–2310. DOI: 10.1016/j.commatsci.2011.02.023.

[62] G. Bergerhoff et al. “The Inorganic Crystal Structure Data Base”. In: *J. Chem. Inf. Comput. Sci.* 23 (1983), pages 66–69.

[63] Saulius Gražulis et al. “Crystallography Open Database (COD): an open-access collection of crystal structures and platform for world-wide collaboration”. In: *Nucleic Acids Research* 40.Database issue (January 2012), pages D420–427. DOI: 10.1093/nar/gkr900.

[64] D. Reyes-Coronado et al. “Phase-pure TiO 2 nanoparticles: anatase, brookite and rutile”. en. In: *Nanotechnology* 19.14 (2008), page 145605. DOI: 10.1088/0957-4484/19/14/145605.

[65] Kristian S. Thygesen and Karsten W. Jacobsen. “Making the most of materials computations”. In: *Science* 354.6309 (2016), pages 180–181. DOI: 10.1126/science.aah4776. eprint: http://science.sciencemag.org/content/354/6309/180.full.pdf.

[66] *NOMAD Repository*.

[67] Claudia Draxl, Francesc Illas, and Matthias Scheffler. “Computational materials: Open data settled in materials theory”. In: *Nature* 548.7669 (August 2017), pages 523–523.

[68] Stefano Curtarolo et al. “AFLOW: An automatic framework for high-throughput materials discovery”. In: *Computational Materials Science* 58 (2012), pages 218–226. DOI: https://doi.org/10.1016/j.commatsci.2012.02.005.

[69] Anubhav Jain et al. “Commentary: The Materials Project: A materials genome approach to accelerating materials innovation”. In: *APL Materials* 1.1 (2013), page 011002. DOI: 10.1063/1.4812323. eprint: http://dx.doi.org/10.1063/1.4812323.

[70] James E. Saal et al. “Materials Design and Discovery with High-Throughput Density Functional Theory: The Open Quantum Materials Database (OQMD)”. In: *JOM* 65.11 (November 2013), pages 1501–1509. DOI: 10.1007/s11837-013-0755-4.

[71] D. D. Landis et al. “The Computational Materials Repository”. In: *Computing in Science Engineering* 14.6 (November 2012), pages 51–57. DOI: 10.1109/MCSE.2012.16.

[72] Peter C. K. Vesborg and Thomas F. Jaramillo. “Addressing the terawatt challenge: scalability in the supply of chemical elements for renewable energy”. In: *RSC Adv.* 2 (21 2012), pages 7933–7947. DOI: 10.1039/C2RA20839C.

[73] Michael W. Gaultois et al. “Data-Driven Review of Thermoelectric Materials: Performance and Resource Considerations”. In: *Chemistry of Materials* 25.15 (August 2013), pages 2911–2920. DOI: 10.1021/cm400893e.

[74] C. Bradford Barber, David P. Dobkin, and Hannu Huhdanpaa. “The Quickhull Algorithm for Convex Hulls”. In: *ACM Trans. Math. Softw.* 22.4 (December 1996), pages 469–483. DOI: 10.1145/235815.235821.

[75] Filippo De Angelis and Prashant Kamat. “A Conversation with Michael Grätzel”. In: *ACS Energy Letters* 2.7 (July 2017), pages 1674–1676. DOI: 10.1021/acsenergylett.7b00523.

[76] O Madelung. *Semiconductors Data Handbook*. Berlin: Springer, 2004, pages 815–835.

[77] Geoffroy Hautier et al. “How Does Chemistry Influence Electron Effective Mass in Oxides? A High-Throughput Computational Analysis”. In: *Chemistry of Materials* 26.19 (2014), pages 5447–5458. DOI: 10.1021/cm404079a. eprint: http://dx.doi.org/10.1021/cm404079a.

[78] Wahyu Setyawan and Stefano Curtarolo. "High-throughput electronic band structure calculations: challenges and tools". In: *Computational Materials Science* 49.2 (August 2010). arXiv: 1004.2974, pages 299–312. DOI: 10.1016/J.Commatsci.2010.05.010.

[79] Shyue Ping Ong et al. "Python Materials Genomics (pymatgen): A robust, open-source python library for materials analysis". In: *Computational Materials Science* 68 (2013), pages 314–319. DOI: http://dx.doi.org/10.1016/j.commatsci.2012.10.028.

[80] Christoph Freysoldt et al. "First-principles calculations for point defects in solids". In: *Rev. Mod. Phys.* 86 (1 March 2014), pages 253–305. DOI: 10.1103/RevModPhys.86.253.

[81] Andriy Zakutayev et al. "Defect Tolerant Semiconductors for Solar Energy Conversion". In: *The Journal of Physical Chemistry Letters* 5.7 (2014). PMID: 26274458, pages 1117–1125. DOI: 10.1021/jz5001787. eprint: http://dx.doi.org/10.1021/jz5001787.

[82] Angela N. Fioretti et al. "Combinatorial Insights into Doping Control and Transport Properties of Zinc Tin Nitride". In: *J. Mater. Chem. C* 3 (2015), pages 11017–11028.

[83] Shiyou Chen et al. "Phase Stability and Defect Physics of a Ternary ZnSnN Semiconductor: First Principles Insights". In: *Adv. Mater.* 26 (2014), pages 311–315.

[84] Prineha Narang et al. "Bandgap Tunability in Zn(Sn,Ge)N Semiconductor Alloys". In: *Adv. Mater.* 26.8 (2014), pages 1235–1241.

[85] Lise Lahourcade et al. "Structural and Optoelectronic Characterization of RF Sputtered ZnSnN ". In: *Adv. Mater.* 25 (2013), pages 2562–2566.

[86] Aaron D. Martinez et al. "Solar Energy Conversion Properties and Defect Physics of ZnSiP ". In: *Ener. Environ. Sci.* 9 (2016), pages 1031–1041.

[87] *Computational Materials repository*. 2017. URL: https://cmr.fysik.dtu.dk/ (visited on October 20, 2017).

[88] Angela N. Fioretti et al. "Combinatorial Insights into Doping Control and Transport Properties of Zinc Tin Nitride". In: *J. Mater. Chem. C* 3 (2015), pages 11017–11028.

[89] Jing Gu et al. "Water Reduction by a p-$GaInP_2$ Photoelectrode Stabilized by an Amorphous TiO_2 Coating and a Molecular Cobalt Catalyst". In: *Nat. Mater.* 15 (2016), pages 456–460.

[90] Aaron D. Martinez et al. "Solar Energy Conversion Properties and Defect Physics of $ZnSiP_2$". In: *Ener. Environ. Sci.* 9 (2016), pages 1031–1041.

[91] Samanthe Perera et al. "Chalcogenide perovskites – an emerging class of ionic semiconductors". English. In: *Nano Energy* 22 (April 2016), pages 129–135. DOI: 10.1016/j.nanoen.2016.02.020.

[92] Shanyuan Niu et al. “Bandgap Control via Structural and Chemical Tuning of Transition Metal Perovskite Chalcogenides”. In: *Advanced Materials* 29.9 (March 2017), page 1604733. DOI: 10.1002/adma.201604733.

[93] Jaeseok Heo et al. “CuTaS 3: Intermetal d–dTransitions Enable High Solar Absorption”. English. In: *Chemistry Of Materials* 29.6 (January 2017), pages 2594–2598. DOI: 10.1021/acs.chemmater.6b04730.

[94] Teodor K. Todorov et al. “Ultrathin high band gap solar cells with improved efficiencies from the world’s oldest photovoltaic material”. In: *Nature Communications* 8.1 (September 2017), page 682. DOI: 10.1038/s41467-017-00582-9.

[95] J. D. Joannopoulos, M. Schlüter, and Marvin L. Cohen. “Electronic structure of trigonal and amorphous Se and Te”. In: *Phys. Rev. B* 11 (6 March 1975), pages 2186–2199. DOI: 10.1103/PhysRevB.11.2186.

[96] K. S. Novoselov et al. “Electric Field Effect in Atomically Thin Carbon Films”. In: *Science* 306.5696 (2004), pages 666–669. DOI: 10.1126/science.1102896. eprint: http://science.sciencemag.org/content/306/5696/666.full.pdf.

[97] Ganesh R. Bhimanapati et al. “Recent Advances in Two-Dimensional Materials beyond Graphene”. In: *ACS Nano* 9.12 (2015). PMID: 26544756, pages 11509–11539. DOI: 10.1021/acsnano.5b05556. eprint: http://dx.doi.org/10.1021/acsnano.5b05556.

[98] Yu Li et al. “One-Dimensional Metal Oxide Nanotubes, Nanowires, Nanoribbons, and Nanorods: Synthesis, Characterizations, Properties and Applications”. In: *Critical Reviews in Solid State and Materials Sciences* 37.1 (2012), pages 1–74. DOI: 10.1080/10408436.2011.606512. eprint: http://dx.doi.org/10.1080/10408436.2011.606512.

[99] *Building neighbor-lists — ASE documentation*. 2017. URL: https://wiki.fysik.dtu.dk/ase/ase/neighborlist.html (visited on October 3, 2017).

[100] Mianzeng Zhong et al. “Large-scale 2D PbI2 monolayers: experimental realization and their indirect band-gap related properties”. In: *Nanoscale* 9 (11 2017), pages 3736–3741. DOI: 10.1039/C6NR07924E.

[101] Binjie Zheng et al. “Vertically oriented few-layered HfS 2 nanosheets: growth mechanism and optical properties”. In: *2D Materials* 3.3 (2016), page 035024.